







# IVW - Schriftenreihe Band 146

Leibniz-Institut für Verbundwerkstoffe GmbH  
Kaiserslautern

---

**Benjamin Kelkel**

**On the influence of source depth and source-to-sensor distance on the acoustic emission signatures of damaging events in cross-ply carbon fibre-reinforced plastics**

Bibliografische Information Der Deutschen Bibliothek

Die Deutsche Bibliothek verzeichnet diese Publikation in der Deutschen Nationalbibliografie; detaillierte bibliografische Daten sind im Internet über <<http://dnb.dnb.de>> abrufbar.

Bibliographic information published by Die Deutsche Bibliothek

Die Deutsche Bibliothek lists this publication in the Deutsche Nationalbibliografie; detailed bibliographic data is available in the Internet at <<http://dnb.dnb.de>>.

Herausgeber: Leibniz-Institut für Verbundwerkstoffe GmbH  
Prof. Dr.-Ing. Ulf Breuer  
Erwin-Schrödinger-Straße 58  
Technische Universität Kaiserslautern  
67663 Kaiserslautern  
<http://www.ivw.uni-kl.de>

Verlag: Leibniz-Institut für Verbundwerkstoffe GmbH

Druck: pri-me Printservice & Medienservice  
Barbarossastraße 1  
67655 Kaiserslautern  
D-386

© Leibniz-Institut für Verbundwerkstoffe GmbH, Kaiserslautern 2021

Alle Rechte vorbehalten, auch das des auszugsweisen Nachdrucks, der auszugsweisen oder vollständigen Wiedergabe (Photographie, Mikroskopie), der Speicherung in Datenverarbeitungsanlagen und das der Übersetzung.

Als Manuskript gedruckt. Printed in Germany.  
ISSN 1615-021X  
ISBN 978-3-944440-43-9

# **On the influence of source depth and source-to-sensor distance on the acoustic emission signatures of damaging events in cross-ply carbon fibre-reinforced plastics**

Vom Fachbereich Maschinenbau und Verfahrenstechnik  
der Technischen Universität Kaiserslautern  
zur Erlangung des akademischen Grades

**Doktor-Ingenieur (Dr.-Ing.)**

genehmigte

**Dissertation**

von

Herrn

Dipl.-Ing. Benjamin Kelkel

aus Euskirchen

Tag der mündlichen Prüfung: 04. November 2020

Prüfungsvorsitzender: Prof. Dr.-Ing. Joachim Hausmann

Berichterstatter: Prof. Dr.-Ing. Ulf Breuer

Prof. Dr.-Ing. Tilmann Beck

Prof. Dr. rer. nat. habil. Marc Kreutzbruck

D386



# Vorwort

Die vorliegende Arbeit entstand im Rahmen meiner Tätigkeit bei der Institut für Verbundwerkstoffe GmbH (IVW) in der Abteilung Werkstoffwissenschaft. Hier war ich von Juli 2014 bis Dezember 2019 als wissenschaftlicher Mitarbeiter im Kompetenzfeld "Tailored and Smart Composites" beschäftigt. An dieser Stelle möchte ich einigen Personen meinen Dank aussprechen, die mich während dieser Zeit unterstützt haben und damit einen wesentlichen Beitrag zu dieser Arbeit geleistet haben.

An erster Stelle möchte ich mich besonders bei meinem Doktorvater Prof. Dr.-Ing. Ulf Breuer bedanken. Für die Betreuung der Arbeit, das ehrliche Feedback und das Vertrauen in meine Person bin ich ihm sehr dankbar. Ebenso geht mein Dank an Prof. Dr.-Ing. Tilmann Beck und Prof. Dr. rer. nat. habil. Marc Kreutzbruck für die Übernahme der Berichterstattung und die leidenschaftlichen Diskussionen, die mir zusätzliche Perspektiven auf meine Arbeit geboten haben. Bedanken möchte ich mich ebenso bei Herrn Prof. Dr.-Ing. Joachim Hausmann, der den Prüfungsvorsitz übernommen hat.

Ein großer Dank geht ebenso an meinen Betreuer Dr. Martin Gurka, der mich immer wieder mit auf eine Reise in die Welt der Physik genommen hat und mir dabei die Unterstützung, den Freiraum und das Vertrauen gegeben hat meiner wissenschaftlichen Neugier nachzugehen. Mein Dank gilt ebenfalls meinem Abteilungsleiter Dr.-Ing. Bernd Wetzel, der mir mit seiner Leidenschaft für wissenschaftliches Arbeiten stets Mut machte.

Ferner gilt mein Dank allen Mitarbeitern des Instituts, die mich auf meiner Reise unterstützt haben und dabei für eine angenehme Arbeitsatmosphäre gesorgt haben. Für die zahlreichen Gespräche, die Unterstützung und die tolle Zeit möchte ich mich besonders bei Vitalij Popow, Bai-Cheng Jim, Andreas Klingler, Julia Vogtmann, Tim Kroos, Mark Kopietz, Kerstin Steidle, Sebastian Nissle, Moritz Hübler, Max Kaiser, Sonja Adler, Emmanuel Isaac Akpan, Stephan Becker, Maurice Gilberg, Daniel Vogelsanger, Oliver Rimmel, Matthias Domm, Thomas Rief, Florian Schimmer, Thorsten Heydt, Benedikt Hannemann, Florian Rieger, Stefan Schmidt und Constantin Bauer bedanken.

In diesem Zusammenhang möchte ich mich speziell bedanken bei Vitalij Popow, mit dem ich die Welt der zerstörungsfreien Prüfung gemeinsam im Büro, im Labor und auf internationalen Konferenzen erkunden durfte und den ich als Kollegen und Freund in dieser Zeit kennen und schätzen gelernt habe. Bei Thomas Rief, der mich als langjähriger Wegbegleiter und Freund mit seinen Worten, Witzen und Taten immer

wieder aus dem Ernst des Lebens holen konnte und mit dem ich sogleich schöne als auch schwere Momente teilen konnte. Bei Andreas Klingler, der mich nicht nur mit seiner Leidenschaft für die Wissenschaft fasziniert hat, sondern ebenso mit seinen Vorlieben für Musik, TV Shows und Suppen. Bei Bai-Cheng Jim, für seine offene Art und Hilfsbereitschaft sowie die zahlreichen kulinarischen Erlebnisse.

Ebenso bedanken möchte mich an dieser Stelle bei Jan Rehra, Stefan Schmidt, Marcel Bücken, Florian Mischo, Tobias Donhauser, Andreas Kenf, Konstanin Mehl, Stefan Brunner, Petra Volk, Heidrun Plocharzik, Ralf Schimmele, Markus Hentzel, Stefan Schmitt, Herrmann Giertzsch, Joachim Stephan, Andreas Gebhard, Barbara Güttler, Nicole Motsch-Eichmann, Liudmyla Gryshchuk, Sergey Gryshchuk, Stefan Gabriel, Rolf Walter, Thorsten Becker, Harald Weber, Christian Ackel, Pia Eichert, Volker Dissandt, Uwe Schmitt, Tobias Neisius, Thomas Schütz, Jörg Blaurock, Matthias Bandler, Karin Panter, Silke Fischer, Ariane McCauley und Regina Köhne für jegliche technische, administrative und moralische Unterstützung.

Bei Brandon Rice und Thomas Rief möchte ich mich zudem für das Korrekturlesen der Arbeit bedanken.

Ferner möchte ich Benedikt Fols und Joshua Müller ein großes Dankeschön für die tatkräftige Unterstützung während ihrer Tätigkeit als Hilfwissenschaftler aussprechen.

Ebenso bedanken möchte ich mich bei allen Studenten, die ich im Rahmen Ihrer Abschlussarbeiten betreuen durfte und die mich mit Ihren Arbeiten unterstützt haben.

Ein großer Dank geht ebenso an Prof. Dr. Markus Sause, der immer ein offenes Ohr für mich hatte und auf die zahlreichen Fragen zur Schallemissionsanalyse auch immer eine adäquate Antwort.

Bedanken möchte ich mich auch bei Herrn Herbert Karzel und Herrn Thomas Thenikl von Vallen Systeme für die Unterstützung während dieser Zeit.

Ebenso möchte ich mich bei Jens Schuster für die Unterstützung bei den Ultraschallprüfungen bedanken.

Zu guter Letzt möchte ich mich besonders bei meiner Familie bedanken. Für die Unterstützung und die Geduld, die sie mir in dieser nicht immer einfachen Zeit entgegengebracht haben. Hier möchte ich mich bei meinen Eltern Alfons und Maria, meinem Stiefvater Uwe, meiner Oma Frieda, meinem Opa Josef, meinem Bruder

Daniel, meiner Schwägerin Sabine sowie meinem Patenkind Jonas und meiner Nichte Linda bedanken, die mich auf ihre eigene Weise immer wieder motivieren konnten weiter zu machen. Ebenso bedanken möchte ich mich bei Engelbert und Angelika für die Unterstützung in Form von Worten und rosinenlosen Kuchen. Ein besonderer Dank geht an dieser Stelle an meine Freundin Sarah, die stets die richtigen Worte gefunden hat und die ich in dieser Zeit einmal mehr kennen und lieben gelernt habe (Danke Danke Danke).

Die Zeit am IVW war für mich ein besonderer Lebensabschnitt, in dem ich viel gelernt habe. Nicht nur über die Komplexität von akustischen Wellen, die Bandbreite von Bleistiftminenbrüchen und die Eigenarten von Faserkunststoffverbunden, sondern auch über das Leben und mich selbst. Ich bin froh mich für diese abenteuerliche Reise entschieden zu haben, auf der viele Kollegen zu Freunden und Wegbegleitern wurden.

Saarbrücken, im Dezember 2020

Benjamin Kelkel

*"That's the way I'm made"*  
- Rocky Balboa -



# Contents

<b>Kurzfassung</b> . . . . .	<b>IV</b>
<b>Abstract</b> . . . . .	<b>V</b>
<b>Zusammenfassung</b> . . . . .	<b>VI</b>
<b>List of abbreviations</b> . . . . .	<b>XI</b>
<b>1 Introduction</b> . . . . .	<b>1</b>
<b>2 State of the art</b> . . . . .	<b>3</b>
2.1 Mechanical failure of continuous fibre-reinforced plastics . . . . .	3
2.1.1 Damaging modes . . . . .	3
2.1.2 Damage evolution in cross-ply laminates . . . . .	4
2.2 Ultrasonic guided waves . . . . .	6
2.2.1 Fundamentals . . . . .	6
2.2.2 Attenuation . . . . .	12
2.3 Acoustic emission analysis . . . . .	15
2.3.1 Working principle and applications . . . . .	15
2.3.2 Localization of AE sources in FRP . . . . .	18
2.3.3 Identification of AE sources in FRP . . . . .	20
2.3.4 The acoustic fingerprint of damaging modes in FRP . . . . .	31
2.4 Influencing factors on AE source characteristics . . . . .	32
2.4.1 The influence of source depth . . . . .	33
2.4.2 The influence of source-to-sensor distance . . . . .	34
2.5 Where is the gap? . . . . .	36
<b>3 Thesis goals and implementation</b> . . . . .	<b>39</b>
<b>4 Design and manufacturing of CFRP laminates</b> . . . . .	<b>43</b>
4.1 Material . . . . .	43
4.2 Design of laminates and loading scenario . . . . .	44
4.3 Manufacturing of laminates . . . . .	46
4.4 Characterization of laminate properties . . . . .	47
<b>5 Characterization of wave propagation</b> . . . . .	<b>51</b>
5.1 Theoretical . . . . .	51
5.1.1 Determination of underlying properties . . . . .	51
5.1.2 Dispersion curves . . . . .	52
5.1.3 Displacement fields . . . . .	56
5.2 Experimental . . . . .	58

---

5.2.1	Setup . . . . .	58
5.2.2	Evaluation methodology . . . . .	61
5.2.3	Limitations . . . . .	65
5.2.4	Results . . . . .	70
5.3	Preliminary conclusion . . . . .	73
<b>6</b>	<b>Preliminary study: AE from artificial sources . . . . .</b>	<b>75</b>
6.1	Experimental . . . . .	75
6.1.1	Setup . . . . .	75
6.1.2	Evaluation methodology . . . . .	76
6.1.3	Results . . . . .	77
6.2	Preliminary conclusion . . . . .	85
<b>7</b>	<b>Main study: AE from damaging events . . . . .</b>	<b>87</b>
7.1	Concept . . . . .	87
7.2	Specimens . . . . .	88
7.3	Environmental conditions . . . . .	89
7.4	Experimental setup: General . . . . .	89
7.4.1	Quasi-static testing . . . . .	89
7.4.2	Acoustic emission analysis . . . . .	89
7.4.3	Specimen edge observation . . . . .	90
7.5	Experimental setup: Specific . . . . .	90
7.5.1	Stage 2: Standard AE . . . . .	90
7.5.2	Stage 3: Modal AE . . . . .	92
7.6	Evaluation methodology . . . . .	93
7.6.1	Stage 2: Standard AE . . . . .	93
7.6.2	Stage 3: Modal AE . . . . .	96
7.6.3	Digital Image Correlation . . . . .	98
7.7	Discussion & Results . . . . .	101
7.7.1	Tensile strength . . . . .	101
7.7.2	Young's modulus . . . . .	102
7.7.3	Transverse matrix cracking . . . . .	103
7.7.4	Group velocity of triggering wave mode . . . . .	106
7.7.5	The influence of source-to-sensor distance . . . . .	109
7.7.6	The influence of source depth . . . . .	119
<b>8</b>	<b>Conclusion . . . . .</b>	<b>135</b>
<b>9</b>	<b>Outlook . . . . .</b>	<b>141</b>
	<b>References . . . . .</b>	<b>142</b>

---

<b>List of figures</b> . . . . .	<b>160</b>
<b>List of tables</b> . . . . .	<b>169</b>
<b>Appendices</b> . . . . .	<b>170</b>
<b>A Laminate properties</b> . . . . .	<b>170</b>
<b>B Microscopic images</b> . . . . .	<b>172</b>
<b>C Recalculation of elastic properties</b> . . . . .	<b>175</b>
<b>D Theoretical dispersion diagrams</b> . . . . .	<b>177</b>
<b>E Fixture for the characterization of wave propagation</b> . . . . .	<b>181</b>
<b>F Limitations to wave characterization</b> . . . . .	<b>184</b>
<b>G Experimental dispersion diagrams</b> . . . . .	<b>188</b>
<b>H Preliminary study: Time signals</b> . . . . .	<b>189</b>
<b>I Preliminary study: Continuous wavelet transforms</b> . . . . .	<b>191</b>
<b>J Preliminary study: Frequency spectra</b> . . . . .	<b>193</b>
<b>K Main study: Tensile strength</b> . . . . .	<b>195</b>
<b>L Influence of source-to-sensor distance: Feature development</b> . . . . .	<b>197</b>
<b>M Influence of source depth: Exemplary signals</b> . . . . .	<b>201</b>
<b>Conferences</b> . . . . .	<b>202</b>
<b>Student theses</b> . . . . .	<b>204</b>
<b>Curriculum Vitae</b> . . . . .	<b>206</b>

## Kurzfassung

Um das Leichtbaupotenzial von Faserkunststoffverbunden voll ausschöpfen zu können, ist ein detailliertes Wissen über ihr fortschreitendes Versagensverhalten unter Last erforderlich. Die Schallemissionsanalyse bietet in diesem Zusammenhang eine Methode, um die zugrundeliegenden Mechanismen näher untersuchen zu können. Durch die Erfassung und Analyse akustischer Wellen, die bei Rissinitiierung und -wachstum emittiert werden, können Ort und Art der Schädigung über den Versuchsverlauf hinweg beschrieben werden. Eine große Herausforderung liegt dabei in der Unterscheidung von faserverbundtypischen Schädigungsereignissen wie Faser- oder Matrixbrüchen auf Grundlage ihrer akustischen Emissionen.

Die vorliegende Arbeit beschäftigt sich mit dem Einfluss von zwei Parametern, die sich maßgeblich auf die akustischen Merkmale von Schädigungsereignissen auswirken können. Dazu zählen die Tiefe, in der das Schädigungsereignis stattfindet (Quellentiefe) sowie der laterale Abstand, den die akustische Welle von der Quelle bis zum Sensor zurücklegen muss (Quelle-Sensor-Abstand). Um ein Verständnis für die Wirkweise beider Parameter zu gewinnen, stellt die Arbeit die Eigenschaften von geführten Wellen in Faserkunststoffverbunden als entscheidend heraus. Durch die Analyse künstlicher Schallquellen und akustischer Emissionen realer Schädigungsereignisse macht die Arbeit deutlich, dass mit Änderungen der Quellentiefe und des Quelle-Sensor-Abstandes, starke Änderungen im Moden- und Frequenzgehalt der akustischen Emissionen einhergehen können. Diese Änderungen können sogar dazu führen, dass ein Faserbruch fälschlicherweise als Matrixbruch eingestuft wird und umgekehrt. Für zuverlässigere Ergebnisse bei der Quellenidentifizierung muss daher der Einfluss der Quellentiefe und des Quelle-Sensor-Abstandes berücksichtigt werden. Dem Einsatz der modalen Schallemissionsanalyse spricht die Arbeit in diesem Zusammenhang großen Nutzen zu, um die zugrunde liegenden Phänomene zu verstehen und darauf aufbauend robustere Bewertungsmethoden zu entwickeln.

## Abstract

In order to exploit the full lightweight potential of fibre-reinforced plastics (FRP), a detailed knowledge of their progressive failure behaviour under load is required. In this context, acoustic emission analysis offers a method to characterize the underlying mechanisms in more detail. By detecting and analysing acoustic waves emitted during crack initiation and growth, the location and type of damage can be described over the course of the test. A major challenge thereby is the differentiation between FRP specific damaging events, such as fibre and matrix fractures, on the basis of their acoustic emissions.

The present work deals with the influence of two parameters which can have a significant impact on the acoustic characteristics of damaging events. These include the depth in which the damaging event occurs (source depth) and the lateral distance the acoustic wave has to travel from the source to the sensor (source-to-sensor distance). In order to gain an understanding of the effects of both parameters, the work highlights the properties of guided waves in fibre-reinforced plastics as crucial. By analysing artificial acoustic emission sources as well as acoustic emissions from real damaging events, the work demonstrates that changes in source depth and source-to-sensor distance can be accompanied by strong changes in the modal and frequency content of the acoustic emissions. These changes can even lead to a fibre break being mistakenly classified as a matrix break and vice versa. Consequently, for more reliable results in source identification, the influence of source depth and source-to-sensor distance must be considered. In this context, the use of modal acoustic emission analysis can be of great benefit in understanding the underlying phenomena and developing more robust evaluation methods.

## Zusammenfassung

Kenntnisse über das komplexe Degradationsverhaltens von Faserkunststoffverbunden (FKV) sind entscheidend, um ihr Leichtbaupotenzial voll ausschöpfen zu können. Die Schallemissionsanalyse (SEA) bietet in diesem Zusammenhang eine Methode, um die zugrundeliegenden Mechanismen näher untersuchen zu können. Durch die Erfassung und Analyse akustischer Wellen, die bei Rissinitiierung und -wachstum emittiert werden, können Ort und Art der Schädigung über den Versuchsverlauf hinweg beschrieben werden. Die Unterscheidung von Schädigungsereignissen wie Faserbrüchen, Matrixrissen oder Delaminationen anhand ihrer akustischen Emissionen stellt dabei eine wesentliche Herausforderung dar, der sich Wissenschaftler seit mehr als 30 Jahren widmen. Schädigungsereignisse wurden in zahlreichen Studien über definierte Prüfzenarien gezielt erzeugt, um ihren akustischen Fingerabdruck zu bestimmen. Die Peakfrequenz wurde in diesem Zusammenhang häufig zur Unterscheidung zwischen Faserbrüchen und Matrixrissen herangezogen. In Übereinstimmung mit der allgemeinen Theorie der Schallemission und den elastischen Eigenschaften von Faser- und Matrixmaterial, wurden Ereignisse mit hohen Peakfrequenzen Faserbrüchen und jene mit niedrigeren Peakfrequenzen Matrixrissen zugeschrieben. Obwohl die absoluten Grenzen zwischen den Autoren aufgrund von Unterschieden im Material, der Messausrüstung und der Auswertungsmethodik variierten, konnte diese Zuordnung in vielen Studien validiert werden.

Ausgangspunkt dieser Arbeit waren Studien, die dieses allgemeine Schema in Frage stellten. Sie konnten zeigen, dass Matrixrisse, die in der Symmetrieebene des Laminates auftraten, akustische Emissionen mit Peakfrequenzen erzeugen können, die denen eines Faserbruchs ähnlich sind. Eine mögliche Erklärung wurde in den Eigenschaften von geführten Wellen gesehen. Jedoch konnten diese nicht experimentell nachgewiesen werden, und es fehlte eine umfassende Diskussion darüber, wie und in welchem Ausmaß der Modengehalt die charakteristische Merkmale im Frequenzspektrum beeinflussen kann. Neben der Quellentiefe wurde auch der Einfluss des Abstands zwischen Quelle und Sensor als potenzielle Quelle für Fehlinterpretationen adressiert.

Ziel dieser Arbeit war es den Einfluss der Quellentiefe und des Quelle-Sensor-Abstandes auf die akustischen Charakteristika von Schädigungsereignissen in CFK-Laminaten systematisch zu untersuchen. Mit dem Schwerpunkt auf Faserbrüchen und Matrixrissen, befasste sich die Arbeit mit der Frage, wie deren akustische Emissionen mit Tiefe und Abstand zum erfassenden Sensor variieren können. Ein Hauptziel dabei war es, diese Abhängigkeiten aufzuzeigen und ein Bewusstsein für die zugrundeliegenden Mechanismen unter Einbeziehung des modalen Wellencharakters

zu schaffen. Dabei zielte die Arbeit darauf ab das Zusammenspiel zwischen Modengehalt, Frequenzgehalt und extrahierten Merkmalen aufzuzeigen, um das Potenzial der modalen Schallemission für die Interpretation von Schallemissionssignalen herauszustellen.

Für die Untersuchungen wurden  $(0^\circ/90^\circ)$  gestapelte Kreuzlamine aus kohlenstofffaserverstärktem Kunststoff mit jeweils 4 und 16 Lagen hergestellt. Als Grundlage für die Interpretation der Schallsignale wurde im ersten Schritt die Ausbreitung von geführten Wellen in diesen Laminaten charakterisiert. Gruppengeschwindigkeiten, Dämpfungskoeffizienten und Verschiebungsfelder wurden theoretisch ermittelt und experimentell mit einer neuen Mess- und Auswertemethodik validiert, welche die individuelle Extraktion und Analyse von symmetrischen und antisymmetrischen Moden ermöglichte. Die Messungen an den  $(0^\circ/90^\circ)_{4S}$ -Laminaten konnten zeigen, dass bei einer Ausbreitung entlang einer der Hauptfaserrichtungen ( $0^\circ$  oder  $90^\circ$ ) die Dämpfung der fundamentalen, symmetrischen Mode  $S_0$  bei ca. 600 kHz vergleichbar ist mit der der antisymmetrischen Mode  $A_0$  bei ca. 100 kHz. Dieses Ergebnis machte deutlich, dass hochfrequente Informationen der Quelle über größere Distanzen hinweg eher über den  $S_0$  Mode erhalten bleiben.

Neben diesen Unterschieden zwischen den Wellenmoden wurde eine Abweichung zwischen den experimentellen Daten und dem theoretischen Modell für die Dämpfung von geführten Wellen beobachtet, die auf die Anisotropie zurückgeführt werden konnte.

Der Einfluss der Quellentiefe und der Laufstrecke auf den Modengehalt und die charakteristischen Merkmale im Frequenzspektrum wurde zunächst im Rahmen einer Vorstudie mit einer künstlichen Schallquelle untersucht. Dazu wurde die Hsu-Nielsen Quelle ausgesucht, die über das Brechen einer genormten Bleistiftmine erzeugt werden kann. Der Bleistift wurde dabei in unterschiedlichen Tiefen an der Kante der 16-lagigen Platte gebrochen, während die resultierende Welle in unterschiedlichen Entfernungen und Ausbreitungsrichtungen detektiert wurde. Dadurch konnte der Moden- und Frequenzgehalt als Funktion der Quellentiefe und der Laufstrecke analysiert werden. Dabei wurde festgestellt, dass bei einer „in-plane“ Anregung die  $A_0$ -Amplitude linear mit zunehmender Tiefe bis zur Symmetrieebene abnimmt, während die  $S_0$  Amplitude nahezu konstant bleibt. Diese Änderung im Modengehalt wirkte sich auf das Frequenzspektrum und daraus abgeleitete Merkmale wie die Peakfrequenz aus, da beide Moden vorwiegend in bestimmten Frequenzbändern auftraten. Die  $S_0$ -Mode überwog in den höheren Frequenzen, während die  $A_0$ -Mode in niedrigeren Frequenzbändern dominierte. Der Ursprung dieser Vorzugsfrequenzen konnte in den Wellenlängen und Verschiebungsfeldern beider Moden gefunden werden.

Der Abstand zwischen Quelle und Sensor beeinflusste das resultierende Frequenzspektrum ebenso, da das Verhältnis beider Moden infolge der unterschiedlichen Dämpfungskoeffizienten variierte. Mit zunehmendem Abstand zwischen Quelle und Sensor wurde die  $S_0$ -Mode dominanter, wodurch der Peak im Frequenzspektrum zu höheren Frequenzen hin verschoben wurde. Der kritische Abstand, bei dem sich die Peakfrequenz von der  $A_0$ - zur  $S_0$ -Mode verschob, nahm dabei mit zunehmender Quellentiefe bis zur Symmetrieebene ab.

Folglich entstanden durch die Variation der Quellentiefe und des Quelle-Sensor-Abstandes zwei separate Cluster mit unterschiedlichen Peakfrequenzen, die aus einer einzigen Quelle hervorgingen. Da nach dem Stand der Technik jedem Cluster ein einzelner Schädigungsmechanismus zugeordnet wird, machte dieses Ergebnis deutlich, dass es dadurch zu Fehlinterpretationen kommen kann.

In der Hauptstudie wurden Schädigungsereignisse über quasistatische Zugbelastung systematisch in verschiedenen Tiefen und Abständen zu den Sensoren erzeugt, um die Erkenntnisse aus der Vorstudie zu validieren. Während unterschiedliche Quelle-Sensor-Abstände durch die asymmetrische Sensorkonfiguration realisiert werden konnten, wurde die Quellentiefe durch das Probendesign systematisch variiert. Die 4- und 16-lagigen ( $0^\circ/90^\circ$ ) Kreuzlamine wurden jeweils in  $0^\circ$ - und  $90^\circ$ -Richtung getestet, um die Positionen der  $0^\circ$ - und  $90^\circ$ -Lagen im Laminat zu tauschen. Folglich konnte die Tiefenposition der transversalen Matrixrisse in der  $90^\circ$  Lage sowie die Tiefenposition der Faserbrüche in der  $0^\circ$  Lage zwischen den Proben systematisch variiert werden.

Zur zuverlässigen Quellenlokalisierung wurde eine neue Auswertemethodik entwickelt, die eine in-situ-Charakterisierung der Gruppengeschwindigkeitsverteilungen der dominanten Moden in der Struktur ermöglichte. Mit dieser Methodik konnte die für die Ankunftszeitbestimmung zugrundeliegende Mode identifiziert werden und damit gleichzeitig die Quellenlokalisierung optimiert werden.

Der Abstand zwischen Quelle und Sensor zeigte einen starken Einfluss auf die charakteristischen Merkmale im Frequenzbereich. Die Schwerpunktsfrequenz sowie die gewichtete Peakfrequenz wurden in diesem Zusammenhang betrachtet. Während mit zunehmendem Quelle-Sensor-Abstand eine stetige Abnahme der Schwerpunktsfrequenz beobachtet werden konnte, wurden bei der gewichteten Peakfrequenz sowohl Zu- als auch Abnahmen beobachtet. Die Zunahmen konnten dabei über eine Änderung im Modengehalt erklärt werden. Mit zunehmender Laufstrecke nahm das Verhältnis von  $A_0$  zu  $S_0$  aufgrund der höheren Dämpfung der  $A_0$ -Mode ab. Dadurch dominierte ab einer gewissen Distanz die  $S_0$ -Mode das Auswertefenster und das resul-



tierende Frequenzspektrum, wodurch der Peak im Spektrum zu höheren Frequenzen hin verschoben wurde. Dieses Ergebnis machte deutlich, dass der Sensor, der am nächsten zur Quelle liegt, nicht immer die beste Wahl für eine Quellenidentifizierung darstellt. Hochfrequente Eigenschaften der Quelle können in unmittelbarer Nähe zur Quelle durch das Vorhandensein der  $A_0$ -Mode unterdrückt werden, so dass die Bandbreite des Schädigungsereignisses unterschätzt wird. Ein Vergleich zwischen den Sensorsignalen eines Ereignisses konnte zeigen, dass sich die Klassifizierung für dasselbe Ereignis deutlich unterscheiden kann, je nachdem, welcher Sensor für die Auswertung berücksichtigt wurde.

Obwohl diese Effekte sowohl bei 4- als auch bei 16-lagigen Proben beobachtet werden konnten, hatte der Abstand zwischen Quelle und Sensor bei den 4-lagigen Proben einen stärkeren Einfluss. Insbesondere aufgrund des Vorhandenseins der  $S_0$ -Mode bei Frequenzen von bis zu 800 kHz, konnten vorwiegend bei diesen Proben starke Verschiebungen der Peakfrequenz beobachtet werden. Diese Unterschiede konnten auf die unterschiedlichen Laminatdicken zurückgeführt werden, die sich direkt auf das Dispersionsverhalten der geführten Wellenmoden auswirkten.

Basierend auf den vorherigen Ergebnissen wurde eine neue Auswertemethodik zur Untersuchung des Einflusses der Quellentiefe vorgeschlagen. Dabei wurden zwei unterschiedliche Messaufbauten ausgewählt: Ein Standardaufbau, der konventionelle, breitbandige Sensoren mit ausgeprägter Resonanz verwendete, und ein fortgeschrittener Aufbau mit breitbandigen, nicht-resonanten Sensoren, bei dem die Symmetrie der zugrundeliegenden Wellenmode durch eine spezielle Sensorkonfiguration bestimmt werden konnte. In beiden Messaufbauten wurde die Probenkante mittels einer Kamera überwacht, um Risse in den  $90^\circ$ -Schichten zu identifizieren. Dabei wurde die digitale Bildkorrelation angewandt, um die Risse anhand der resultierenden Dehnungssprünge zu detektieren.

Je nach Tiefe der  $0^\circ$  und  $90^\circ$  Lage, konnten bei den 4-lagigen Proben deutliche Unterschiede in den Schallemissionsdaten festgestellt werden. Schallereignisse mit gewichteten Peakfrequenzen von über 500 kHz wurden vorwiegend in den Proben gefunden, bei denen die  $90^\circ$ -Lage in der Symmetrieebene lag. Diese hohen gewichteten Peakfrequenzen konnten daher auf die transversalen Matrixrisse in den inneren  $90^\circ$  Lagen zurückgeführt werden. Als eine ideal in der Ebene wirkende Quelle können transversale Matrixrisse in der Symmetrieebene vorwiegend die  $S_0$ -Mode anregen. Aufgrund der geringen Dämpfung dieser Mode - insbesondere in einer der Hauptfaserrichtungen - bleiben hochfrequente Komponenten erhalten und können vom Sensor detektiert werden. Mit dem zweiten Versuchsaufbau konnte die symmetrische Mode sogar als zugrundeliegende Mode für die Mehrzahl der hochfrequenten Ereignisse verifiziert werden. Dies konnte durch eine statistische Auswertung der

Phasenverschiebung zwischen den Signalen zweier gegenüberliegender Sensoren realisiert werden. Bei den 16-lagigen Proben konnten die Ereignisse mit hohen gewichteten Peakfrequenzen ebenfalls verstärkt bei den Proben mit der 90°-Lage in der Symmetrieebene festgestellt werden. Es gab jedoch aufgrund unterschiedlicher Dispersionseigenschaften deutlich weniger hochfrequente Ereignisse als bei den 4-lagigen Proben.

Insgesamt konnte in dieser Arbeit der Einfluss der Quellentiefe und des Quelle-Sensor-Abstandes auf Signalmerkmale und Klassifikationsergebnisse im Rahmen der Quellenidentifikation in Kreuzlaminaten aufgezeigt werden. Die Bedeutung der modalen Schallemissionsanalyse wurde dabei als entscheidend für das Verständnis der zugrundeliegenden Phänomene und die Erhöhung der Zuverlässigkeit der Quellenidentifikation aufgezeigt.

## List of abbreviations

### Abbreviations

Abbreviation	Description
$A_i$	Antisymmetric mode of $i^{th}$ order
AE	Acoustic emission
AIC	Akaike Information Criterion
CFRP	Carbon fibre-reinforced plastics
CLT	Classical Laminate Theory
CWT	Continuous wavelet transform
DCB	Double cantilever beam
DFT	Discrete Fourier transform
DIC	Digital image correlation
DWT	Discrete wavelet transform
EFIT	Elastodynamic finite integration technique
FEM	Finite element method
FF	Fibre fracture
FFT	Fast Fourier transform
FIR	Finite impulse response
FRP	Fibre-reinforced plastics
GFRP	Glass fibre-reinforced plastics
GMM	Gaussian mixed models
IFF	Inter-fibre fracture
IIR	Infinite impulse response
LDA	Linear discriminant analysis
MAE	Modal acoustic emission
NDT	Non-destructive testing
PCA	Principal component analysis
PLB	Pencil lead break
$S_i$	Symmetric mode of $i^{th}$ order
SAFE	Semi-analytical finite element
$SH_i$	Shear horizontal mode of $i^{th}$ order
SOM	Self-organizing Map
SVD	Singular value decomposition
TMC	Transverse matrix cracking
UD	Unidirectional
WP	Work package

---

**Latin variables (Part I)**


---

Symbol	Unit	Description
$A$	V	Amplitude
$A_0$	V	Original amplitude
$A_1$	V	Amplitude at source-to-sensor distance $x_1$
$A_2$	V	Amplitude at source-to-sensor distance $x_2$
$A_{mod}$	V	Modified amplitude
$A_w$	$\text{g/m}^2$	Area weight of prepreg
$A_{w_f}$	$\text{g/m}^2$	Area weight of fibres
$A_{w_m}$	$\text{g/m}^2$	Area weight of matrix
$AIC$	1	Akaike information criterion
$C_{ij}$	GPa	Stiffness tensor
$c_L$	m/s	Velocity of bulk longitudinal waves
$c_T$	m/s	Velocity of bulk transversal waves
$d$	mm	Laminate thickness
$d_i$	$\mu\text{m}$	Layer thickness
$E$	GPa	Young's modulus
$E_{\parallel}$	GPa	Young's modulus of UD layer parallel to the fibre direction
$E_{\perp}$	GPa	Young's modulus of UD layer perpendicular to the fibre direction
$E_{f\perp}$	GPa	Young's modulus of fibre perpendicular to the fibre direction
$E_m$	GPa	Young's modulus of the matrix material
$E_x$	GPa	Young's modulus of laminate in x-direction
$F_B$	1	Complex Fourier transform of bottom sensor signal
$F_T$	1	Complex Fourier transform of top sensor signal
$f$	Hz	Frequency
$f_c$	Hz	Frequency centroid
$f_p$	Hz	Peak frequency
$f_{wp}$	Hz	Weighted peak frequency
$G_{\perp\parallel}$	GPa	Shear modulus of UD layer
$G_{f\perp\parallel}$	GPa	Shear modulus of fibre
$G_m$	GPa	Shear modulus of matrix material
$k$	$\text{m}^{-1}$	Wave number
$k'$	$\text{m}^{-1}$	Real part of wave number
$k''$	dB/m, Np/m	Imaginary part of wave number (Attenuation coefficient)

---

**Latin variables (Part II)**

Symbol	Unit	Description
$L$	1	Maximum likelihood
$N$	1	Number of samples
$n_v$	m	y-intercept from linear regression analysis (Determination of group velocity)
$n_a$	1	y-intercept from linear regression analysis (Determination of attenuation coefficient)
$PP_i$	1	Partial power in frequency band $i$
$p$	1/m	Aggregated variable in Rayleigh-Lamb frequency relation
$q$	1/m	Aggregated variable in Rayleigh-Lamb frequency relation
$R_{\perp}^+$	MPa	Fracture strength of the UD layer under tensile load as a result of stresses acting perpendicular to the fibre direction
$R_m$	1	Energy portion of mode $m$
$S_i$	$V^2$	Partial energy of signal
$S'_i$	$V^2$	Modified partial energy of signal
$S_m$	$V^2$	Signal energy of mode type $m$
$S_N$	$V^2$	Total partial energy of signal
$\bar{S}$	$V^2$	Average signal energy of symmetric and antisymmetric modes
$T_g$	$^{\circ}\text{C}$	Glass transition temperature
$t$	s	Time
$V_f$	vol.-%	Fibre volume content
$v_{gr}$	m/s	Group velocity
$v_{ph}$	m/s	Phase velocity
$x$	m	Distance
$x_1$	m	Distance from the source to sensor 1
$x_2$	m	Distance from the source to sensor 2
$x_{12}$	m	Distance between sensors 1 and 2
$x_{A_s}$	m	Starting position of actuator
$x_{A_e}$	m	End position of actuator
$x_{A_{step}}$	m	Step size for actuator position
$x_{S_1}$	m	Position of sensor 1
$x_{S_2}$	m	Position of sensor 2

**Greek variables**

Symbol	Unit	Description
$\alpha$	1	Delay factor (Hinkley criterion)
$\alpha_{\parallel}$	1/K	Linear coefficient of thermal expansion of the UD layer parallel to the fibre direction
$\alpha_{\perp}$	1/K	Linear coefficient of thermal expansion of the UD layer perpendicular to the fibre direction
$\alpha_{f\parallel}$	1/K	Linear coefficient of thermal expansion of the fibre parallel to the fibre direction
$\alpha_{f\perp}$	1/K	Linear coefficient of thermal expansion of the fibre perpendicular to the fibre direction
$\alpha_m$	1/K	Linear coefficient of thermal expansion of the matrix material
$\delta$	V <sup>2</sup>	Trend variable
$\lambda$	m	Wavelength
$\mu$	variable	Arithmetic mean
$\nu_{\perp\parallel}$	1	Poisson's ratio of UD layer, ratio of strain induced in the direction parallel to the fibre by a strain applied perpendicular to the fibre direction
$\nu_{\parallel\perp}$	1	Poisson's ratio of UD layer, ratio of strain induced in the direction perpendicular to the fibre by a strain applied parallel to the fibre direction
$\nu_{\perp\perp}$	1	Poisson's ratio of UD layer, ratio of strain induced in the direction perpendicular to the fibre by a strain applied perpendicular to the fibre direction
$\nu_{f\perp\parallel}$	1	Poisson's ratio of fibre, ratio of strain induced in the direction parallel to the fibre by a strain applied perpendicular to the fibre direction
$\nu_m$	1	Poisson's ratio of matrix material
$\rho$	g/cm <sup>3</sup>	Density
$\rho_f$	g/cm <sup>3</sup>	Density of fibre
$\rho_m$	g/cm <sup>3</sup>	Density of matrix material
$\sigma$	variable	Standard deviation
$\sigma_{xTMC}$	MPa	Critical tensile stress in x direction for transverse matrix cracking
$\tau$	s	Relaxation time
$\phi$	rad	Phase shift
$\Psi_m$	wt.-%	Content of matrix material by weight
$\omega$	rad/s	Angular frequency

# 1 Introduction

Carbon fibre-reinforced plastics (CFRP) show a steadily growing market share with an average annual growth rate of around 12% (2010 to 2018) [1]. Due to the flexibility in the design of the material itself along with its outstanding specific strengths and stiffness, CFRP has become a vital material for modern lightweight design. Nowadays, it can be found in primary structures of aircrafts (e.g. wings and fuselage of A350 [2]), passenger cars (e.g. chassis of BMWi3 [3]) and wind turbine blades (e.g. Vestas V164-10 MW [4]). Detailed knowledge on the initiation and propagation of cracks is thereby crucial in order to exploit the full lightweight potential of CFRP in these applications. For multiaxial CFRP laminates, however, this is a challenging task due to the various damaging mechanisms that can be triggered and the complex interaction between them within a heterogeneous, layered structure with pronounced anisotropy.

Acoustic emission (AE) analysis has proven to be a valuable tool in this context. As an in-situ, non-destructive testing (NDT) method with high sensitivity, it allows to characterize damage progression through the detection and analysis of released acoustic emissions from crack initiation and propagation during mechanical loading [5]. This way, AE analysis has been successfully utilized to increase the reliability and outcome of coupon tests in the scope of material characterization [6–13] and to support component testing for the validation of simulation results [14–18] or the quality assurance of high performance products (e.g. composite pressure vessels [19, 20] and formula 1 monocoques [21]). In this context, the identification of damaging events such as fibre fracture or matrix cracking based on their resulting acoustic emissions has been a vivid field of research for more than 30 years [22]. In order to accomplish this task, a common scheme has been developed that involves the extraction of characteristic features of the acquired AE waveforms, the identification of patterns in the resulting multi-dimensional feature space and the correlation of identified clusters with crack patterns that are visualized inline through optical NDT methods or offline through microscopy or X-ray techniques [6]. Following this approach, authors have come up with classification windows for various damaging events (e.g. delaminations, fibre breakage, matrix cracking, fibre/matrix pull-out,...) based on certain characteristic features. The peak frequency represents one of these features that has been considered by many authors to distinguish between matrix cracking and fibre breakage, for example. A common scheme has been established that fibre breakage and matrix cracking result in acoustic events with high and low peak frequencies, respectively [23].

Despite the validation through several authors, this scheme was questioned recently, by showing that transverse matrix cracks evolving in the inner 90° layers of a cross-ply laminate could result in AE with peak frequencies that are comparable to those of fibre breaks [24–26]. This drastic change in frequency content was attributed to a change in modal content with increasing source depth. However, this could not be experimentally

validated and comprehensive studies on how and to what extent modal content could affect frequency characteristics were missing.

Besides the influence of source depth, several authors also pointed out the influence of source-to-sensor distance on signal characteristics [26, 27]. Due to the low-pass filter characteristics of the material itself, frequency bandwidth can be reduced and characteristic features such as the peak frequency can significantly shift with increasing propagation distance. Potential fibre breaks could therefore be misinterpreted as matrix cracks after a certain propagation distance.

The goal of this study is to systematically investigate both - the influence of source depth and source-to-sensor distance - on signal characteristics of damaging events. While the focus is put on fibre breaking and transverse matrix cracking as in-plane acting damaging modes, the work is concerned with the question of how their AE footprint is modified when source depth and source-to-sensor distance vary. One main goal is to visualize this dependency and create awareness for the underlying mechanisms. This involves a fundamental understanding of initiation and propagation of guided waves and the incorporation of modal acoustic emission analysis (MAE) as an essential tool in this work. By evaluating the effect of source depth and source-to-sensor distance on modal content, frequency content and characteristic features, the thesis aims to create the link between these and highlight the potential of MAE for the interpretation of acoustic emission signals.



## 2 State of the art

### 2.1 Mechanical failure of continuous fibre-reinforced plastics

#### 2.1.1 Damaging modes

Continuous fibre-reinforced plastics (FRP) show a complex damaging behavior due to their heterogeneous structure and their anisotropic properties [28, 29]. On the microscopic scale, the material can fail locally through fibre filament fracture, matrix cracking, fibre-matrix interface de-bonding or fibre-matrix pull-out, depending on the loading conditions, the physical properties of the fibre and matrix material as well as the strength of the fibre-matrix interface [30, 31]. The occurrence of these damaging mechanisms is often promoted by local anomalies in the structure like fibre undulations, voids, resin-rich areas or even pre-existing cracks. They can modify the local stress conditions in the laminate and thereby promote the initiation of microscopic damaging mechanisms. The same applies to residual stresses that are inherently present in FRP laminates after manufacturing. They can develop during cooling from cure temperature due to the differences in thermal expansion coefficients of fibre and matrix and the shrinkage of the matrix during polymerization [30]. Since, on the microscopic scale, anomalies and residual stresses are typically not known by the designer of a FRP structure, predictions on the initiation and development of microscopic failure mechanisms are challenging. Stress analysis is therefore shifted to the macroscopic scale where fibre and matrix are homogenized and treated as continuum in the form of a layer. This layer consists of endless fibres embedded in a matrix and is treated as transversely isotropic in the Classical Laminate Theory (CLT) [30]. The stress state in a single layer can be described in terms of the two remaining principal directions: The direction parallel ( $\parallel$ ) and perpendicular ( $\perp$ ) to the fibre direction [30]. On the lamina level, one can distinguish between two types of failure: **Fibre fracture (FF)** and **inter-fibre fracture (IFF)** [29].

The FF defines the fracture of a whole bundle of fibre filaments. The corresponding load is called the fibre fracture limit. FF is to be distinguished from the fracture of single fibre filaments that already takes place around 50% to 70% of the fibre fracture limit [29]. Since the majority of the load is carried by the fibres, FF usually initiates the final fracture of the laminate.

The IFF, on the other hand, describes the formation of a macroscopic crack that runs through the matrix or along the fibre-matrix interface. Depending on the loading conditions, the IFF takes place on different fracture planes. If a unidirectional laminate is loaded in tension parallel to the fibre direction, the IFF is created on a plane parallel to the fibre direction. This is defined as **longitudinal matrix splitting**. If the same unidirectional laminate is loaded perpendicular to the fibre direction, the fracture plane

is perpendicular to the loading direction, resulting in the so-called **transverse matrix cracking (TMC)**. In multi-axial laminates, TMC is a frequently encountered damaging mode that can already occur at 30% to 40% of the ultimate strain in cross-ply CFRP laminates under quasi-static tensile loading [30, 32, 33]. In contrast to the FF, FRP laminates can usually tolerate TMC by transferring the load to adjacent plies. TMC as a first-ply failure does therefore not necessarily lead to the disintegration of the whole laminate. However, it can be detrimental to the residual structural performance by reducing the stiffness of the laminate and initiating stress concentrations at the interface that promote the creation of fibre fracture and **inter-ply delaminations**. The latter represents an additional damaging mode that appears on the laminate level. It defines the separation of layers as a result of critical tensile stresses acting in thickness direction or shear stress along the interface of adjacent plies.

The critical failure loads for damaging modes are derived from failure theories. In this context, **Puck's failure criterion** is well established for the layer-wise prediction of failure loads for FF and IFF in arbitrary loading scenarios. With a fracture hypothesis that contains all possible fracture planes for FF and IFF, a master fracture body can be created on the basis of the elastic properties and the basic strengths values of the laminate [29]. This fracture body allows the determination of a stress exposure factor for FF and IFF based on the stress state inside a layer. This stress exposure factor runs from 0 to 1 with increasing stress intensity. If the current stress vector reaches the closed surface of the master fracture body, stress exposure is equal to 1 and critical stress condition for failure is reached. This way, first-ply failure can be predicted analytically. More details on Puck's failure theory can be found in [29, 30].

If a structure is designed to withstand loads above first-ply failure, a **degradation analysis** has to be performed to guarantee the structural integrity in the presence of cracks. This analysis is mainly done for IFF as FF generally leads to the final failure of the laminate. In Puck's approach to degradation analysis, elastic properties are degraded with increased load to compensate for the presence of cracks. The consequence of these cracks is thereby smeared over the whole layer, neglecting the effect of local stress concentrations. For the degradation of elastic constants as a function of crack density, many theoretical models have been developed. Carraro et al. give a comprehensive overview in [34].

### **2.1.2 Damage evolution in cross-ply laminates**

Since this thesis focuses on cross-ply laminates, a closer look is taken at the evolution of damage for these laminates when subjected to quasi-static tensile loading. Figure 2.1 depicts a typical sequence of damaging modes in a balanced ( $0^\circ/90^\circ$ ) cross-ply laminate loaded in the  $0^\circ$  direction. The figure as well as the following notes are based

on [28].

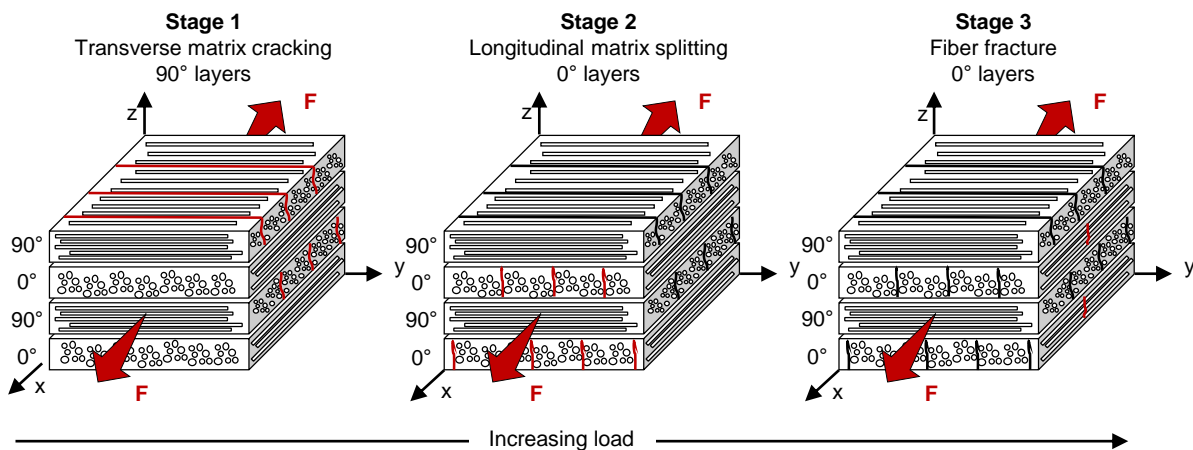


Figure 2.1: Schematic evolution of damage in a cross-ply laminate under quasi-static tensile loading in the  $0^\circ$  direction.

If no premature cracks existed after manufacturing, the first microcracks in the matrix material already develop at stress exposure factors of around 0.5 in the  $90^\circ$  layer, predominantly where stress is concentrated due to anomalies or residual stresses after manufacturing. With increased loading, microcracks coalesce and grow until the stress exposure factor for IFF in the  $90^\circ$  layer reaches 1. At this point, a macroscopic crack develops across the whole thickness of the layer (stage 1 in figure 2.1). The force that was carried by the  $90^\circ$  layer is transferred to the adjacent layers at the position of the crack. This abrupt redistribution of load can cause other  $90^\circ$  layers to fail around the same lateral position. Through interlaminar shear stress, the load can be steadily reintroduced in the broken  $90^\circ$  layers. After a certain distance, the full stress is built up again, resulting in another TMC in the  $90^\circ$  layer. As a consequence of growing crack density, the Young's modulus  $E_{\perp}$ , shear modulus  $G_{\perp\parallel}$  and Poisson's ratio  $\nu_{\perp\parallel}$  are reduced [29, 30]. A saturation in crack density is reached, when the distance between two cracks is too small in order to build up the necessary stress for IFF in the broken  $90^\circ$  layers. While the  $90^\circ$  layers continuously degrade, more load is redistributed to the neighboring  $0^\circ$  plies. Eventually, lateral contraction in the  $0^\circ$  layer due to the Poisson's effect can initiate longitudinal matrix splitting in the  $0^\circ$  layer as a second ply failure (stage 2 in figure 2.1). As the fibres are still intact, the laminate is capable of bearing the load. However, when stress exposure factor for FF reaches 1, fibre bundles in the  $0^\circ$  layer break, resulting in the disintegration of the whole laminate (stage 3 in figure 2.1). Depending on the fibre-matrix interface, the laminate can also fail through delamination. Due to the differences in Poisson's ratios of  $0^\circ$  and  $90^\circ$  layers, interlaminar shear stresses can develop that promote the initiation and growth of inter-ply delaminations at the free edge of the laminate [30]. Crossing points of IFF in the  $0^\circ$  and  $90^\circ$  layers can thereby promote the development through further stress concentrations.

AE analysis can serve as tool to characterize this complex damaging behaviour and derive material properties for degradation analysis. Knowledge on the characteristics of ultrasonic guided waves is thereby crucial for the analysis.

## 2.2 Ultrasonic guided waves

### 2.2.1 Fundamentals

Acoustic waves can propagate as longitudinal or transversal wave modes in bulk material following Navier's equation of motion [35]. When wave propagation is constrained through interfaces, guided waves can develop as a result of continuous reflection, refraction and mode conversion. Lord Rayleigh discovered this phenomenon in 1885 for waves that form at the free surfaces of a solid [36]. The so-called Rayleigh waves show a combined displacement of longitudinal and transversal motion that decays exponentially with distance from the surface. Another type of guided wave was discovered by Horace Lamb in 1917 [37] in shell like structures that are infinitely extended in two directions while bounded by two parallel surfaces. Since FRP components are commonly designed as shell like structures, this type of wave has a high relevance for FRP. In these thin-walled structures, interference between incident and reflected waves can take place, if the wavelength of the acoustic waves is larger than the plate thickness. This interference is constructive for the development of the so-called Lamb waves. The displacement field of these waves is limited to the propagation direction and the direction normal to the plane of the plate. Depending on its symmetry towards the center plane of the plate, one can distinguish between symmetric and antisymmetric wave modes. The schematic displacement fields of the fundamental **symmetric** ( $S_0$ ) and **antisymmetric** ( $A_0$ ) wave modes are illustrated in figure 2.2.

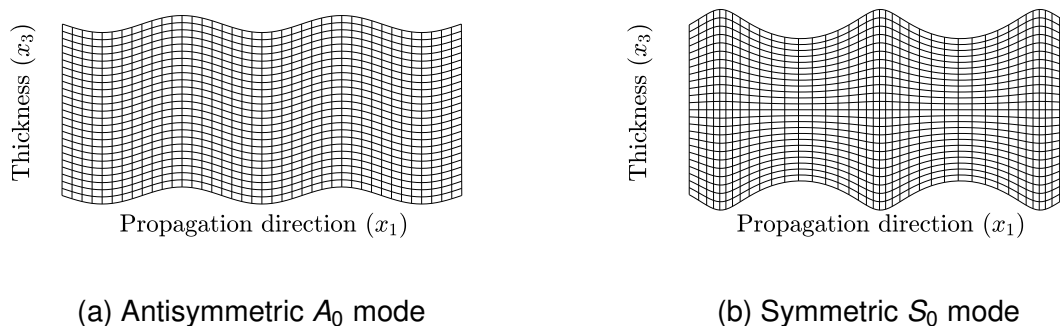


Figure 2.2: Schematic displacement fields of fundamental Lamb wave modes - generated with [38].

First comprehensive solutions for these modes were found by Mindlin [39] and Viktorov [40] by solving Navier's equation of motion with the condition of stress free bound-

aries at the interfaces. Two characteristic equations could be derived that govern the propagation characteristics symmetric (2.1) and antisymmetric (2.2) Lamb wave modes in isotropic materials with thickness  $d$ . The **symmetric** ( $S_i$ ) modes follow

$$\frac{\tan(qd)}{\tan(pd)} = -\frac{4k^2qp}{(q^2 - k^2)^2} \quad (2.1)$$

whereas the **antisymmetric** ( $A_i$ ) modes can be derived from

$$\frac{\tan(qd)}{\tan(pd)} = -\frac{(q^2 - k^2)^2}{4k^2qp}. \quad (2.2)$$

The variables  $p$  and  $q$  are a function of angular frequency  $\omega$ , velocity of bulk longitudinal  $c_L$  or transversal wave  $c_T$  and the wave number  $k$ .

$$p^2 = \frac{\omega^2}{c_L^2} - k^2, \quad q^2 = \frac{\omega^2}{c_T^2} - k^2 \quad (2.3)$$

Angular frequency  $\omega$  and wave number  $k$  can thereby be expressed as well in terms of wavelength  $\lambda$  and frequency  $f$ .

$$k = \frac{2\pi}{\lambda} \quad (2.4)$$

$$\omega = 2\pi f \quad (2.5)$$

Equations (2.1) and (2.2) are known as the Rayleigh-Lamb frequency relations. They correlate wave number  $k$  and angular frequency  $\omega$  to the plate thickness  $d$  and thereby visualize the dispersive nature of Lamb waves. In contrast to bulk waves, the velocity of Lamb waves for a given plate thickness  $d$  depends on the frequency.

In addition to Lamb waves modes, **shear horizontal** ( $SH_i$ ) modes can be found in shell-like structures. They are typically distinguished from Lamb wave modes, because particle vibrations are limited to in-plane motions parallel to the surface of the plate. These horizontally polarized waves exist in the form symmetric and antisymmetric modes that are denoted with even (0,2,4,...) and odd numbers (1,3,5,...) respectively. More details on their characteristic equations can be found in [35, 41].

Numerical methods such as Newton's method have to be utilized to find the the **solutions for the Rayleigh-Lamb equation** [35]. For every combination of frequency  $f$  and thickness  $d$ , an infinite number of solutions exist for  $k$ . Among those, there is only a finite number of propagating wave modes with real valued wave numbers  $k$ . Multi-layered structures, like FRPs, introduce another level of complexity for the calculation of Lamb wave modes. Here, each individual layer is constrained by two interfaces, where continuity of stress and displacement has to be ensured. Furthermore, anisotropic properties have to be considered for every layer. Thomson [42]

and Haskell [43] introduced the Transfer Matrix Method as one numerical method to find solutions for Lamb wave modes in multi-layered structures. In this approach, the equations of each individual layer are condensed into a set of four equations that relate the boundary condition of the first and last interface with each other. Whereas the method is computational fast, for large values of  $fd$ , it becomes ill conditioned leading to unstable solutions for the characteristic equation. In order to overcome these drawbacks, the Transfer Matrix Method was reformulated. In this context, Rohklin and Wang [44] developed the Stiffness Matrix Method which was revisited and adapted by Huber and Sause [45] later on. The Global Matrix Method was suggested as an another alternative approach by Knopoff [46]. In contrast to the Transfer Matrix Method, this method assembles a single matrix that comprises the equations of all layers. A more detailed view on matrix techniques for the calculation of Lamb waves in anisotropic, multi-layered structures can be found in [47, 48]. As an alternative to matrix techniques, Finite Element Analysis has been considered to model guided wave propagation in fibre-reinforced composites. Besides the classical Finite Element Modelling [49], various methods such as the semi-analytical finite element (SAFE) method [50–52] and the elastodynamic finite integration technique (EFIT) [53,54] have been successfully applied in this context. A benchmark of some of these methods can be found in [55].

For the identified wave modes and pairs of wave number  $k$  and frequency  $\omega$ , the propagation speed can be determined. In dispersive media, one has to distinguish between the **group velocity**  $\mathbf{v}_{gr}$  and the **phase velocity**  $\mathbf{v}_{ph}$  in this context [35]. Phase velocity thereby describes the propagation of a point of constant phase inside the wave packet and is given by the ratio of  $\omega$  to  $k$  or the product of wavelength  $\lambda$  and frequency  $f$ .

$$v_{ph} = \frac{\omega}{k} = \lambda \cdot f \quad (2.6)$$

The group velocity, on the other hand, represents the speed of energy transportation which is given by

$$v_{gr} = \frac{\partial \omega}{\partial k} \quad (2.7)$$

and often referred to as the energy velocity or the velocity of the wave packet.

Due to the anisotropy in FRP, the direction of energy propagation can differ from the direction of the wave vector, resulting in a **skewing angle** between the directions of group and phase velocity [35]. This skewing angle for the fundamental wave modes  $A_0$ ,  $S_0$  and  $SH_0$  as a function of propagation direction in a unidirectional CFRP laminate is shown in [56]. Only for a propagation parallel or perpendicular to the fibre direction, the direction of energy and phase velocity coincide. All other directions result in a

skewing angle that is unequal to zero. Regarding the  $A_0$  and  $S_0$  mode, for a wide range of phase velocity directions, the energy is directed towards the fibre direction, resulting in a natural focusing of energy in this direction. This can be expressed in the form of an energy focusing factor that depends on propagation direction and frequency as shown experimentally in [56] for the  $A_0$  mode in a unidirectional and a cross-ply CFRP laminate.

Another interesting aspect in FRP laminates is the coupling of Lamb wave and shear horizontal modes. If the direction of propagation does not coincide with a principal fibre direction, SH and Lamb wave modes are coupled, resulting in "hybrid" wave modes with a three dimensional displacement pattern [35, 41, 50, 56]. In addition, the SH mode can split into multiple wave packets with different group velocities as illustrated for unidirectional and cross-ply laminates in [50, 56]. The energy velocity of the fastest SH mode was found to be comparable to the energy velocity of the  $S_0$  mode, making a temporal separation of both modes challenging for practical propagation distances.

**Dispersion diagrams** relate frequency  $f$  or the product of frequency and plate thickness  $fd$  to the group or phase velocity of present wave modes. An exemplary dispersion curve for a unidirectional (UD) laminate with a thickness of 2 mm is shown in figure 2.3 (a) for a propagation parallel to the fibre direction. All dispersion diagrams were generated with Dispersion Calculator Software v1.5.1 developed by Huber [45] and provided as freeware by the German Aerospace Center [38]. Several aspects are interesting to point out. First, from the set of wave modes, the two fundamental symmetric and antisymmetric Lamb waves modes  $S_0$  and  $A_0$  as well as the shear horizontal mode  $SH_0$  are the only ones that exist over the whole frequency range. Higher order Lamb modes join at specific cut-off frequencies that can be calculated based on the bulk longitudinal and transversal wave velocity [35]. At these frequencies, a standing longitudinal or shear wave is present across the thickness and the group velocity approaches zero. The second aspect refers to the fundamental Lamb wave modes  $A_0$  and  $S_0$ . For low frequencies, the  $S_0$  mode shows a group velocity that is around five times higher than that of the  $A_0$  mode. However, with increasing frequency, group velocity of the  $S_0$  mode significantly drops, whereas that of the  $A_0$  mode rises. Eventually both modes approach each other in terms of group velocity. At last, it is interesting to note that the  $SH_0$  mode shows no dispersion over the whole frequency range. Since dispersion introduces complexity in the interpretation of acoustic signals, this particular aspect can be valuable for NDT applications. However, as pointed out earlier, pure SH modes only exist in fibre direction. In the non-principal fibre directions, SH modes are coupled with Lamb wave modes and show dispersion as well.

Another view on the characteristics of guided waves modes is given in figure 2.3 (b), where the wavelength is illustrated as a function of frequency for the same UD CFRP

plate. In the presented frequency range, the wavelengths are typically in the order of millimeters. While the  $S_0$  mode appears at higher wavelengths than the  $A_0$  mode, the wavelengths of both modes drop with increasing frequency.

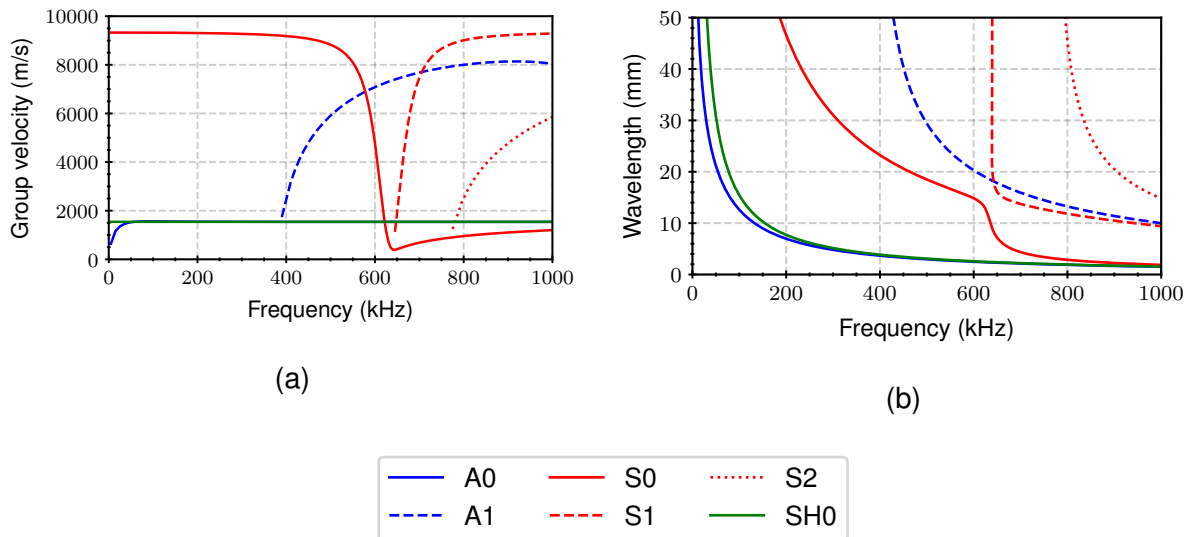


Figure 2.3: Dispersion diagram showing the group velocities (m/s) (a) and wavelengths (mm) (b) of guided wave modes as a function of frequency (kHz) for a 2 mm UD CFRP laminate and propagation in the fibre direction. Calculations were realized with [38].

The **anisotropy** in elastic properties of FRPs is also reflected in the **group velocity** of Lamb wave modes. This is visualized in figure 2.4 where the group velocities of  $A_0$  and  $S_0$  mode are illustrated as a function of propagation direction at a frequency of 200 kHz for the same UD CFRP laminate.

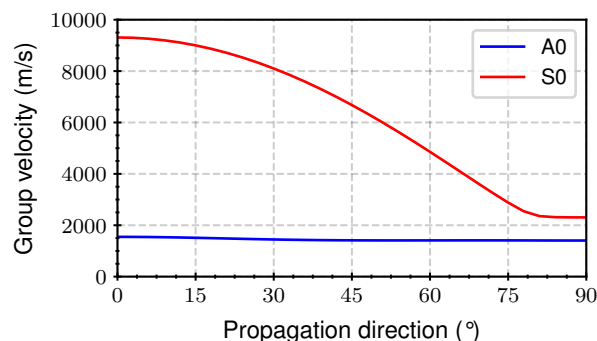


Figure 2.4: Group velocity (m/s) of fundamental Lamb wave modes  $A_0$  and  $S_0$  as a function of propagation direction (°) for a 2 mm UD CFRP laminate at 200 kHz. Calculations were realized with [38].



The fibre direction corresponds to  $0^\circ$  degree. A strong dependency of group velocity can be observed for the  $S_0$  mode. Its velocity drops from around 9,500 m/s in fibre direction to 2,500 m/s perpendicular to it. The group velocity of the  $A_0$  mode, however, is only slightly affected by the laminate's anisotropy. The fact that both modes are affected differently by laminate anisotropy, results from their individual **displacement fields**. These are shown in 2.5 (a) and (d) as a function of source depth for the 2 mm UD CFRP laminate for a propagation in fibre direction at 200 kHz. The displacement fields are divided in in-plane (red), out-of-plane (blue) and shear-horizontal (green) components in relation to the laminate plane. The calculations were done with Dispersion Calculator software [38]. Since the software did not allow the calculation of absolute values, displacement components are shown on a relative scale.

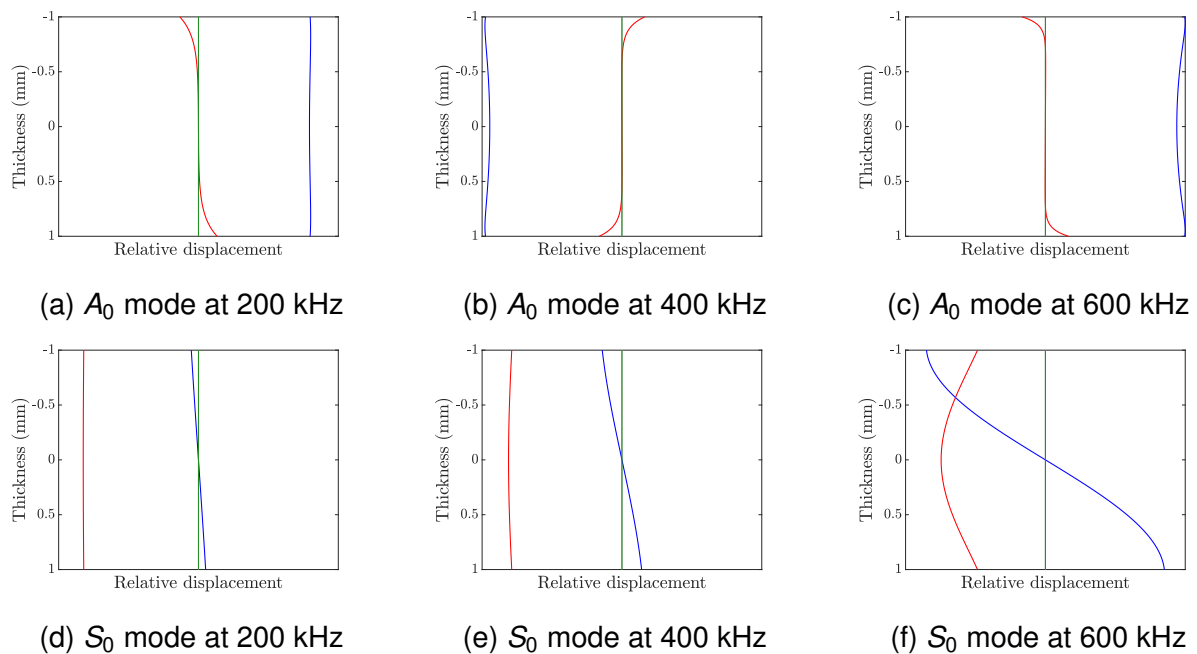


Figure 2.5: In-plane (red), out-of-plane (blue) and shear horizontal displacement (green) components of the fundamental Lamb wave modes  $A_0$  (a,b,c) and  $S_0$  (d,e,f) as a function of frequency (200, 400 and 600 kHz) for a 2 mm UD CFRP laminate and propagation in the fibre direction. Calculations were realized with [38].

Whereas the  $S_0$  mode shows a strong in-plane displacement, the displacement field of the  $A_0$  mode is dominated by an out-of-plane motion. Due to these characteristics, both modes are often referred to as extensional ( $S_0$ ) and flexural mode ( $A_0$ ). In terms of FRP, anisotropy in group velocity is more pronounced for the  $S_0$  mode, because it is mainly influenced by the in-plane elastic properties that are subject to significant change depending on the propagation direction. On the other hand, the  $A_0$  mode is only slightly affected by the propagation direction due to the strong linkage to the out-of-plane laminate properties that are less influenced by in-plane fibre direction.

However, with increasing product of frequency and thickness, the displacement fields of both modes change. This is illustrated in figures 2.5 (b),(c) and (e),(f) that show the displacement fields of both modes for the same laminate at 400 and 600 kHz. Regarding the  $S_0$  mode, the out-of-plane motion at the surface becomes stronger as frequency increases. The in-plane displacement, on the other hand, concentrates at the center of the plate. In contrast to the  $S_0$  mode, the displacement components of the  $A_0$  mode are only slightly affected in the selected frequency range. Whereas the relative in-plane displacement stays almost constant, the out-of-plane motion concentrates at the surface.

### 2.2.2 Attenuation

Wave attenuation describes the loss in amplitude of an acoustic wave with increasing propagation distance [57]. Regarding AE source identification, wave attenuation is the cause for the loss of information with increasing source-to-sensor distance. According to Pollock [58], there are four main mechanisms that contribute to wave attenuation in thin-walled structures:

1. **Geometric spreading:** Originating from the excitation source, acoustic waves propagate in all directions, creating a wave front that grows with increasing propagation distance. Due to this geometric spreading, the energy is distributed among a steady growing wave front, resulting in a decay of wave amplitude along a ray path with increasing propagation distance. For ultrasonic guided waves originating from an omnidirectional excitation source, the ratio of amplitudes  $A_1$  and  $A_2$ , measured at respective distances  $x_1$  and  $x_2$  from the source, is given by

$$\frac{A_2}{A_1} = \frac{\sqrt{x_1}}{\sqrt{x_2}} \quad (2.8)$$

according to [59]. Geometric spreading is the dominant attenuation mechanism in the near field [57, 59]. As already discussed earlier in this section, in FRP, the energy is forced to propagate along the fibre direction, due to the natural focusing effect resulting from the skewing angle between wave front and energy velocity direction. This can reduce the effect of geometric spreading for waves propagating in principal fibre directions, as pointed out in [60].

2. **Material damping:** Internal friction and scattering lead to inherent material damping. In viscoelastic materials, part of the mechanical energy of the acoustic wave, is transferred into heat and absorbed by the material itself. The absorption of energy is thereby expected to be proportional to the frequency of particle vibration [61]. Scattering, on the other hand, describes the loss of energy due to the interaction of acoustic waves with inhomogeneities inside the material. This interaction leads to an

excitation of inhomogeneities which again act as omnidirectional emitters of acoustic waves. Since these secondary waves are spread inside the material and are generally not in phase with the primary waves, part of the energy gets lost. As with internal friction, scattering depends on frequency. The size of acoustic wavelength compared to the dimensions of inhomogeneities thereby determines scattering phenomena and characteristics [61]. Compared to metallic structures, scattering can lead to significant wave attenuation in FRP where inhomogeneities inherently exist through the layered structure and the presence of fibres and voids. Material damping is the dominating attenuation mechanism in the far field [59]. The resulting loss in amplitude is generally described through an exponential law. The ratio of amplitudes  $A_1$  and  $A_2$  at respective distances  $x_1$  and  $x_2$  from the source, is given by [59]:

$$\frac{A_2}{A_1} = e^{-k''(x_2-x_1)} \quad (2.9)$$

In this equation,  $k''$  represents the imaginary part of the complex wave vector  $k = k' + i \cdot k''$  and is often referred to as attenuation coefficient, given in units of Neper/m or dB/m. In FRP, the attenuation coefficient depends on wave mode, frequency and propagation direction. Exemplary values for the attenuation coefficient of Lamb wave modes  $A_0$  and  $S_0$  are shown as a function of frequency and propagation direction for unidirectional and cross-ply CFRP plates in figures 2.6 (a)-(d).

According to theory, the trend can be observed that attenuation increases with frequency for both modes. However, the attenuation of the  $A_0$  mode is significantly stronger than that of the  $S_0$  mode. This can also be observed for other laminates and propagation directions [51, 59, 60, 62–64].

A strong anisotropy is visible when comparing the attenuation coefficients for propagation parallel and perpendicular to the fibre direction in unidirectional laminates. When the wave propagates perpendicular to the fibre direction, wave scattering intensifies, resulting in higher attenuation coefficients for both modes [51, 64].

Another interesting aspect is the fact that some of the attenuation coefficients in figure 2.6 are negative. This effect was encountered by several authors already [56, 63, 65]. One possible explanation for this behavior could lie in the natural focusing of energy towards the fibre direction that could result in an anisotropic geometrical spreading function that differs from equation 2.8 as pointed out in [56, 60].

**3. Dissipation into adjacent media:** When the wave propagating medium is surrounded by another media other than vacuum, acoustic waves can be transmitted in the form of leaky waves into the adjacent media. The portion of wave energy that is transmitted and reflected at the interface thereby depends on the wave mode, the incident angle and the acoustic impedances of both media [35, 61]. Regarding longitudinal waves with normal incidence, the amount of energy that is reflected at the interface is

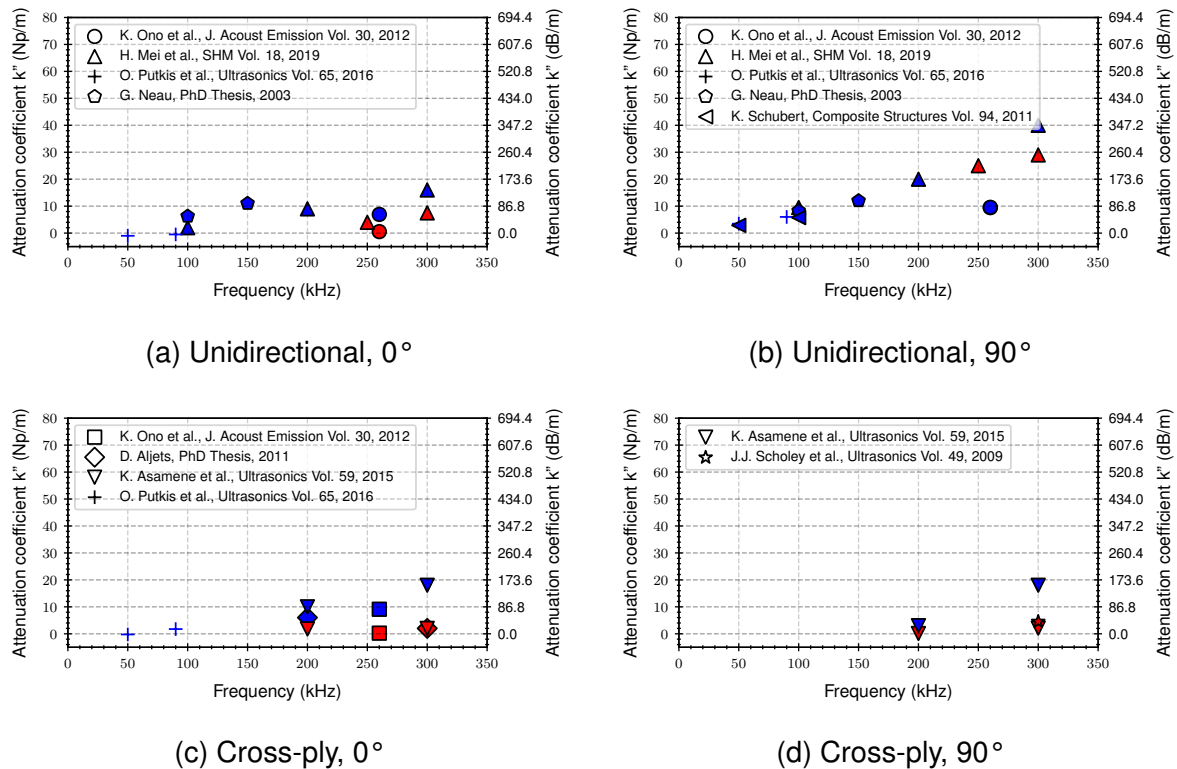


Figure 2.6: Experimentally determined attenuation coefficients (Np/m and dB/m) of the fundamental Lamb wave modes  $A_0$  (blue) and  $S_0$  (red) in unidirectional (a,b) and cross-ply (c,d) CFRP laminates as a function of frequency (kHz) and propagation direction (a,c:  $0^\circ$ ; b,d:  $90^\circ$ ).

proportional to the square difference in acoustic impedances of both media [61]. Depending on the surrounding media (e.g. air or water), dissipation into adjacent media can therefore contribute significantly to wave attenuation [66].

**4. Dispersion:** In dispersive media, an initially short pulse with a broad bandwidth will be spread in time with propagation distance, due to the fact that the energy in a wave packet travels at different speed depending on its frequency. As the energy is distributed among diverging wave packets, the amplitude of the whole wave packet decays with increasing propagation distance. The loss in amplitude thereby depends not only on the propagation distance but also on the steepness of the dispersion curve and the bandwidth of the initial pulse [67].

In FRP, additional attenuation can result from **continuous mode conversion**. This phenomena was observed first by Willberg et. al [68] in a CFRP plate partially made of woven fabric. Through experimental and numerical studies, they could show that the  $S_0$  mode is continuously converted into the  $A_0$  mode due to the periodic differences in stiffness induced by the structure of the fabric. Later on, this phenomenon was also verified numerically and experimentally for a cross-ply CFRP plate made from

unidirectional prepreg for wave propagation along the principal fibre directions [69]. The phenomenon seems to be limited to the attenuation of the  $S_0$  mode specifically. However, analytical models for the determination of its amplitude loss have not been suggested.

## 2.3 Acoustic emission analysis

### 2.3.1 Working principle and applications

**Acoustic emissions** are defined as transient elastic waves that are generated through the rapid release of energy caused by processes such as crack initiation and propagation [5]. AE analysis deals with the detection, processing and interpretation of these acoustic waves in order to get information about the source that caused them. Besides the point in time of the AE event, its location, size and type can be of particular interest. In its nature, AE analysis is similar to seismology where earthquakes are characterized and classified through the detection and analysis of released seismic waves. However, in contrast to seismology, AE analysis focuses on processes on the microscopic scale and the analysis of released AE in the ultrasonic frequency range. The bandwidth taken for the detection and evaluation of AE signals is typically confined to frequencies between 10 kHz and 1 MHz [5]. In this frequency range, AE can be generated and detected not only from crack formation and propagation but also from plastic deformation (e.g. twinning in tin), phase transformations (e.g. martensitic transformation in steel), friction, leakage and corrosion.

**The typical setup for AE analysis** is shown in figure 2.7. Although AE analysis is defined as a non-destructive testing (NDT) method [5], a damaging event is necessary for its application. In this case, the event is represented by a crack that is formed as a result of an external force. In the moment of its initiation, the crack acts as an omnidirectional emitter for acoustic waves that propagate inside the structure and eventually hit a piezoelectric sensor that is attached to the surface of the structure with a coupling agent (e.g. silicon grease). Through the piezoelectric effect, the sensor is able to convert the mechanical displacement caused by the acoustic wave into an electrical signal that is amplified and digitized in the next step. The result is a digital waveform that can be analysed further to retrieve more information about the underlying source than its moment of detection. Through signal processing and feature extraction, the location as well as the type of the source are accessible. Readers are referred to sections 2.3.2 and 2.3.3 for further information on the underlying methodology.

In the field of NDT, **AE analysis** stands out by the following **characteristics**:

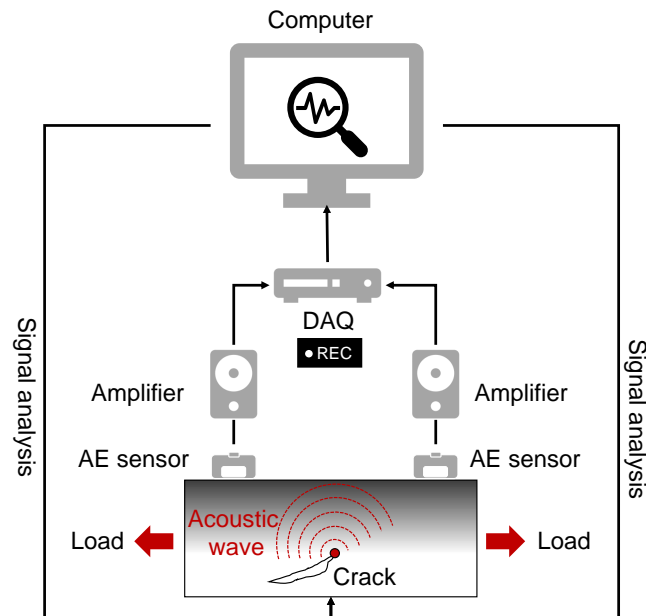


Figure 2.7: Typical setup for acoustic emission analysis.

- **Passive** - In AE analysis, the detected energy is released by the object itself and not being supplied by the NDT method as in ultrasonic testing or radiography. The necessary hardware can therefore be reduced to a sensor, an amplifier and a data acquisition unit.
- **Sensitive** - Due to its passive nature and the high sensitivity of the piezoelectric sensors, AE analysis is capable of detecting events on the microscopic scale. This involves phase transformations, plastic deformation or even single fibre filament failure in fibre reinforced plastics. On the other side, this sensitivity can cause further challenges due to perception of ambient noise.
- **Integral** - Most AE sources act as omnidirectional point emitters, releasing acoustic waves in all directions. These waves can propagate in the structure and eventually trigger a sensor that is located in the vicinity of the source. This integral aspect allows the monitoring of large and inaccessible areas. Compared to ultrasonic testing where structures need to be completely scanned with a transducer to find flaws, the damaging event is the transducer itself in AE analysis.
- **Dynamic** - The potential of AE analysis is limited to dynamic processes. Flaws that are already in the structure cannot be detected unless these get acoustically active again through an external load that forces flaws to grow or to produce AE through friction.
- **In-situ** - Damaging processes can be observed inline with AE analysis without any disturbance to the specimen or the need to interrupt the test for the investi-

gation. AE analysis is a suitable in-situ method for the monitoring of structures, processes or proof tests.

Due to these characteristics AE analysis has found its way in many **industrial applications** in engineering since its discovery in the middle of the 20th century. In the beginning, metallic components and concrete structures from civil engineering were in the center of attention. Classic applications include the detection of valve leaks, the monitoring of corrosion in tanks and pipes, the inspection of bridges as well as the proof testing of pressure vessels [70–72]. Later on, applications were extended to the field of fibre reinforced plastics where AE analysis has been implemented for the quality inspection and proof testing of composite pressure vessels [19, 20] and Formula 1 monocoques [21].

Besides industrial applications, research has revealed **further potential for AE analysis of composite structures**. In this context, extensive effort has been spent to advance AE analysis to an in-situ monitoring tool for failure analysis that enables the localization and identification of damaging modes in FRP. Potential application scenarios have been presented in the following fields:

1. **Material characterization:** By identifying the damaging mode and location from first to last ply failure, AE analysis can support the interpretation of stress-strain curves and the generation of reliable material properties. Examples include the determination of
  - apparent interlaminar strength via short-beam-shear test according to ASTM D2344 or ISO 14130 [6],
  - fracture strength distributions via fibre bundle testing [10],
  - mode I and mode II interlaminar fracture toughness via double-cantilever beam according to ASTM D5528 (ISO 15024) for mode I and ASTM D7905 (ISO 15114) for mode II [7–9],

Furthermore, AE analysis can detect the onset and progression of failure and thereby support the understanding of complex degradation behavior in FRP. Results can be utilized to access necessary properties for degradation analysis or to validate corresponding theoretical models. Examples include

- the determination of transverse matrix crack densities during quasi-static tensile testing [25, 73, 74],
- the identification of failure onset and progression of damaging modes during quasi-static [11–13] and fatigue testing [75–78]

- the time dependency of damaging modes during creep tensile testing [79] as well as
  - the tracking of delamination growth in mode I and mode II or mixed mode fracture toughness tests [8, 9, 80–83]
2. **Structural component testing:** AE source identification can function as a tool for the validation of failure loads and modes derived from finite element analysis and the visualization of damage progression during quasi-static and fatigue tests. Source identification has therefore been performed on full-scale structural tests of wind turbine blades [15–18], frames [14], torsion shafts [6] and pressure vessels [20, 84].
  3. **Structural Health Monitoring:** Structural Health Monitoring (SHM) applications could benefit from AE source identification through access of information on the damaging mode and its location. This way, the effects of local failure on remaining stiffness and strength of the component could be assessed through FEA which, in turn, could serve as valuable information for the definition and scheduling of repair jobs and predictions of remaining life time. Possible applications include the monitoring of wind turbine blades as shown in [17, 18].

### 2.3.2 Localization of AE sources in FRP

Knowledge on the the location of an AE source can be valuable information for the interpretation of AE measurements. Especially in the field of source identification, the location of the damaging event is of particular interest. In this context, localization can support the correlation of AE with damaging events by matching the source positions with crack positions from imaging NDT methods [23, 74]. Furthermore, source-to-sensor distance can have a strong impact on signal characteristics. Source localization was therefore termed as a necessary step for the interpretation and assessment of classification results [26, 85]. In the following paragraphs, an overview is given on the fundamentals of source localization with a focus on the challenges encountered in thin-walled FRP structures.

The differences in arrival times between sensor pairs are the foundation for AE source localization. With knowledge on the group velocity of the triggering wave modes, these differences in time can be translated into differences in propagation path. In a one-dimensional problem where only two sensors were triggered by the acoustic wave, the source can be positioned relatively on the connecting line between those sensors. The same principle can be applied to higher dimensional problems. However, source localization in two dimensions already requires a minimum of three sensors.



While a detailed explanation on the procedure for source localization can be found in [5], only the most relevant parts for this thesis are presented here. A major step in AE source localization involves the **determination of time of arrival** of the acoustic wave at every triggering sensor. This can be realized by a simple threshold where the first threshold crossing denotes the time of arrival. However, since threshold based methods are not reliable for the detection of signal onset [86, 87], other methods have been suggested. One prominent example includes the Akaike Information Criterion (AIC) [88] that was introduced as time of arrival picker by Maeda [89] and later on adapted by several authors [87, 90]. An alternative to the AIC picker was suggested by Grosse on the basis of the Hinkley criterion [91]. In this approach, the time of arrival is represented by the global minimum of the modified partial energy  $S'_i$ . This energy can be calculated according to equation 2.10 as a function of the partial energy  $S_i$  which is the cumulative sum of all samples  $i$  of the time series  $x$  and a variable trend  $\delta$  which is calculated according to equation 2.11 as a function of the total partial energy  $S_N$  of the signal, the number of sample points  $N$  and a delay factor  $\alpha$  that lies between 2 and 200.

$$S'_i = S_i - i \cdot \delta = \sum_{m=0}^i A_m^2 - i \cdot \delta \quad (2.10)$$

$$\delta = \frac{S_N}{\alpha \cdot N} \quad (2.11)$$

Further time of arrival pickers with a detailed discussion on their strengths can be found in [86, 87].

Since FRP structures are often designed as shell-like structures, dispersion has to be considered for source localization. The determination of time of arrival is therefore often accomplished in the time-frequency domain. This way the time of arrival can be determined for every single frequency using the before mentioned methods. In this context, many authors have utilized the wavelet transform as one signal processing method that enables the transformation to the time-frequency domain for burst type signals commonly encountered in AE analysis [92–95]. In the next step, the corresponding mode that triggered the time of arrival has to be identified. Since the group velocity of  $A_0$  and  $S_0$  mode can differ up to factor of five in unidirectional CFRP laminates (see figure 2.3(a)), this can have a significant impact on localization results. In order to increase the reliability of source localization results, authors have therefore suggested to identify the individual arrival times of both modes [85, 95, 96]. In this context, additional studies have shown that this can even reduce the number of necessary sensor pairs for the localization in one [95, 96] and two dimensions [97]. If frequency, mode and corresponding time of arrival are determined for every sensor that was triggered by the acoustic wave, the location of the source can be calculated with the corresponding

group velocity  $v_{gr}$ . For the one-dimensional case, where two sensors 1 and 2 are positioned at distance  $x_{12}$  to each other, the distance  $x$  between the first hit sensor and the source can be calculated as

$$x = \frac{1}{2}(x_{12} - \Delta t \cdot v_{gr}), \quad (2.12)$$

where  $\Delta t$  denotes the difference in arrival times between both sensors. For FRP structures, it should be noted that group velocity is also a function of propagation direction as shown in figure 2.4. This aspect makes localization of AE source in two-dimensions challenging for FRP structures since the propagation direction is not known from the beginning. Since the two-dimensional case is not relevant for this thesis, the reader is referred to [92, 98–102] for numerical algorithms, neural networks and advanced sensor configurations that can be applied in simple and complex FRP structures.

### 2.3.3 Identification of AE sources in FRP

The identification of damaging mechanisms in FRP based on their acoustic emissions has been an ongoing field of research for more than 30 years. In order to intensify the knowledge on the complex degradation behavior of FRP (see section 2.1), many studies have been performed to advance AE analysis to an in-situ monitoring tool for failure analysis that enables the identification of damaging modes such as fibre fracture (FF) and inter-fibre fracture (IFF) on the basis of their acoustic emissions. Before the procedure for AE source identification is explained in detail, a closer look is taken at the foundation for AE source identification.

#### Foundation

Damaging mechanisms excite acoustic emissions due to the abrupt relaxation of stresses during crack forming and propagation. The resulting acoustic wave can be treated as a fingerprint for the damaging mechanism that allows its traceability. The **foundation** for this **acoustic fingerprint** lies in the crack kinematics as explained in [6]. When a critical stress level is reached locally, new surfaces are created to form a crack. In the moment of stress release, these surfaces are deflected within a characteristic time span that is defined as the **source rise time**. Upon deformation the crack surfaces start oscillating until they find a new equilibrium state. This deflection results in an acoustic wave according to the elastic wave equation, if displacement can be regarded as small and elastic. The abrupt excitation in the form of an impulse thereby creates a broad spectrum of acoustic waves where the bandwidth is proportional to the inverse of the source rise time [103]. Since the rise time is again linked through the generalized theory of AE to the elastic properties of the cracking material and the local loading conditions, the excited wave is characteristic for the damaging event [104, 105]. It carries valuable information for source identification that is accessible through AE analysis.

Brittle and ductile failure, for example, can be distinguished because the characteristic time span generally decreases with increasing brittleness [106]. In terms of FRP, this means that the failure of a brittle fibre should be accompanied by a higher frequency content than that of the ductile polymeric matrix. Although the characteristic rise times of these damaging mechanisms are not readily accessible by measurement, numerical methods have been developed for their determination. Sause et al. [107] developed an AE source model based on finite element modelling that allows the determination of rise times by capturing the whole process from crack initiation towards propagation to resulting acoustic emissions. This way, the characteristic rise times for fibre fracture (HTA carbon fibre) and matrix cracking (RTM6 epoxy resin) were determined to 1.2 ns and 1.1  $\mu$ s respectively. Consequently, the theoretical bandwidth of acoustic emissions excited by these two damaging mechanisms should differ around 3 orders of magnitude (1000 MHz for fibre fracture to 1 MHz for matrix cracking). The validation of source rise times was realized with success by comparing the simulated AE with the resulting AE from fibre fracture and matrix cracking from carefully designed experiments.

Another aspect for the differentiation of fibre and matrix fracture was introduced by Bohse [108] with the concept of visco-elastic relaxation processes and intrinsic frequencies adapted from [109]. Due to the differences in elastic modulus  $E$  and densities  $\rho$ , the relaxation times  $\tau$  and the resulting intrinsic frequencies  $f$  of fibre and matrix fracture differ according to

$$f \sim 1/\tau \sim \sqrt{\frac{E}{\rho}} \quad (2.13)$$

With typical properties for carbon fibres ( $E=245$  GPa,  $\rho=1800$  kg/m<sup>3</sup>) and the epoxy matrix ( $E=3.4$  GPa,  $\rho=1200$  kg/m<sup>3</sup>) taken from [30], the intrinsic frequencies of fibre fracture and matrix fracture should relate in a ratio of around 7:1 in CFRP.

Besides source rise time and relaxation times, the **three dimensional displacement field of the crack surface** during formation is another characteristic of a damaging mechanism that affects the resulting AE and thereby offers another potential for source discrimination. Regarding thin-walled structures, this potential is accessible through **modal acoustic emission analysis (MAE)**. This technique delivers qualitative information on the direction of crack surface displacement (in-plane or out-of-plane) by analysing the strength of the fundamental symmetric ( $S_0$ ) and anti-symmetric ( $A_0$ ) wave modes in the respective acoustic emission signal. As already pointed out in section 2.2.1, the displacement fields of the fundamental wave modes differ. The  $A_0$  mode shows a strong out-of-plane characteristic (flexural mode) compared to the  $S_0$  mode where the in-plane portion dominates the displacement field (extensional mode) for low  $f \cdot d$  products. A crack will predominantly excite the wave mode whose displacement field resembles that of the crack during forming. Information on the

displacement field is therefore accessible through analysis of the relative modal content. A classification towards in-plane or out-of-plane source can therefore be realized by analysing the ratio of  $S_0$  to  $A_0$  mode in the resulting AE. The potential of MAE was visualized first in the work of Gorman et al. where a differentiation between in-plane and out-of-plane Hsu-Nielsen sources was accomplished by analysing the proportion of  $S_0$  to  $A_0$  in the resulting signals [110, 111]. In terms of FRP, several authors applied the MAE analysis to support source identification and distinguish between delaminations as an out-of-plane source and fibre fracture or transverse matrix cracking as typical in-plane sources for example [57, 112–122].

Since the displacement fields of  $S_0$  and  $A_0$  depend on depth, the MSEA can also be utilized to gain information on the source depth. Regarding "in-plane" source for example, the ratio of  $S_0$  to  $A_0$  increases with increasing source depth up to the plane of symmetry where theoretically no  $A_0$  can be excited with pure "in-plane" displacement [93, 121, 123]. This phenomenon was also observed during quasi-static tensile testing, where transverse matrix cracking in the outer and inner layers of cross-ply CFRP laminates produced significantly different frequency characteristics due to the change in modal content [24–26]. The reason for this drastic change is mainly due to the different attenuation characteristics of  $S_0$  and  $A_0$  in CFRP and will be discussed further in sections 2.4.1 and 2.4.2.

The underlying methodology on how these fingerprints of damaging modes are identified on the basis of the acoustic waveforms is going to be explained in the next paragraph.

### **Procedure**

The **procedure for AE source identification** has developed in the last 30 years, as processing power and capacity of computers have improved, measurement hardware systems have advanced and sophisticated software solutions have become available. The common procedure for source identification nowadays is based on a statistical analysis that aims to reveal patterns in a data set of characteristic features from the acquired waveforms. These patterns often appear in the form of clusters - a group of events that show similar characteristics. Following the concept of the acoustic fingerprint, as explained earlier in this section, acoustic emissions of a single damaging mechanism should sound similar and share characteristic features so that they should be found in one of these clusters in the feature space. The correlation of the clusters with their underlying damaging mechanism, however, requires a method for validation that aims to either visualize the corresponding damaging event or simulate its acoustic fingerprint for comparison. Whereas these clusters were identified manually in the past, there are numerous machine learning methods available nowadays that can sup-

port in this process. The whole procedure, starting from the crack that releases the acoustic wave up to its identification, is visualized in figure 2.8.

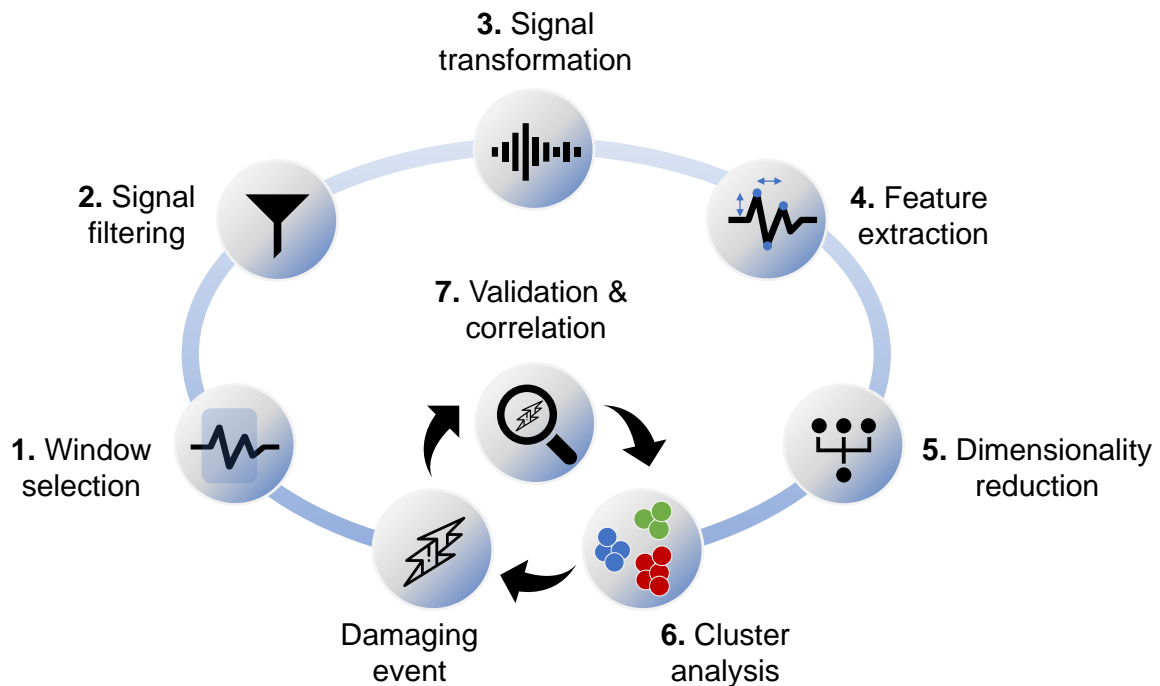


Figure 2.8: Typical procedure for the source identification of damaging events in fibre reinforced plastics.

Seven consecutive steps can be recognized that are discussed in detail in the following paragraphs.

### 1. Window selection

A defined window of  $N$  samples of the acquired waveforms is selected based on the time of arrival. This part of the signal is extracted and serves as the basis for further analysis. Typically 100 to 200  $\mu\text{s}$  are selected for evaluation [25, 26]. As shown in [6], the evaluation window can have strong impact on the extracted features due to the influence of edge reflections and wave dispersion. The relevant portion of the signal is at the beginning and should carry the excited wave modes in the structure [6, 124]. A typical example of such a signal that was acquired from a damaging event in a cross-ply CFRP laminate is shown in figure 2.9. The evaluation window is shown in blue.

### 2. Signal filtering

In the next step, the signals can be filtered in the frequency domain to remove noisy and non-relevant data that originate from the surrounding (e.g. mechanical vibrations, electromagnetic interference, etc.) or to separate wave modes for individual analysis [114]. Filtering can either be accomplished by hardware prior to waveform acquisition and/or by software in a post-processing step through digital filters with either finite (FIR) or infinite impulse response (IIR). For further details on digital filters and their implementation in python the reader is referred to [125].

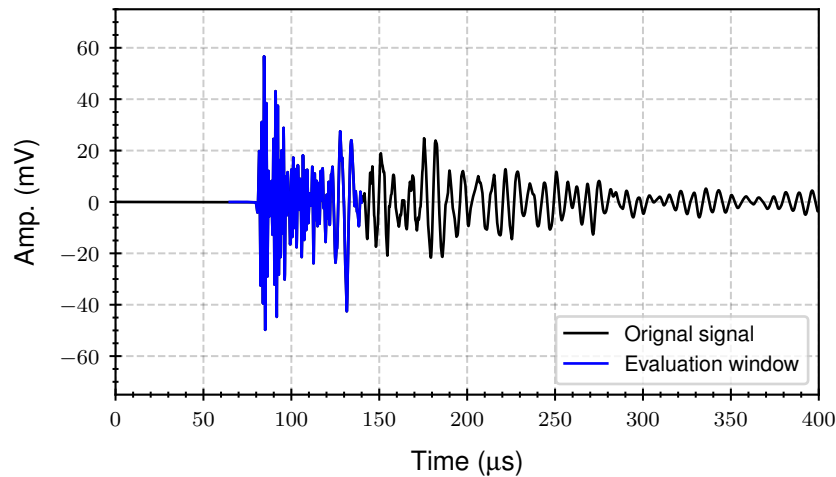


Figure 2.9: Typical example for an acquired waveform from a damaging event in a cross-ply CFRP laminate. The evaluation window is shown in blue.

### 3. Signal transformation

The transformation of the signal into another domain enables different perspectives on the signal, revealing further characteristics for classification. For the processing of AE transient signals the Discrete Fourier Transform (DFT) and the Continuous (CWT) and Discrete Wavelet Transform (DWT) are well established methods to investigate the frequency as well as time-frequency domain of the signal.

The **DFT** is an analytical method that represents the discrete signal, with equally-spaced samples, as a superposition of complex sine and cosine functions. The result is a complex series that can be expressed in the form of an amplitude and phase spectrum. In terms of AE analysis, the amplitude spectrum represents a valuable source of information since dominant frequencies and frequency bands in the signal can be easily identified. Figure 2.10 shows the amplitude spectrum of the signal window from figure 2.9. A distinct peak around 150 kHz can be observed that is characteristic for the damaging event. The DFT was realized through the algorithm of the Fast Fourier Transform (FFT) which is computationally more efficient than the standard DFT, especially if the number of signal samples equals a power of two. More information on the DFT and FFT can be found in [126].

Although the DFT is a valuable tool for the visualization of the frequency content, the assumption of a periodic signal is not true for the transient, burst type signals that are frequently encountered in AE analysis. The DFT suppresses the time domain and thereby does not allow to extract information on the time sequence of single frequency components which could support the identification of wave modes and the characterization of their dispersion characteristics. For this purpose, the Wavelet Transform was introduced. It enables a time-frequency representation of non-stationary signals [127].

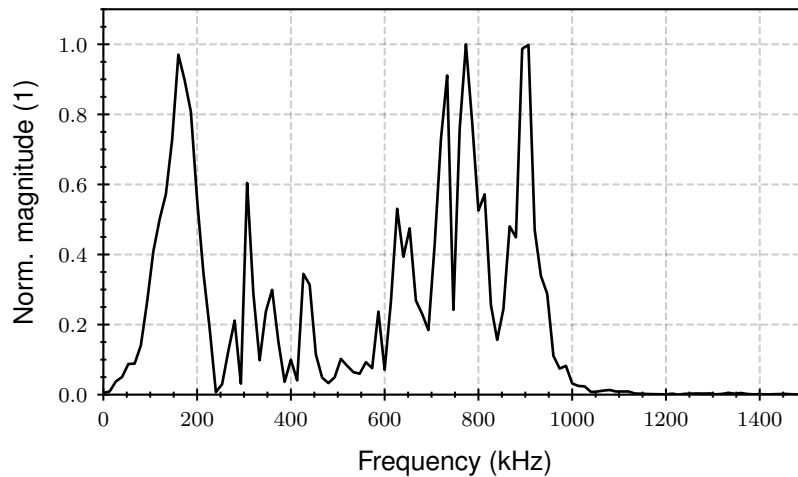


Figure 2.10: Normalized FFT spectrum of the time signal in figure 2.9.

With respect to other time-frequency transformations like the Short-Time Fourier Transform, the analysing time window for the Wavelet Transform varies in size, allowing a systematic variation of time and frequency resolution according to the uncertainty principle. This makes the Wavelet Transform ideal for the analysis of short high-frequency as well as extended low-frequency components that are frequently found in AE signals.

The **CWT** decomposes the signal into a set of wavelets. These wavelets are derived from a mother wavelet and scaled and shifted in order to match the original signal. The CWT coefficients describe the corresponding match as a function of scale and position parameter of the wavelet.

The CWT has been applied by many authors to investigate the modal content of the AE signal [79, 93, 116, 121, 128]. Depending on the shape of the signal, different mother wavelets can be selected [127]. Among these, the Morlet wavelet is common for the representation of burst type signals in AE analysis. It is applied for the CWT of the filtered signal. The time signal as well as the resulting time-frequency representation are illustrated in figure 2.11. The colors represent the standardized magnitude of wavelet coefficients. Position and scale parameters were converted to time and frequency.

The **DWT** decomposes the analysed signal into frequency bands by applying two complementary filters. At each level of decomposition, the approximation (high scale, low frequency) and details (low scale, high frequency) of the original signal are acquired this way [127]. In contrast to the CWT, the scales of the DWT are discretized to integer powers of 2 which results in a coarser representation of the scales. However, similar to the FFT, this leads to higher computational efficiency for the DWT. The DWT has been utilized by many authors to decompose AE signals and identify their characteristics on different levels of decomposition [79, 82, 129–131]

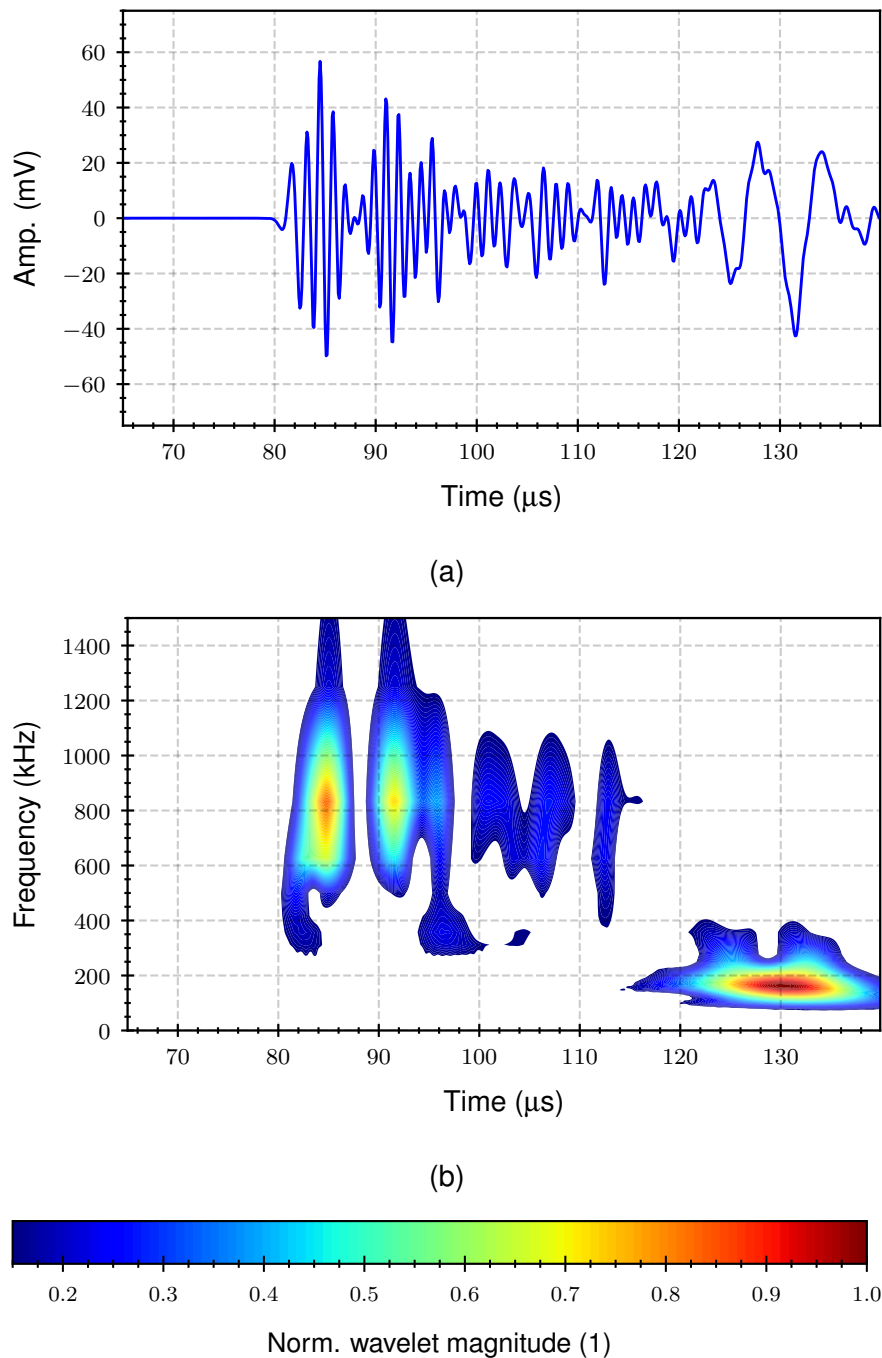


Figure 2.11: Time signal (a) from figure 2.9 and its CWT (b) showing the normalized wavelet magnitude (1) as a function of time ( $\mu\text{s}$ ) and frequency (kHz). The complex Morlet Wavelet was used as mother wavelet.

#### 4. Feature extraction

Features are numerical parameters that aim to describe the unique characteristics of the signal. Features for AE analysis are typically extracted from the time, frequency and time-frequency domain. Exemplary features from the time domain include the maximum amplitude, rise time, duration and counts (number of peaks above threshold) of the signal. Regarding the frequency domain, the peak frequency  $f_p$ , frequency cen-



centroid  $f_c$  and the partial powers  $PP_i$  of frequency bands are prominent features that have been utilized for source identification in FRP [25, 26, 73, 117, 130, 132–134]. Besides these directly accessible features, mathematical combinations of existing features have been proposed as valuable descriptors. Examples include the average frequency as ratio of number of counts divided by signal duration as well as the weighted peak frequency  $f_{wp}$  as the geometrical mean of the peak frequency  $f_p$  and frequency centroid  $f_c$  [134]. Some of the features from the frequency domain can be found in the amplitude spectrum in figure 2.12.

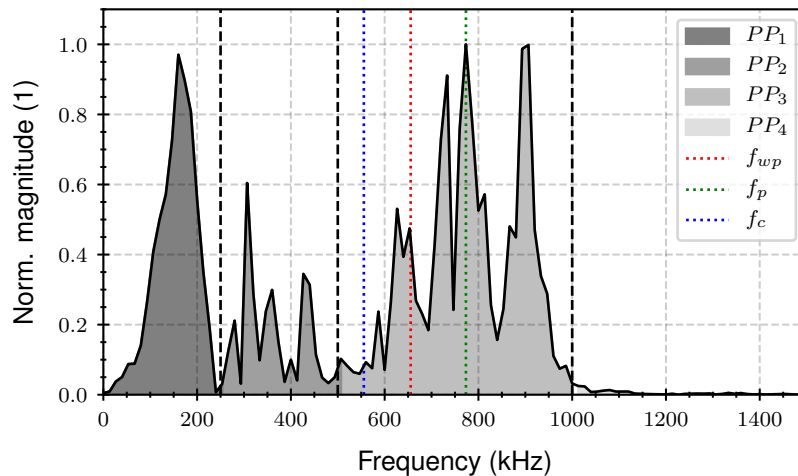


Figure 2.12: Normalized FFT spectrum from 2.10 with characteristic features.

Regarding the time-frequency domain, technically, most of the before mentioned features from the time and frequency domain could be determined as a function of frequency and time respectively. However, many authors limit the features to the energy in specific frequency bands [79, 130, 135].

In thin-walled structures, further information can be extracted by discriminating between the individual contribution of wave modes. As mentioned in section 2.3.3 the relative strength of the fundamental wave modes  $S_0$  and  $A_0$  can be a valuable feature for source identification in thin-walled structures [120–122].

A more comprehensive list of features with details on their calculations can be found in [6, 136, 137].

## 5. Dimensionality reduction

Reducing the dimension of a data set is crucial for efficient classification. Irrelevant and redundant features should be dropped from the list of features in order to reduce computational costs and complexity, ease data visualization and improve classification quality. Dimensionality reduction is therefore highly recommended prior to cluster analysis. Existing techniques can be divided into **feature selection** and **feature extraction** methods. In the latter, features are projected into a new space with lower dimensionality. Examples include the Principal Component Analysis (PCA), Singular

Value Decomposition (SVD) and Linear Discriminant Analysis (LDA). Among these, the PCA is a common tool in AE analysis. It represents an orthogonal linear transformation into a new coordinate system of uncorrelated features, called the principal components. It has been widely utilized in the context of AE source identification in composites to reduce the feature space for subsequent cluster analysis and aid data visualization [73, 129, 130, 133, 138–140].

Feature selection, on the other hand, aims to find a suitable subset among the existing features by evaluating each feature in terms of variance and separability. According to [141], there are three different approaches that can be followed:

- (a) Filter approach,
- (b) wrapper approach and
- (c) hybrid approach

Filter techniques examine the intrinsic properties of the data. One can distinguish between univariate and multivariate approaches. In univariate approaches, a key figure (score) is calculated for each feature individually that allows a comparison among them. In contrast to supervised learning, where data is labeled and features can be evaluated based on their contribution and relevance to the target, it remains a challenge to find suitable scores for unsupervised learning problems [142]. In the past, several approaches have been suggested that include the determination of maximum variance, Laplacian score [143] as well as spectral filtering [144]. Regarding AE source identification, applications for the Laplacian score can be found in [23, 73, 133, 145]. Multivariate approaches, on the other hand, try to identify correlations between features, for example. One figure of merit can be the Pearson correlation coefficient that specifically looks at linear dependencies between variables. Following this approach, redundancy in the data set has been eliminated by several authors in the AE community [73, 133, 138, 139, 146–150].

Wrapper approaches evaluate each feature subset iteratively based on the quality of the resulting partition from cluster analysis. The quality is thereby determined by clustering indices that measure the separation and compactness among the resulting clusters. Exemplary indices include the Davis-Bouldin index [151], the Silhouette coefficient [152], the Calinski-Harabasz score [153], the Tou-index [154], the partition coefficient [155] and partition index [156] which have been widely used in the field AE source identification [23, 79, 129, 133, 134, 146, 149, 157–159]. Since each index looks at different aspects of the partition, authors have suggested voting schemes that aim to identify the optimal feature subset based on a whole set of clustering indices [134, 159]. However, due to the amount of possible feature combinations, these approaches are computationally intensive. A sequential feature selection algorithm

was therefore suggested that starts with a single feature and only adds those features to the set which contribute to cluster separability [16, 76].

Another way to decrease computational costs can be realized through hybrid approaches. Direct filtering techniques are combined with wrapper techniques for efficient feature selection this way. The amount of features is reduced through filtering techniques in the first step, thereby limiting the amount of feature combinations for the subsequent wrapping.

## 6. Cluster analysis

The goal of cluster analysis is to find groups of similar data points (clusters) that can be correlated to damaging events in a later step. As an unsupervised learning method, no prior knowledge on the classification of data points is given. Instead, one has to find these classes solely based on the structure of the data itself. Figure 2.13 gives an example for a data set that was derived from quasi-static tensile testing of a cross-ply CFRP laminate. Each AE event is plotted in terms of weighted peak frequency  $f_{wp}$  and  $PP2$  (200 to 300 kHz). A clustering algorithm was applied in order to group data automatically into clusters. These clustering algorithms are based on some kind of similarity measure between data points [160]. The euclidean distance is an example for such a measure. If two data points are close to each other, they are grouped in the same cluster. Among the available methods, k-means [16, 23, 73, 82, 133, 134, 138, 139, 147, 150, 161]), Self-Organizing Maps (SOM) in combination with k-means [117, 122, 157, 162], and Fuzzy C-means clustering [79, 82, 129, 130, 139, 163] are widely used in the field of AE source identification.

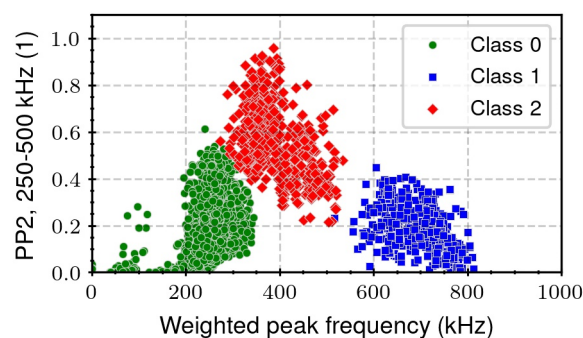


Figure 2.13: Identification of clusters in an AE data set from quasi-static tensile tests of a cross-ply CFRP laminate. AE events are represented based on weighted peak frequency (kHz) and partial power 2 between 200 and 300 kHz (1).

These methods do not only differ in their measure of similarity and their initialization but also in the labeling of data points. Whereas for k-means, data points can only be

assigned to a single class (hard clustering), data points can be associated to every class to a certain degree in Fuzzy C-means clustering (soft clustering). An important aspect that one should keep in mind when selecting an appropriate algorithm is that its performance highly depends on the shape of the clusters. A comprehensive overview on the algorithms and comparison of their performance can be found in [160, 164, 165]. Besides the choice of the clustering algorithm, the definition of the number of clusters represents another major challenge. This number is usually unknown but required as input parameter by most of the clustering algorithms. One way to overcome this problem, is to follow wrapping approaches that are similar to those performed for feature selection. Instead of varying the feature subset, the number of clusters is altered iteratively while looking at clustering performance through clustering indices like the Davies-Bouldin index [23, 133, 134, 146, 149, 157–159], the Silhouette coefficient [23, 133, 134, 159], the Tou-index [134, 146, 149, 158], the Calinski-Harabasz index [159], Hubert's Gamma statistic [134] as well as the partition coefficient and index [79, 129]. The partition with the best score in one or several of these indices, based on a voting scheme [134, 159], is then selected for further analysis.

## 7. Validation & correlation

Now that clusters in the data set have been identified, they have to be connected to the underlying source in the next step. The correlation of identified clusters with their corresponding damaging mechanism requires a method of validation. This has been accomplished by:

- performing post-fracture analysis using light microscopy [25], scanning electron microscopy [81–83, 129, 130, 159, 166, 167] or ultrasonic testing [116, 122, 132, 168],
- comparing representative signals from each cluster with signals derived from:
  - mechanical tests that are designed for a specific failure on single constituent level (e.g. fibre filament and neat resin testing) [83, 108, 114, 130, 149, 167, 169–171],
  - mechanical tests that are designed for a specific failure on laminate level (e.g. tensile testing of a unidirectional laminate parallel and perpendicular to the fibre direction for the predominant generation of fibre fracture and transverse matrix cracking respectively) [79, 101, 132, 140, 157, 162, 167, 169, 171],
  - simulations of AE initiation, propagation and detection for each single damaging mode [81, 172, 173],
  - experiments with artificial sources with known characteristics (e.g. pulsed Laser with various spot shapes as in and out-of-plane acting source) [116],
- matching the onset of cluster activity with

- failure predictions from FEM simulations [130, 174],
- theoretical considerations on the order of damaging modes (e.g. transverse matrix cracking in  $90^\circ$  layers generally appears prior to fibre fracture in  $(0^\circ/90^\circ)$  cross-ply CFRP laminates under tensile loading in  $0^\circ$  direction) [117, 129, 140],
- findings from step wise loading and repeated inspection with ultrasonic testing [101, 175], active Thermography [175], X-Ray radiography and Computer Tomography [174] or light microscopy [148]
- findings from in-situ observation through visual inspection [116, 140], passive Thermography [74, 147, 168] passive Thermography in combination with Digital Image Correlation [146], or Digital Image Correlation combined with specimen edge observation [23, 24],
- theoretical considerations based on AE theory (e.g. the intrinsic frequency of relaxation processes that differs between fibre and matrix) [82, 83],
- following existing classification schemes from other authors (e.g. based on peak frequency) [79, 82, 129, 130, 133, 163])

In many cases, validation and correlation is not limited to a single method of the above mentioned but rather a combination of several approaches.

### 2.3.4 The acoustic fingerprint of damaging modes in FRP

Following the procedure from the section 2.3.3 many authors have tried to define the acoustic fingerprint of damaging modes in FRP based on single or multiple features from the resulting acoustic emissions. The peak frequency and maximum amplitude of the acoustic wave are two prominent features in this context. Due to their direct linkage to source characteristics according to the generalized AE theory (see foundation for source identification in section 2.3.3) and their straight forward physical interpretation, both features have been frequently considered to characterize the fingerprint of damaging modes such as fibre breakage, matrix cracking or delaminations [129, 132, 166, 169, 176, 177]. Due to statistical variations in the resulting AE of these events, the fingerprint of a damaging event is rather represented by classification windows than by absolute values. Regarding the peak frequency, figure 2.14 gives an overview on classification windows for damaging modes in FRP that were proposed by different authors [80, 114, 129, 130, 132, 133, 166, 167, 169, 178] in the past. For a comprehensive overview on classification windows, the reader is referred to [22, 23]. Despite the differences in material and experimental setup, a systematic trend can be observed from figure 2.14 that fibre breakage leads to AE with higher peak frequencies than matrix cracking. This result is in accordance with theoretical considerations

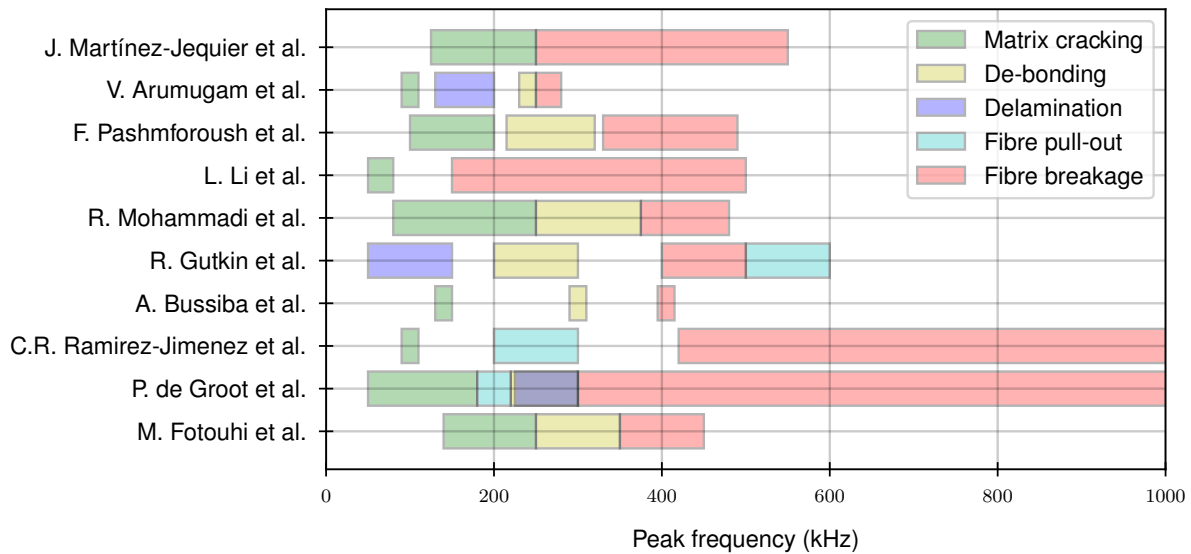


Figure 2.14: Classification windows for damaging events in FRP that were derived by different authors [80, 114, 129, 130, 132, 133, 166, 167, 169, 178] based on the value of peak frequency (kHz) of the resulting AE.

from generalized AE theory. Other damaging events such as de-bonding, delamination or fibre pull-out typically show peak frequency values that lie in between. However, classification windows for damaging events shift and overlap among authors, creating doubts on their validity and transferability. Nevertheless, similar trends were discovered in the extensive studies by Sause et al. who introduced the weighted peak frequency, as geometrical mean of peak frequency and frequency centroid, as valuable feature for source discrimination in FRP [81, 134, 172]. Mainly based on this feature, matrix cracking, fibre-matrix interface failure and fibre fracture could be successfully distinguished in various applications [6]. In contrast to these trends, recent studies have shown that transverse matrix cracking in the plane of symmetry of a cross-ply laminate can produce peak frequencies that are similar to those of fibre breakage [24, 25]. The common belief that these two damaging mechanisms can be experimentally separated based on their resulting frequency content was therefore questioned as well. As already pointed out by [27], there is no universal signature for a damaging mode.

**Despite theoretical foundations, the acoustic fingerprint of a damaging mode seems to become a vague concept when it comes to its experimental verification.**

## 2.4 Influencing factors on AE source characteristics

The characteristics of an AE source can be modified along the whole measurement chain. Specimen, sensor and amplifier show individual transfer functions that affect the measurement signal and its characteristics [179]. The fingerprint of the actual source is

in a way disguised by the elements of the measurement chain. Exemplary aspects have been numerically and experimentally studied. These include the influence of specimen geometry [6, 124, 180, 181], laminate layup [6, 113, 181], internal damage [6], source-to-sensor distance [6, 26, 81, 124, 172, 180], source depth [24, 25, 124, 172, 180], sensor type [6, 180, 182] as well as sensor coupling [182–184]. A comprehensive discussion on all influencing factors is beyond the scope of this work. Therefore, the following paragraphs focus on the main aspects of this thesis: the influence of source depth and source-to-sensor distance. The discussion relates to ultrasonic guided waves because most of the work regarding composites is done with thin-walled structures.

#### 2.4.1 The influence of source depth

The fact that the displacement fields of the fundamental guided waves modes  $A_0$  and  $S_0$  is a function of depth is crucial in order to understand the influence of source depth on AE signal characteristics in thin-walled structures. As already stated in section 2.3.3, wave modes are predominately excited, if the resulting displacement field of the crack resembles the displacement field of the wave mode in the depth that the crack occurs. Hamstad et al. performed simulations in aluminum plates in order to demonstrate this effect [93]. In- and out-of-plane sources were introduced in different depths and the resulting waves were analysed in the time-frequency domain. For pure in-plane sources, they could show that the  $A_0$  mode vanishes with increasing source depth up to the plane of symmetry. This behavior could be explained by the displacement field of the  $A_0$  mode. Since the  $A_0$  mode does not show any in-plane displacement component in the plane of symmetry, it cannot be excited by a pure in-plane source in this depth. The same observation was made for pure out-of-plane sources and the  $S_0$  mode that lacks out-of-plane displacement components in the plane of symmetry. For the depths in between, a steady decrease in  $A_0$  amplitude was observed for in-plane sources up to the plane of symmetry. These results were verified later on by [180] who also performed numerical simulations on aluminum plates. Regarding CFRP laminates, similar conclusions could be drawn experimentally, through the introduction of artificial sources in different depths [116, 123].

Although a change in modal content does not have to result in a change in frequency content and characteristic features, there are four aspects that promote it:

1. **Wave attenuation:** As visualized in figure 2.6, the  $A_0$  mode shows significantly higher attenuation than the  $S_0$  mode in CFRP, leading to significant differences in frequency spectra with increasing propagation distance.
2. **Displacement field:** In typical AE experiments, the sensors are set-up to be sensitive towards the out-of-plane displacement component. Since the extent of out-of-plane displacement at the surface differs between  $A_0$  and  $S_0$  as a function

of frequency, sensitivity towards both wave modes is, in turn, a function of frequency as well (see figure 2.5). Since the out-of-plane character of the  $S_0$  mode develops with increasing frequency, the frequency spectrum is shifted towards higher frequencies for  $S_0$  dominant signals. The fact that the  $S_0$  mode is also less attenuated than the  $A_0$  mode, promotes this aspect once more.

3. **Wavelength:** Wavelength affects detectability of waves modes due to the aperture effect of standard AE sensors [5, 185]. If the wavelength is in the order of the sensor diameter, local maxima and minima can cancel each other out, leading to reduced signal amplitudes or even blind spots in the sensitivity of the sensor. Due to differences in the course of wavelength as a function of frequency, this affects both modes differently. Again, higher frequency content of the  $S_0$  mode is more likely to be preserved due to its larger wavelength compared to the  $A_0$  mode at the same frequency (see figure 2.3(b)).
4. **Excitation bands:** Fundamental guided wave modes are predominantly excited in specific frequency bands [93, 186]. The  $S_0$  mode is predominantly excited at higher frequencies than the  $A_0$  mode. This translates to different characteristic frequencies depending on which mode dominates.

All these aspects favour the spectrum to shift towards higher frequencies for  $S_0$  dominant AE signals. This was observed experimentally by several authors who investigated the effect of source depth on the resulting AE of transverse matrix cracks in cross-ply CFRP [23–26]. In contrast to the common classification scheme from figure 2.14, where matrix cracks are typically characterized by low ( $< 250$  kHz) and fibre breaks by high peak frequencies ( $> 250$  kHz), the authors could show that transverse matrix cracks in the inner plies - close to the plane of symmetry - can create AE with peak frequencies that are comparable to those of fibre breaks. The predominant generation of the  $S_0$  mode as a result of inner matrix cracks acting as in-plane sources was made responsible for this significant shift in frequency characteristics. However, an experimental verification of this  $S_0$  mode was not accomplished. In contrast to these results, Sause et al. concluded from simulations that fibre and matrix cracking could still be distinguished despite the influence of source depth [172]. The question remains whether the influence of source depth can lead to the misclassification of damaging modes in CFRP.

#### 2.4.2 The influence of source-to-sensor distance

As ultrasonic guided waves propagate, they are attenuated and thereby lose part of their characteristics. As already pointed out in section 2.2.2, this attenuation results



from geometric spreading, dispersion, mode conversion at discontinuities, scattering at the fibres and visco-elastic damping effects of the polymeric matrix.

Since attenuation is a function of frequency, the spectrum and its characteristic features are subject to change with source-to-sensor distance. In general, the specimen will act as a filter with low-pass characteristics, suppressing higher frequency components while preserving the lower frequency content with increasing propagation path.

In [26], the influence of source-to-sensor distance on the peak frequency is visualized through AE from damaging events in a cross-ply CFRP coupon specimen. The same AE event, was registered by two sensors of the same type with distances of around 1 and 40 mm to the source. The resulting drop in peak frequency from 700 to 100 kHz highlighted the strong impact of source-to-sensor distance on this prominent feature for source classification. Frequency centroid, on the other hand, was modified from around 1000 kHz to 650 kHz in the same signals. The authors therefore suggested the frequency centroid as a more robust feature for source identification due to its more steady decrease as a function of source-to-sensor distance. Similar results and conclusions were drawn by [182, 187]. The impact of source-to-sensor distance on weighted peak frequency and partial power was investigated in [81] on a CFRP DCB specimen. Three different artificial sources, potentially representing three different damaging mechanisms, were introduced at distances between 80 and 280 mm to the sensor, while compactness and separability among resulting clusters was evaluated. A significant shift in feature values was observed that led to higher scattering within each cluster. Although most sources could still be distinguished, the risk for misclassification could be demonstrated as well. Similar results were found in [161] for a large CFRP plate (500 x 500 mm) and various artificial signal sources. Depending on the modal content of the excited AE, the influence of source-to-sensor distances varies due to different attenuation characteristics of the wave modes. As already presented in section 2.2.2, in terms of CFRP laminates, the  $S_0$  mode shows lower attenuation than the  $A_0$  mode. Information on the frequency content of the source is therefore preserved for larger propagation distances when the  $S_0$  mode is predominantly excited by the source. Since the modal content depends also on the source depth, as shown earlier, there is a direct coupling between the influence of source depth and source-to-sensor distance.

Due to the anisotropic properties, attenuation depends on propagation direction, introducing another variable to the influence of source-to-sensor distance in CFRP. The influence of propagation direction on characteristics of the acoustic wave was shown in an experimental study on unidirectional, cross-ply and quasi-isotropic CFRP laminates in [6]. Out-of-plane and in-plane sources were artificially introduced through pencil lead breaks at the surface and the edge of the plate in order to excite a strong

$A_0$  and  $S_0$  mode respectively. Variations in partial power and weighted peak frequency were observed as a function of propagation direction at a constant source-to-sensor distance of 100 mm. Again, a shift in feature values was observed that varied with layup configuration and source type. For the unidirectional plate, the in-plane source resulted in the formation of single clusters that could accidentally be classified to various sources according to the procedure described in section 2.3.3. For the out-of-plane sources, cluster formation could not be observed. This example shows again the differences between wave modes. The in-plane source which generates predominantly the  $S_0$  mode is more affected by propagation direction than the  $A_0$  mode that resulted from the out-of-plane source. As already presented in section 2.2.1 this is due to the stronger anisotropy that can be found for the  $S_0$  mode due to its pronounced in-plane characteristics.

In order to compensate for these attenuation effects, attempts have been made to correct parameters for source identification based on source-to-sensor distance [122, 161, 188]. However, these approaches are usually limited to the sources that were utilized to calibrate the underlying model.

## 2.5 Where is the gap?

Despite numerous studies in the field of source identification in FRP laminates, there are aspects regarding the influence of source depth and source-to-sensor distance which are not fully understood and need more clarification.

Despite the strong influence of **source-to-sensor distance**, there are only a few studies that take it into account for the interpretation of source classification results. As already suggested in [26, 85], limitations should be given by incorporating source position as an essential feature and interpreting results with respect to source-to-sensor distance by default. This way, potential misclassification can be identified and misinterpretations can be avoided. In this context, it is of particular interest to determine the critical distance at which the acoustic emissions from damaging events such as fibre breaking and matrix cracking cannot be distinguished anymore. However, there is only little awareness on this distance and the parameters that affect it. Studies that investigated the effect of source-to-sensor distance were mainly accomplished with artificial sources in the past. Comprehensive experimental studies that investigate the AE from damaging events during tensile testing as a function of source-to-sensor distance are missing.

The influence of **source depth** is directly linked to the characteristics of fundamental guided waves modes. However, there is a lack of awareness on the link between

modal content, frequency content and resulting features for source classification. In fact, MAE analysis seems to be limited to the discrimination between in-plane and out-of-plane sources in FRP laminates. However, modal properties affect signal characteristics from wave initiation up to propagation and detection and should therefore be incorporated in the setup and analysis for a more robust interpretation of source classification results. Although the influence of source depth has been investigated in a couple of studies, modal content has not been directly accessed and evaluated. Furthermore, whether or not the influence of source depth can lead to matrix cracks that show similar peak frequencies as fibre fracture is reported contradictory in the literature and needs more clarification.

Since modal content of the resulting acoustic wave depends on **source depth and source-to-sensor distance**, both influencing parameters are linked and must therefore be investigated together. To the authors knowledge, there has not been a study, that explicitly dealt with the interaction of these two parameters while taking MAE analysis into account.



### 3 Thesis goals and implementation

The thesis aims to investigate the **influence of source depth and source-to-sensor distance** on the acoustic signatures from damaging events in CFRP laminates. While the focus is put on fibre breaking and transverse matrix cracking as in-plane acting damaging modes, the work is concerned with the question how their acoustic emission signature is modified when source depth and source-to-sensor distance vary. One main goal is to visualize this dependency and create awareness for the underlying mechanisms. This involves a fundamental understanding of the initiation and propagation of guided waves and the incorporation of **modal acoustic emission analysis** as an **essential tool** in this work. By evaluating the effect of source depth and source-to-sensor distance on modal content, frequency content and characteristic features, the thesis aims to create the link between these and highlight the potential of modal acoustic emission for the interpretation of acoustic emission signals. By presenting critical scenarios where source depth and source-to-sensor distance can prevent the discrimination between acoustic emissions from fibre breaks and matrix cracks, the thesis aims to create awareness for these influencing factors while defining guidelines and limitations for reliable source identification.

In detail, the following scientific questions are central to this work:

1. How does released modal content vary as a function of source depth and source-to-sensor distance for in-plane acoustic emission sources in CFRP laminates?
2. How can a change in modal content affect signal features for source classification? How sensitive are features towards a change in modal content?
3. Can transverse matrix cracks in the symmetry plane produce acoustic emissions with similar frequency components as fibre breaks?
4. What is the critical source-to-sensor distance in cross-ply CFRP laminates where acoustic emissions from transverse matrix cracking and fibre breakage cannot be distinguished anymore? Which parameters affect this critical distance?

The work schedule in figure 3.15 was developed as a guideline to answer these questions. It comprises four work packages (WP) that focus on different aspects but build up on each other to get a comprehensive view on the influence of source depth and source-to-sensor distance on AE in CFRP laminates.

**WP1** starts with the **design and manufacturing of CFRP laminates** and is structured in three tasks. The first task aims to find appropriate laminate layups and mechanical testing scenarios that allow for the systematic generation of fibre breaks and transverse

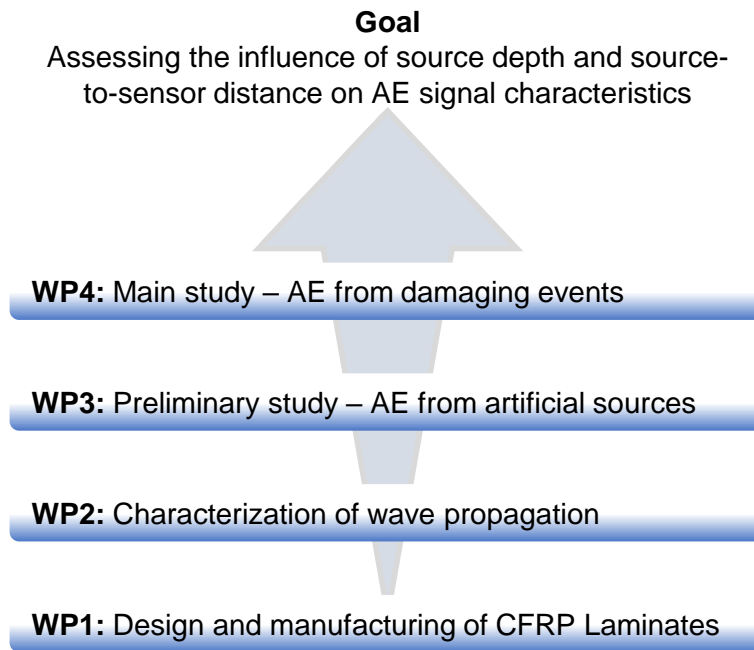


Figure 3.15: Work schedule

matrix cracks in various source depths and source-to-sensor distances. The dispersion characteristics of wave modes should be similar among layups to minimize further influencing factors that could affect the acoustic signature of the investigated damaging events. The second task deals with the manufacturing of the laminates. To assure a stable process, a routine for quality control is established as a third part of the work package. In this context, laminate properties such as cured ply thickness, fibre volume content and density are determined as fundamental requirements for part of the work in **WP2** which deals with the **characterization of wave propagation**.

Fundamental properties such as group velocities, wavelengths, displacement fields and attenuation coefficients are determined as a function of frequency and propagation direction for the ultrasonic guided wave modes present in the manufactured laminates. This step is crucial for the interpretation of AE signals derived from the upcoming experiments. Characterization is thereby accomplished in a two-step process where numerical calculations are followed by carefully designed experiments that aim to validate and extend the information content from theoretical calculations.

With the gained knowledge on wave propagation, the influence of source depth and source-to-sensor distance is investigated in a **preliminary study** in **WP3**. **Artificial AE sources** are systematically introduced in different depths and distances to the sensors in order to study the effects on resulting signals in the time and frequency domain as well as on respective features that are commonly considered for source identification in CFRP.

This preliminary study is accompanied by the **main study** in **WP 4**, where artificial AE sources are replaced by **sources from damaging events** in order to transfer the in-

vestigations to the real application scenario. By matching laminate layup, specimen geometry, loading scenario and sensor layout, transverse matrix cracks and fibre fracture are systematically initiated in various source depths and source-to-sensor distances during testing. Regarding AE analysis, two types of setups are presented: A standard setup utilizing broad band resonant AE sensors as frequently found in literature and a modal AE setup that allows the individual evaluation of symmetric and antisymmetric wave modes. Whereas the first setup serves as a reference, the later was designed to investigate modal content in more detail to be able to create the link between modal content, frequency content and extracted features. In order to identify damaging events and catch the variation in their acoustic fingerprint, accompanying non-destructive testing methods are incorporated in the setup. These need to be capable of visualizing matrix cracking and fibre fracture in various depths while being in sync with the AE setup. In the end, results are combined to assess the influence of source-to-sensor distance and source depth on the acoustic signature of matrix cracking and fibre breakage in CFRP.





## 4 Design and manufacturing of CFRP laminates

### 4.1 Material

In order to guarantee high manufacturing quality and allow flexibility in the layup of the laminates, the autoclave process was selected as the manufacturing method. The pre-impregnated unidirectional tape (Cycom 977-2-35-12kHTS-134-1500) manufactured by Solvay [189] based on Teijin Tenax carbon fibre HTS40 (standard modulus) [190] and Cycom 977-2 toughened epoxy resin [191] was selected. This system has a high relevance due to its application in primary and secondary structures of aircrafts (fuselage, vertical and horizontal tail plane), space structures and cryogenic tanks [191]. Furthermore, its mechanical behaviour has been thoroughly characterized [192, 193] so that elastic properties and fracture strengths are available for further investigations. Properties of the fibre and matrix material from literature can be found in tables 4.1a and 4.1b.

Table 4.1: Properties of the 12k HTS40 carbon fibre (a) and Cycom 977-2 toughened epoxy resin (b) [190, 191, 193, 194]

(a)		(b)	
Property	Value	Property	Value
Density (g/cm <sup>3</sup> )	1.77	Density (cured) (g/cm <sup>3</sup> )	1.31
Tensile strength (MPa)	4400	Tensile strength (MPa)	81
Tensile modulus (GPa)	240	Tensile modulus (GPa)	3.5
Failure strain in tension (%)	1.8	Failure strain in tension (%)	2.5
Yield (tex)	800	Glass temperature (dry) (°C)	170

For quality assurance, the manufacturer also performed measurements on the delivered product. Among other things, this involved the determination of

- mass of prepreg per unit area according to EN-2557,
- mass of fibre per unit area according to EN-2559,
- resin content according to EN-2559,
- tensile strength of 8-ply unidirectional laminates according to EN-2563 and
- tensile modulus of 8-ply unidirectional laminates according to EN-2563

A statistical overview on the distribution of resulting properties is given in table 4.2. Results are presented with average ( $\mu$ ), standard deviation ( $\sigma$ ) as well as minimum

Table 4.2: Statistical overview on the properties of the supplied Cycom 977-2-35-12kHTS-134-1500 prepreg material

Property	$N$	$\mu$	$\sigma$	$Min$	$Max$
Prepreg area weight (g/m <sup>2</sup> )	50	207.89	1.32	205.02	211.34
Fibre area weight (g/m <sup>2</sup> )	50	134.38	1.25	130.9	137.37
Resin content (wt.-%)	50	35.52	0.31	34.96	36.29
Tensile strength (MPa)	30	2303.3	57.03	2208	2413
Tensile modulus (GPa)	30	146.6	2.68	141	150

( $Min$ ) and maximum ( $Max$ ) value of each property. Additionally, the number of samples  $N$  per measurement is given.

On the basis of the fibre ( $\rho_f$ ) and matrix densities ( $\rho_m$ ) as well as their respective area weights ( $A_{w_f}$  and  $A_{w_m}$ ) in the prepreg, the cured ply thickness  $d_i$  as well as the fibre volume content  $V_f$  can be estimated based on equations 4.14 and 4.15 [30].

$$d_i = \frac{A_{w_f}}{\rho_f} + \frac{A_{w_m}}{\rho_m} = \frac{A_{w_f}}{\rho_f} + \frac{A_w \cdot \psi_m}{\rho_m} \quad (4.14)$$

$$V_f = \frac{A_{w_f}}{\rho_f \cdot d_i} \quad (4.15)$$

The area weight of the matrix is thereby determined based on the resin content  $\psi_m$  (by weight) and the total area weight of the prepreg  $A_w$ . By inserting the average values from table 4.2 in equations 4.14 and 4.15, layer thickness and fibre volume content can be determined to 132.3  $\mu\text{m}$  and 57.4 % respectively. With this fibre volume content, the laminate density can be estimated through equation 4.16 to 1.574 g/cm<sup>3</sup> [30].

$$\rho = V_f \cdot \rho_f + (1 - V_f) \cdot \rho_m \quad (4.16)$$

The absolute errors in these properties can be calculated based on the errors of the underlying variables through linear error propagation. By neglecting the error in fibre and resin density, and defining the respective standard deviations as errors of the remaining variables, the errors in layer thickness, fibre volume content and laminate density can be determined to 1.6  $\mu\text{m}$ , 0.1% and 0.001 g/cm<sup>3</sup> respectively. Consequently, for the majority, manufactured laminates should show a layer thickness of 132.3 $\pm$ 1.6  $\mu\text{m}$ , a fibre volume content of 57.4 $\pm$ 0.1% and a density of 1.574 $\pm$  0.001g/cm<sup>3</sup>. Calculations thereby assume no porosity in the manufactured laminates and zero resin loss during cure.

## 4.2 Design of laminates and loading scenario

In order to systematically produce fibre fracture and transverse matrix cracking in various depths and source-to-sensor distances, laminate layup and loading conditions

have to be selected accordingly. This should be accomplished with layups that show similar dispersion characteristics in terms of guided wave propagation in order to reduce further influencing factors on AE initiation and propagation. Furthermore, mechanical testing should be limited to a single scenario where stress conditions are comparable and specimen geometry remains constant. An adequate solution was found in the quasi-static tensile test scenario of ( $0^\circ/90^\circ$ ) cross-ply laminates. If such a laminate is loaded in tension in one of the principal fibre directions, FF and TMC are generated in the layers that are oriented parallel and perpendicular to the loading direction respectively (see section 2.1.2). By iterating the stacking sequence of the  $0^\circ$  and  $90^\circ$  layers in the laminate, TMC and FF can be systematically produced in different depths without significantly changing the underlying elastic properties that govern wave initiation and propagation in the loading direction. The variation of source-to-sensor distance can be accomplished with the same specimen. If a layer fails through TMC, load is reintroduced in the broken layer after a characteristic distance, causing another crack at a different lateral position (see section 2.1.2). Since this process continues until the whole layer is saturated, source-to-sensor distance varies inherently for TMC in a cross-ply laminate. A similar statistical variation of lateral source position can be assumed for the fracture of single fibre filaments that occur randomly at inhomogeneities in the laminate.

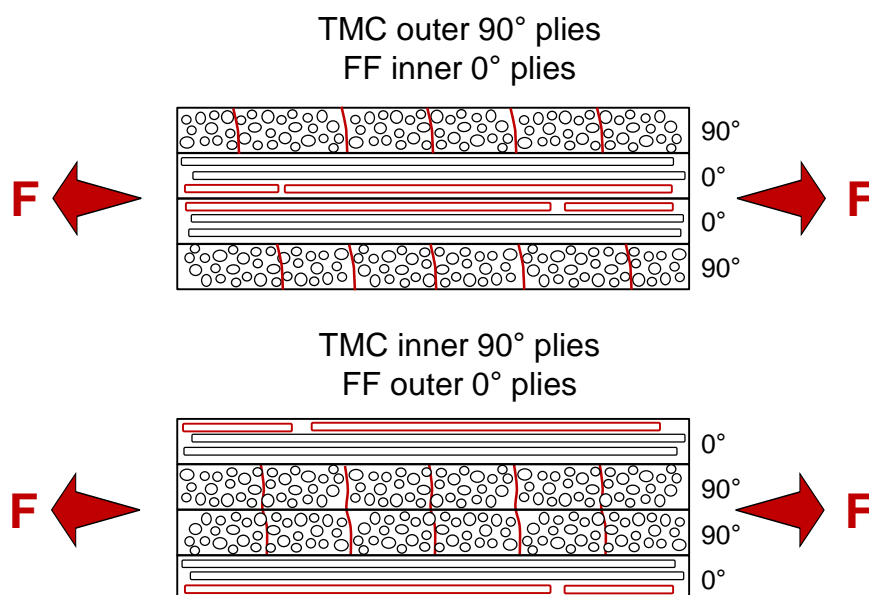


Figure 4.16: Layups and loading directions were selected to create transverse matrix cracking (TMC) and fibre fracture (FF) in different depths and lateral positions.

Symmetric and balanced cross-ply ( $0^\circ/90^\circ$ ) layups with 4 and 16 layers were chosen for the investigations. Consequently, investigations were divided in two stages that could

be evaluated separately. For the first stage, the  $(0^\circ/90^\circ)_s$  laminates with only four plies and a nominal thickness of around 0.5 mm were considered. In these laminates, TMC and FF could be constrained to a single layer. As shown in figure 4.16, depending on the loading direction, the initiation of TMC and FF is limited to the inner or outer layer respectively, allowing straight forward investigations on the influence of source depth on their acoustic signature.

In the second stage, investigations were extended to  $(0^\circ/90^\circ)_{4s}$  laminates with 16 plies (Nominal thickness: 2 mm), where the influence of source depth could be studied in more detail. Through the progressive failure of  $90^\circ$  oriented layers, TMC could be generated in various depths, allowing a systematic investigation on the effect of source depth on the fingerprint of TMC. The influence of source-to-sensor distance could be investigated equally in both stages through the above mentioned aspects.

### 4.3 Manufacturing of laminates

Laminates with  $(0^\circ/90^\circ)_s$  and  $(0^\circ/90^\circ)_{4s}$  layup were manufactured in the autoclave according to the recommendations of the manufacturer [191]. The plies were cut to sheets of 600 x 600 mm and stacked accordingly. No peel-ply or other bleeder materials were put in direct contact with the stack. Polished steel plates were used as tooling for the top and bottom half in order to create a smooth surface on the finished product. Laminates were cured at  $180^\circ\text{C}$  and 7 bar for 3 hours in a sealed vacuum bag. The pressure inside the bag was below 0.1 mbar, resulting in a total consolidation pressure of around 8 bar. The autoclave cycle, showing the course of temperature ( $^\circ\text{C}$ ) and autoclave pressure (bar) as a function of processing time (min) is shown in figure 4.17.

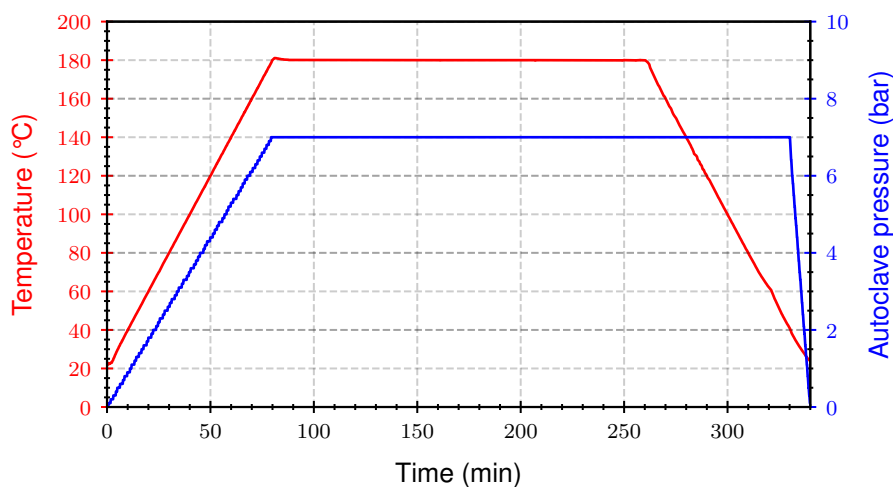


Figure 4.17: Autoclave cycle for the manufacturing of the Cycom 977-2 HTS40 laminates. Autoclave pressure (bar) and temperature ( $^\circ\text{C}$ ) are shown as a function of processing time (in min).

In each autoclave run, a single  $(0^\circ/90^\circ)_s$  and  $(0^\circ/90^\circ)_{4s}$  laminate was manufactured in one batch. In total, two batches were produced, resulting in two plates for each layup.

#### 4.4 Characterization of laminate properties

In order to assess the quality of the manufactured laminates, each laminate was characterized after manufacturing. In the first step, each laminate was scanned with a 5 MHz ultrasonic transducer in an immersion setup in impulse-echo mode in order to check for macroscopic flaws such as delaminations, dry spots and accumulation of porosity. As a common criteria, a 6dB drop in the amplitude of the back-wall echo was defined as indicator for these flaws. However, such a drop could not be observed for any of the manufactured laminates.

Afterwards, the following properties were determined according to the procedures described below:

- **Laminate thickness  $d$ :** Laminate thickness was measured with an outside micrometer with a resolution of 0.01 mm at 12 positions on the plate.
- **Laminate density  $\rho$ :** Laminate density was determined for 5 samples per plate (35 x 10 mm) according to DIN EN ISO 1183 in an immersion setup with an Ohaus DV214C scale (resolution 0.1 mg).
- **Glass temperature  $T_g$ :** Dynamic mechanical thermal analysis (DMTA) was performed to access the glass transition temperature of the cured epoxy matrix experimentally. A total of 5 samples per plate were tested in single cantilever mode with a span width of 17.67 mm on a TA Instruments DMA Q800. The samples were cut to dimensions 35 x 10 mm with the fibre direction of the top layer being parallel to the lengthwise direction of the sample. While mechanical loading was oscillated at a frequency of 1 Hz, samples were heated up from 0°C up to 270°C with 5 K/min. After cooling down, a second heating cycle was performed to analyze the glass temperature after post-curing from the first run. The onset of the storage modulus  $E'$  as well as the peak in  $\tan(\delta)$  were evaluated in each heating cycle. In order to take into account the different thicknesses of the samples, the displacement amplitudes of the  $(0^\circ/90^\circ)_s$  and  $(0^\circ/90^\circ)_{4s}$  were set to 15  $\mu\text{m}$  and 45  $\mu\text{m}$  accordingly. This resulted in a similar strain in the outer layer for both laminates. Prior to testing, the samples were dried at 105°C until an equilibrium state was reached to exclude the influence of moisture on experimental results.
- **Layer thickness  $d_j$ :** Light microscopic analysis was performed in order to determine the cured ply thickness. For each plate, 3 cross-sections in the 0° and 90° direction were extracted and embedded in a polymeric matrix in order to be

grinded and polished on a machine. From each cross-section, 3 images were taken with 100x magnification with a Leica DM6000 M. The layer thickness was determined manually by measuring the distances between layers in each image. For the  $(0^\circ/90^\circ)_s$  and  $(0^\circ/90^\circ)_{4s}$  laminates, this resulted in 54 and 270 measuring points per plate.

- **fibre volume content  $V_f$** : The same microscopic images that were taken for the determination of layer thickness were also utilized for the analysis of fibre volume content. This was achieved through a threshold based method by the software of the manufacturer. In total, 18 images per plate were analysed this way.

Tables 4.3 and 4.4 give a statistical overview on the respective results for each layup. Due to the similarity between batches, measurement data was grouped together layup wise. For a batch-wise comparison, the reader is referred to appendix A.

Table 4.3: Properties of the manufactured  $(0^\circ/90^\circ)_s$  laminates

Property	$N$	$\mu$	$\sigma$	Min	Max
Laminate thickness $d$ (mm)	24	0.52	0.01	0.45	0.55
Laminate density $\rho$ (g/cm <sup>3</sup> )	10	1.579	0.006	1.572	1.589
$T_g$ , Onset $E'$ (°C), 1 <sup>st</sup> cycle	10	181.4	7.2	171.6	188.6
$T_g$ , Onset $E'$ (°C), 2 <sup>nd</sup> cycle	10	210.6	4.4	205.3	214.8
$T_g$ , Peak $\tan(\delta)$ (°C), 1 <sup>st</sup> cycle	10	203.8	5.8	196.9	209.2
$T_g$ , Peak $\tan(\delta)$ (°C), 2 <sup>nd</sup> cycle	10	215.3	4.6	209.7	219.5
Layer thickness $d_i$ ( $\mu\text{m}$ )	108	127.1	9.1	96.2	153.2
Fibre volume content $V_f$ (Vol.-%)	36	55.5	2.1	51.8	59.4

Table 4.4: Properties of the manufactured  $(0^\circ/90^\circ)_{4s}$  laminates

Property	$N$	$\mu$	$\sigma$	Min	Max
Laminate thickness $d$ (mm)	24	2.05	0.04	2.00	2.14
Laminate density $\rho$ (g/cm <sup>3</sup> )	10	1.576	0.006	1.567	1.585
$T_g$ , Onset $E'$ (°C), 1 <sup>st</sup> cycle	10	177.1	6.3	170.0	183.8
$T_g$ , Onset $E'$ (°C), 2 <sup>nd</sup> cycle	10	184.8	5.7	178.0	191.5
$T_g$ , Peak $\tan(\delta)$ (°C), 1 <sup>st</sup> cycle	10	202.2	5.7	196.4	208.8
$T_g$ , Peak $\tan(\delta)$ (°C), 2 <sup>nd</sup> cycle	10	210.0	4.9	204.8	215.9
Layer thickness $d_i$ ( $\mu\text{m}$ )	540	130.5	8.2	106.9	157.4
Fibre volume content $V_f$ (Vol.-%)	36	56.1	2.0	52.0	59.1

Values for fibre volume content, layer thickness and laminate density overlap with the theoretically estimated windows of  $132.3 \pm 1.6 \mu\text{m}$ ,  $57.4 \pm 0.1\%$  and  $1.573 \pm 0.001 \text{g/cm}^3$ .

The small deviations in the average values could be explained through remaining porosity, resin loss during cure, variations in plate thickness and errors in the manual evaluation of image data.

Porosity as well as potential fiber misalignment was not quantified for the manufactured laminates. For a qualitative look on laminate quality, the reader is referred to appendix B where exemplary microscopic cross-sections are shown.





## 5 Characterization of wave propagation

### 5.1 Theoretical

Theoretical calculations were realized with Dispersion Calculator software [38] on the basis of the Stiffness Matrix Method [45] as discussed in 2.2.1. The software was utilized to determine group and phase velocities as well as displacement fields of guided wave modes present in the CFRP laminates. The underlying properties for these calculations are derived from the following section.

#### 5.1.1 Determination of underlying properties

The Dispersion Calculator software requires the following properties as input:

- Layer sequence
- Layer thickness  $d_i$
- Laminate density  $\rho$
- Elastic constants  $E_{\parallel}$ ,  $E_{\perp}$ ,  $G_{\perp\parallel}$ ,  $\nu_{\perp\parallel}$ ,  $\nu_{\perp\perp}$

Whereas layer sequence was already defined prior to manufacturing in section 4.2, layer thickness and laminate density were experimentally determined according to the procedure described in section 4.4. Due to the similarities in these properties (see tables 4.3 and 4.4),  $(0^\circ/90^\circ)_s$  and  $(0^\circ/90^\circ)_{4s}$  laminates were grouped together for the calculation of dispersion curves. Consequently, average values and standard deviations were updated for these properties based on the modified populations (see table 5.5).

Table 5.5: Properties of the manufactured cross-ply laminates based on the combination of  $(0^\circ/90^\circ)_s$  and  $(0^\circ/90^\circ)_{4s}$  properties from tables 4.3 and 4.4

Property	$N$	$\mu$	$\sigma$	$Min$	$Max$
Laminate density $\rho$ (g/cm <sup>3</sup> )	20	1.578	0.006	1.572	1.589
Layer thickness $d_i$ ( $\mu\text{m}$ )	648	130.0	8.4	96.2	157.4
Fibre volume content $V_f$ (Vol.-%)	72	55.8	2.1	51.8	59.4

The elastic constants for the Cycom 977-2 HTS40 system were extracted from literature [195]. They are presented in table 5.6. Since a fibre volume content was not given in the reference source, it was estimated through a rule of mixture [30] based on the Young's modulus  $E_{\parallel}$  and the tensile moduli of fibre  $E_f$  and matrix material  $E_m$  from table 4.1. This resulted in the presented fibre volume content of 57.4%.

Table 5.6: Elastic properties of Cycom 977-2 HTS40 from [195]. The fibre volume content was estimated based on a rule of mixture [30] on the basis of Young's modulus  $E_{\parallel}$ .

Property	Value
Fibre volume content (vol.-%)	57.4
Young's modulus $E_{\parallel}$ (GPa)	139.4
Young's modulus $E_{\perp}$ (GPa)	8.80
Shear modulus $G_{\perp\parallel}$ (GPa)	4.60
Poisson's ratio $\nu_{\perp\parallel}$ (1)	0.29
Poisson's ratio $\nu_{\perp\perp}$ (1)	0.37

Before these properties could be adapted for the laminates in this thesis, they had to be recalculated due to the differences in fibre volume content. This was realized with analytical rules of mixture derived from micro mechanic models as presented in [30]. In order to account for statistical variations, the elastic properties were determined for fibre volume contents of 53.7, 55.8 and 57.9%. The resulting properties are shown in table 5.7. For more insights in the recalculation of elastic properties, the reader is referred to appendix C.

Table 5.7: Calculated elastic properties of Cycom 977-2 HTS40 with 53.7, 55.8 and 57.9% fibre volume content

Property	Values		
	53.7	55.8	57.9
Fibre volume content (vol.-%)	53.7	55.8	57.9
Young's modulus $E_{\parallel}$ (GPa)	130.50	135.47	140.43
Young's modulus $E_{\perp}$ (GPa)	8.24	8.55	8.88
Shear modulus $G_{\perp\parallel}$ (GPa)	4.20	4.42	4.66
Poisson's ratio $\nu_{\perp\parallel}$ (1)	0.29	0.29	0.29
Poisson's ratio $\nu_{\perp\perp}$ (1)	0.37	0.37	0.37

In order to account for the statistical variation in layer thickness, dispersion curves were calculated with thicknesses of 121.6, 130.0 and 138.4  $\mu\text{m}$  as additional input variable. Together with the variation in fibre volume content and respective elastic properties, nine combinations were analysed for each layer sequence.

### 5.1.2 Dispersion curves

Figures 5.18 (a) and (b) show the group velocities of  $A_0$  and  $S_0$  mode for a propagation in the  $0^\circ$  fibre direction in a  $(0^\circ/90^\circ)_{4s}$  laminate as a function of frequency for the selected combinations of fibre volume content  $V_f$  and layer thickness  $d_i$ . Whereas

the resulting curve from the mean values of  $V_f$  and  $d_i$  is represented as a black solid line, every other combination is visualized in the form of lines with varying gray scale, marker and line style according to the legend.

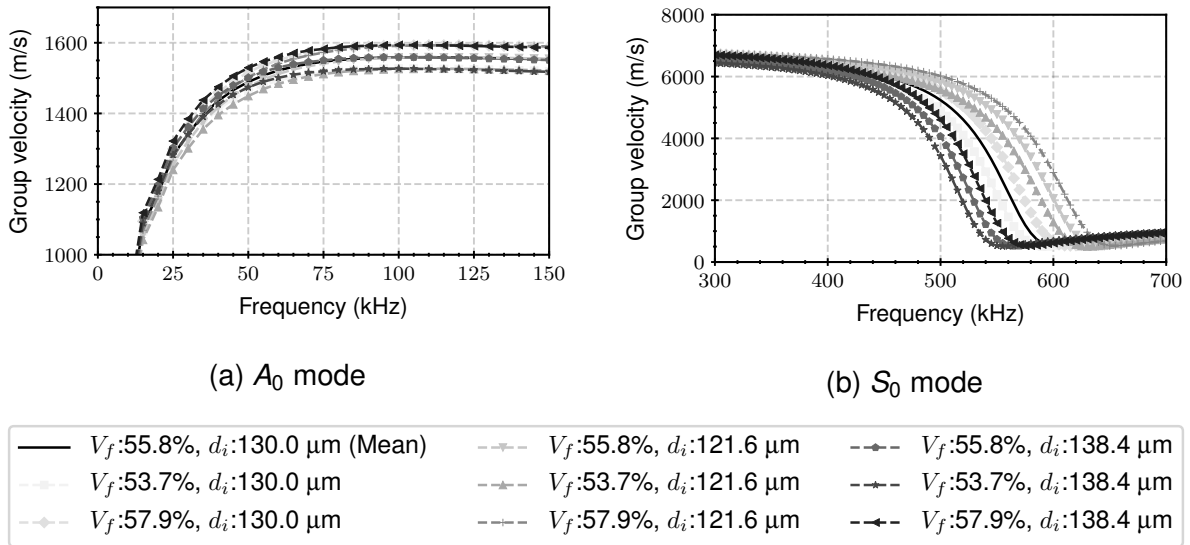


Figure 5.18: Group velocities (m/s) of the fundamental Lamb wave modes  $A_0$  (a) and  $S_0$  (b) for the  $(0^\circ/90^\circ)_{4s}$  laminate as a function of frequency (kHz), fibre volume content  $V_f$  (%) and layer thickness  $d_i$  ( $\mu\text{m}$ ) for propagation in the  $0^\circ$  direction.

The group velocities of both modes are affected as fibre volume content and layer thickness varies. In terms of fibre volume content, the group velocities of  $A_0$  and  $S_0$  mode increase with increasing fibre volume content. This is due to the coupling of fibre volume content with elastic constants as illustrated by the results in table 5.7. As pointed out by the sensitivity study in [59], the propagation characteristics of  $A_0$  and  $S_0$  mode are affected differently by the coefficients of the elastic stiffness matrix  $C_{ij}$ . For a unidirectional laminate and a propagation in fibre direction, a strong influence on the  $S_0$  mode was found for coefficient  $C_{11}$  which, in turn, is governed by the Young's modulus  $E_{\parallel}$  in fibre direction and the Poisson's ratios  $\nu_{\perp\parallel}$  and  $\nu_{\parallel\perp}$  [30]. As  $E_{\parallel}$  increases with fibre volume content and Poisson's ratios stay nearly constant, group velocity of  $S_0$  mode increases. The  $A_0$  mode on the other hand, was found to be strongly influenced by coefficient  $C_{55}$  which is solely determined by the shear modulus  $G_{\perp\parallel}$  [30] in fibre direction. As this modulus increases likewise with fibre volume content, similar trends can be found for the  $A_0$  mode.

In terms of layer thickness, the group velocities of  $A_0$  and  $S_0$  mode are affected differently. Since group velocity of  $A_0$  mode increases with increasing product of frequency and thickness, the highest group velocities can be found for the largest layer thickness of 138.4  $\mu\text{m}$ . The opposite behaviour can be found for the  $S_0$  mode. Here, group velocity falls with increasing product of frequency and thickness in the beginning of the

curve. Consequently, the highest group velocities can be found for the lowest layer thickness of 121.6  $\mu\text{m}$  in this section of the curve.

Another interesting aspect deals with the drop in group velocity of the  $S_0$  mode between 500 and 600 kHz. This drop is shifted towards higher frequencies for increasing fibre volume content and decreasing layer thickness.

For simplicity, the number of combinations was reduced from nine to three for the following diagrams. Besides the mean values for fibre volume content and layer thickness, those combinations of  $V_f$  and  $d_l$  were selected that represented the extreme values (min, max) in terms of the visualized property. Following the procedure described for the  $A_0$  and  $S_0$  mode, these combinations were determined for every mode and direction. Instead of visualizing a single line, bands are shown in pale color for every mode that account for the statistical variations of fibre volume content and layer thickness. Figures 5.19 (a) and (b) show the group velocities of Lamb and shear horizontal wave modes for a propagation in the  $0^\circ$  direction in the  $(0^\circ/90^\circ)_{4s}$  (a) and  $(0^\circ/90^\circ)_s$  (b) laminates, respectively.

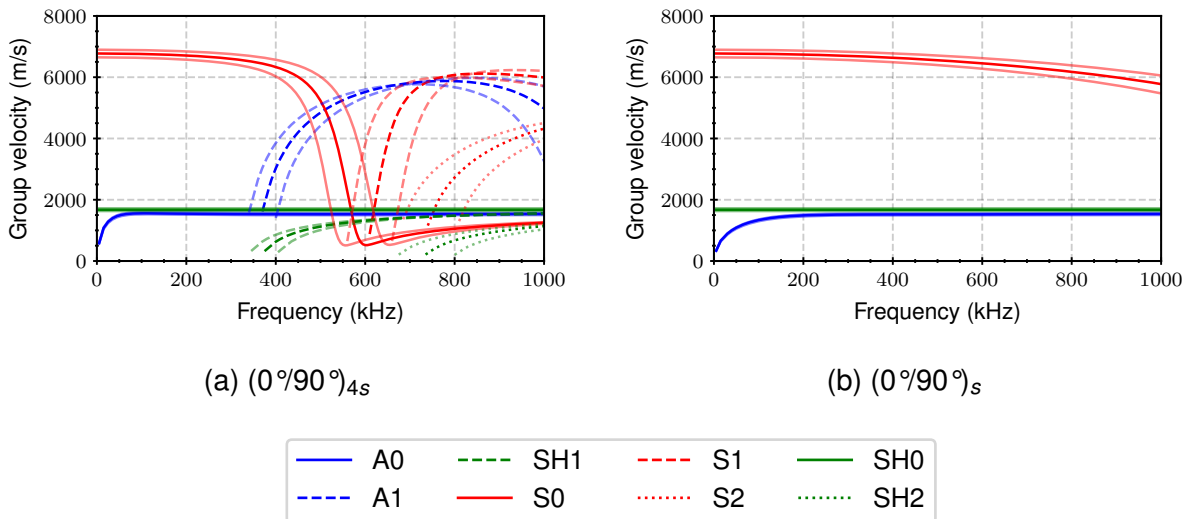


Figure 5.19: Group velocities (m/s) of the Lamb wave and shear horizontal wave modes as a function of frequency (kHz) for the  $(0^\circ/90^\circ)_{4s}$  (a) and  $(0^\circ/90^\circ)_s$  (b) laminates and propagation in the  $0^\circ$  direction.

In the selected frequency range, a total of 8 modes can be found in the  $(0^\circ/90^\circ)_{4s}$  laminate, whereas only 3 modes are present in the  $(0^\circ/90^\circ)_s$  laminate. Whereas for the  $(0^\circ/90^\circ)_s$  laminates, the influence of fibre volume content and layer thickness is barely visible in the illustrated frequency range, there is a significant effect on wave modes in  $(0^\circ/90^\circ)_{4s}$  laminates. Besides the influence on fundamental wave modes (especially  $S_0$ ), the cut-off frequencies for the higher order wave modes vary with fibre volume content and layer thickness as elastic constants and laminate thickness are altered. For both laminates, the  $S_0$  mode shows a group velocity that is around 4.5 times higher

than that of the  $A_0$  mode. This holds true until the velocity of the  $S_0$  mode significantly drops (for  $(0^\circ/90^\circ)_{4s}$  laminates around 500 kHz).

To get a more complete view on wave propagation, group velocities of  $A_0$ ,  $S_0$  and  $SH_0$  mode are illustrated at 250 kHz as a function of propagation direction for both cross-ply laminates in figures 5.20 (a) and (b). Similar to the observations in figure 2.4, the

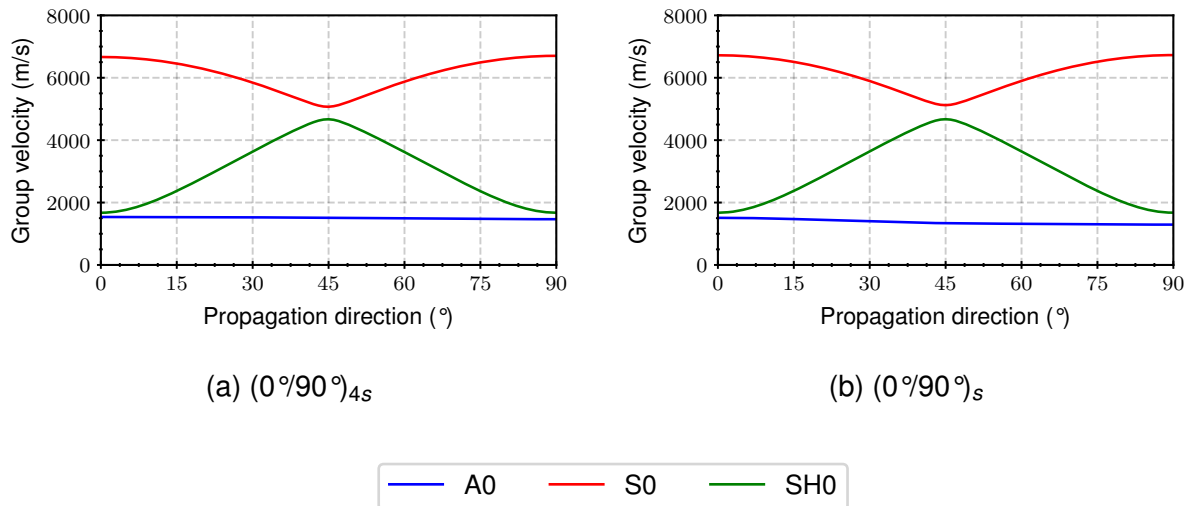


Figure 5.20: Group velocities (m/s) of the Lamb wave and shear horizontal wave modes as a function of propagation direction ( $^\circ$ ) for the  $(0^\circ/90^\circ)_{4s}$  (a) and  $(0^\circ/90^\circ)_s$  (b) laminates at 250 kHz.

$S_0$  and  $SH_0$  mode show stronger anisotropy than the  $A_0$  mode which is only slightly affected by propagation direction. Besides this, there are two other aspects that are interesting to note. For a propagation in  $45^\circ$  direction,  $S_0$  and  $SH_0$  mode show similar group velocities. This can impede the separation of both wave modes. The other aspect involves the  $A_0$  mode, that shows a slightly different group velocity in  $0^\circ$  and  $90^\circ$  fibre direction in the  $(0^\circ/90^\circ)_s$  laminate. This can be explained by a change in bending stiffness, that governs propagation of the  $A_0$  mode. Due to the small thickness, bending stiffness varies depending on the orientation of fibre direction in the outer layer to the respective propagation direction. Other than that, wave propagation seems to be similar in  $0^\circ$  and  $90^\circ$  direction as requested by the design of the cross-ply laminates in section 4.2.

Besides group velocity, wavelength is an important property to look at. It determines the near field length [61] and can affect frequency characteristics of the sensor due to the aperture effect [5, 185]. Figure 5.21 gives an overview on wavelengths of present wave modes for a propagation in the  $0^\circ$  direction in the  $(0^\circ/90^\circ)_{4s}$  (a) and  $(0^\circ/90^\circ)_s$  (b) laminates. Similar to the observations in figure 2.3 (b), the wavelengths of the  $S_0$  mode are higher than those of the  $A_0$  mode. In the frequency range between 200 and 400 kHz, wavelengths typically lie between 4 and 6 mm for the  $A_0$  and 18 to 34 mm for the

$S_0$  mode.

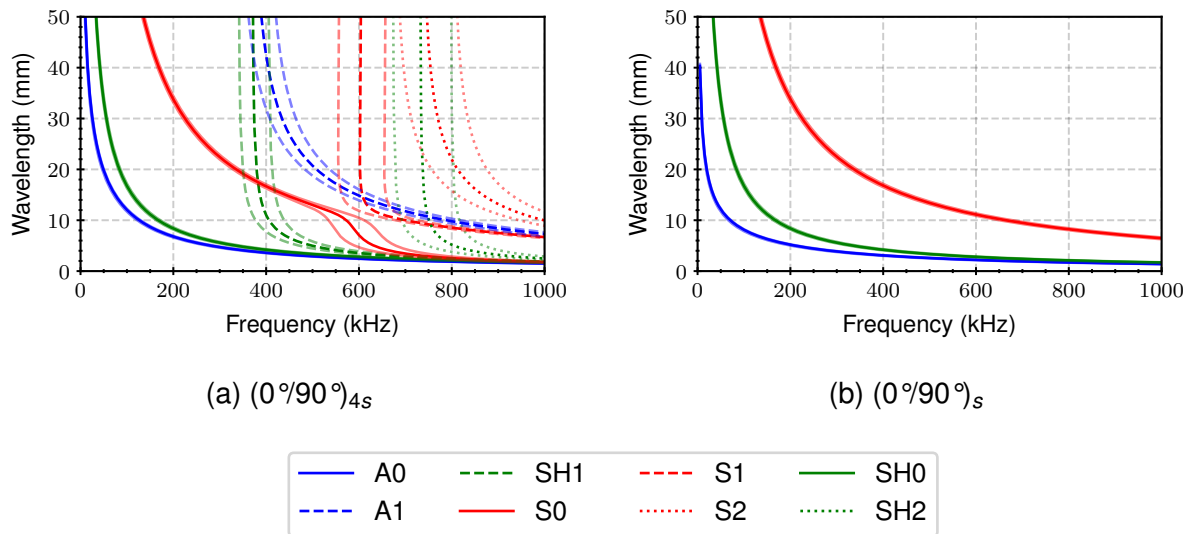


Figure 5.21: Wavelengths (mm) of the Lamb wave and shear horizontal wave modes for the  $(0^\circ/90^\circ)_{4s}$  (a) and  $(0^\circ/90^\circ)_s$  (b) laminates for propagation in the  $0^\circ$  direction.

For a more detailed look on the other propagation directions, the reader is referred to appendix D where dispersion diagrams for propagation in the  $0^\circ$ ,  $45^\circ$  and  $90^\circ$  directions can be found for both types of laminates.

### 5.1.3 Displacement fields

Knowledge on the displacement fields of present wave modes is fundamental in order to understand their initiation and propagation characteristics. As already shown in section 2.2.1, Dispersion Calculator software allows the determination of displacement fields of wave modes in terms of relative portions of in-plane (red), out-of-plane (blue) and shear horizontal components (green). Figure 5.22 shows these displacement components for  $A_0$  (a,b,c) and  $S_0$  (d,e,f) mode for a propagation in fibre direction in the  $(0^\circ/90^\circ)_{4s}$  laminate at 200, 400 and 600 kHz. The calculations were based on the mean values for  $V_f$  and  $d_i$

Similar observations as for the unidirectional laminate in figure 2.5 can be made in terms of dispersion behaviour. The out-of-plane character of the  $S_0$  mode grows with increasing frequency, whereas its in-plane component is focused more and more to center of the plate. The displacement field of the  $A_0$  mode, on the other hand, is only slightly affected in the selected frequency range.

A drastic change of displacement fields is seen in the  $45^\circ$  direction as shown in figure 5.23. Besides  $A_0$  (a,b,c) and  $S_0$  (d,e,f) mode, the displacement fields of the  $SH_0$  (g,h,i)

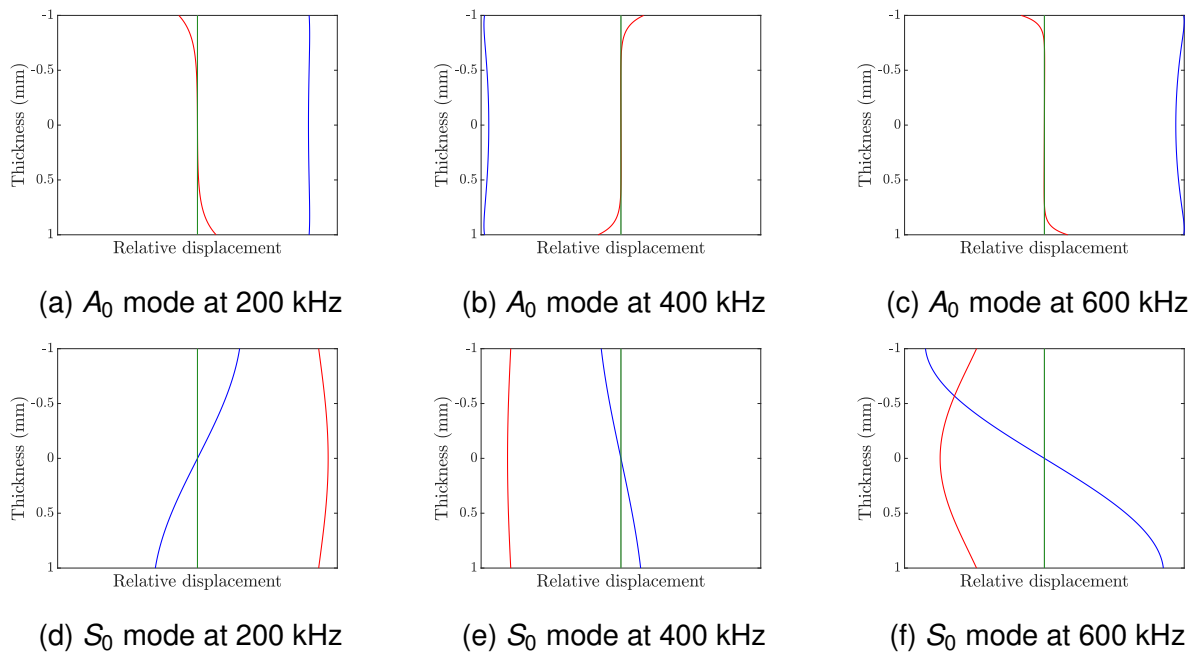


Figure 5.22: In-plane (red), out-of-plane (blue) and shear horizontal displacement (green) components of the fundamental Lamb wave modes  $A_0$  (a,b,c) and  $S_0$  (d,e,f) as a function of frequency (200, 400 and 600 kHz) for the  $(0^\circ/90^\circ)_{4s}$  laminate and propagation in the  $0^\circ$  direction.

mode are shown as a function of frequency as well. Due the coupling of Lamb wave and shear horizontal modes, the displacement fields of  $A_0$ ,  $S_0$  and  $SH_0$  wave modes show components in all three dimensions.

Again, the  $A_0$  mode is only slightly affected in the selected frequency range. However, for the  $S_0$  mode, in-plane shear as well as out-of-plane character grow with increasing frequency. At 600 kHz, the displacement field of the  $S_0$  mode is even dominated by in-plane shear. The  $SH_0$  mode, on the contrary, loses its dominant in-plane shear character with increasing frequency and shows a displacement field at 600 kHz that is comparable to that of the  $S_0$  mode in the  $0^\circ$  direction. In AE analysis, where the sensors are generally sensitive towards the out-of-plane displacement direction, the  $SH_0$  mode can indeed be detected at higher frequencies.

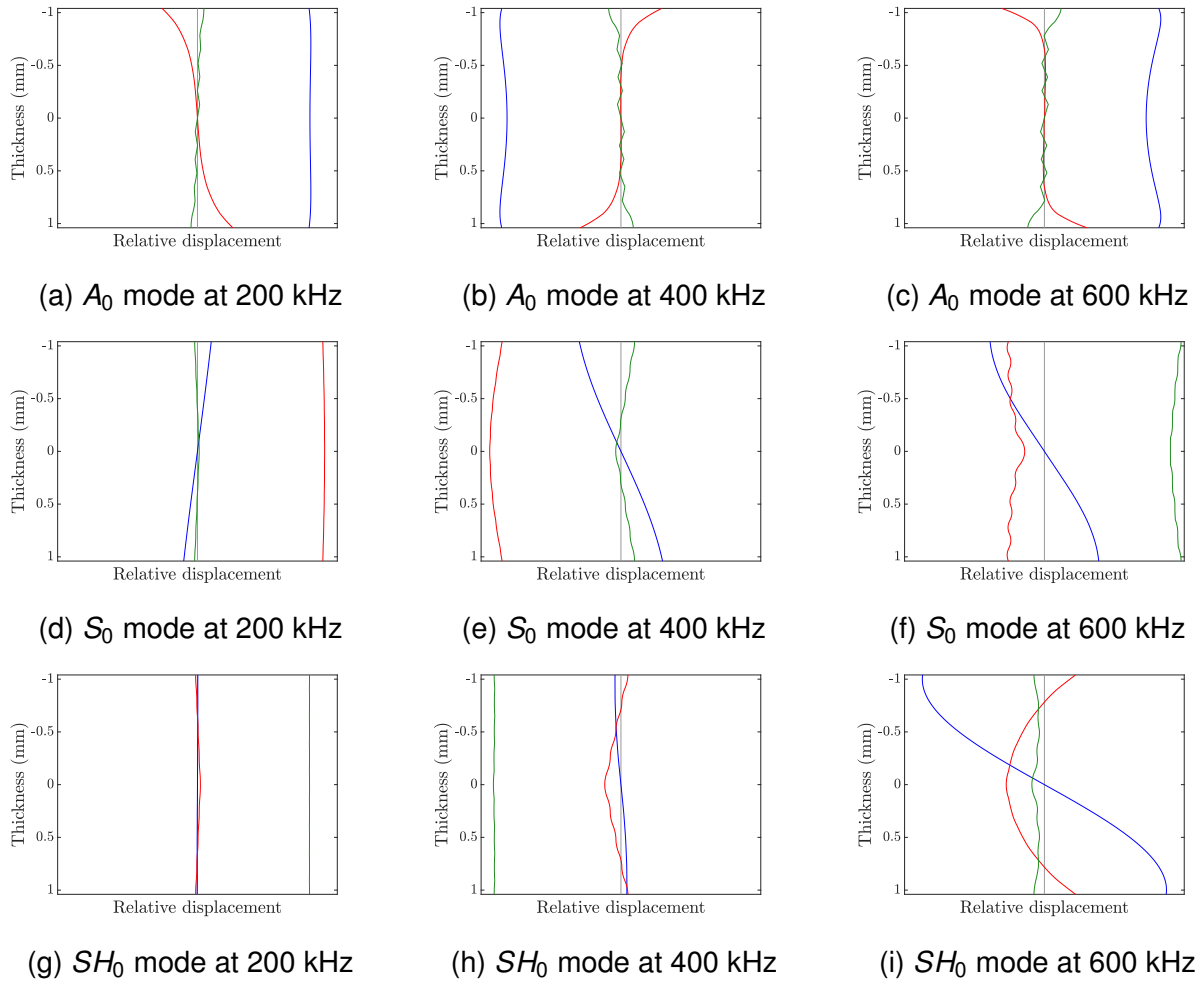


Figure 5.23: In-plane (red), out-of-plane (blue) and shear horizontal displacement (green) components of the guided wave modes  $A_0$  (a,b,c),  $S_0$  (d,e,f) and  $SH_0$  (g,h,i) as a function of frequency (200, 400 and 600 kHz) for the  $(0^\circ/90^\circ)_{4S}$  laminate and propagation in the  $45^\circ$  direction.

## 5.2 Experimental

The experimental characterization of wave propagation was limited to the determination of group velocities and attenuation coefficients. Results on group velocities could be directly compared to the theoretical results from the previous section in order to validate them.

### 5.2.1 Setup

In order to determine group velocities and wave attenuation experimentally, arrival times as well as maximum amplitudes have to be measured as a function of source-to-sensor distance for each mode individually. This can be very challenging due to the fact that fundamental wave modes  $A_0$  and  $S_0$  are always present and can interfere with each other. In FRP materials, the  $S_0$  mode can propagate up to a factor 5 faster than



the  $A_0$  mode at the same frequency (see figure 2.3). Hence, reflections of the  $S_0$  mode from the plate edges can interfere with the primary wave packet of the  $A_0$  mode and impede its evaluation. In the past, this challenge has been encountered through the use of large plates, spatial and temporal filtering via 2D FFT [51, 56] or mode selective excitation or detection [63, 64, 66]. In this work, the concept of mode selective detection was adopted and implemented with a custom fixture that is shown in figure 5.24 in side view (see appendix E for more views).

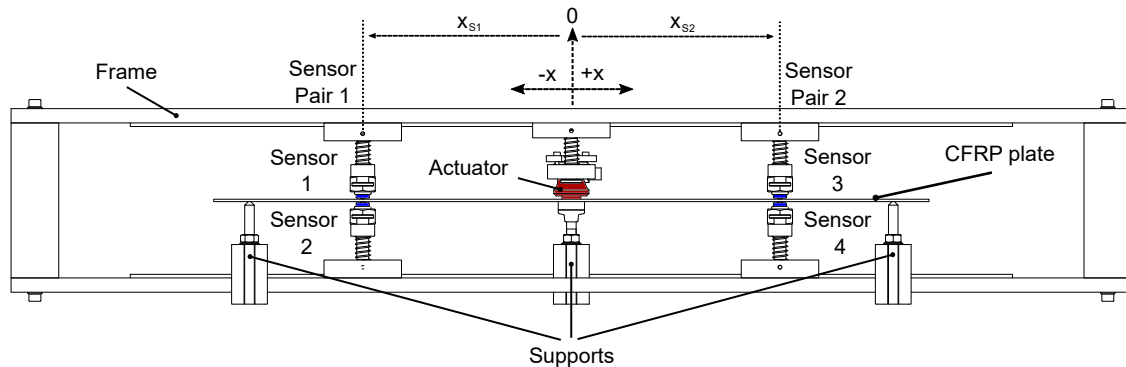


Figure 5.24: Experimental setup for the characterization of Lamb wave propagation shown in side view. More views can be found in appendix E.

The main part of the fixture is a metallic frame that holds a **piezoelectric transducer** (V103-RB, Olympus) and two pairs of **sensors** (KRNBB-pcp, KRN Services) in place. The specimen in the form of a 600 x 600 mm CFRP plate is supported by stands at the edges of the plate and positioned in the center plane of the frame. The **piezoelectric transducer (actuator)** and the **sensors** are pressed against the plate through springs and set up in a line that represents the direction of characterization. The **actuator** is positioned at the top half of the plate in between the two pairs of **sensors**. It is supported by another stand to avoid bending of the plate. The **sensors** are set up pair wise on opposite sides of the plate in a way that they share a common vertical axis (see closeup in figure 5.25 (b)). This way, the symmetric and antisymmetric wave components can be extracted through the superposition of individual sensor signals.

For the measurement, sensors were pair wise aligned and fixed in position through the available hole pattern. The lateral offset between opposing sensors of a pair could thereby be constrained to around 0.25 mm. The actuator and its support could be manually moved and locked in position through the clamping force of the spring (see figure 5.25 (a) for setup in the laboratory). Actuator and sensors were both coupled with silicon grease (OKS 1110). At each actuator position, the transducer was excited through an analog signal that was generated by a function generator (PXI-5422, National Instruments) and directed through a high voltage amplifier (PZD350A, Trek). Through the incorporation of two sensor pairs, the evaluation was not affected by variations in the absolute strength of the excitation signal which can result from

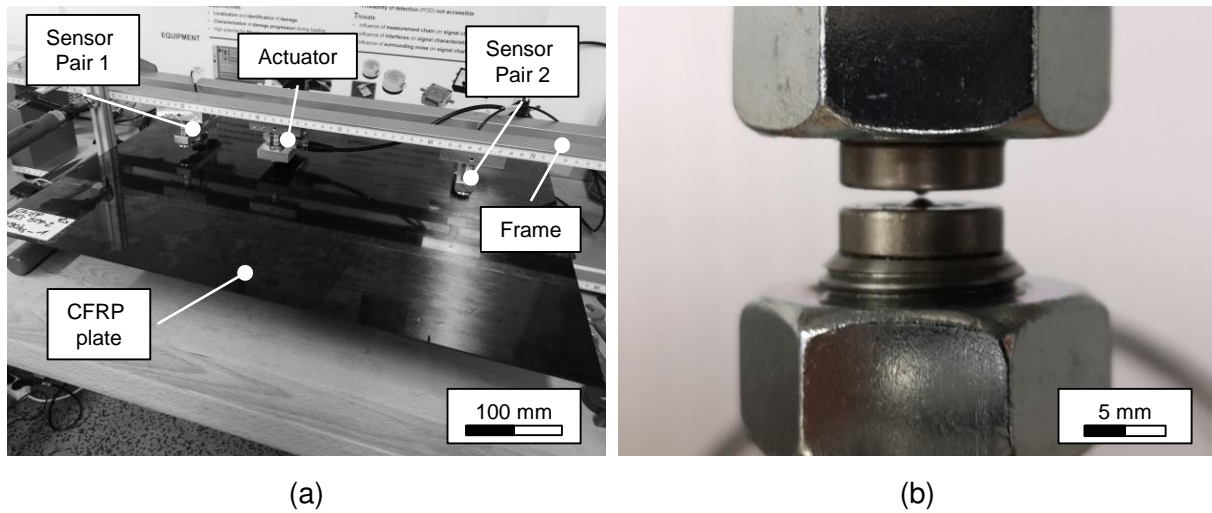


Figure 5.25: Experimental setup for the characterization of Lamb wave propagation in the laboratory (a) with a closeup of a sensor pair (b).

different coupling situations. The excitation signal was sinusoidal and superimposed with a Hanning window [126] to result in a burst type signal. The center frequency was varied in steps of 25 kHz from 50 to 1000 kHz to iteratively catch the dispersion characteristics in this frequency range. The number of periodic cycles was adjusted to the center frequency in order to remain a constant bandwidth. This resulted in a longer burst for higher frequencies and vice versa. The captured sensor signals were directed through charge amplifiers (Vallen AEP4, 40 dB Gain) and digitized and recorded with the Vallen AMSY 5 measurement system. The corresponding acquisition parameters for the transient recording are summarized in table 5.8. Sensor pairs were pooled together and triggered individually as soon as one sensor experienced a threshold crossing. The pre-trigger samples were chosen in order to correct the threshold based time of arrival with the Hinkley picker presented in 2.3.2.

Table 5.8: Vallen AMSY 5 acquisition parameters for the characterization of wave propagation

Property	Value
Sample rate (MS/s)	10
Samples per set (1)	4096
Duration per set ( $\mu$ s)	409.6
Pre-trigger samples (1)	1024
Threshold (dB)	36
Duration discrimination time ( $\mu$ s)	100
Rearm time ( $\mu$ s)	100

One plate of each layup type was characterized in the  $0^\circ$  and  $90^\circ$  direction. Sensor pairs were fixed at respective positions  $x_{S1}$  and  $x_{S2}$  and the actuator was moved between  $x_{A_s}$  and  $x_{A_e}$  in steps of  $x_{A_{step}}$  according to table 5.9. The values refer to the coordinate system defined in figure 5.24 where  $x = 0$  defines the vertical axis that is at the center of the plate.

Table 5.9: Sensor and actuator positions for the characterization of wave propagation according to the coordinate system in figure 5.24

Property	$(0^\circ/90^\circ)_{4s}$	$(0^\circ/90^\circ)_s$
Sensor pair 1 position $x_{S1}$ (mm)	-175	-125
Sensor pair 2 position $x_{S2}$ (mm)	+175	+125
Actuator starting position $x_{A_s}$ (mm)	-75	-30
Actuator end position (mm) $x_{A_e}$	+75	+30
Actuator step size (mm) $x_{A_{step}}$	25	15
No. actuator positions (1)	7	5

Due to lower signal-to-noise ratios, the actuator and sensor positions had to be adjusted for the  $(0^\circ/90^\circ)_s$  laminate.

Statistical variations were captured by repositioning the actuator three times and reintroducing each frequency three times per measurement position. This resulted in 63 data points for the  $(0^\circ/90^\circ)_{4s}$  and 45 for the  $(0^\circ/90^\circ)_s$  laminate for each evaluation frequency.

## 5.2.2 Evaluation methodology

The methodology for the evaluation of group velocities and attenuation coefficients is schematically illustrated in figure 5.26. It is divided into 4 steps, that are explained in detail in the following paragraphs. Steps 1 to 3 have to be accomplished for the signals of every sensor pair at the actuator positions  $x_A$  and excitation frequencies  $f_i$  specified in the previous section in order to perform the regression analysis in the 4<sup>th</sup> step.

1. **Signal filtering:** In the first step, the time signals were filtered around the center frequency of the excitation signal. This step was necessary to reduce the influence of frequencies apart from the center frequency that were excited and detected due to the burst-type excitation and the individual transfer functions of material, transducer and sensor. Furthermore, a narrow band filtered signal allowed the pair wise adjustment of sensor output for proper modal separation in the next step. Filtering was accomplished by applying a 2<sup>nd</sup> order band-pass filter with 6dB cut-off frequencies at  $\pm 12.5$  kHz around the excitation frequency. Filtering was performed twice, forward and backward, in order to eliminate phase shifts.

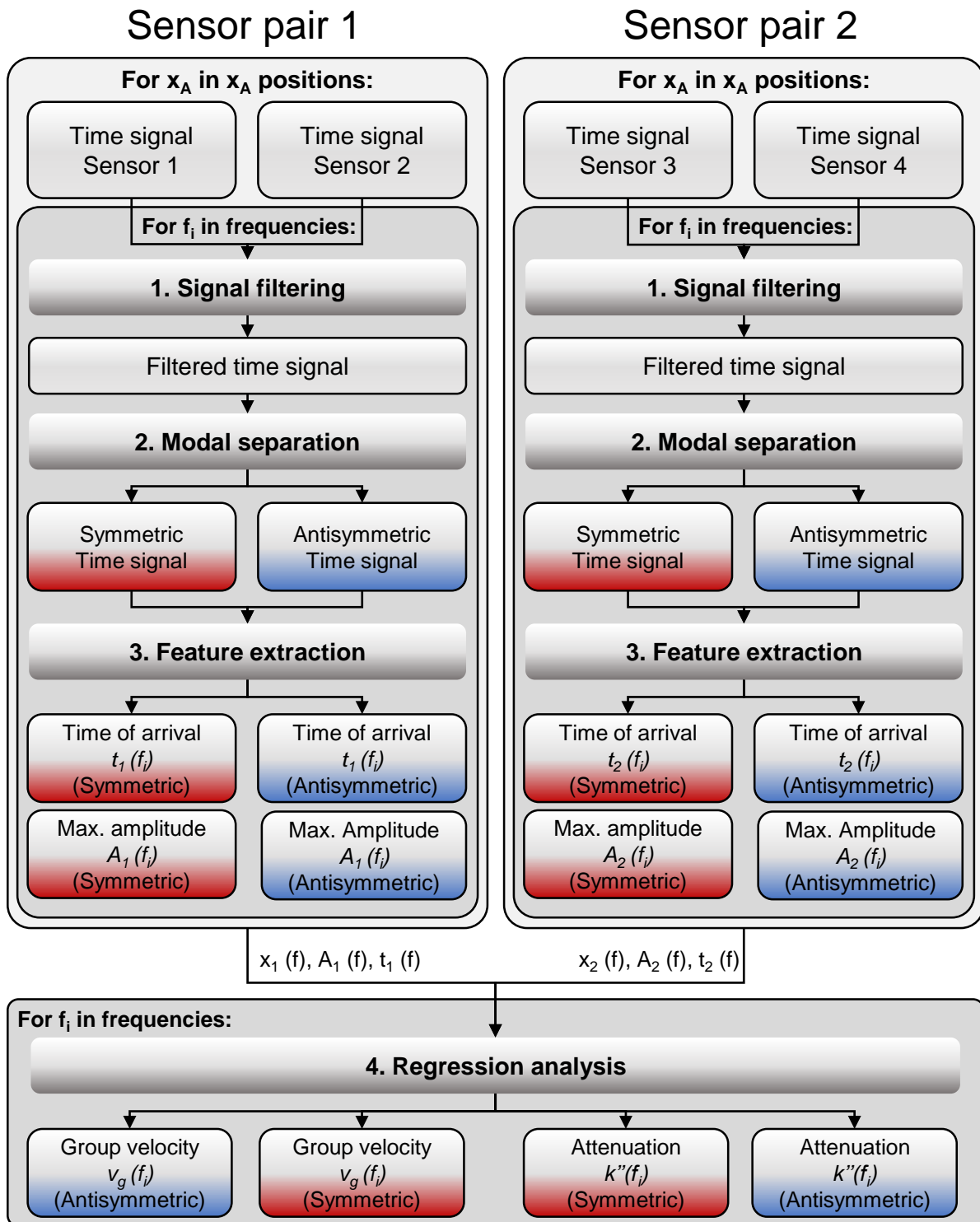


Figure 5.26: Evaluation methodology for the characterization of wave propagation.

**2. Modal separation:** In the next step, the symmetric and antisymmetric wave mode components were separated. Due to variations in sensor output, signals from each pair had to be adjusted first. This was realized by normalizing each signal by its maximum amplitude and multiplying the resulting signal with the mean of the maximum amplitude values from both signals. Figure 5.27 (top) gives an example of adjusted time signals

of the top and bottom sensors of a pair. There are sections where the signals are in phase (symmetric) and  $180^\circ$  shifted (antisymmetric). By simple addition and subtraction of signals from top and bottom sensor, the symmetric (middle) and antisymmetric (bottom) wave components can be extracted (see figure 5.27 bottom).

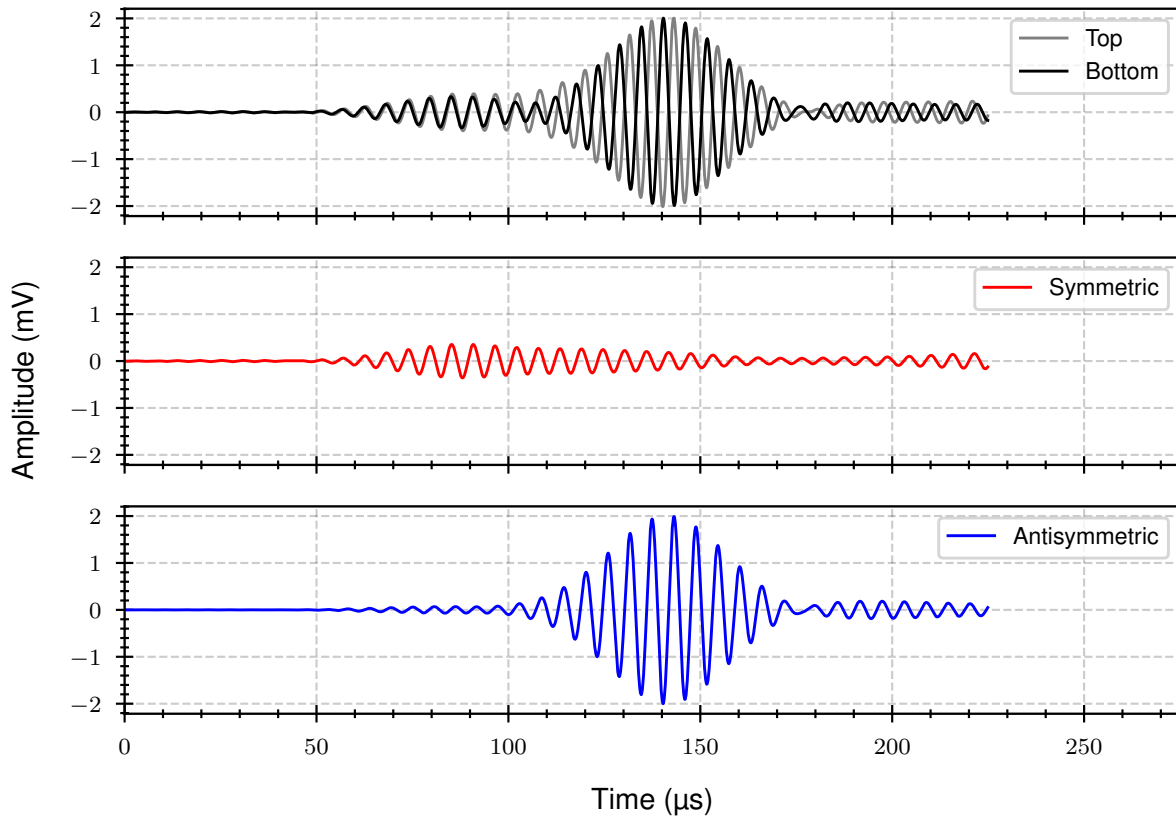


Figure 5.27: Extraction of symmetric and antisymmetric time signals through the addition and subtraction of time signals from the top and bottom sensors of a sensor pair.

**3. Feature extraction:** Time of arrival and maximum amplitude are determined from the filtered symmetric and antisymmetric time signals in the next step. Whereas the extraction of maximum amplitude is straight forward, the time of arrival is estimated with the Hinkley picker [196] that was already introduced in section 2.3.2. Figure 5.28 shows how the individual arrival times of  $S_0$  and  $A_0$  mode can be identified through the minimum in the characteristic function (black line) in the symmetric and antisymmetric time signal. The characteristic function was normalized by its absolute maximum.

**4. Regression analysis:** With the arrival times  $t_i(f)$  and the maximum amplitude  $A_i(f)$  at each sensor pair at distance  $x_i$  from the source, the amplitude ratios  $A_2(f)/A_1(f)$  and differences in arrival times  $\Delta t(f) = t_2(f) - t_1(f)$  can be analysed as a function of differences in propagation paths  $\Delta x = x_2 - x_1$  between sensor pairs. This can be realized as a function of frequency individually for the symmetric and antisymmetric

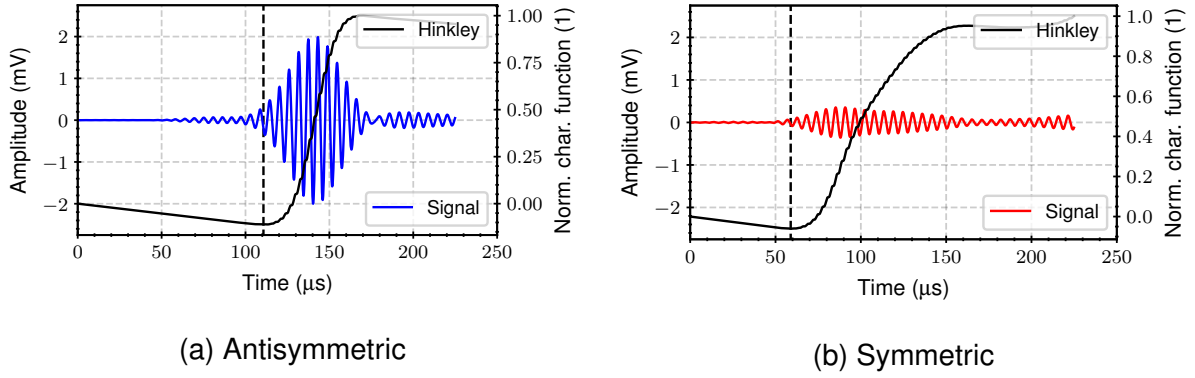


Figure 5.28: Picking the time of arrival of symmetric and antisymmetric time signals through the Hinkley picker [196]. The time of arrival is defined as the minimum in the characteristic function from equation 2.10.

signals.

The group velocity  $v_g(f)$  can be directly extracted from the underlying model in equation 5.17 as the slope in the linear regression of  $\Delta x$  and  $\Delta t(f)$  values.

$$\Delta x = v_g(f) \cdot \Delta t(f) + n_v(f) \quad (5.17)$$

An additional offset  $n_v(f)$  is incorporated to account for the fact that the actuator position at  $x_A = 0$  might not be exactly in the middle of the two sensor pairs. An example for such a linear regression is given in figure 5.29 (a) for symmetric (red) and antisymmetric (blue) data collected at an excitation frequency of 225 kHz in the  $(0^\circ/90^\circ)_{4s}$  laminate. At this frequency, symmetric and antisymmetric signals can be directly linked to the  $S_0$  and  $A_0$  mode according to figure 5.19.

If dispersion and wave leaking can be neglected, the attenuation coefficient  $k''(f)$ , can be determined by combining equations 2.8 and 2.9 from section 2.2.2 according to

$$\log \left( \frac{A_2(f)}{A_1(f)} \cdot \frac{\sqrt{x_2}}{\sqrt{x_1}} \right) = -k(f)'' \Delta x + n_a(f) \quad (5.18)$$

The offset  $n_a(f)$  is incorporated to not only account for misalignment of sensor and actuator positions but also for differences in the coupling and transfer functions of individual sensor pairs. By performing a linear regression with  $\Delta x$  values and the term on the left hand side of equation 5.18, the attenuation coefficient can be extracted from the resulting slope. Figure 5.29 (b) shows a corresponding example for the regression of symmetric and antisymmetric amplitude data acquired at 225 kHz in the  $(0^\circ/90^\circ)_{4s}$  laminate.

For each property extracted from linear regression the standard error is calculated along with the margin of error for a two sided 95 % confidence interval on the basis of the t-statistics.

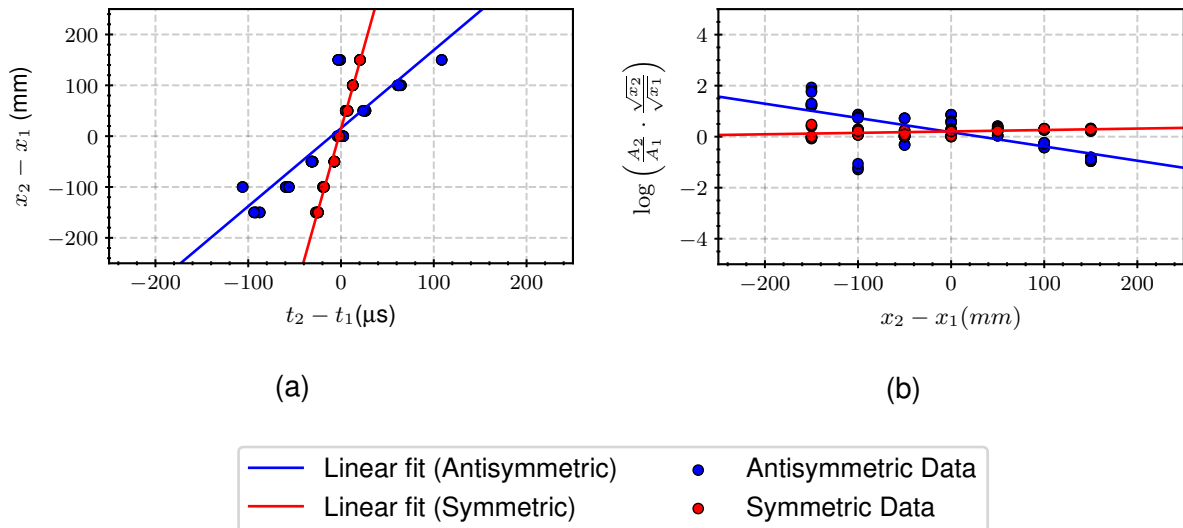


Figure 5.29: Linear regression analysis for the determination of group velocities (a) and attenuation coefficients (b) of the symmetric (red) and antisymmetric modes (b) at an excitation frequency of 225 kHz in the  $(0^\circ/90^\circ)_{4s}$  laminate.

### 5.2.3 Limitations

Before presenting the results, the following four aspects need to be considered that limit the frequency range where symmetric and antisymmetric wave modes  $A_0$  and  $S_0$  can be reliably characterized with the presented approach.

- 1. Near field effects:** Ultrasonic waves show different characteristics in the near field. In the proximity of the source, significant diffraction phenomena can take place when the diameter of the transducer is in the order of the acoustic wavelength [61]. This can affect the local signal amplitude. Guided waves, in particular, also need a characteristic distance in order to develop as incident and reflected longitudinal and transversal waves superimpose to form it. In this transition zone, propagation characteristics are expected to be different from those in the far field. As a rule of thumb, one can define a critical distance of 3 to 5 wavelengths as the end of the near field zone. The evaluation frequencies can be restricted accordingly by following figures 5.30 (a) and (b) that show the minimum number of wavelengths of  $A_0$  and  $S_0$  mode as a function of frequency for the  $(0^\circ/90^\circ)_{4s}$  and  $(0^\circ/90^\circ)_s$  setup from table 5.9.

Calculations were based on the corresponding minimum source-to-sensor distances of 100 and 95 mm and the average dispersion curves from section 5.1. For the evaluation, a minimum of 3 wavelengths was requested (see dashed horizontal black line). For the  $A_0$  mode, this was the case for all selected excitation frequencies. In terms of the  $S_0$  mode, however, evaluation had to be limited to frequencies above 205 and 215 kHz in terms of the  $(0^\circ/90^\circ)_{4s}$  and  $(0^\circ/90^\circ)_s$  laminate.

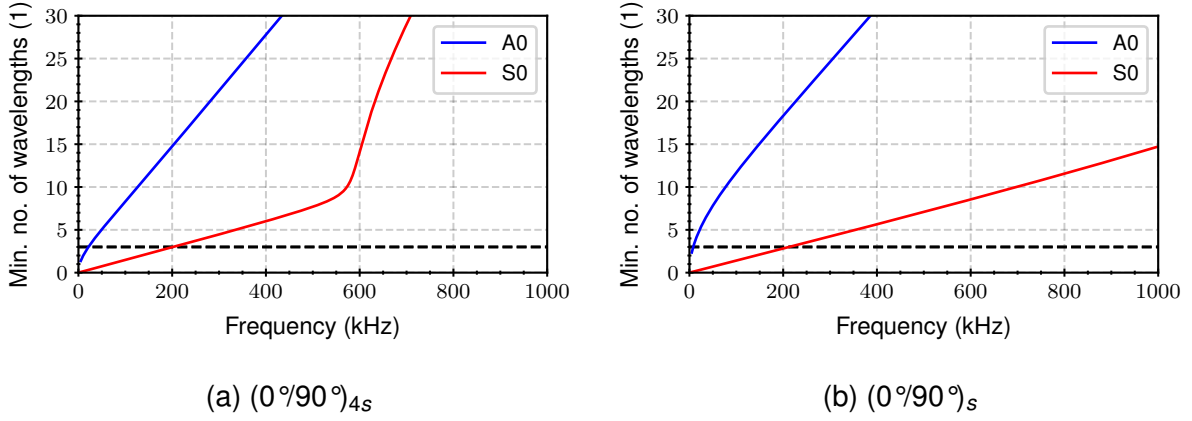


Figure 5.30: Minimum number of wavelengths ( $l$ ) of the  $A_0$  and  $S_0$  modes as a function of frequency (kHz) for the  $(0^\circ/90^\circ)_{4s}$  and  $(0^\circ/90^\circ)_s$  setup from table 5.9.

**2. Excitability and detectability of wave modes:** Excitability and detectability of Lamb wave modes differ due to differences in displacement fields and wavelengths. This can limit the individual frequencies for evaluation. For surface mounted transducers, the excitability of Lamb wave modes is governed by the ratio of acoustic wavelength to transducer dimensions as pointed out by [197]. If the wavelength matches the effective length of a transducer, excitability will be low. On the other side, excitability will be high, if the wavelength equals twice the effective length. This results in local amplitude minima and maxima as a function of excitation frequency that are different for each wave mode [59, 66, 197]. The same principle can be applied to the detection of Lamb waves as illustrated in [5, 185]. Another aspect that influences the excitability and detectability of a wave mode is found in the displacement field. For the common out-of-plane excitation and detection, the  $A_0$  mode is favoured over the  $S_0$  mode at lower frequencies due the more pronounced out-of-plane characteristic (see section 2.2.1).

Excitability and detectability of wave modes were handled together by empirically evaluating the individual strength of symmetric and antisymmetric signals as a function of frequency. This was realized on the basis of their energy portion  $R_m$  that was determined by relating signal energy  $S_m$  of mode type  $m$  (either symmetric or antisymmetric) to the average signal energy  $\bar{S}$  from the raw time signals  $j$  (see equation 5.19). Signal energy was thereby determined as the sum of squares of signal amplitudes  $A_i$  for samples  $i = 1 \dots N$ .

$$R_m = \frac{S_m}{\bar{S}} = \frac{\sum_{i=0}^N A_{i,m}^2}{\frac{1}{2} \cdot \sum_{j=0}^N \sum_{i=0}^N A_{i,j}^2} \quad (5.19)$$

Figure 5.31 shows the corresponding energy portions of symmetric and antisymmetric signals as a function of excitation frequency for a propagation in the  $0^\circ$  direction in the



$(0^\circ/90^\circ)_{4s}$  (a) and  $(0^\circ/90^\circ)_s$  (b) laminate. The signals from every sensor pair and actuator position were extracted to compute the respective mean and standard deviation values given in the figures.

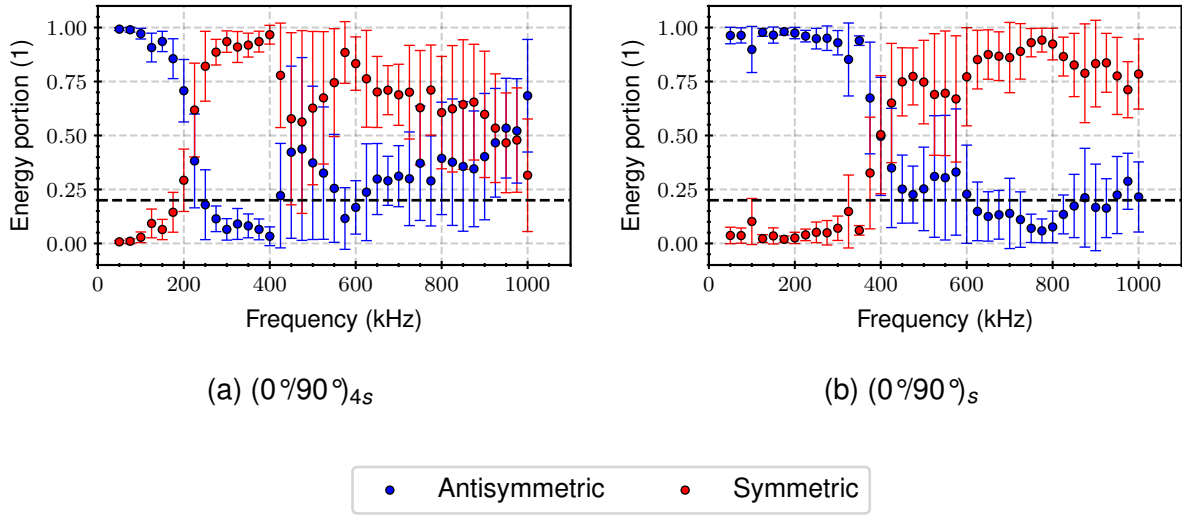


Figure 5.31: Energy portions of the symmetric and antisymmetric signals (1) as a function of excitation frequency (kHz). The values were experimentally determined from acquired signals in the  $0^\circ$  fibre direction in the  $(0^\circ/90^\circ)_{4s}$  (a) and  $(0^\circ/90^\circ)_s$  (b) laminate.

For both laminates, a shift in modal content can be seen with increasing frequency. Whereas the antisymmetric signals dominate at lower excitation frequencies, the symmetric signals are more pronounced at higher frequencies. The corresponding frequencies at which the shift takes place differ between the  $(0^\circ/90^\circ)_{4s}$  ( $\sim 400$  kHz) and  $(0^\circ/90^\circ)_s$  laminate ( $\sim 200$  kHz) due to the different thicknesses.

A minimum energy portion of 20% was defined as a requirement for the analysis (see dashed horizontal black line). Consequently, evaluation was constrained to frequencies where the symmetric or antisymmetric energy portion was above this critical value.

**3. Modal separation:** The proposed method for the separation of symmetric and antisymmetric wave components is only reliable if the opposing sensors are perfectly aligned. Any mismatch between them will lead to errors in the form of symmetric signal portions in the antisymmetric signal and vice versa. In order to quantify this error, a closer look is taken at the superposition of acoustic waves. For two plane wave fronts with amplitude  $A_0$  propagating in phase at frequency  $\omega$  and speed  $c = \omega/k$  the resulting amplitude  $A$  of their superposition can be described as

$$A = A_0 \cdot e^{i(kx - \omega t)} + A_0 \cdot e^{i(kx - \omega t)} = 2A_0 \cdot e^{i(kx - \omega t)} \quad (5.20)$$

However, if one wave is shifted in space by an offset  $\phi$ , the resulting amplitude  $A$  follows

$$A = 2A_0 \cdot \cos\left(-\pi \cdot \frac{\phi}{\lambda}\right) \cdot e^{i(k(x+\phi/2)-\omega t)} \quad (5.21)$$

which can be reduced to

$$A = A_{mod} \cdot e^{i(k(x+\phi/2)-\omega t)} \quad (5.22)$$

with the modified amplitude

$$A_{mod} = 2A_0 \cos\left(-\pi \cdot \frac{\phi}{\lambda}\right). \quad (5.23)$$

For an offset that equals half the wavelength of the acoustic wave, the resulting amplitude becomes zero. In terms of modal separation, this would mean that a symmetric signal portion would be falsely interpreted as antisymmetric in this case.

The relative amplitude  $A_{mod}$  is presented graphically in figures 5.32 (a-d) for the  $A_0$  and  $S_0$  mode in the  $(0^\circ/90^\circ)_{4s}$  (a,b) and  $(0^\circ/90^\circ)_s$  (c,d) laminates as a function of frequency (kHz) and spatial offset (mm). The figures are based on equation 5.23 and the mean dispersion properties in the  $0^\circ$  direction (see figure 5.21). The design of the fixture from figure 5.24 allowed the tolerance of the sensor offset to be below 0.25 mm. With this tolerance (white dashed line in figure 5.32) critical frequency limits can be identified where the procedure for modal separation will cause significant errors. In this case, a maximum error of 5 % in the resulting amplitude was tolerated. Due to the smaller wavelengths of the  $A_0$  mode compared to the  $S_0$  mode, the  $A_0$  mode determined the frequency limit for both modes. This limit was found at 590 kHz for the  $(0^\circ/90^\circ)_{4s}$  and at 520 kHz for the  $(0^\circ/90^\circ)_s$  laminate in this case.

**4. Higher order modes:** The existence of more than one symmetric or antisymmetric mode can lead to errors due to potential superposition of wave modes and uncertainties in the determination of individual times of arrival. The evaluation of symmetric and antisymmetric signals was therefore constrained to frequencies where only the fundamental wave modes  $S_0$  and  $A_0$  were present. For the  $(0^\circ/90^\circ)_{4s}$  laminate, evaluation of the symmetric and antisymmetric signals was limited accordingly to frequencies below 600 and 325 kHz respectively.

The evaluation frequencies for  $A_0$  and  $S_0$  mode were found by looking at the intersection of respective frequency windows regarding each aspect. Table 5.10 summarizes these frequencies for the  $(0^\circ/90^\circ)_{4s}$  and  $(0^\circ/90^\circ)_s$  laminates for propagation in the  $0^\circ$  and  $90^\circ$  directions. The frequencies were accordingly rounded up or down to the next excitation frequency. The remaining figures that were not presented here can be found in appendix F.

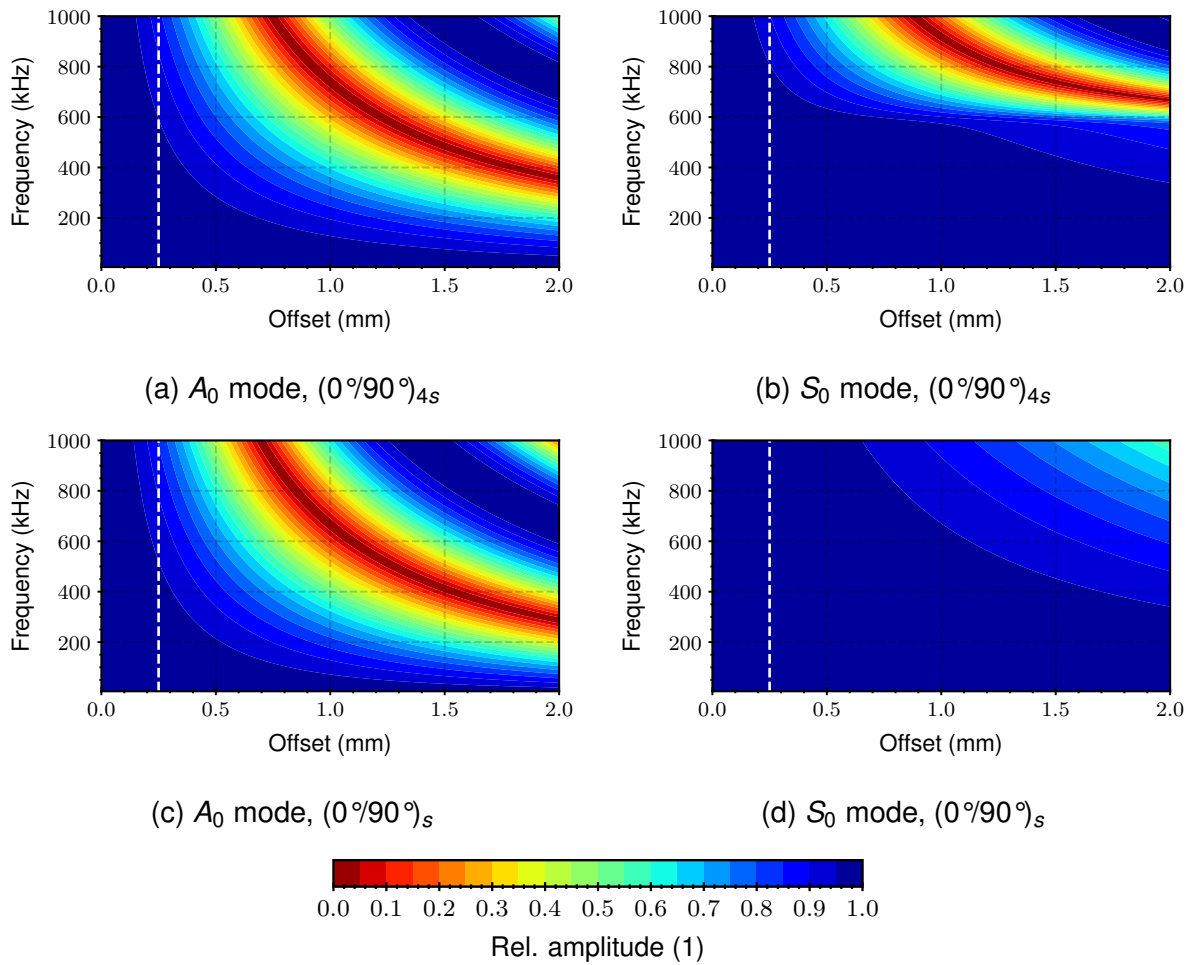


Figure 5.32: Relative amplitude (1) as a function of frequency (kHz) and spatial offset (mm) for the superposition of wave packets from the  $A_0$  and  $S_0$  mode propagating in the  $0^\circ$  direction in the  $(0^\circ/90^\circ)_{4s}$  (a,b) and  $(0^\circ/90^\circ)_s$  (c,d) laminate.

Table 5.10: Summary on resulting frequency windows for the  $(0^\circ/90^\circ)_s$  and  $(0^\circ/90^\circ)_{4s}$  laminates for propagation in the  $0^\circ$  and  $90^\circ$  direction

Laminate	Direction	Evaluation frequencies (in kHz)	
		$A_0$ mode	$S_0$ mode
$(0^\circ/90^\circ)_s$	$0^\circ$	50-500	375-500
$(0^\circ/90^\circ)_s$	$90^\circ$	50-325 375	300-325 375
$(0^\circ/90^\circ)_{4s}$	$0^\circ$	50-225	225-575
$(0^\circ/90^\circ)_{4s}$	$90^\circ$	50-200	225-550

## 5.2.4 Results

### Group velocity

The group velocities (m/s) are presented as a function of frequency (kHz) in the following figures. The experimental results from the evaluation of symmetric and antisymmetric signals are shown as red and blue dots respectively. Only frequencies within the evaluation windows from table 5.10 were considered (see appendix G for all frequencies). The horizontal error bars are based on the 6dB bandwidth of the applied band-pass filter, whereas the margin or error from regression analysis represents the vertical error. The theoretical dispersion curves are shown together with experimental results for direct comparison. The figures 5.33 (a-d) show the results for the  $(0^\circ/90^\circ)_{4s}$  and  $(0^\circ/90^\circ)_s$  laminate for the  $0^\circ$  and  $90^\circ$  direction.

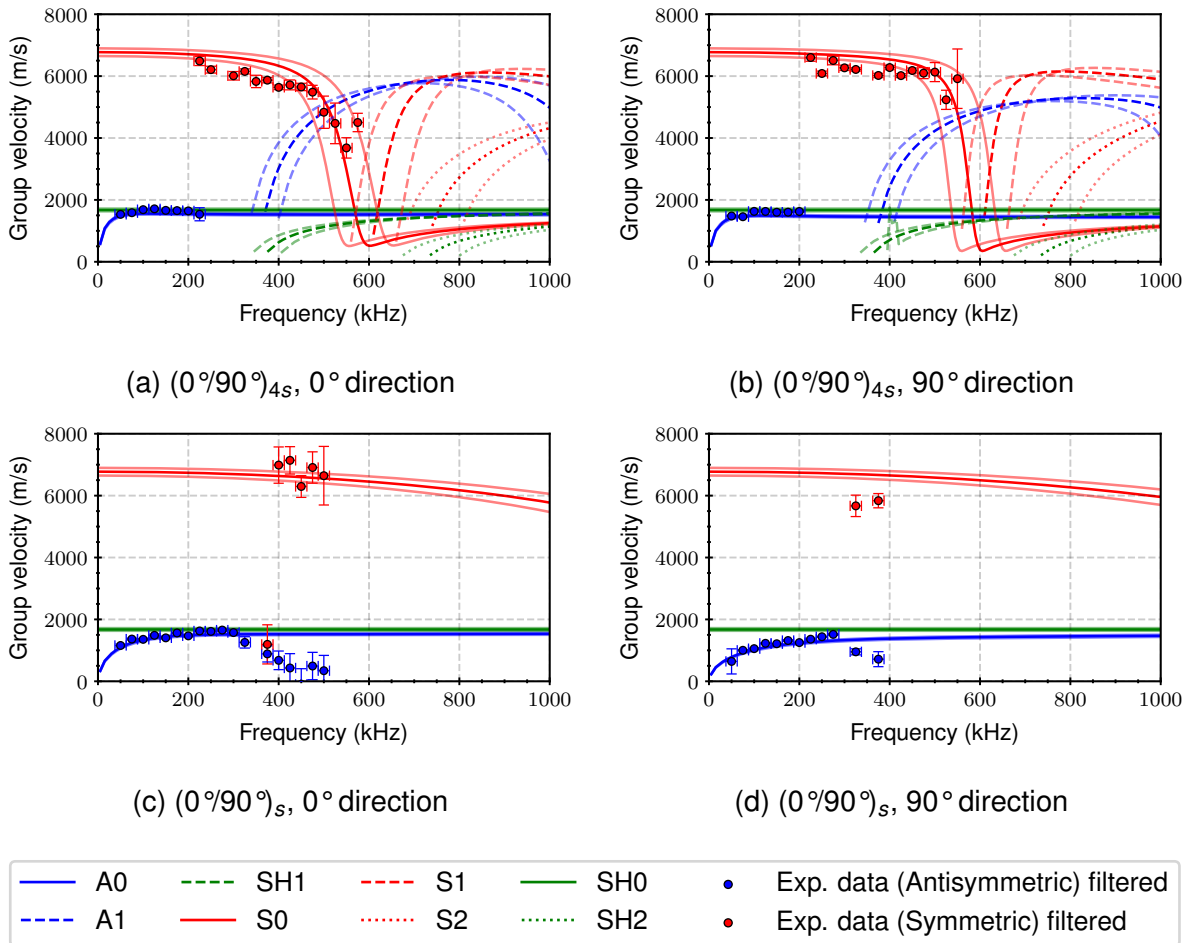


Figure 5.33: Experimental (dots) and theoretical results (lines) for the group velocities (m/s) of wave modes as a function of frequency (kHz) for the  $(0^\circ/90^\circ)_{4s}$  and  $(0^\circ/90^\circ)_s$  laminate in the  $0^\circ$  (a,c) and  $90^\circ$  (b,d) direction.

With a few exceptions, the experimental results are in good agreement with the theoretical dispersion curves of the  $A_0$  and  $S_0$  modes. Deviations can be found, when

the signals are dominated by one mode (see energy portions in figure 5.31). In these cases, remaining antisymmetric signal portions can determine the time of arrival in the symmetric signal and vice versa (see symmetric data point at 375 kHz in 5.33 (c)). The critical limit of energy portion might have to be raised in order to avoid these mistakes. Further deviations can be seen in the antisymmetric data above 300 kHz in figures 5.33 (c) and (d), where the group velocity of the  $A_0$  mode is underestimated. This could also be due to low energy levels at these frequencies as illustrated in figure 5.31. However, in this case, it is not the symmetric mode that is picked but rather a superposition of reflections that are stronger than the primary wave packet.

The group velocity of the  $S_0$  mode propagating in the  $90^\circ$  direction in the 4-ply specimens is also lower than expected. This could result from deviations between the principal fiber directions in each layer and the direction of characterization, since for the  $S_0$  mode, small changes in the propagation angle can already lead to significant changes in the resulting group velocity (see figure 5.20).

### Wave attenuation

Results on the wave attenuation had to be constrained to the  $(0^\circ/90^\circ)_{4S}$  laminate due to challenges arising from low signal-to-noise ratios and unequal sensor coupling in the  $(0^\circ/90^\circ)_S$  laminate. However, due to the similar elastic properties, the results should transfer to the  $(0^\circ/90^\circ)_S$  laminate with a shift in frequencies according to the differences in thickness. Attenuation coefficients  $k''$  (Np/m and dB/m) are shown as a function of frequency (kHz) for the  $0^\circ$  and  $90^\circ$  direction in the  $(0^\circ/90^\circ)_{4S}$  laminate in figures 5.34 (a) and (b). The values extracted from the symmetric and antisymmetric time signals are presented as red and blue dots respectively. Additionally, attenuation coefficients of the  $S_0$  and  $A_0$  modes from literature (as previously presented in figure 2.6) are shown for comparison. The corresponding markers are filled in red and blue to represent data for the  $S_0$  and  $A_0$  modes respectively. These values were also derived from experiments on cross-ply CFRP laminates in the  $0^\circ$  and  $90^\circ$  direction.

There are several interesting aspects to point out that can be related to the  $0^\circ$  and  $90^\circ$  direction. First of all, one can observe a steady increase in the attenuation coefficient of the  $A_0$  mode for frequencies ascending from 50 to 225 kHz. A similar trend can be seen in the  $0^\circ$  direction for the  $S_0$  mode between 300 and 600 kHz. However, the corresponding rate of change in the attenuation coefficient is higher for the  $A_0$  mode, which is in accordance with literature [59, 63]. Consequently, the attenuation coefficients of the  $A_0$  mode are significantly higher than that of the  $S_0$  mode at the same frequency (see 225 kHz in  $0^\circ$  direction as example). In fact, the attenuation of the  $A_0$  mode at around 100 kHz is similar to that of the  $S_0$  mode at elevated frequencies up to 600 kHz. The  $S_0$  mode is therefore capable of preserving the higher

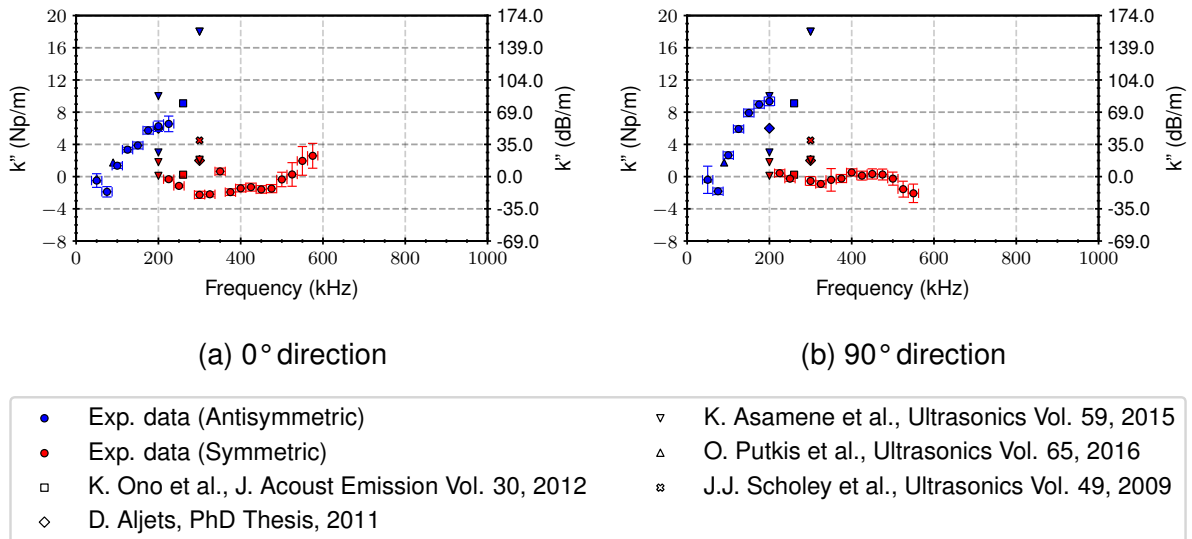


Figure 5.34: Attenuation coefficients  $k''$  (dB/m and Np/m) as a function of frequency (kHz) for the  $(0^\circ/90^\circ)_{4s}$  laminate in the  $0^\circ$  (a) and  $90^\circ$  (b) direction. Experimental results (dots) from symmetric (red) and antisymmetric data (blue) are shown along with results for the  $S_0$  (red) and  $A_0$  modes (blue) from literature as previously presented in figure 2.6.

frequency content of AE sources for larger source-to-sensor distances.

Secondly, there are negative attenuation coefficients for the  $A_0$  and  $S_0$  mode. This behaviour has already been observed by other authors [56, 63, 65] and could be attributed to the limitations of the common geometric spreading function to isotropic media. Due to the anisotropic properties, energy is inherently focused in the fibre direction in FRP as already pointed out in section 2.2.2. This can lead to a non-uniform spread of energy where amplitude reduction does not follow equation 2.8 in all directions. Especially in the fibre direction, attenuation due to geometric spreading seems to be overestimated, resulting in the partly negative attenuation coefficients in figures 5.34 (a) and (b).

Finally, the attenuation coefficients for  $A_0$  and  $S_0$  mode are comparable with the presented values from the literature. The results are in the same order of magnitude and show similar trends. Deviations could be attributed to differences in the CFRP plate (e.g. thickness, type of fibre, type of matrix, fibre volume content, etc.), the measurement setup (e.g. minimum source-to-sensor distances, number of sensors, etc.) or the evaluation methodology (e.g. method for filtering and modal separation).

### 5.3 Preliminary conclusion

Characterization of guided wave propagation was accomplished in a two step process on a theoretical and experimental basis. Group velocities, wavelengths and displacement fields of guided wave modes were calculated as a function of frequency and propagation direction. Results were presented with tolerance windows by taking into account the variation in fibre volume content and layer thickness in the manufactured laminates. The assumption of similar dispersion characteristics in the  $0^\circ$  and  $90^\circ$  direction could be confirmed for the two types of cross-ply laminates in this study. Theoretical data on group velocities of the  $A_0$  and  $S_0$  modes could be validated with experimental results at selected frequencies. These had to be constrained due to near field effects, the presence of higher order modes, errors in wave superposition as well as limited excitability and detectability of wave modes. Regarding wave attenuation, it could be shown that the attenuation of the  $A_0$  mode around 100 kHz is similar to that of the  $S_0$  mode at elevated frequencies up to 600 kHz. For larger source-to-sensor distances, the  $S_0$  mode is therefore capable of preserving more of the high frequency content than the  $A_0$  mode.





## 6 Preliminary study: AE from artificial sources

### 6.1 Experimental

#### 6.1.1 Setup

The goal of this section is to investigate the influence of source depth and source-to-sensor distance through the systematic introduction of artificial AE sources. The standardized Hsu-Nielsen source (ASTM E976) was chosen as the source in this context due to its high recognition in the AE community and its ability to produce broadband AE. It is created by breaking a specific pencil lead (hardness 2H, diameter 0.5 or 0.3 mm, length  $3 \pm 0.5$  mm) through a guide ring under a defined angle on the object of investigation. By breaking the lead either on the surface or the edge of the plate, one can create a strong out-of-plane or in-plane source respectively. In order to simulate fibre breakage and transverse matrix cracking as typical in-plane sources, the pencil lead was broken at different depths on the edge of the plate. For this objective, the fixture in figure 6.35 was designed. It allows to systematically perform pencil leads breaks (PLB) at different depths through an end stop that can be adjusted in height through a linear stage. The design thereby allows the plate to be locked in position in a way that its surface is oriented parallel to the surface of the end stop.

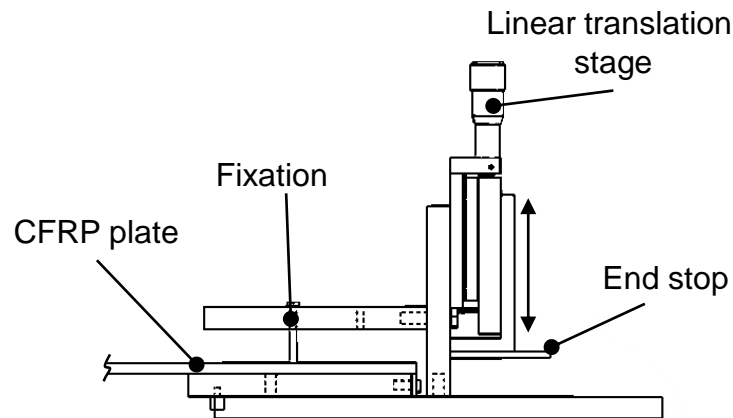


Figure 6.35: Fixture for the systematic introduction of in-plane Hsu-Nielsen sources in different depths in the CFRP laminate.

The fixture was incorporated in the setup shown in figure 6.36 (a) to introduce in-plane Hsu-Nielsen sources (diameter: 0.35 mm, length: 3 mm) in 12.5, 25.0, 37.5 and 50% relative depth position in the  $(0^\circ/90^\circ)_{4s}$  laminate (red dots). The linear translation stage thereby allowed an accuracy of  $5 \mu\text{m}$ . A closeup on the setup in the lab can be seen in figure 6.36 (b).

The resulting acoustic waves were measured in the  $0^\circ$  and  $45^\circ$  direction with a Vallen VS900 sensor at 50, 100 and 150 mm distance from the source (blue dots). The

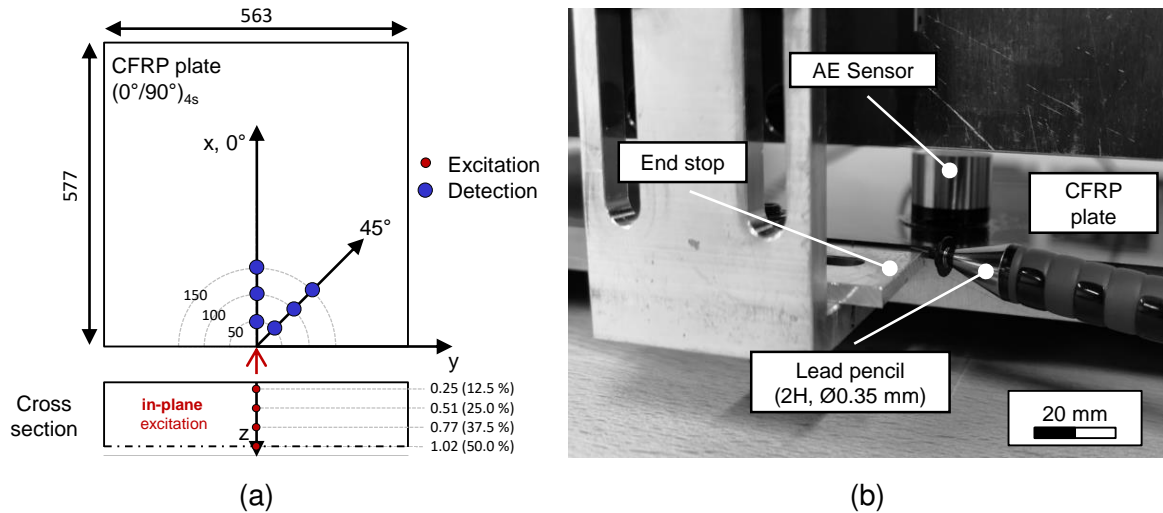


Figure 6.36: Schematic sketch on the experimental setup for the preliminary study (a) and closeup from the setup in the laboratory (b). Dimensions are given in millimeters.

signals were amplified with an AEP4 amplifier and recorded with the Vallen AMSY 5. The corresponding acquisition parameters are listed in table 6.11.

Table 6.11: Vallen AMSY 5 acquisition parameters for the preliminary study

Property	Value
Sample rate (MS/s)	10
Samples per set (1)	4096
Duration per set ( $\mu$ s)	409.6
Pre-trigger samples (1)	512
Threshold (dB)	50
Duration discrimination time ( $\mu$ s)	100
Rearm time ( $\mu$ s)	100

At each depth position, the pencil was broken 10 times to capture statistical variations. Prior to evaluation, the signals were filtered with a high pass filter with a cut-off frequency at 25 kHz to reduce the low frequency noise.

### 6.1.2 Evaluation methodology

The evaluation was divided into the following four steps:

1. **Waveforms:** First of all, the influence of source depth on the resulting signal waveforms in the time and time-frequency domain were investigated qualitatively. The CWT was applied in this context, to visualize changes in the modal content through the time-frequency representation. The complex Morlet wavelet was

utilized as mother wavelet due to its similarity to the experimentally measured waveforms.

2. **Modal ratio:** In the next step, the change in modal ratio with source depth was quantified by evaluating the  $A_0$  to  $S_0$  ratio on the basis of their maximum amplitudes. This was accomplished frequency wise by computing the corresponding wavelet magnitude at respective scales. Modal separation was realized on a temporal level at source-to-sensor distance of 150 mm where primary wave packets of the  $A_0$  and  $S_0$  modes could be clearly distinguished. Theoretical dispersion curves were utilized to identify and extract the corresponding signal amplitudes.
3. **Frequency spectrum:** A closer look was taken at the frequency spectra in the next step to investigate how a change in modal content can affect frequency characteristics. In this context, source-to-sensor distance was incorporated in the analysis in order to visualize the combined influence with source depth.
4. **Extracted features:** Finally, a closer look was taken at common features for source identification that were extracted from the frequency domain. These were determined as a function of source depth and source-to-sensor distance in order to visualize the impact of both influencing factors. In this context, the effect of the evaluation windows on resulting features was investigated as well.

The corresponding results are presented in the next section.

### 6.1.3 Results

#### Waveforms

Figure 6.37 illustrates how signal waveforms vary with increasing source depth in the CFRP laminate for detection in the  $45^\circ$  direction at a distance of 100 mm. Acquired signals are presented in the time-frequency domain along with theoretical dispersion curves of the  $S_0$  and  $A_0$  modes from section 5.1 to ease the identification of wave modes. Dispersion curves are illustrated in corresponding color with mean values (solid line) and lower and upper borders (dashed line). The  $SH_0$  mode was omitted since it did not show any considerable out-of-plane displacement in the excited frequency range. Time signals can be found in appendix H.

The  $S_0$  and  $A_0$  modes can be clearly distinguished through the theoretical dispersion curves in figure 6.37. Whereas both modes show a similar magnitude for excitations at 12.5% relative depth, the  $S_0$  becomes more and more dominant with increasing source depth up to the plane of symmetry (50% relative source depth). This behaviour is in accordance with results from previous work [93, 123, 180]. In fact, the  $A_0$  mode should theoretically vanish for a pure in-plane excitation in the plane of symmetry because it does not show any in-plane displacement component at this depth (see

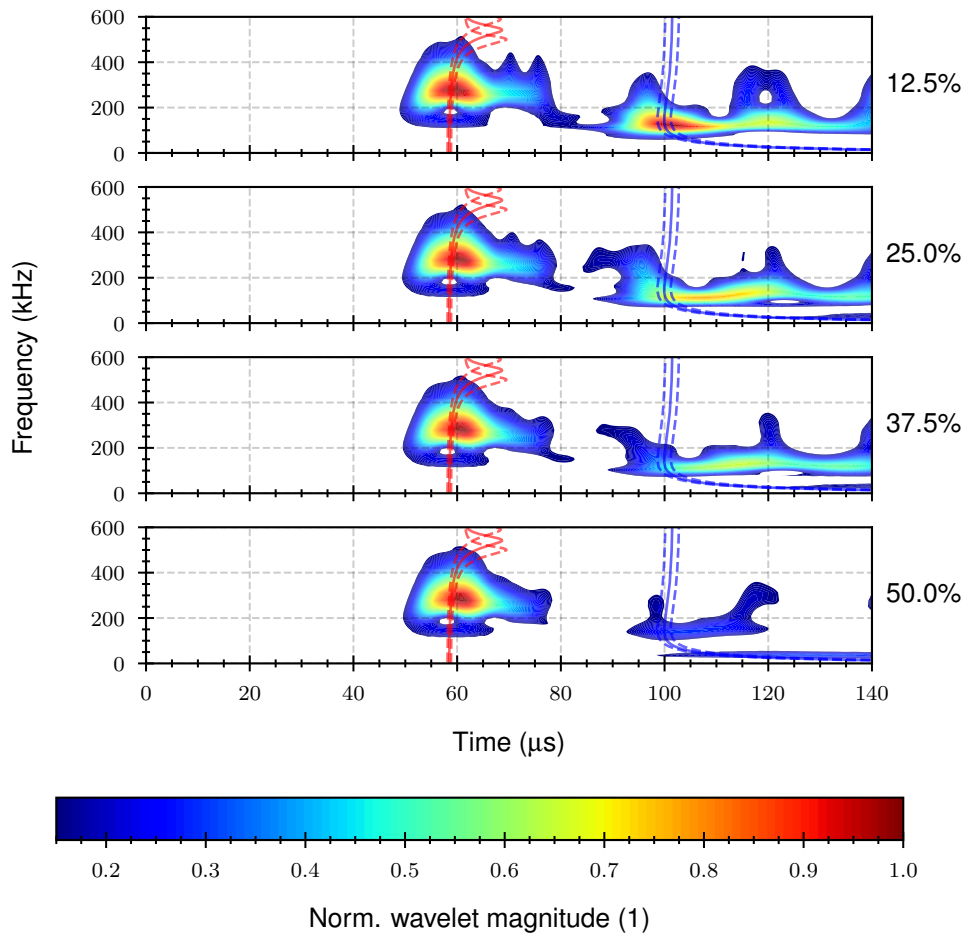


Figure 6.37: Normalized wavelet magnitude (1) as a function of time ( $\mu\text{s}$ ) and frequency (kHz) for relative source depths of 12.5, 25.0, 37.5 and 50.0% for detection in the  $45^\circ$  direction at 100 mm distance. Theoretical dispersion curves of the  $S_0$  and  $A_0$  mode are shown with mean values (solid line) and lower and upper borders (dashed line).

figure 5.23). However, this situation is hard to recreate in an experiment because the diameter of the pencil is not infinitesimal small, might not break exactly in the plane of symmetry and may cause some out-of-plane displacement if it is broken under an angle to the plane of the plate. Hence, a measurable portion of the  $A_0$  mode still exists for excitation in the plane of symmetry. The same observations on the  $A_0$  and  $S_0$  modes can be made for the other distances and a detection in the  $0^\circ$  direction as shown in the appendix I.

### Modal ratio

Following the procedure described in section 6.1.2, the change in modal content can also be quantified. Figures 6.38 (a-d) show how the maximum magnitudes of the  $A_0$  and  $S_0$  modes are affected as source depth varies for a detection in the  $0^\circ$  and  $45^\circ$  direction at 150 mm distance from the source. Mean values are shown along with

single standard deviations as error bars. Evaluation was performed at frequencies of 125, 175, 225 and 275 kHz where both modes could be detected.

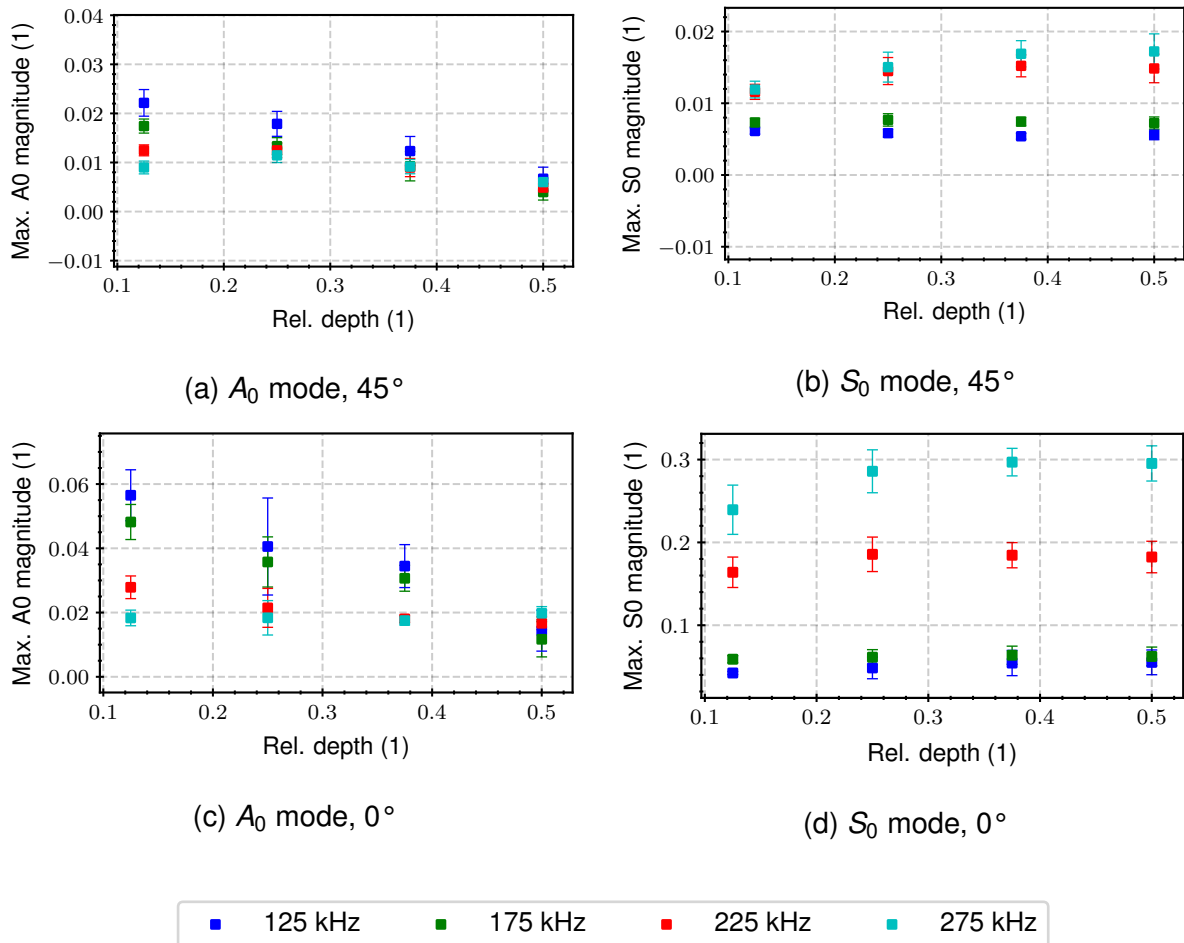


Figure 6.38: Maximum magnitude (1) of the  $A_0$  (a,c) and  $S_0$  (b,d) mode as a function of relative source depth (1) and frequency (kHz) for detection in the  $0^\circ$  (c,d) and  $45^\circ$  (a,b) direction at 150 mm distance from the source.

Whereas the magnitude of the  $S_0$  mode is only slightly affected by the variations in source depth, a steady decrease in magnitude can be seen for the  $A_0$  mode up to the plane of symmetry. The loss in magnitude is thereby most pronounced at low frequencies. This behaviour is in accordance with results from simulations that were published previously [123]. The drop in  $A_0$  magnitude was found to be linear in this study and the corresponding slopes decreased with increasing frequency.

The resulting  $A_0$  to  $S_0$  ratios as a function of source depth are shown for the  $0^\circ$  and  $45^\circ$  direction in figures 6.39 (a) and (b).

As  $A_0$  magnitude drops with increasing source depth and  $S_0$  magnitude remains nearly constant, a steady decrease in the  $A_0$  to  $S_0$  ratio can be observed.

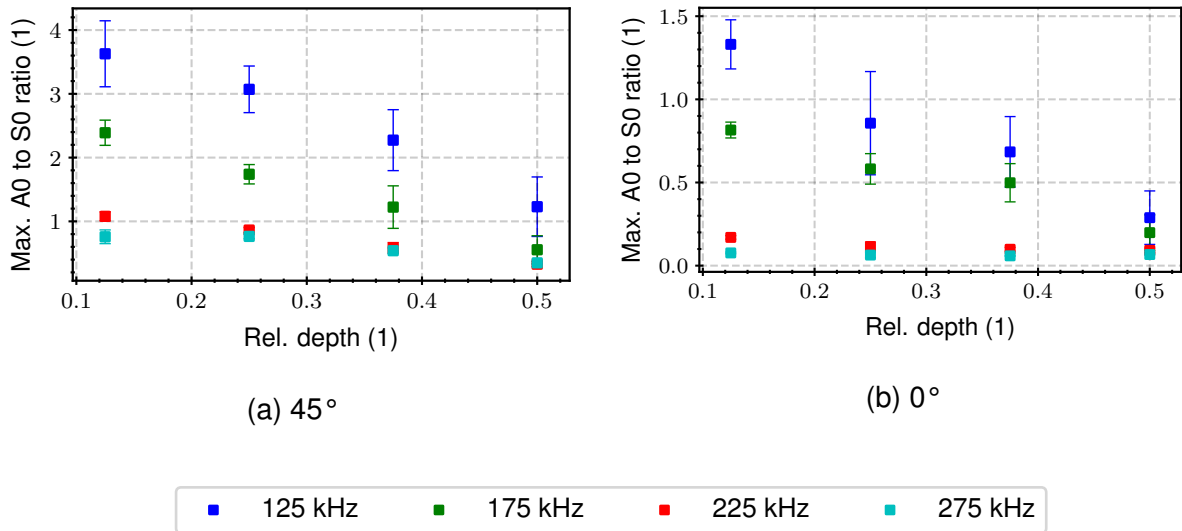


Figure 6.39:  $A_0$  to  $S_0$  ratio (1) as a function of relative source depth (1) and frequency (kHz) for detection in the  $45^\circ$  (a) and  $0^\circ$  (b) direction at 150 mm distance from the source.

### Frequency spectrum

As modal ratio changes with source depth, resulting frequency spectra can differ due to the factors discussed in section 2.4.1. In fact, significant changes can be observed when looking at figure 6.40 where normalized amplitude spectra of the acquired time signals ( $45^\circ$  direction, 100 mm distance) are shown for the various source depths. The spectra were generated from the signal section between 0 and 150  $\mu$ s to capture the primary wave packets of  $A_0$  and  $S_0$  mode. The spectra are represented by the mean values (black, solid line) along with lower and upper boundaries (grey, dashed line) that were defined through the standard deviation.

Two main frequency bands between 100 and 200 kHz as well as 250 and 350 kHz can be identified in figure 6.40. By looking at the CWTs in figure 6.37, these bands can be linked to the fundamental  $A_0$  and  $S_0$  modes, respectively. The fact that both modes are dominant at different frequency bands leads to inevitable changes in frequency spectra when modal content varies. As the amplitude of the  $A_0$  mode decreases with increasing source depth up to the plane of symmetry (see figure 6.38), the magnitude of the frequency band between 100 and 200 kHz is reduced accordingly. The peak frequency (blue, dashed line) thereby switches from the  $A_0$  dominant region around 125 kHz to the  $S_0$  dominant region at 275 kHz when going from 12.5% to 37.5% relative source depth. This change in peak frequency will consequently affect source classification as will be shown later in this section.

At this point, it is also interesting to include the source-to-sensor distance in the analysis. For this purpose, figure 6.41 shows a matrix plot that visualizes the influence

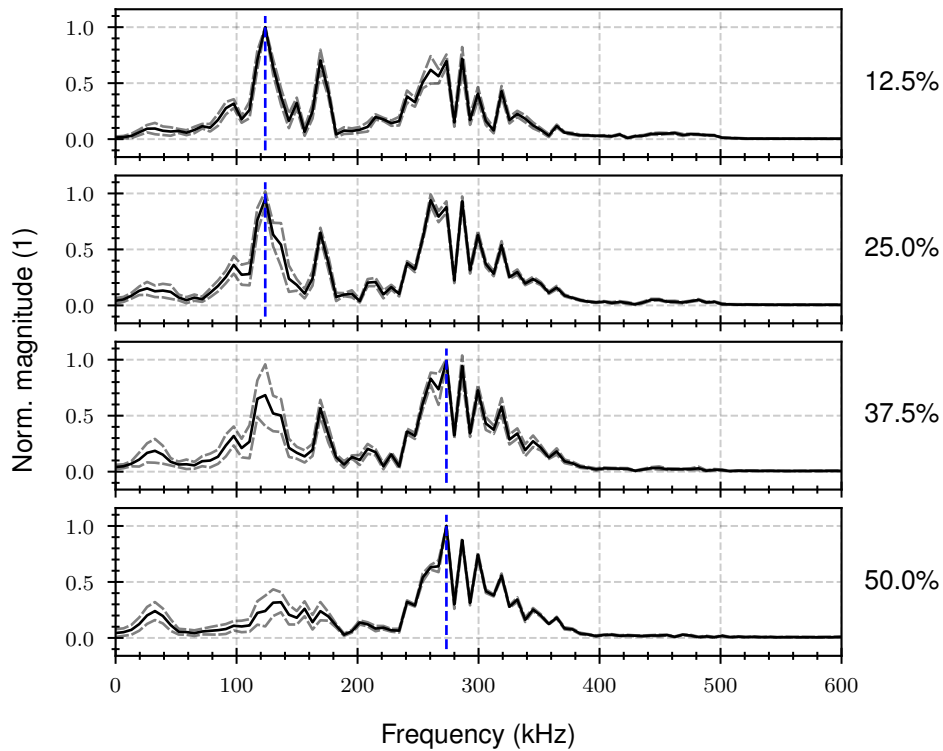


Figure 6.40: Normalized FFT magnitude (1) for relative source depths of 12.5, 25.0, 37.5 and 50.0%. Signals were acquired in the  $45^\circ$  direction at 100 mm distance from the source.

of both: relative source depth (%) and source-to-sensor distance (mm) on the resulting frequency spectra. For every source-to-sensor distance, we can observe the same trend on the reduction of magnitude of the  $A_0$  mode (between 100 and 200 kHz) with increasing source depth. However, the relative source depth position where peak frequency switches from the  $A_0$  (175 kHz) to the  $S_0$  mode (275 kHz) differs. With larger source-to-sensor distances, this switch in peak frequency is shifted towards lower source depths due to the stronger attenuation of the  $A_0$  mode compared to the  $S_0$  mode [59]. Whether or not a Hsu-Nielsen source is characterized through a peak frequency of 175 kHz or 275 kHz therefore strongly depends on both influencing factors.

Regarding the  $0^\circ$  direction, no switch in peak frequency could be observed, due to the small signal amplitude of the  $A_0$  mode at already low relative source depths. The corresponding matrix plot can be seen in appendix J.

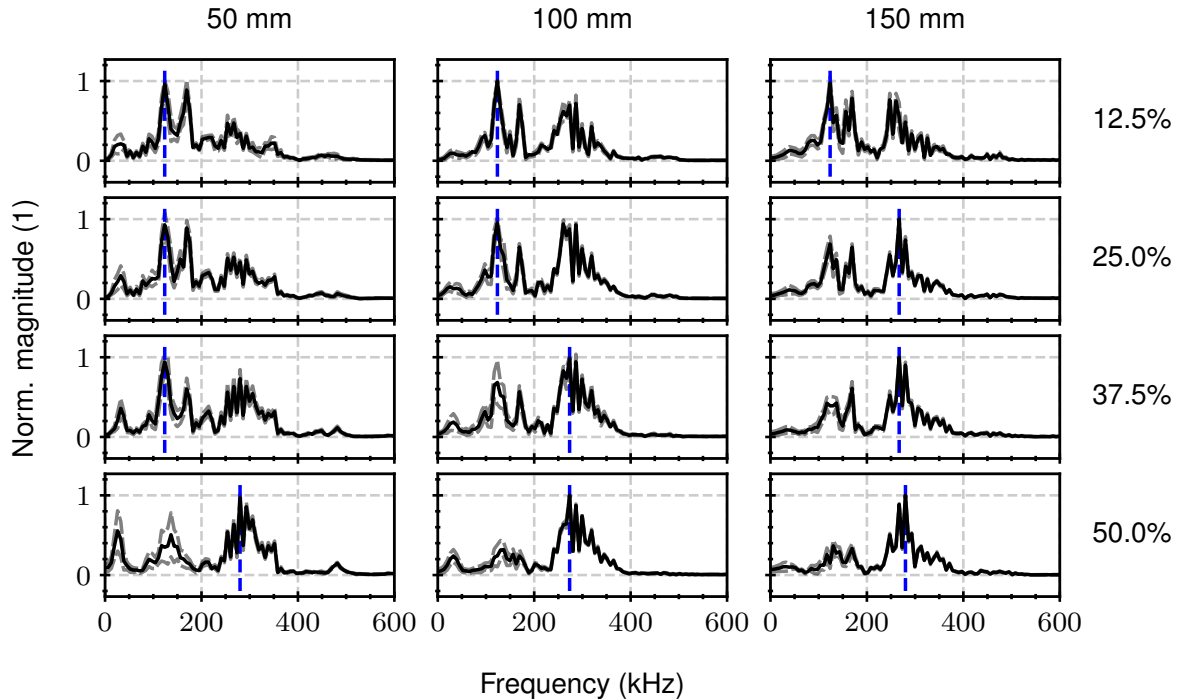


Figure 6.41: Matrix plot of normalized FFT magnitude (1) as function of source-to-sensor distance (50, 100 and 150 mm) and relative source depth (12.5, 25.0, 37.5 and 50.0%). Signals were acquired in the  $45^\circ$  direction.

### Extracted features

The development of common features from the frequency domain as a function of source depth and source-to-sensor distance is illustrated in figure 6.42 for the  $45^\circ$  (a,c,e) and  $0^\circ$  (b,d,f) direction. Peak frequency, weighted peak frequency and partial power 2 between 100-200 kHz were selected in this case. The values were normalized by the respective maximum to visualize the relative change.

As already discussed in the previous section, in terms of the  $45^\circ$  direction, peak frequency jumps from the  $A_0$  (175 kHz) to the  $S_0$  dominant region (275 kHz) depending on the interaction of source depth and source-to-sensor distance. Accordingly, weighted peak frequency and partial power 2 are affected likewise. In the  $0^\circ$  direction, however, changes are not that significant due to the fact that the  $S_0$  mode dominates in all configurations. The highest variations in the  $0^\circ$  direction can be seen for PP2. However, this is due to the already low absolute values.

When putting together all signals from the  $0^\circ$  and  $45^\circ$  directions, the effect on feature variation becomes obvious. This is done in figure 6.43 in terms of the weighted peak frequency (kHz) and partial power 2 between 100 and 200 kHz (1).

Two separate clusters are visible in the feature space that could be correlated to different sources when following the standard procedure described in section 2.3.3. However, all signals can be traced back to a single source. The existence of these two



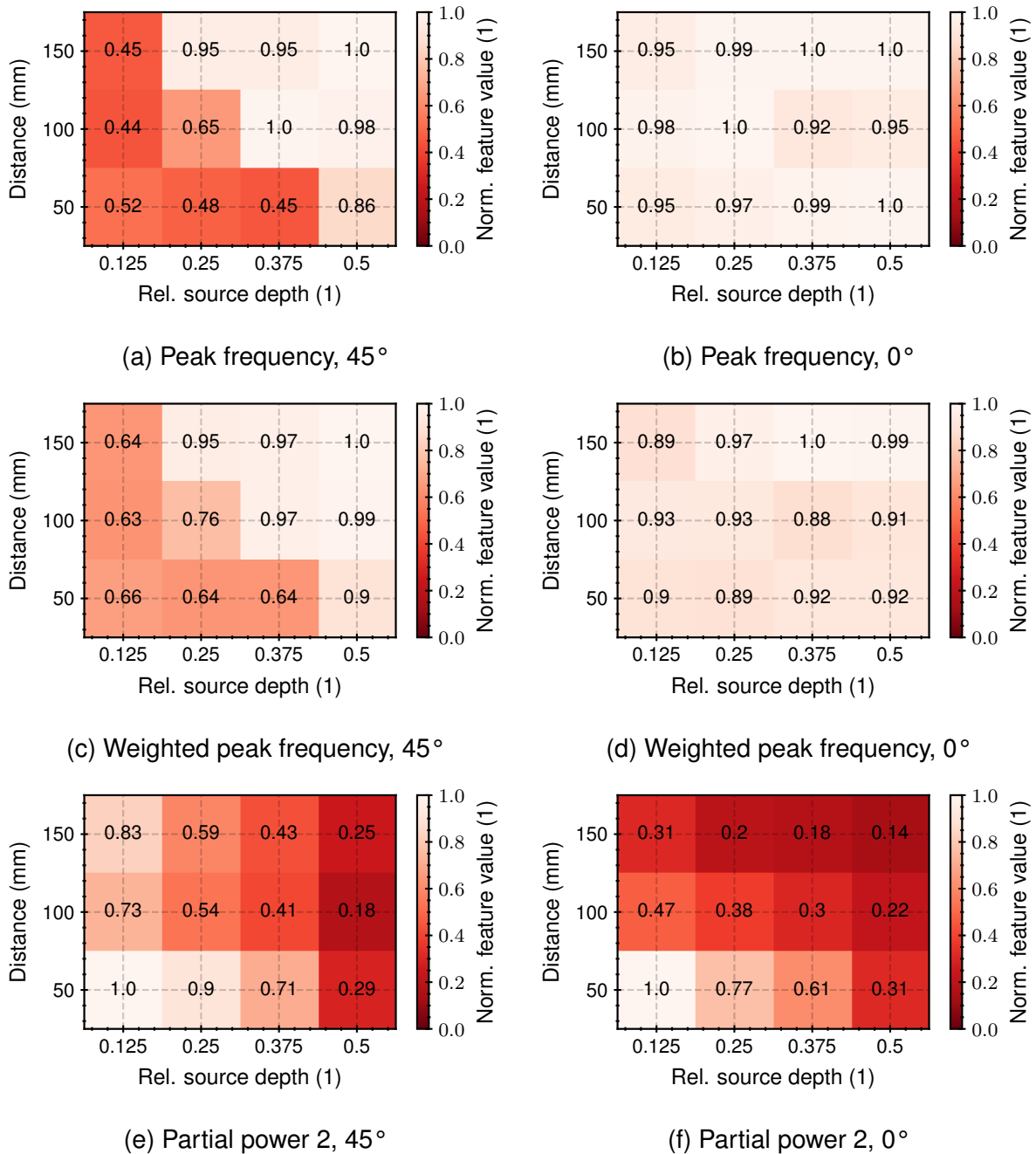


Figure 6.42: Normalized peak frequency (1), weighted peak frequency (1) and partial power 2 between 100-200 kHz (1) as a function of relative source depth (1) and source-to-sensor distance (mm) for the 0° (b,d,f) and 45° (a,c,e) direction.

clusters is just a result of the different frequency bands of the  $A_0$  and  $S_0$  modes that compete against each other as source depth and source-to-sensor distance varies. A change in modal content can thereby lead to different cluster assignments for a single source.

This simple example demonstrates the effect of modal content on resulting frequency spectra and features that are utilized for source classification. It visualizes the

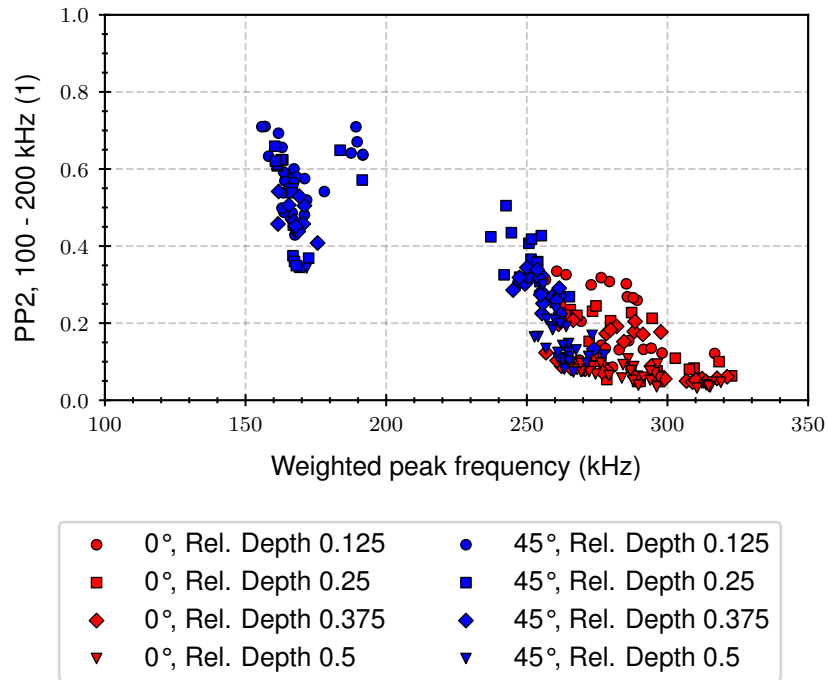


Figure 6.43: Weighted peak frequency (kHz) and partial power 2 between 100 and 200 kHz (1) of signals acquired at various source depths and source-to-sensor distances in the 0° and 45° direction. Evaluation window from 0 to 150  $\mu$ s.

bandwidth in acoustic fingerprint of a single source that can result from the variation of source depth and source-to-sensor distance and thereby highlights potential risks for misclassification.

### The influence of the evaluation window

The evaluation window can have a significant impact on resulting features. The results in the previous section were presented for a window that contained the primary wave packets of both:  $S_0$  and  $A_0$  modes. If this window size is reduced to contain only the  $S_0$  mode, resulting features are not affected by the  $A_0$  mode and its dependency from source depth and source-to-sensor distance. Consequently, cluster separation from figure 6.43 can be avoided through the new evaluation window as shown in figure 6.44.

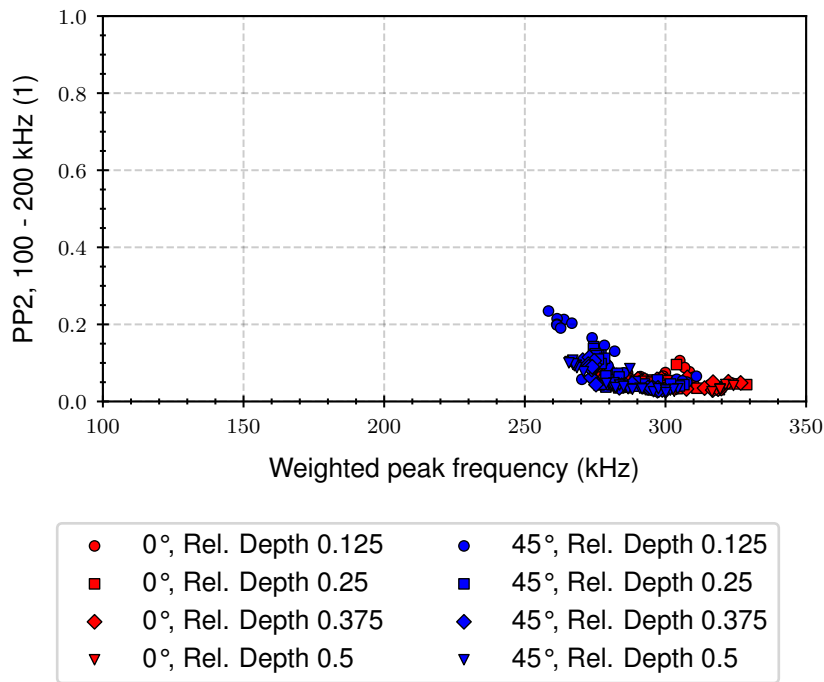


Figure 6.44: Weighted peak frequency (kHz) and partial power 2 between 100 and 200 kHz (1) of signals acquired at various source depths and source-to-sensor distances in the  $0^\circ$  and  $45^\circ$  direction. Evaluation window from 0 to 75  $\mu$ s.

## 6.2 Preliminary conclusion

The influence of source depth and source-to-sensor distance was investigated by means of artificial in-plane AE sources. It could be shown that the  $A_0$  amplitude reduces almost linear with increasing source depth up to the plane of symmetry. Due to characteristic frequency bands of the  $A_0$  and  $S_0$  modes, frequency spectra and resulting features were affected as well. This was especially true for the  $45^\circ$  direction. At a critical source depth position, peak frequency was shifted from the  $A_0$  dominated frequency band between 100 and 200 kHz to the  $S_0$  dominated frequency band between 250 and 350 kHz. This critical depth was found to decrease with increasing source-to-sensor distance due to the stronger attenuation of the  $A_0$  mode compared to the  $S_0$  mode. Consequently, two clusters were visible in the feature space as a result of the

influence of source depth and source-to-sensor distance. These clusters could be directly attributed to the fundamental wave modes and their dominant frequency bands. In order to avoid this cluster formation, the evaluation window had to be adjusted to only contain the  $S_0$  mode which was less affected by variations in source depth and source-to-sensor distance in this setup.

## 7 Main study: AE from damaging events

### 7.1 Concept

Specimens for the quasi-static tensile tests were prepared from the manufactured 4- and 16-ply laminates according to the procedure described in section 7.2. In order to alternate the depth position of the 0° and 90° layers, specimens were cut out in a way that the fibre orientation of the outer layer was either 0° or 90° and thereby either parallel or perpendicular to the loading direction in 0°. This resulted in four different specimen types that are denoted as  $(0^\circ/90^\circ)_s$ ,  $(90^\circ/0^\circ)_s$ ,  $(0^\circ/90^\circ)_{4s}$  and  $(90^\circ/0^\circ)_{4s}$  in the following.

The main study was divided into 3 stages according to the test matrix in table 7.12. Specific goals were assigned to each stage that built up on each other. The intention of the first stage was to define load limits for the stage 2 and 3 experiments, where acoustic emission analysis was incorporated in the setup. These load limits were necessary to avoid specimen failure and potential associated damage to the AE sensors. Stage 1 was therefore constrained to the determination of ultimate strengths of the 4- and 16-ply specimens.

Table 7.12: Test matrix for the quasi-static tensile tests in the scope of the main study

Stage	Name	Specimen	Goal
1	Mechanical Characterization	$(0^\circ/90^\circ)_s$ $(90^\circ/0^\circ)_s$ $(0^\circ/90^\circ)_{4s}$ $(90^\circ/0^\circ)_{4s}$	Define load limits for stage 2 and 3 experiments
2	Standard AE	$(0^\circ/90^\circ)_s$ $(90^\circ/0^\circ)_s$ $(0^\circ/90^\circ)_{4s}$ $(90^\circ/0^\circ)_{4s}$	Investigate the influence of - source depth and - source-to-sensor distance on signal characteristics
3	Modal AE	$(0^\circ/90^\circ)_s$ $(90^\circ/0^\circ)_s$	Investigate the influence of source depth on modal content and signal characteristics

At stages 2 and 3, damaging events were systematically initiated in different depths and distances to the AE sensors in order to characterize variations in their acoustic emission signature with respect to these parameters. The mid section of the specimen edge was thereby observed with a camera during the test in order to visualize and validate these damaging events. Digital image correlation (DIC) was utilized in this context to ease the detection of TMC in the 90° layers. The structure of the layer itself served as a "quasi-random" pattern for the tracking of local displacement.

Stages 2 and 3 differed mainly in the AE setup and evaluation methodology. At stage 2, AE analysis was accomplished with a state of the art setup using wideband AE sensors. The influence of source depth and source-to-sensor distance were investigated for all types of 4- and 16-ply specimen at this stage. For stage 3 experiments, an advanced setup was developed that provided additional information on the modal character of perceived acoustic emissions. This way, the influence of source depth on modal content and resulting signal characteristics could be studied in more detail. Experiments were limited to the 4-ply specimens at this stage, where the number of symmetric and antisymmetric wave modes could be limited to the  $A_0$  and  $S_0$  modes for frequencies up to 1500 kHz.

## 7.2 Specimens

The specimen geometry for the quasi-static tests is shown in figure 7.45. The specimens show a length of 315 mm and an original width of 28 mm that narrows down to 25 mm in the mid section following a Bézier type curve. The tapered design allowed to focus the evaluation to the mid section where damaging events should be generated predominantly due to the smaller cross-section and the higher resulting stresses. A CNC milling machine was utilized to cut out the specimens from the manufactured plates. To improve the surface quality, specimen edges were grinded manually with fine abrasive sandpaper (1200 grit) afterwards. For the experiments of stages 2 and 3, a section of  $\pm 5$  mm from the centre of the specimen was prepared further with 2500 and 4000 grit sandpaper to create a polished edge that could be traced with digital image correlation during mechanical testing.

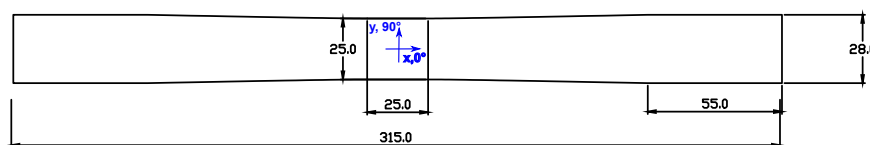


Figure 7.45: Specimen geometry for the quasi-static tensile tests. Dimensions are given in millimeters.

End tabs had to be installed for some specimen types to reduce the chance for early failure in the gripping area. For the  $(0^\circ/90^\circ)_s$  and  $(90^\circ/0^\circ)_s$  laminates, the thin gripping areas were reinforced with GFRP tabs (28 x 50 x 1 mm) with  $\pm 45^\circ$  layup to promote a smooth load transfer. Tabs were bonded to the specimen surface with two-component epoxy adhesive. Among the 16-ply specimens, tabs had to be utilized for the  $(0^\circ/90^\circ)_{4s}$  specimens as well to protect the outer  $0^\circ$  layer from early failure. Kraft paper tabs (180 g/m<sup>2</sup>) were bonded to the specimen gripping area with super glue in this case.

Prior to testing, the specimens were dried to create a common reference state. This

was accomplished in an oven at 105°C where specimens were stored for 72 hours to reach a stable condition where the relative change in mass within 24 hours was below 0.01%. Afterwards, specimen remained in a desiccator with dry environment to stabilize the condition until testing.

Specimen thickness was measured at 3 points in the 25 mm long centre section of the specimen with an outside micrometer. Specimen width was measured at the same positions with a calliper. The respective average values were taken for the calculation of the nominal tensile stress. For every stage from the test matrix in table 7.12, five specimens of each type were prepared this way. This resulted in a total of 50 specimens.

### 7.3 Environmental conditions

Temperature and relative humidity were recorded at the beginning of each test through all stages. A statistical overview on the average values, standard deviations as well as minima and maxima over all stages can be found in table 7.13.

Table 7.13: Statistical overview on environmental conditions during quasi-static tensile tests

Parameter	$N$	$\mu$	$\sigma$	Min	Max
Temperature (°C)	50	21.4	0.5	20.0	22.9
Rel. humidity (%)	50	41.5	6.3	32.5	56.8

## 7.4 Experimental setup: General

### 7.4.1 Quasi-static testing

Quasi-static testing was realized with a Zwick 1474 universal testing machine. Specimens were clamped with custom hydraulic grips, resulting in a free length of 215 mm. Testing speed was controlled by the machine head and set to 1 mm/min. The applied force was measured with a 100 kN load cell. The axial strain was measured by the machine head at stage 1 and by DIC of the specimen edge at stages 2 and 3. Static preloads of 50 MPa at stage 1 and 10 MPa at stages 2 and 3 were selected to account for settling effects.

### 7.4.2 Acoustic emission analysis

Acoustic emission analysis was carried out with the Vallen AMSY 5 system.

Two different types of broad band AE sensors were chosen for the experiments. For

stage 2, acoustic waves were captured solely with VS900-M sensors from Vallen systems. With an aperture of around 19 mm, the sensor offers a high sensitivity in the frequency band between 100 and 900 kHz where damaging events in FRP materials are commonly detected. Its response is characterized by two peaks at 190 and 350 kHz with anti-resonances at 200 and 400 kHz. The full frequency characteristics can be found online [198].

The VS 900-M sensors were also incorporated in the setup of stage 3 experiments. However, they were only used as guard sensors while source localization and identification was realized with the KRNBB-PCP sensors from KRN Services at this stage. With their small aperture and flat response in the frequency range between 100 kHz and 2.5 MHz, they were suitable for source identification with the additional option of performing modal analysis. More details on sensor characteristics can be found online [199].

Sensor signals were amplified with AEP4 amplifiers from Vallen systems. The gain was set to 34 dB for the VS900 sensors and to 40 dB for the KRNBB-PCP sensors.

### **7.4.3 Specimen edge observation**

The polished specimen edge was observed with a CP90-25-M/C-72 camera from Optronis at stages 2 and 3 during testing. With a sensor size of 5120 by 5120 pixels it allowed to capture 72 frames per second at full frame resolution. The Makro-Symmar 120/5.6 lens was installed along with a 200 mm long extension tube, to image the specimen edge on the 23.04 by 23.04 mm detector. Illumination was realized with Proxistar LED lights to reduce temperature rise of the specimen during testing. Illumination was optimized for the 90° oriented layers where transverse matrix cracking would take place. Frame grabbing was controlled through an external signal that defined the frame rate. This signal was triggered through the start of the test and was fed as well into the acoustic emission system to synchronize the systems. The active detector size of the camera was constrained to 5120 by 1000 pixels while specimen edge deformation was captured at 5 frames per second within the 10 mm long polished section in the centre of the specimen. The geometrical resolution was at around 3  $\mu\text{m}/\text{pixel}$ .

## **7.5 Experimental setup: Specific**

### **7.5.1 Stage 2: Standard AE**

The experimental setup for stage 2 is shown in the figures 7.46 (a) and (b). Four wide band VS900-M sensors were attached to the specimen with spring loaded clamps at the positions shown in figure 7.46 (a). Silicon grease was utilized as coupling agent between the sensors and the specimen. The sensors were placed asymmetrically to the



centre of the specimen to support the creation of different source-to-sensor distances. The two inner sensors (1 and 2) were used for source localization and identification whereas the outer sensors (3 and 4) served as guard sensors to filter out noise from the gripping area. Each pair of sensors, on either side of the specimen ((1,3) and (2,4)), was, in turn, utilized to identify the triggering waves modes and characterize their distribution of group velocities.

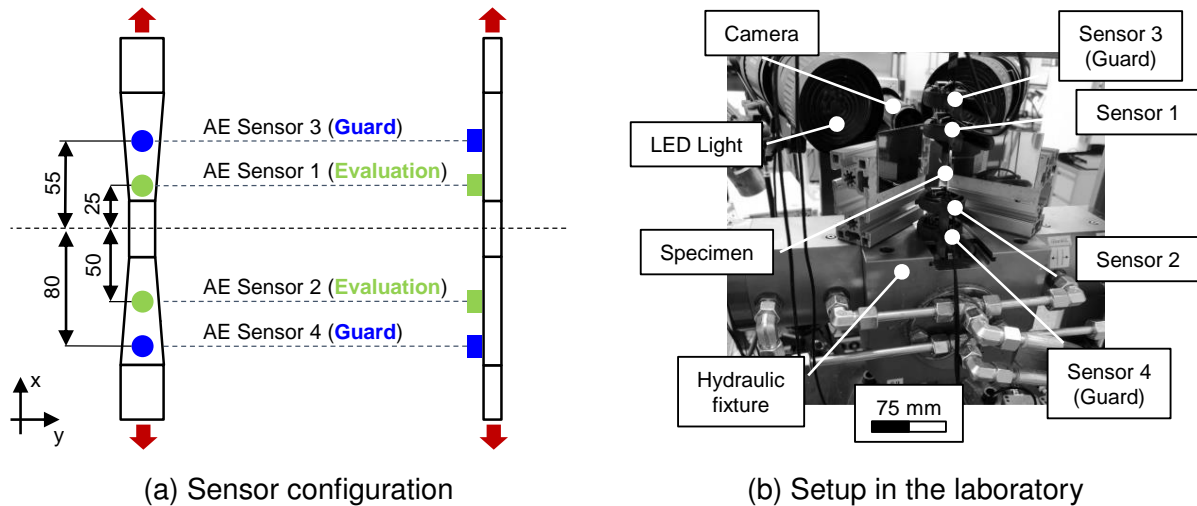


Figure 7.46: Experimental setup for stage 2 experiments.

Figure 7.46 (b) shows a closeup from the setup in the laboratory where camera and LED lights can be seen along with the specimen and the attached AE sensors. The mirrors were utilized for passive thermography measurements that are not part of this thesis.

The acquisition settings for the acoustic emission analysis are summarized in table 7.14. Each sensor was triggered individually with a threshold crossing.

Table 7.14: Vallen AMSY 5 acquisition parameters for stage 2 experiments

Property	Value
Sample rate (MS/s)	10
Samples per set (1)	4096
Duration per set ( $\mu$ s)	409.6
Pre-trigger samples (1)	800
Threshold (dB)	55
Duration discrimination time ( $\mu$ s)	100
Rearm time ( $\mu$ s)	100

Prior to each test, sensor coupling was validated by pulsing consecutively with all VS900-M sensors while the specimen was under the static preload of 10 MPa.

### 7.5.2 Stage 3: Modal AE

The fixture in figure 7.47 was designed and manufactured for stage 3 experiments. Similar to the fixture from section 5.2, the design allowed to position two sensors of a pair on opposite sides of the specimen so that they share a common axis (black horizontal dashed line). This way, the symmetric and antisymmetric wave portions could be extracted and analysed individually. Sensor pairs could be positioned on the upper and lower half of the specimen. The clamping force of each sensor could thereby be adjusted individually through the preload of the compression springs. In order to reduce vibrations from the surroundings, the fixture was decoupled from the hydraulic clamping system by rubber pads. The mirrors were utilized for passive thermography measurements that are not part of this thesis.

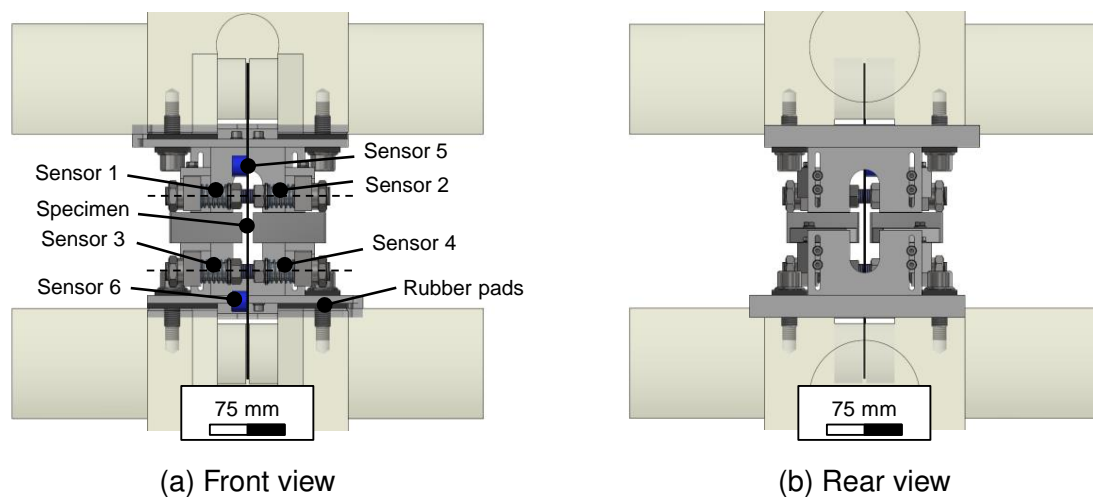


Figure 7.47: Front (a) and rear view (b) of the fixture for stage 3 experiments.

The fixture was set up to achieve the same asymmetric sensor configuration as in stage 2 with the only exception that the inner evaluation sensors were replaced by two evaluation pairs (see figure 7.48 (a)). Each pair ((1,2) and (3,4)) consisted of two KRNBB-PCP sensors that were mounted to the fixture and aligned to share a common horizontal axis. Two additional VS900-M sensors (5 and 6) were attached with spring loaded clamps to the positions shown in figure 7.48 (a) to filter out noise from the gripping area. Localization and identification of acoustic events were based on the four inner evaluation sensors (1,2,3 and 4).

Figure 7.48 (b) shows a closeup from the setup in the laboratory where the fixture, the specimen, the camera and the sensors can be seen.

The acquisition settings for the acoustic emission analysis are summarized in table 7.15. The outer guard sensors as well as each sensor pair were triggered individually through a threshold crossing. However, sensors of a pair were grouped together and triggered simultaneously to share the same time axis. Due to the differences in sensi-

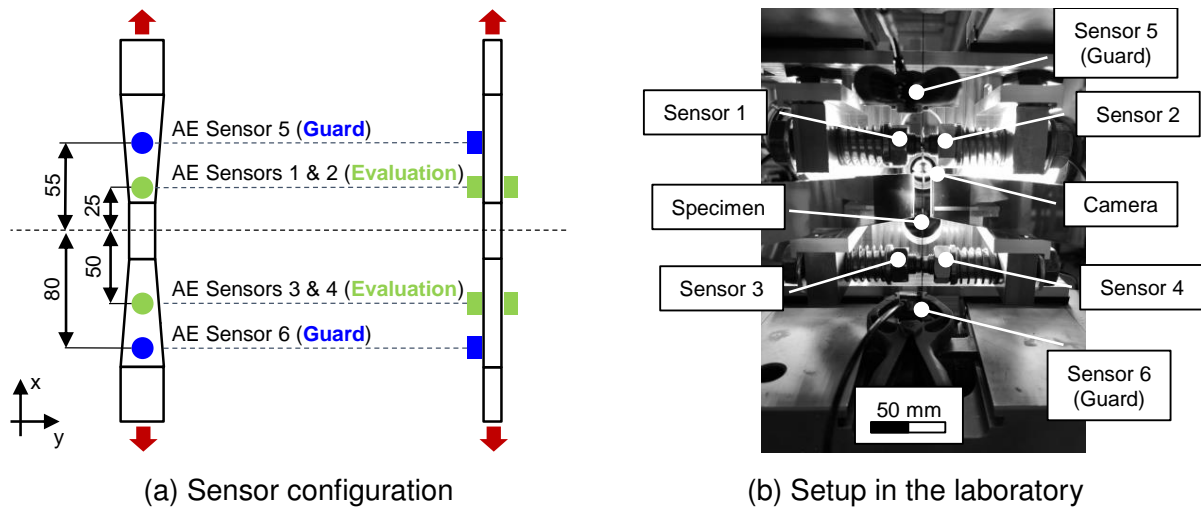


Figure 7.48: Experimental setup for stage 3 experiments.

tivity, the threshold values for the VS900-M (55 dB) and KRNBB-PCP sensors (45 dB) were adjusted accordingly.

Table 7.15: Vallen AMSY 5 acquisition parameters for stage 3 experiments

Property	Value
Sample rate (MS/s)	10
Samples per set (1)	4096
Duration per set ( $\mu$ s)	409.6
Pre-trigger samples (1)	800
Threshold (dB)	45 (55)
Duration discrimination time ( $\mu$ s)	100
Rearm time ( $\mu$ s)	100

Prior to each test, sensor coupling and alignment was validated by pulsing with the outer VS900-M sensors while the specimen was under the static preload of 10 MPa.

## 7.6 Evaluation methodology

### 7.6.1 Stage 2: Standard AE

The evaluation of acoustic emission data was accomplished in the following seven steps:

1. **Grouping hits to events:** Whenever a sensor is triggered through a threshold crossing, an acoustic hit is detected. These hits at individual sensors can be grouped to single AE events that caused them. This was accomplished by defining a tolerance for the time difference of consecutive hits of an event. This

tolerance can be estimated based on the slowest group velocity of present guided waves modes and the maximum difference in source-to-sensor distance between sensors. Assuming a minimum group velocity of 1550 m/s, the time difference between the first and last hit of an event should not exceed 87  $\mu\text{s}$  for the sensor configuration in figure 7.46 where the position of sensors 3 and 4 define the maximum distance between sensors. With a safety factor of 1.5, the tolerance was set to 130  $\mu\text{s}$ . Following this procedure, each hit can be linked to a corresponding event. Depending on the order of triggering, one can distinguish between the 1<sup>st</sup>, 2<sup>nd</sup>, 3<sup>rd</sup> and 4<sup>th</sup> hit sensor. Their individual time signals were analysed in the next steps to determine the location of the event and characterize its source. Events that originated from the gripping area were excluded from further analysis. For these events, one of the outer sensors (3,4) represented the first triggering sensor. Analysis was constrained further to events that triggered at least the evaluation sensors (1,2) since event localization was based on the difference in times of arrival between these sensors.

2. **Defining the evaluation window:** The evaluation window defines the part of the signal that is considered for feature extraction. This window has to be chosen carefully due to its strong impact on features and classification results (see end of section 6.1.3). In the first step of defining this window, the threshold based signal onset was dynamically adjusted through the Hinkley picker (see equation 2.10 and 2.11). As energy based criteria, the Hinkley picker allowed a more reliable determination of signal onset than the AIC or common threshold based methods. Furthermore, early threshold crossings due to the increasing noise level during the test could be corrected within the recorded 4096 signal samples. In the next step, the window size was estimated. In order to assess the individual contribution of symmetric and antisymmetric wave modes, the signal window should contain at least the primary wave packets of  $A_0$  and  $S_0$  mode. By constraining the evaluation to the area between the two inner sensors (1,2), the maximum source-to-sensor distance could be limited to 75 mm. Consequently, the maximum time difference between  $S_0$  and  $A_0$  mode was estimated to be around 40  $\mu\text{s}$  based on the corresponding group velocities of 1550 and 6900 m/s. Allowing a wave packet length of 20  $\mu\text{s}$ , the window size was set to 60  $\mu\text{s}$ . However, since either  $A_0$  or  $S_0$  could trigger the signal onset, the 60  $\mu\text{s}$  defined the recorded time span prior to and after the signal onset, resulting in a total window size of 120  $\mu\text{s}$ .
3. **Adjusting the time of arrival:** The threshold based times of arrival had to be corrected in the next step so that arrival times at both evaluation sensors would be based on the same mode and the same frequency. This was accomplished through band-pass filtering and subsequent determination of signal onset through the Hinkley picker. A 2<sup>nd</sup> order Butterworth filter was chosen and applied twice,

forward and backward, in order to eliminate phase shifts. For the  $(0^\circ/90^\circ)_s$  laminates, the frequency band between 20 and 250 kHz was chosen as a reference because modal content could be limited to the  $A_0$  mode in this band. The sensors resonance at 190 kHz thereby promoted the existence of this frequency band in the measured signals. A different approach had to be followed for the  $(0^\circ/90^\circ)_{4s}$  laminates, where the  $S_0$  mode became more dominant in the lower frequencies (see figure 5.31). In this case, the  $S_0$  mode had to be selected as the reference. With a band-pass filter between 125 and 375 kHz, the  $S_0$  mode was found to be identified reliably through the Hinkley picker. Both sensor resonances at 190 and 350 kHz thereby supported the presence of this frequency band in the measured signals. The alpha value for the Hinkley criteria was set to 5 for all instances.

4. **Visualizing and characterizing the triggering wave modes:** The triggering wave modes along with their distribution in group velocities could be identified during mechanical testing with the selected sensor configuration. This was achieved by evaluating the difference in arrival times among the sensor pairs (1,3) and (2,4), for every AE event registered. The time of arrival was thereby determined by following the methodology from the previous section. This approach allowed an inline characterization of wave propagation where differences between specimens (e.g. thickness, fibre direction), anisotropy, near field effects and changes in elastic properties due to continuous degradation could be statistically accounted for. From the acquired group velocities only the ones with a value smaller than 10,000 m/s were kept since group velocities of the  $A_0$  and  $S_0$  mode in the manufactured laminates were found to be below this value (see figures 5.33). In order to identify groups in the data that could be attributed to triggering wave modes, Gaussian Mixed Models (GMM) with a full covariance matrix were fitted to the resulting distributions of group velocities. For the determination of the number of gaussians, a wrapper approach was followed in combination with the Akaike information criterion (AIC) as figure of merit. With the maximum likelihood function  $L$  for the model and the number of estimated parameters  $p$ , the AIC can be computed according to equation 7.24

$$AIC(p) = 2 \cdot p - 2 \cdot \ln(L) \quad (7.24)$$

As one method for model selection, the AIC provides a measure to optimize likelihood while penalizing model complexity with increasing number of Gaussians. The selection was based on the knee in the course of the AIC score. With the extracted information, the methodology for the determination of time of arrival was adjusted iteratively to identify appropriate frequency bands for source localization.

5. **Localizing events:** One dimensional localization along the specimen length axis was realized by evaluating the differences in arrival times between the evaluation sensors 1 and 2. With the average group velocity of the most prominent Gaussian distribution from the previous section, source position was estimated through equation 2.12.
6. **Extracting characteristic features:** Feature extraction was limited to prominent features from the frequency domain that have been frequently utilized for source discrimination in FRP. These include the peak frequency  $f_p$ , frequency centroid  $f_c$ , weighted peak frequency  $f_{wp}$  as well as partial powers ( $PP_1$ : 0-250 kHz,  $PP_2$ : 250-500 kHz,  $PP_3$ : 500-1000 kHz,  $PP_4$ : 1000-1500 kHz). For the extraction of these features, the spectrum was constrained to the frequency band between 0 and 1500 kHz. Details on the calculation of these features, can be found in [81].
7. **Identifying clusters in the feature space:** Cluster analysis was realized with GMM with either shared or full covariance matrix. These could be fitted to the various cluster shapes that could be found in the feature space. Before clustering, each feature of a data set was standardized to show unit variance and zero mean. If not otherwise stated, the number of Gaussians was determined based on a wrapper approach with the AIC (see equation 7.24) as figure of merit.

### 7.6.2 Stage 3: Modal AE

The evaluation methodology for stage 3 followed the concept from stage 2 with the following exceptions:

- Evaluation was constrained to the 4-ply specimens as already explained in section 7.1.
- Analysis was constrained to events that were triggered by one of the evaluation sensors (1,2,3 or 4) first to filter out noise from the gripping area. Furthermore, only events were considered that triggered both sensor pairs ((1,2) and (3,4)) so that source localization could be realized.
- Signals were filtered with a 2<sup>nd</sup> order Butterworth band-pass filter between 20 and 2000 kHz prior to analysis. The filter was applied twice, forward and backward to eliminate phase shifts.
- The distribution of group velocities of the triggering wave mode was not determined during the test. The underlying group velocity was extracted from stage 2.
- Source localization was realized with one sensor of each sensor pair.

## Challenges

The goal of the setup in figure 7.48 was to extract the symmetric and antisymmetric portions from the measurement signals and analyse their individual characteristics. In the scope of section 5.2 experiments, symmetric and antisymmetric signals could be extracted by simple addition or subtraction of opposing sensor signals. Differences in the sensitivity of opposing sensors could be compensated by adjusting signal amplitudes based on the ratio of their corresponding maximum amplitudes. This procedure worked well for the artificial burst-type signals with a major central frequency. For the broad band AE signals that were captured during mechanical testing, this methodology could not be applied because sensitivities for the symmetric and antisymmetric wave modes varied between sensors of a pair. Since both type of modes are detected at different frequency bands, the sensitivity can vary between symmetric and antisymmetric signal portions due to differences in the frequency response of opposing sensors that directly result from manufacturing tolerances. Simple normalization of signal amplitude by the maximum was therefore not sufficient.

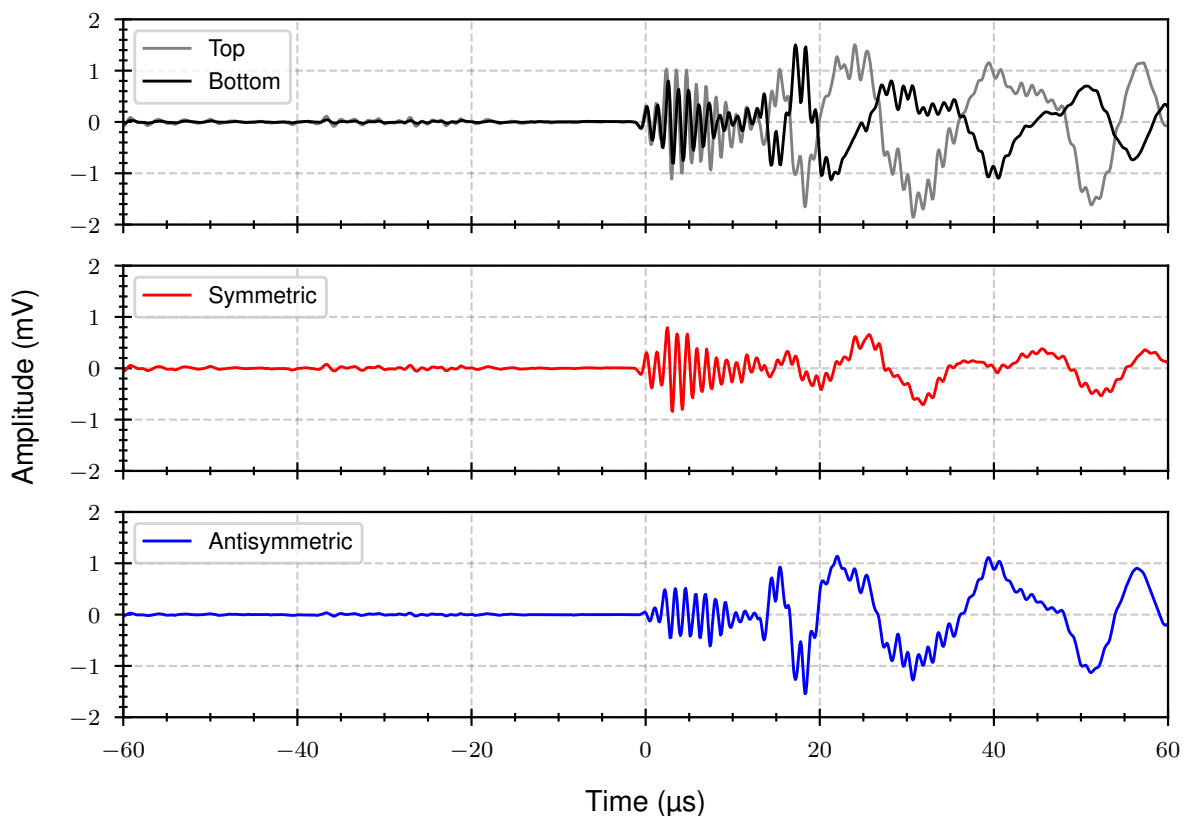


Figure 7.49: Top and bottom sensor signals and resulting symmetric and antisymmetric signal portions.

Figure 7.49 demonstrates this effect with an example. It shows the time signals from an acoustic event that were captured by two opposing sensors (top and bottom). As can be seen, there are differences between the amplitudes of the signal portions

that are in phase (symmetric) in comparison to those that are  $180^\circ$  shifted in phase (antisymmetric). Consequently, simple addition or subtraction of these signals did not lead to pure symmetric or antisymmetric signals.

As an alternative, the underlying type of mode - symmetric or antisymmetric - was identified by evaluating the phase difference  $\phi$  between the signals of opposing sensors. By applying the FFT to each time signal, this phase difference was determined as a function of frequency  $f$  based on the complex Fourier coefficients of top ( $F_T(f)$ ) and bottom sensor ( $F_B(f)$ ) according to

$$\phi(f) = \arctan \left( \frac{F_T(f)}{F_B(f)} \right). \quad (7.25)$$

The peak frequency was thereby selected as the evaluation frequency to identify the corresponding mode that caused it. As an example, figure 7.50 shows the time signals of opposing sensors from two events where the underlying mode was found to be either symmetric (a) or antisymmetric (b). The corresponding absolute phase differences were determined to  $0.07\pi$  and  $0.99\pi$  at the respective peak frequencies of around 600 and 200 kHz.

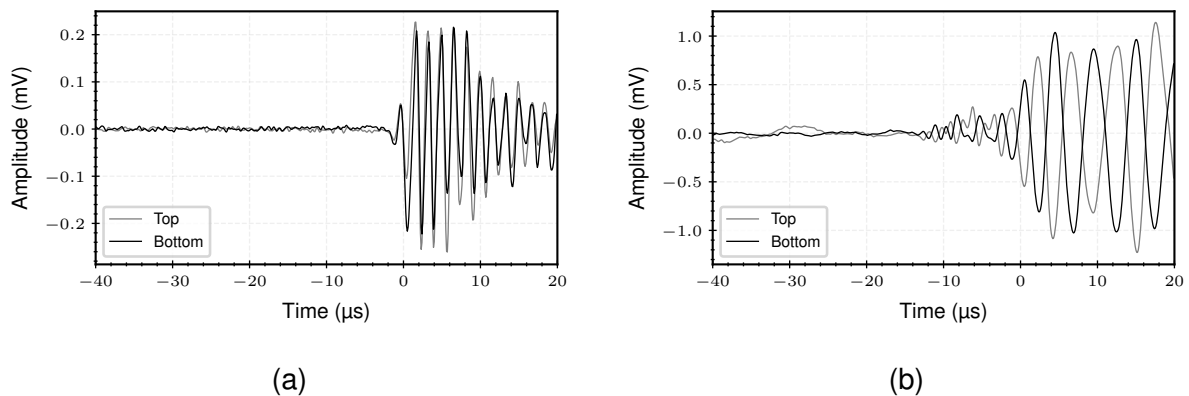


Figure 7.50: Time signals of top and bottom sensors of a pair for an event with symmetric (a) and antisymmetric (b) signal portions. The corresponding absolute phase differences were determined to  $0.07\pi$  and  $0.99\pi$  at the respective peak frequencies of around 600 and 200 kHz.

As shown in figure 7.50, this technique can be successfully applied if the evaluation window contains a single mode. The evaluation methodology had to be adjusted accordingly.

### 7.6.3 Digital Image Correlation

Captured image stacks of the specimen edge were analysed using GOM Correlate software. The structure within the  $90^\circ$  oriented layers thereby served as "quasi-random"



pattern to track the local deformation during the test. As an example, figure 7.51 shows the cross section of a  $(0^\circ/90^\circ)_{4s}$  coupon specimen with area components in the  $90^\circ$  oriented layers. The axial strain in the loading direction is shown color coded. The black marks constrain the area of evaluation that spans around  $\pm 5$  mm from the centre of the specimen. Depending on the quality of the polished edge, the size and distance between tracked area units (facets) had to be optimized individually.

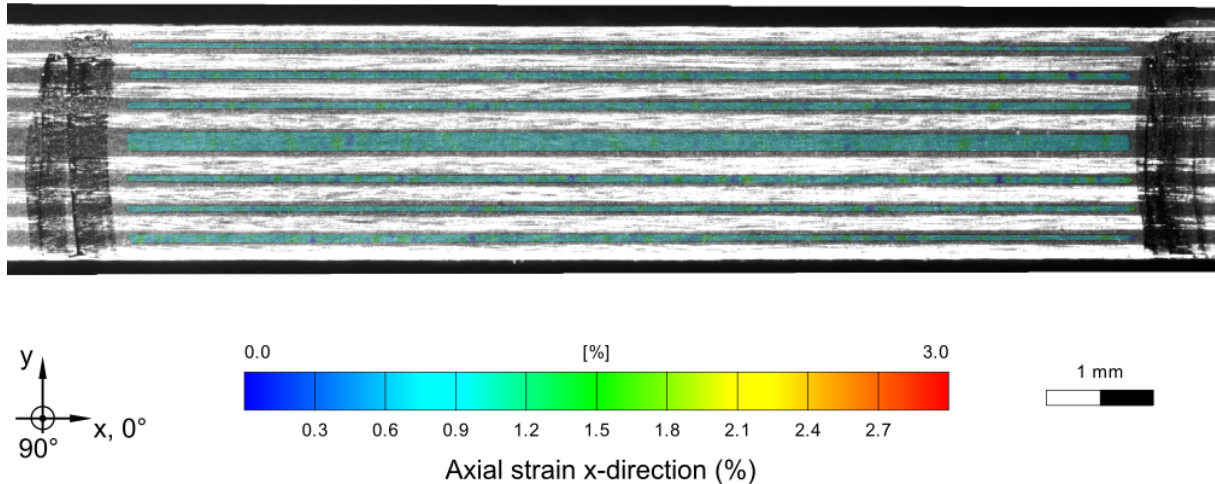


Figure 7.51: Cross-section of a  $(0^\circ/90^\circ)_{4s}$  coupon specimen where DIC was utilized to track local displacement in the  $90^\circ$  oriented layers. The axial strain (%) in the x-direction is shown color coded.

DIC was utilized

- to validate the Young's modulus of the manufactured specimens and
- to determine the stress and strain level at which transverse matrix cracks in the  $90^\circ$  layer appeared.

For the determination of Young's modulus  $E_x$ , the axial strain was extracted from a single  $90^\circ$  layer, where local strain was averaged and tracked as a function of applied stress in the  $\pm 5$  mm window in the centre of the specimen. Young's modulus was determined by a linear fit of stress and strain data between 0.05 and 0.25% axial strain according to DIN EN ISO 527-4.

TMC detection was based on the fact that these cracks lead to an increase in local strain. Figure 7.52 shows a cross section of a  $(0^\circ/90^\circ)_s$  coupon specimen where two transverse matrix cracks caused a visible contrast in the local axial strain.

The crack detection was accomplished by analysing cross-sections of the area components inside the  $90^\circ$  layers. Figure 7.53 gives an example for such a cross section

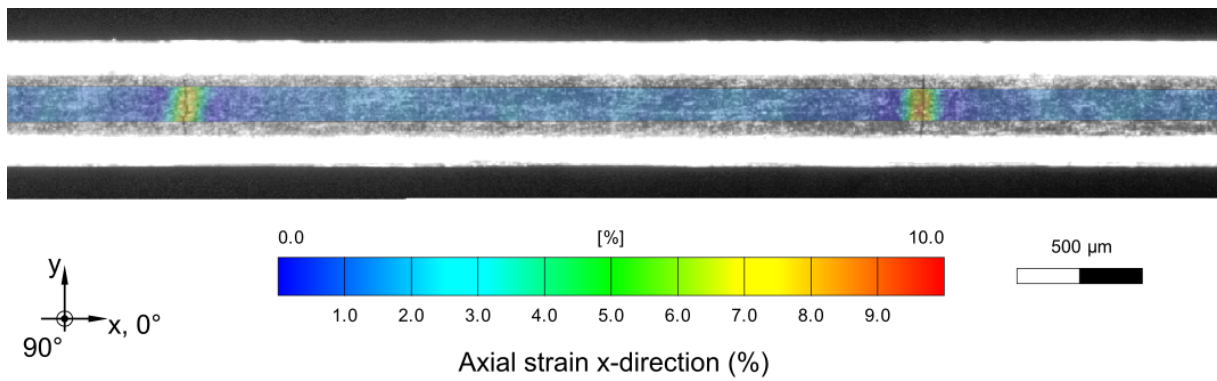


Figure 7.52: Cross-section of a  $(0^\circ/90^\circ)_s$  coupon specimen where DIC was utilized to identify transverse matrix cracks in the  $90^\circ$  oriented layers. The axial strain (%) in the x-direction is shown color coded.

that maps tensile strain (%) against the relative x position (mm) from the centre of the specimen. A total of four cracks can be seen that are characterized by a local increase in axial strain of around 5 to 7 % while the average strain level is around 1 %. A software was written to identify these cracks automatically and assign the corresponding global stress and strain level to them. However, each potential crack had to be reviewed manually in order to avoid false interpretation of artifacts that temporarily appeared as peaks in the strain data. These artifacts generally develop from disturbances in the recognition and assignment of facets.

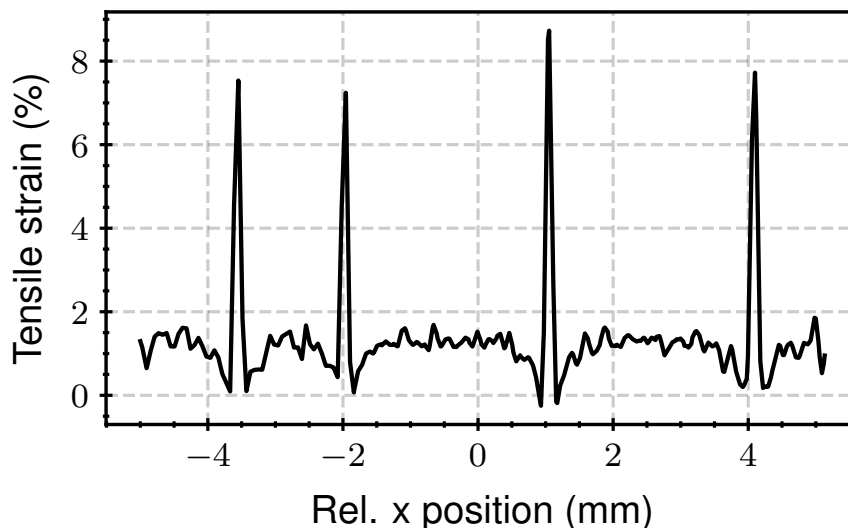


Figure 7.53: Tensile strain (%) in x-direction as a function of relative x position (mm) from the centre of the specimen.

## 7.7 Discussion & Results

### 7.7.1 Tensile strength

The nominal tensile stress (MPa) as a function of machine head displacement (mm) can be found for the 4- and 16-ply specimens in the figures 7.54 (a) and (b) respectively. The tensile stress was determined based on the average cross-section of the specimen in the 25x25 mm centre part (see figure 7.45) that was measured prior to testing. Specimens with  $(0^\circ/90^\circ)_s$  and  $(0^\circ/90^\circ)_{4s}$  layup are shown in red while  $(90^\circ/0^\circ)_s$  and  $(90^\circ/0^\circ)_{4s}$  specimens are shown in blue.

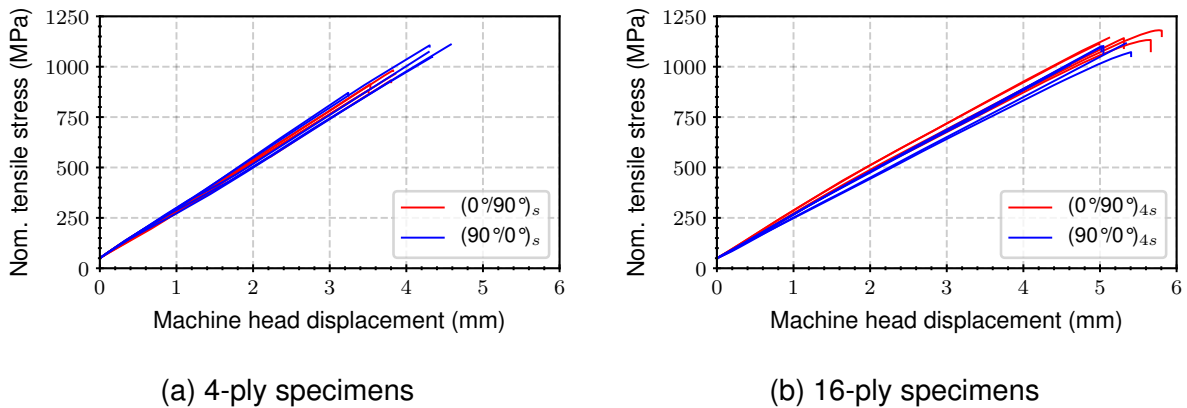


Figure 7.54: Nominal tensile stress (MPa) versus machine head displacement (mm) for the  $(0^\circ/90^\circ)_s$  and  $(90^\circ/0^\circ)_s$  (a) as well as  $(0^\circ/90^\circ)_{4s}$  and  $(90^\circ/0^\circ)_{4s}$  specimens (b).

Results on the tensile strength are summarized in table 7.16. None of the 4-ply specimens showed a valid failure in the centre part. Despite the tapered geometry and the installation of bonded tabs, the final failure of these specimens was a result of failure close to the gripping area as can be seen from the pictures of broken samples in appendix K. Tensile strength values were therefore generally lower and showed higher scattering compared to the 16-ply specimens.

Table 7.16: Statistical overview on the tensile strengths  $\sigma_m$  (MPa) derived from quasi-static tensile tests in the  $0^\circ$  direction

Layup	$N$	$\mu$	$\sigma$	$Min$	$Max$	No. valid failure
$(0^\circ/90^\circ)_s$	5	935.6	35.4	883.5	982.4	0
$(90^\circ/0^\circ)_s$	5	1041.9	88.5	870.7	1110.3	0
$(0^\circ/90^\circ)_{4s}$	5	1142.8	21.7	1114.7	1181.0	5
$(90^\circ/0^\circ)_{4s}$	5	1080.8	38.1	1010.1	1116.3	5

Nevertheless, based on these tensile strength values, the maximum stresses in table 7.17 were defined for stage 2 and 3 experiments where any type of final failure should

be avoided to protect the AE sensors from potential damage.

Table 7.17: Tensile stress limits (MPa) for stage 2 and 3 experiments

Layup	Stress limit (MPa)
$(0^\circ/90^\circ)_s$	875
$(90^\circ/0^\circ)_s$	950
$(0^\circ/90^\circ)_{4s}$	1050
$(90^\circ/0^\circ)_{4s}$	950

### 7.7.2 Young's modulus

The tensile stress versus strain (based on DIC) curves for the determination of Young's modulus  $E_x$  can be found for the 4- and 16- ply specimens in the figures 7.55 (a) and (b) respectively. Specimens with  $(0^\circ/90^\circ)_s$  and  $(0^\circ/90^\circ)_{4s}$  layup are shown in red while  $(90^\circ/0^\circ)_s$  and  $(90^\circ/0^\circ)_{4s}$  specimens are shown in blue.

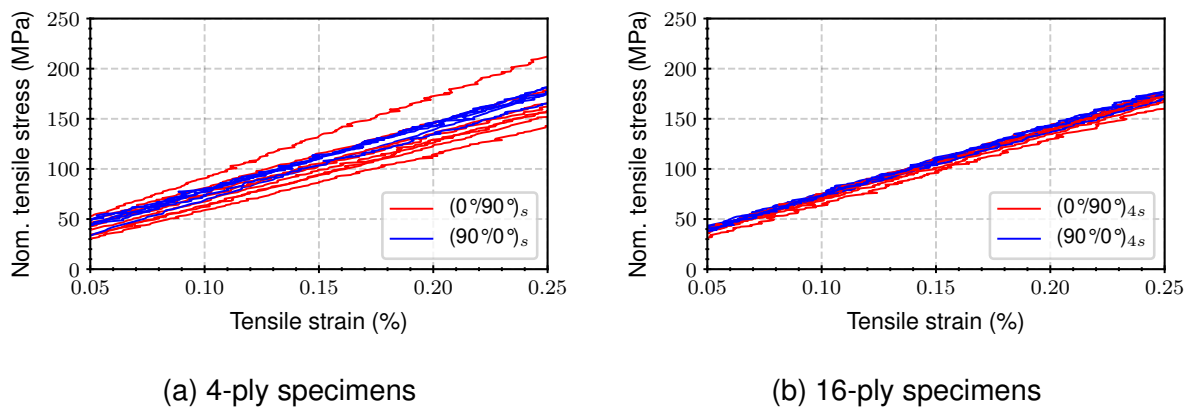


Figure 7.55: Nominal tensile stress (MPa) versus tensile strain (%) for the determination of Young's modulus  $E_x$  for the  $(0^\circ/90^\circ)_s$  and  $(90^\circ/0^\circ)_s$  (a) as well as  $(0^\circ/90^\circ)_{4s}$  and  $(90^\circ/0^\circ)_{4s}$  specimens (b). Strain data is based on DIC of the specimen edge.

Experimental results for the Young's moduli  $E_x$  of the cross-ply laminates are summarized in table 7.18. Due to variations in the quality of the polished edge, strain data could not be reliably recorded from all specimens. The number of specimens that were incorporated in the evaluation therefore differs between layups. Similar average values could be observed for the 4- and 16- ply specimens. However, higher standard deviations were found for the  $(0^\circ/90^\circ)_s$  and  $(90^\circ/0^\circ)_s$  specimens. This could be due to the small amount of  $0^\circ$  layers. In contrast to the 16-ply specimens, any misalignment of fibres or variation in fibre volume content of a single  $0^\circ$  layer can already have a strong impact on the resulting stiffness of the whole specimen.

Table 7.18: Statistical overview on Young's moduli  $E_x$  (GPa) derived from quasi-static tensile tests in the  $0^\circ$  direction

Layup	$N$	$\mu$	$\sigma$	Min	Max
$(0^\circ/90^\circ)_s$	8	62.7	7.5	55.8	80.2
$(90^\circ/0^\circ)_s$	6	66.1	3.5	61.4	70.2
$(0^\circ/90^\circ)_{4s}$	8	66.7	1.2	65.1	68.6
$(90^\circ/0^\circ)_{4s}$	5	67.4	2.2	64.5	69.8

Based on the elastic properties that were derived in the scope of section 5.1.1, a tolerance window for the theoretical Young's modulus of the cross-ply laminates can be determined using CLT [30]. This way, the theoretical elastic properties can be validated with the experimental values. For a balanced  $(0^\circ/90^\circ)$  cross-ply laminate follows

$$E_x = 0.5 \cdot \frac{E_{\parallel}}{1 - \nu_{\perp\parallel} \cdot \nu_{\parallel\perp}} + 0.5 \cdot \frac{E_{\perp}}{1 - \nu_{\perp\parallel} \cdot \nu_{\parallel\perp}} \quad (7.26)$$

with the Young's moduli  $E_{\parallel}$  and  $E_{\perp}$  as well as the Poisson ratios  $\nu_{\parallel\perp}$  and  $\nu_{\perp\parallel}$  from the single layer. With the respective properties from table 5.7, the Young's modulus  $E_x$  should be between 69.7 to 75.1 GPa. However, the measured values from table 7.18 are below this tolerance window. Deviations could be due to miss-alignments of fibres resulting from the manual layup process. Nevertheless, dispersion curves from figure 5.19 are likely to be shifted as a result of lower in-plane stiffness. This should mainly affect the properties of the  $S_0$  mode. However, deviations of less than 10% in  $E_{\parallel}$  do not significantly affect the dispersion properties of the  $S_0$  mode as shown for the different fibre volume contents in figure 5.18 (b).

### 7.7.3 Transverse matrix cracking

Before discussing the experimental results, theoretical calculations on the onset of transverse matrix cracking are presented first.

#### Theoretical

The critical stress for transverse matrix cracking can be calculated using CLT in combination with Puck's failure theory. Assuming constant strain between all plies in the loading direction, the critical stress  $\sigma_{x_{TMC}}$  for TMC can be determined by

$$\sigma_{x_{TMC}} = \frac{E_x}{E_{\perp}} \cdot R_{\perp}^+ \quad (7.27)$$

where  $E_x$  represents the Young's modulus of the laminate in x-direction,  $E_{\perp}$  the Young's modulus of the single layer perpendicular to the fibre direction and  $R_{\perp}^+$  denotes

the fracture strength of the single layer under tensile load as a result of stresses acting perpendicular to the fibre direction [25, 30]. For simplicity, laminate types are grouped together for the calculation. The measured Young's Modulus  $E_x$  in loading direction is therefore averaged over all specimens. Regarding  $E_{\perp}$ , the configuration with the average fibre volume content from table 5.7 was chosen. The fracture strength  $R_{\perp}^+$  was found to be 82 MPa [192]. With these assumptions, the critical stress for TMC should be around 628 MPa.

However, residual stresses from the curing process can potentially modify this window. As a result of the different coefficients of thermal expansion of fibre and matrix material, residual tensile stresses can arise perpendicular to the fibre direction. These stresses can be determined based on the coefficients of thermal expansion  $\alpha_{\perp}$  and  $\alpha_{\parallel}$  of the single layer and the temperature difference  $\Delta T$  between the curing temperature (180°C) and the testing temperature (21°C). Since the parameters  $\alpha_{\perp}$  and  $\alpha_{\parallel}$  are unknown, they have to be determined first following the theoretical models in [30]. These models require, in turn, the coefficients of thermal expansion of the matrix material  $\alpha_m$  as well as of the fibre material parallel ( $\alpha_{f\parallel}$ ) and perpendicular ( $\alpha_{f\perp}$ ) to the fibre direction. For Cycom 977-2, the coefficient of thermal expansion could be extracted from [200] to  $24.3 \cdot 10^{-6}$  1/K. For the HTS40 fibre,  $\alpha_{f\parallel} = -0.1 \cdot 10^{-6}$  1/K could be extracted from the data sheet of the manufacturer [190]. The  $\alpha_{f\perp}$  value, however, was not accessible and therefore had to be taken from another fibre. The T800 fibre was taken as reference with  $\alpha_{f\perp} = 12.5 \cdot 10^{-6}$  1/K [30]. With the elastic properties from the average fibre volume content in table 5.7, this resulted in  $\alpha_{\perp} = 1.69 \cdot 10^{-5}$  1/K and  $\alpha_{\parallel} = 1.79 \cdot 10^{-7}$  1/K.

Using CTE, the residual tensile stresses acting perpendicular to the fibre direction within a single layer can be determined to 20.7 MPa, based on the elastic properties of the average fibre volume content. This can shift the theoretical onset for TMC to external stresses of 469 MPa.

Due to the uncertainty in the actual extent of these residual stresses, TMC would be expected between the lower end of 469 MPa (with residual stresses) and the higher end of 628 MPa (no residual stresses).

## Experimental

Transverse matrix cracks could be experimentally identified following the procedure defined in section 7.6.3. Each crack could thereby be linked to a global stress and strain level. This way the onset and development of TMC could be visualized. This is accomplished in the form of the histograms in figures 7.56 (a) to (d) that show the number of detected transverse matrix cracks as a function of nominal stress (MPa) and strain level (%) for the 4- (a,b) and 16-ply specimens (c,d). The window for the

theoretical onset of TMC is given as well. In total, 41 cracks could be detected over all specimen types. The majority of cracks was thereby found in the inner and outermost  $90^\circ$  layers.

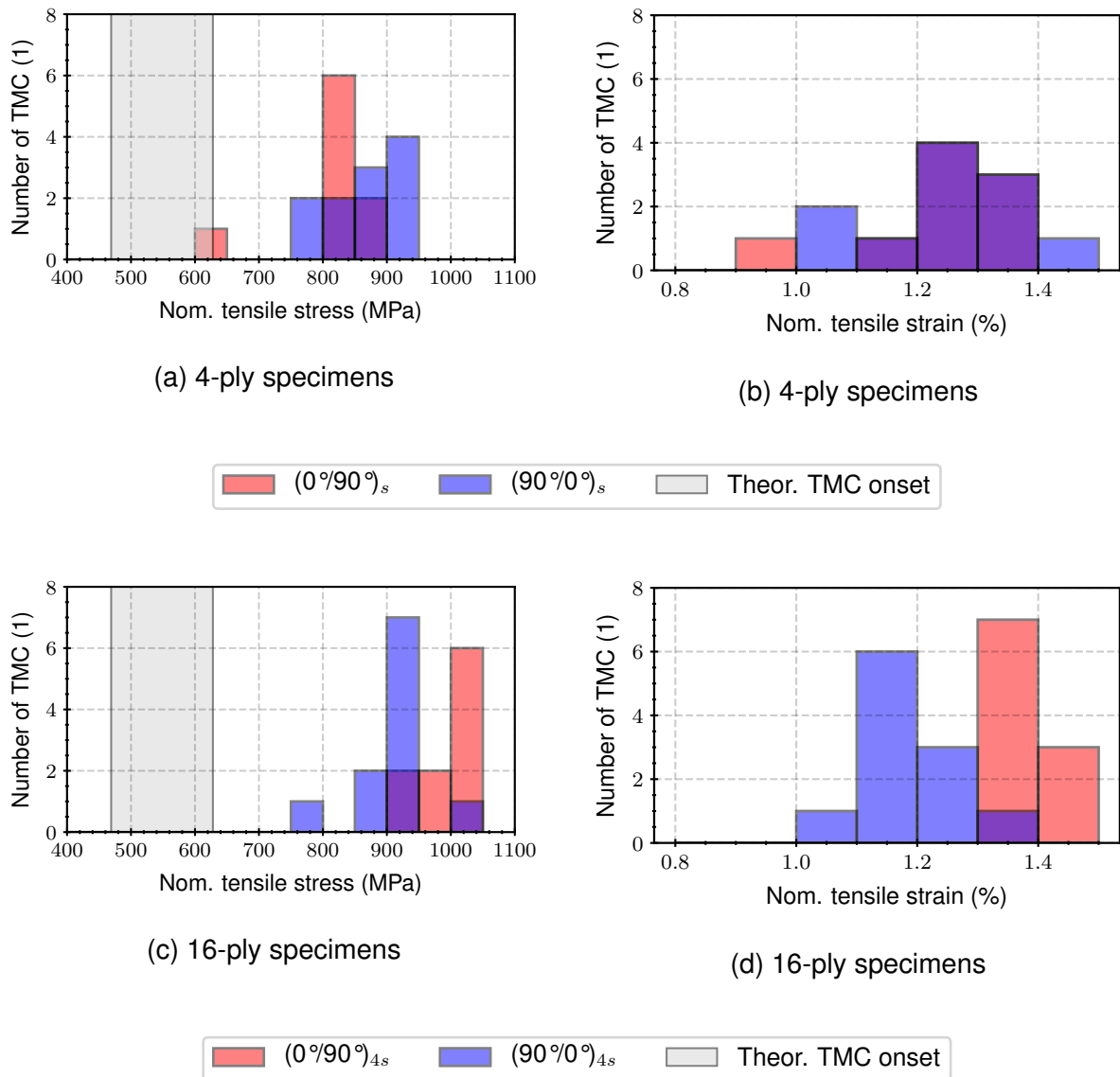


Figure 7.56: Histograms showing the number of detected transverse matrix cracks in the  $90^\circ$  layers (1) with respect to the nominal tensile stress (MPa) and tensile strain (%) for the  $(0^\circ/90^\circ)_s$  and  $(90^\circ/0^\circ)_s$  (a,b) and  $(0^\circ/90^\circ)_{4s}$  and  $(90^\circ/0^\circ)_{4s}$  specimens (c,d).

There are several different aspects to point out from these charts. The first aspect deals with the overall onset of TMC. The first visible crack was found at around 600 MPa which is in line with upper end of the theoretical window for TMC. However, the majority of TMC could be observed at stresses above 800 and 900 MPa for the 4-ply and 16-ply specimens respectively. This deviation from the theoretical results could be explained by the following two aspects:

1. Only a small section of 10 mm of one specimen edge could be analysed during the test. However, microscopic analysis of selected specimens after the test could reveal that cracks also appeared outside the 10 mm section. These cracks as well as cracks that did not extend to the observed specimen edge could not be detected and might have appeared at lower stresses.
2. The toughened epoxy resin could delay crack propagation through crack pinning mechanisms [201, 202]. The critical stress for macroscopic crack development - that could be identified with DIC - could therefore be shifted to higher levels.

As already mentioned, TMC started to intensify at higher stress levels in the 16-ply specimens, where the majority of cracks were detected between 900 and 1050 MPa. However, this could result from differences in individual laminate stiffnesses since the critical strain (0.9 to 1.0%) for TMC onset was comparable between 4- and 16-ply laminates.

Regarding the orientation of the outer layer, TMC onset and development was comparable between the 4-ply specimens. However, higher stress and strain levels were found for the  $(0^\circ/90^\circ)_{4S}$  specimens among the 16-ply specimens. TMC in the outer  $90^\circ$  layers of the  $(90^\circ/0^\circ)_{4S}$  intensified at lower stress and strain levels than in the inner  $90^\circ$  layers of the  $(0^\circ/90^\circ)_{4S}$  specimens. This could be due to the fact that the outermost  $90^\circ$  layers in the  $(90^\circ/0^\circ)_{4S}$  specimens are only supported on one side by a single  $0^\circ$  layer.

#### 7.7.4 Group velocity of triggering wave mode

The group velocity of the triggering wave mode could be characterized with the chosen sensor configuration following the procedure described in section 7.6.1. Filter configurations were iteratively optimized to constrain the triggering wave mode with its corresponding group velocity for both types of specimen. The resulting differential and cumulative distributions of group velocities for the 4- and 16-ply specimens are visualized in the figures 7.57 (a-d) for the filter conditions specified in 7.6.1. Since the stacking order only had a small impact on the group velocities (see figure 5.20) of the cross-ply laminates in the  $0^\circ$  direction, data of 4- and 16-ply specimen types were merged respectively.

Broad distributions can be observed for the 4- and 16-ply specimens with distinct peaks at different group velocities. In terms of the 4-ply specimens, a single peak can be identified between 1000 and 2000 m/s. Around 50% of registered AE events showed a group velocity in this range. This part of the distribution can be attributed to the  $A_0$  mode that dominates the low frequency band (20 to 250 kHz) that was selected for the estimation of time of arrival in this case. A different result was achieved for the 16-ply specimens, where around 60% of AE events lead to a group velocity between 7000 and 8500 m/s. This peak could be attributed to the  $S_0$  mode which was favoured as



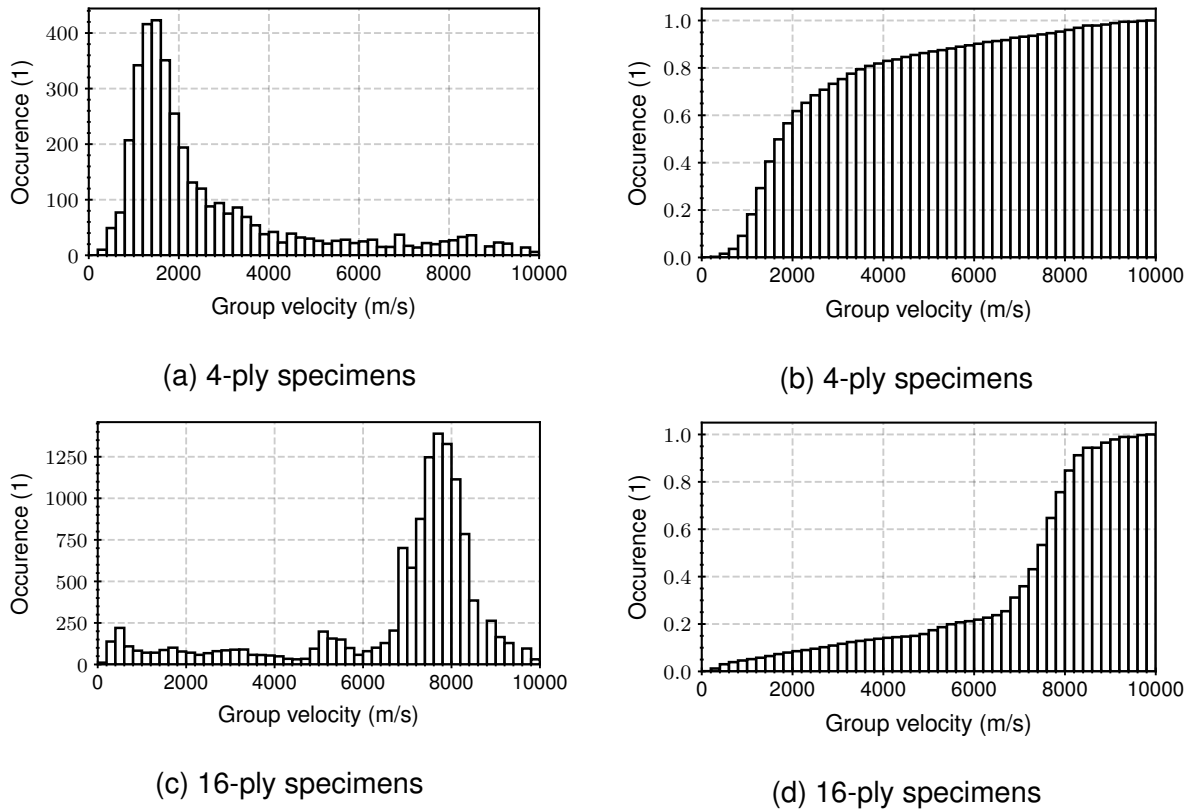


Figure 7.57: Histograms showing the differential (a,c) and cumulative (b,d) distributions of group velocities (m/s) resulting from AE events registered in the 4- (a,b) and 16-ply (c,d) specimens. The arrival times were estimated based on band-pass filtered signals following the approach from section 7.6.1.

triggering wave mode in the thicker 16-ply specimens in the frequency band between 125 and 375 kHz.

Although the major triggering wave mode with its group velocity could be identified this way, around 40% of AE events still resulted in different group velocities. These velocities may not necessarily be assigned to a certain wave mode but might be the result of the following situations:

- The presented methodology for the determination of group velocity assumes a constant difference in propagation distance (30 mm) between the sensors of a pair. For acoustic events that occur between the two inner sensors 1 and 2, this assumption is met. However, for AE events that originate between the sensors of a pair (e.g. 1 and 3), different propagation paths arise and the assumption is violated. A variety of group velocities can result from these situations depending on the actual location of the source. This effect can therefore lead to a certain noise level in the histograms.
- Another assumption that is required for the analysis aims at the triggering wave mode. When the arrival times of both signals from a sensor pair are based on

the same wave mode and group velocity, reliable results can be achieved. However, this wave mode along with its group velocity could change along the 30 mm propagation path due to wave attenuation and near field effects. This effect could again contribute to the noise level but also potentially lead to systematic peaks in the histograms when similar mode combinations (e.g.  $S_0$  at one sensor and  $A_0$  on the other) are encountered.

- Finally, the methodology requires both sensors to be triggered by the same AE event. In cases where both sensors are triggered by different events, these events might be merged to one event and evaluated accordingly. As a result, various differences in the times of arrival can arise, which again can contribute to an increase in noise level.

As these situations do not necessarily imply another wave mode to be triggering wave mode for sensors 1 and 2, the probability of a triggering group velocity between 1000 and 2000 m/s can therefore actually be higher than 50% for the 4-ply specimens. The same applies to the 16-ply specimens where the triggering velocity should lie between 7000 and 8500 m/s for a big majority (> 60%) of events.

In order to extract the group velocity distribution of the triggering wave mode, GMM are fitted to the data. The number of Gaussians was determined by iterative cluster analysis with 1 to 10 Gaussians and evaluating the course of the corresponding AIC values. For both types of specimen, an appropriate fit of the data could be achieved already with two Gaussians. The resulting distributions with their respective mean  $\mu$  and standard deviation  $\sigma$  can be seen in the figures 7.58 (a) and (b).

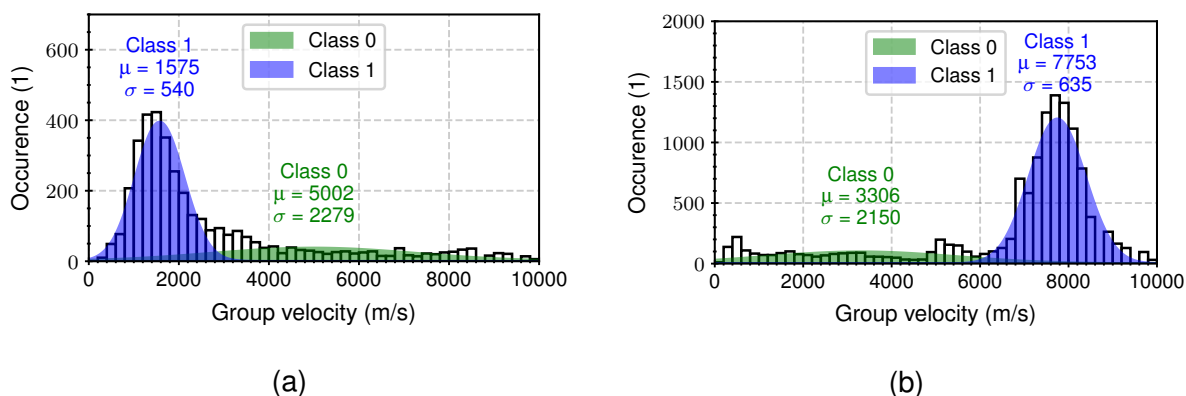


Figure 7.58: Histograms showing the differential distributions of group velocities (m/s) resulting from AE events registered in the 4- (a) and 16-ply (b) specimens with fitted Gaussian distributions.

Regarding the 4-ply specimens, the average group velocity of class 1 matched the profile of the  $A_0$  mode in the frequency band between 20 and 250 kHz (see figure G.15 for reference). Class 0, on the other hand, could be attributed to the previously described

situations. For source localization in the 4-ply specimens, the average group velocity of class 1 (1575 m/s) was therefore chosen as an appropriate estimate of the underlying group velocity of the triggering wave mode.

In terms of the 16-ply specimens, class 1 could be correlated with the  $S_0$  mode, whereas class 0 could again be attributed to the previously described effects. Consequently, the average group velocity of 7753 m/s was chosen for source localization in the 16-ply specimens.

Another interesting aspect to point out here, is that the group velocity of the associated  $S_0$  mode is above its theoretical level (around 6900 m/s) from figure 5.33. This deviation could be due to near field effects that cannot be neglected due to the large wavelength (15 to 60 mm) of the  $S_0$  mode in the frequency band between 125 and 375 kHz.

### 7.7.5 The influence of source-to-sensor distance

The influence of source-to-sensor distance is presented separately for the 4- and 16-ply specimens in the following sections based on stage 2 experiments.

#### $(0^\circ/90^\circ)_s$ and $(90^\circ/0^\circ)_s$ specimens

In order to visualize the effect of source-to-sensor distance on characteristic features and classification results, clusters were identified in the feature space in the first step. AE data sets from the  $(0^\circ/90^\circ)_s$  and  $(90^\circ/0^\circ)_s$  specimens were merged which resulted in 13,767 hits and 4,751 corresponding events. Cluster analysis was based on weighted peak frequency (kHz) and partial power between 250 and 500 kHz (1). Following the state of the art procedure, features for each event were solely extracted from the signals of the first triggering sensor among the evaluation sensors 1 and 2, since source characteristics are more likely to be preserved for the sensor with the lowest source-to-sensor distance. Classification of feature data was realized with GMM with a shared covariance matrix. The most appropriate fit was identified for five Gaussians on the basis of the course of the AIC. The resulting partitioning is shown in figure 7.59 along with the absolute number of events per class.

According to the state of the art, each of these clusters would potentially represent a single damaging event. However, instead of accomplishing this correlation, the focus for now lies on the stability of classification results with respect to changes in source-to-sensor distance.

This can be assessed by localizing each event and incorporating the features from the second hit sensor among the evaluation sensors. This way, each feature can be visualized as a function of source-to-sensor distance. This is accomplished class wise for the

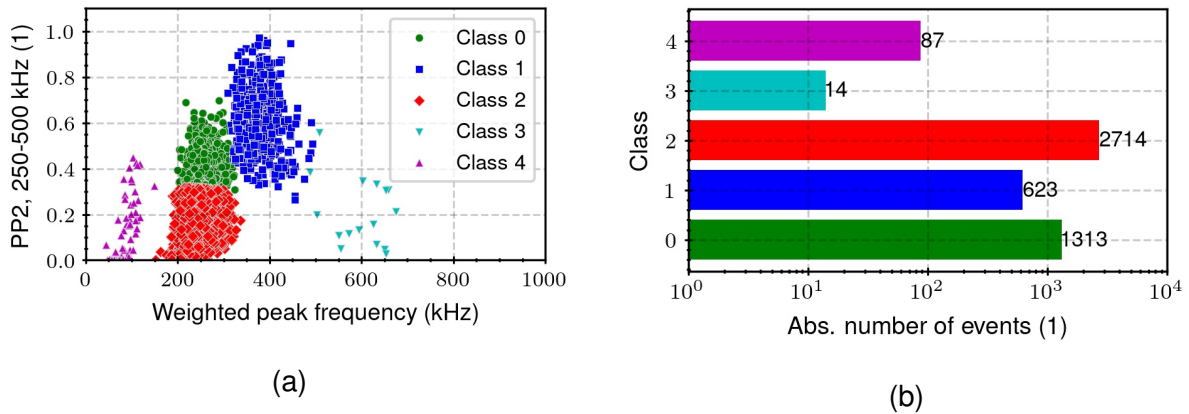


Figure 7.59: Partial power 2 (1) between 250 and 500 kHz and weighted peak frequency (kHz) of AE events from the  $(0\%/90^\circ)_s$  and  $(90\%/0^\circ)_s$  specimens with corresponding partitioning based on GMM (a) and absolute number of events per class (1) (b). Features were extracted from the first triggering evaluation sensor.

weighted peak frequency and the frequency centroid as one of the main discriminators for source identification. Figure 7.60 shows the results for classes 1, 2 and 3. The figures of the remaining classes can be found in appendix L. The class label for each data point was based on the first triggering evaluation sensor. The source-to-sensor distance is given with respect to the centre of the sensor. A minimum source-to-sensor distance of 9.5 mm, which corresponds to the radius of the active area of the sensor, was necessary for reliable source localization. This is indicated by the black vertical line which corresponds to the sensors edge.

These charts give a good impression on the stability of both features with respect to the source-to-sensor distance. There are several interesting aspects to point out here. A steady decrease in frequency centroid can be observed with increasing source-to-sensor distance for events from classes 1 and 3 as a result of the low pass filter characteristics of the material (see section 5.2). The rate of change is thereby significantly higher for class 3 events that are characterized by the highest weighted peak frequencies among all classes. After around 60 mm, frequency centroid decreased from 600 to 400 kHz for these events. Class 2 events show a broad spectrum of frequency centroids with no systematic trend with respect to source-to-sensor distance.

The weighted peak frequency, on the other hand, shows a completely different behaviour. Although a trend towards smaller values can be identified in the course of events from classes 1 and 3, this trend is accompanied by high fluctuations. Due to the discrete nature of the peak frequency, significant shifts can be observed in the weighted peak frequency as well. Consequently, classification results based on the weighted peak frequency can vary substantially with source-to-sensor distance.

Another interesting result can be seen for class 2, where events with weighted peak

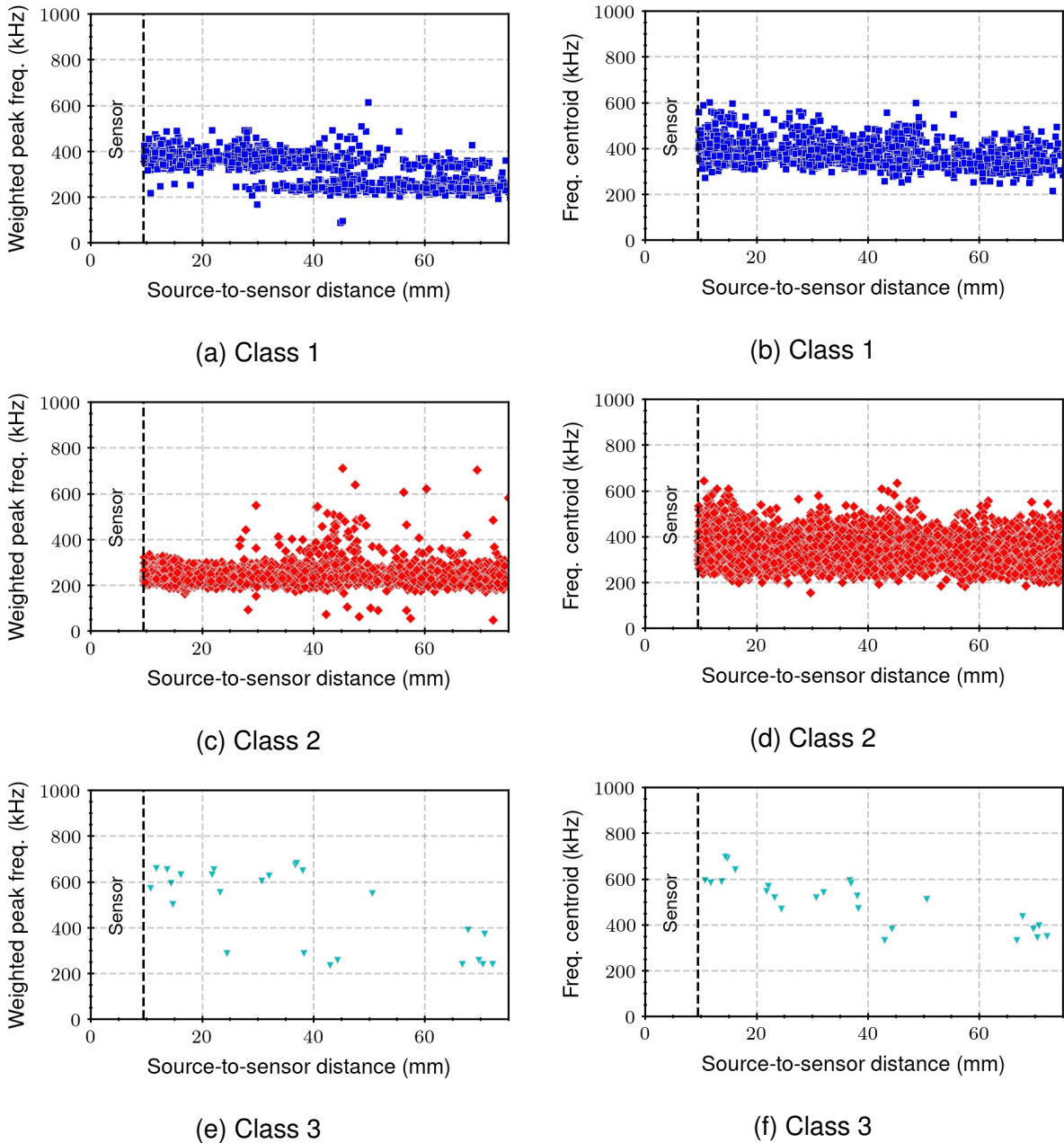


Figure 7.60: Weighted peak frequency (kHz) (a,c,e) and frequency centroid (kHz) (b,d,f) as a function of source-to-sensor distance (mm) for AE events from classes 1 (a,b), 2 (c,d) and 3 (e,f). Classification was based on the signals of the first triggering evaluation sensor.

frequencies up to 700 kHz can be found with increasing source-to-sensor distance. This increase in weighted peak frequency seems irrational at first glance, but is a phenomena that can be understood when looking at the following example. Figure 7.61 shows signals of a single event that was localized around 10 mm away from the first and 65 mm away from that of the second hit sensor. Time signals (a,b) are shown along with frequency spectra (c,d) and continuous wavelet transforms (e,f).

In the time-frequency domain, the fundamental  $S_0$  and  $A_0$  modes can be recognized

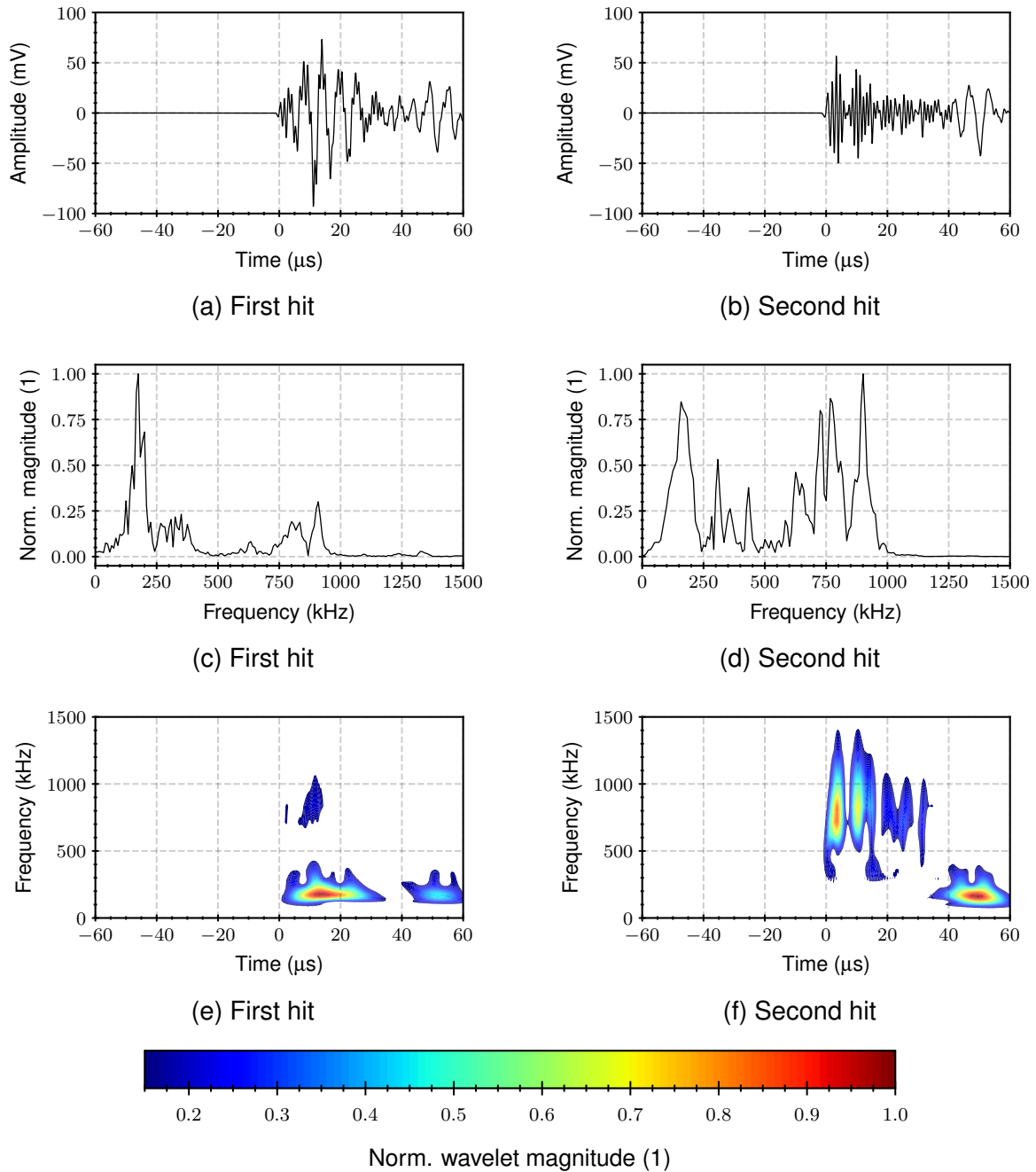


Figure 7.61: Time signals (a,b), normalized frequency spectra (c,d) and continuous wavelet transforms (e,f) of first (a,c,e) and second hit data (b,d,f) of the same event.

through their dominant frequency bands around 800 and 200 kHz, respectively. Besides the primary wave packet, multiple reflections of the  $S_0$  mode can be recognized in the time signal and the corresponding time-frequency representation. With increasing source-to-sensor distance both modes separate due to their different group velocities. Whereas the  $A_0$  mode dominates the spectrum of the first hit sensor signal, the  $S_0$  mode becomes more dominant with increasing source-to-sensor distance. With a

change in modal content, frequency spectra are affected likewise as can be seen in figures 7.61 (c) and (d). Whereas the  $A_0$  related peak around 200 kHz represents the peak frequency for the first hit sensor signal, peak frequency is determined by the  $S_0$  related peak around 800 kHz for the second hit sensor. This phenomena has already been encountered in the preliminary study in section 6.1.3 and could be validated here once more. As mentioned before, this can be traced back to the different attenuation characteristics of both modes as presented in section 5.2. Due to this effect, the peak frequency can significantly shift for the same event, depending on where it is detected. Following the state of art procedure, where peak frequency or weighted peak frequency are commonly considered for the discrimination between fibre breaks and matrix cracking, the event in figure 7.61 could be connected to either one of these damaging events depending on the distance that it was detected.

The influence of source-to-sensor distance on classification results can be seen in figure 7.62, where the features from the second triggered evaluation sensor are shown with the corresponding class labels from the first for each event registered.

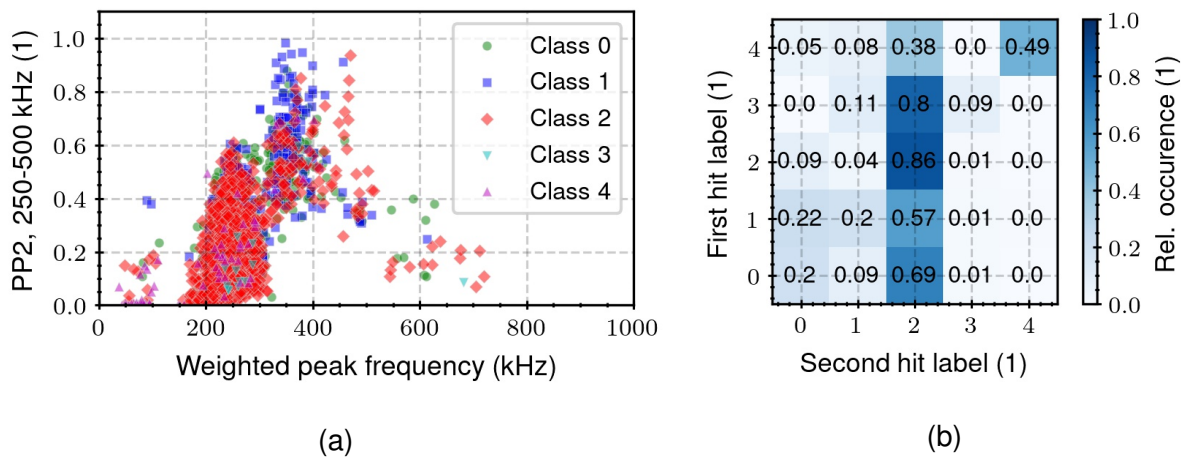


Figure 7.62: Partial power 2 (1) between 250 and 500 kHz and weighted peak frequency (kHz) of AE events from the  $(0^\circ/90^\circ)_s$  and  $(90^\circ/0^\circ)_s$  specimens based on the second triggered evaluation sensor with corresponding class labels from the first (a) and heatmap showing the correlation of classes derived from first and second hit data.

Although the original cluster shapes can still be recognized, classification of single events would differ greatly. In order to assess the stability of each class, classification was accomplished for the second hit data based on the identified Gaussian distributions from the first hit data. This way, the correlation between first and second hit classes could be visualized in the form of the heatmap shown in figure 7.62 (b). For every class label based on the first hit sensor, the heatmap shows the relative fractions of class labels if the corresponding second hit sensor would have been considered for classification instead. The fractions were determined based on the



respective population of each first hit class. For example, 86% of class 2 events would keep their class label if the second hit sensor would have been considered for classification. However, approximately 11% would be classified as class 0 events instead. It is interesting to note that only for the classes 2 and 4, the class label would be retained for the majority of events. Regarding classes 0, 1 and 3, however, the majority of events would be assigned to class 2 instead. This underlines the effect of source-to-sensor distance on classification results based on the weighted peak frequency.

### $(0^\circ/90^\circ)_{4S}$ and $(90^\circ/0^\circ)_{4S}$ specimens

The 16-ply specimens were evaluated following the previous approach. The data sets from  $(0^\circ/90^\circ)_{4S}$  and  $(90^\circ/0^\circ)_{4S}$  specimens were merged, which resulted in 50,315 hits that could be assigned to 16,822 events. Classification was again realized based on the weighted peak frequency (kHz) and partial power 2 (1) of first hit sensor signals as visualized in figure 7.63 (a). Four different Gaussian distributions were identified in the data set using the expectation maximization algorithm. The resulting number of events per class is shown in figure 7.63 (b).

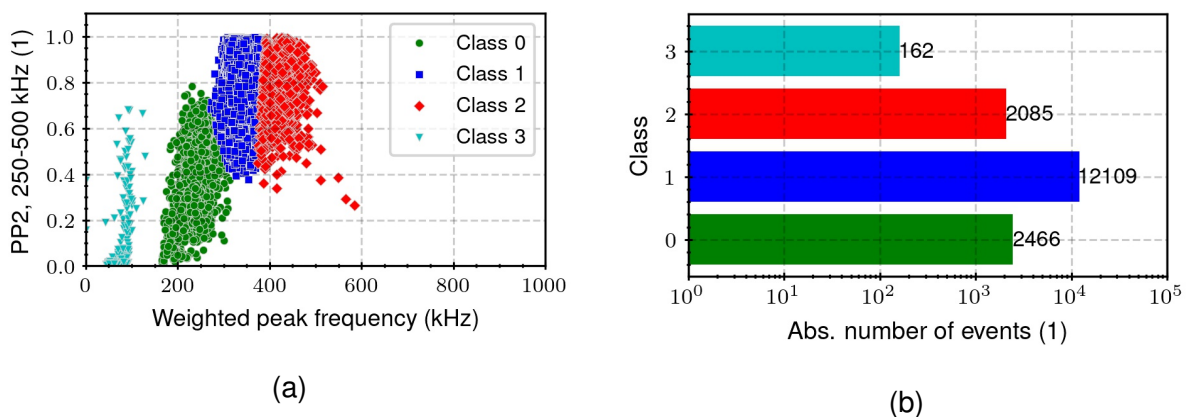


Figure 7.63: Partial power 2 (1) between 250 and 500 kHz and weighted peak frequency (kHz) of AE events from the  $(0^\circ/90^\circ)_{4S}$  and  $(90^\circ/0^\circ)_{4S}$  specimens with corresponding partitioning based on GMM (a) and absolute number of events per class (1) (b). Features were extracted from the first triggering evaluation sensor.

Since only a few events with weighted peak frequencies above 500 kHz were found for the 16-ply specimens, there was no separate cluster assigned to them. Events from classes 1 and 2 could also be merged to one cluster, but were split by the algorithm. Nevertheless, the effects of source to sensor distance on cluster stability could still be investigated for individual clusters.

For each class, feature development was analysed in the next step by incorporating the



second hit data and assigning the corresponding source-to-sensor distance to each hit. The resulting plots are shown for classes 0 and 2 in figures 7.64 (a-d). The weighted peak frequency (kHz) and frequency centroid (kHz) were selected as features in this case. The plots for the remaining classes can be found in appendix L.

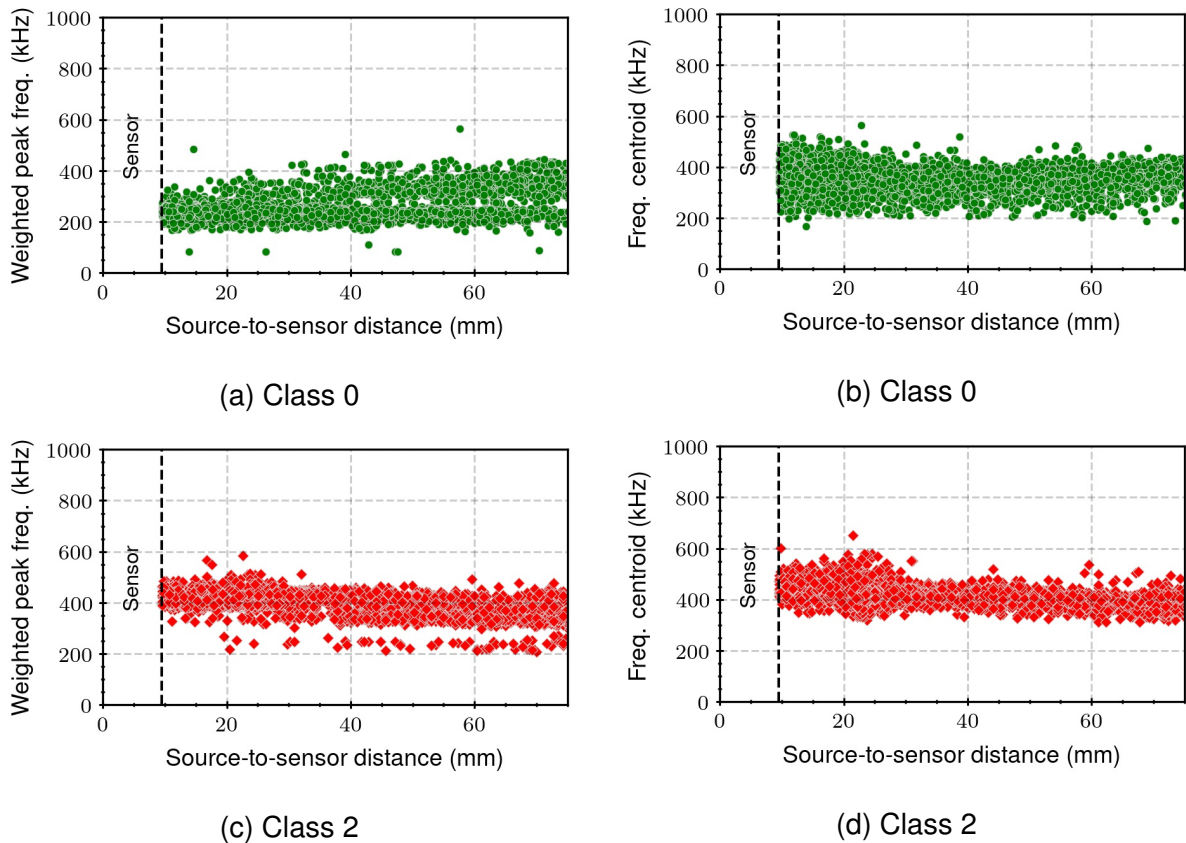


Figure 7.64: Weighted peak frequency (kHz) and frequency centroid (kHz) as a function of source-to-sensor distance (mm) for AE events from classes 0 and 2 (a-d). Classification was based on the signals of the first triggering evaluation sensor.

For events from class 2, a steady decrease in frequency centroid can be observed with increasing propagation distance. Similar observations can be made for class 0 events. However, changes are limited to the first 30 mm here, where the distribution of frequency centroids seems to narrow down to a state that seems robust against a further increase in source-to-sensor distance.

Regarding the weighted peak frequency, a steady decrease can be observed for class 2 events as well. However, when looking at class 0, there were events that show substantial higher weighted peak frequencies for larger propagation distances. This could again be attributed to the different attenuation coefficients of symmetric and antisymmetric wave modes which can lead to an abrupt change in peak frequency with increasing source-to-sensor distance.

Similar to the 4-ply specimens, cluster analysis based on second hit data would lead

to completely different classification results as can be seen in figure 7.65 (a), where the second hit features are visualized with their corresponding class labels from the first triggering evaluation sensor. A comprehensive view on the correlation between first and second hit classes can be drawn from the heatmap shown in figure 7.65 (b).

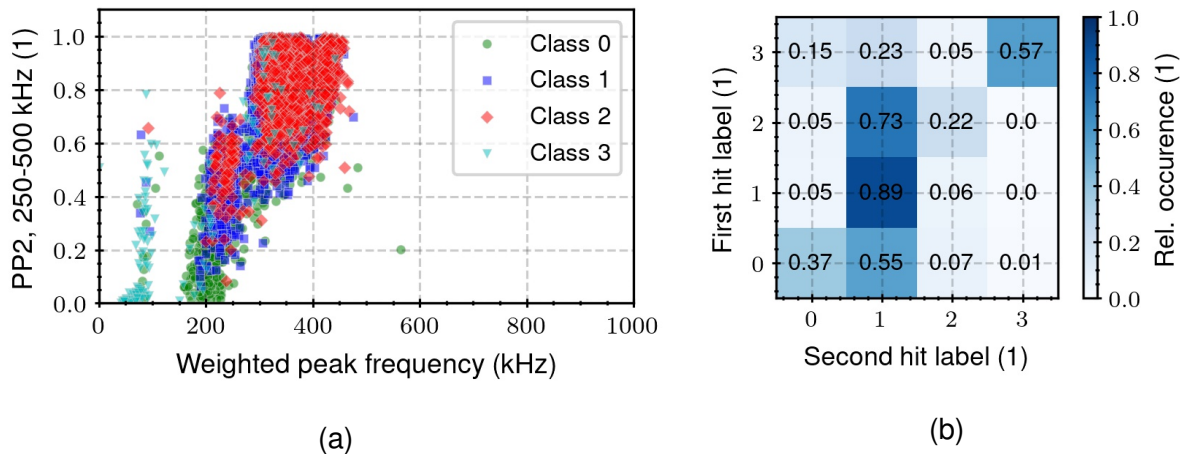


Figure 7.65: Partial power 2 (1) between 250 and 500 kHz and weighted peak frequency (kHz) of AE events from the  $(0^\circ/90^\circ)_{4s}$  and  $(90^\circ/0^\circ)_{4s}$  specimens based on the second triggered evaluation sensor with corresponding class labels from the first (a) and heatmap showing the correlation of classes derived from first and second hit data.

In contrast to the 4-ply specimens, more events would retain their class when evaluation is shifted from first to second hit data. Especially for the classes 1 and 3, the majority of events would still be grouped in the same cluster. For classes 0 and 2 on the other hand, the majority of events would be assigned to class 1 instead. Nevertheless, clusters seem to be more stable in the 16-ply specimens. The reason for this could be found in the differences in dispersion characteristics that directly result from the differences in laminate thickness. Since shifts in the peak frequency towards 800 kHz could be attributed to the  $S_0$  mode in the 4-ply specimens, a closer look is taken at the displacement fields of this mode in the 4- and 16-ply laminates at this particular frequency. These are illustrated with respect to their in-plane (red), out-of-plane (blue) and shear horizontal components (green) in the figures 7.66 (a) and (b) for a propagation in the  $0^\circ$  direction. Fundamental differences can be observed regarding the in- to out-of-plane displacement components of the  $S_0$  mode in both types of laminates. In the 4-ply laminates, the displacement field of the  $S_0$  mode is still dominated by in-plane components whereas for the 16-ply laminates, it is strongly determined by out-of-plane components. These changes in displacement fields affect the group velocity and attenuation of the  $S_0$  mode. The impact on the group velocity of the  $S_0$  mode was already visible in figure 5.33 where a sudden drop could be recognized

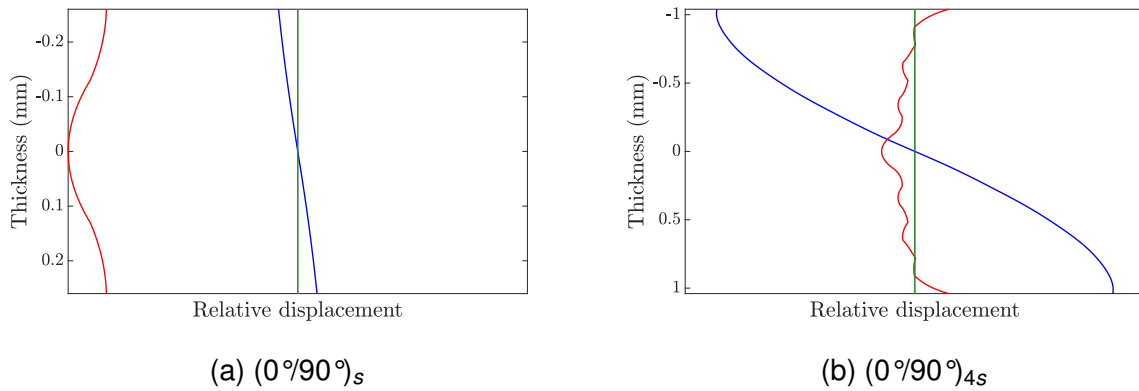


Figure 7.66: In-plane (red), out-of-plane (blue) and shear horizontal displacement (green) components of the fundamental Lamb wave mode  $S_0$  at 800 kHz for the  $(0^\circ/90^\circ)_s$  (a) and  $(0^\circ/90^\circ)_{4s}$  (b) laminate and propagation in the  $0^\circ$  direction.

between 500 and 600 kHz. The attenuation of the  $S_0$  mode is affected likewise and can increase significantly as shown in [59]. Consequently, the  $S_0$  mode is less capable of retaining peak frequencies above 500 kHz. Higher order symmetric modes could potentially take over, however there is a lack of studies dealing with the propagation and attenuation properties of these modes.

### Preliminary conclusion

Source-to-sensor distance can have a strong impact on signal features for source identification. Analysis was focused on the weighted peak frequency and the frequency centroid as two prominent features for source classification. A systematic reduction in frequency centroid was observed with increasing source-to-sensor distance due to the low pass filter characteristic of the material. This reduction was especially noticeable for those classes that stood out with initially high weighted peak frequencies of 300 kHz and above. For the weighted peak frequency, significant shifts to either higher or lower values could be observed due to the discrete nature of the underlying peak frequency. The increase in weighted peak frequency could be traced back to a change in modal content. In the 4-ply specimens, the  $S_0$  mode became the dominant mode in the evaluation window with increasing source-to-sensor distance due to its lower attenuation at high frequencies compared to the  $A_0$  mode. The peak frequency could thereby shift from around 200 kHz to 800 kHz. In the 16-ply specimens, these shifts were not as pronounced. Nevertheless, strong differences in classification results could be observed for both types of specimen whether classification was based on the first or second triggering sensor. Consequently, the influence of source-to-sensor distance should be taken into account for reliable source identification.

### **How to deal with the influence of source-to-sensor distance?**

With increasing propagation path, source characteristics will inherently vanish due to the attenuation of the acoustic waves that carry them. Authors have tried to compensate this loss by calibrating models with information on attenuation characteristics [122, 161, 188]. However, these models are limited to the small set of artificial sources that were utilized to calibrate them since any change in modal or frequency content of the underlying wave would lead to different results. Instead of compensating the influence of source-to-sensor distance, it should rather be constrained by limiting source identification to acoustic events that originated from a specific area. This area of evaluation could be limited to the direct vicinity of a sensor so that the influence of source-to-sensor distance could be minimized. However, wave modes would not be separated for these short propagation distances and peak frequency would highly depend on the relative strengths of wave modes in the evaluation window. Furthermore, one would have to deal with near field effects that would affect symmetric and antisymmetric wave modes differently due to their differences in wavelengths (see figure 5.21). These effects could not only modify signal characteristics but also affect source localization that is required to constrain the area of evaluation in the first place. In order to overcome these issues, a different approach is suggested here that aims to focus the evaluation to the first arriving mode. In order to achieve this, evaluation is constrained to events that originate from a distance at which wave modes could be separated in time. The size of the evaluation window is thereby reduced in order to constrain the window to the first arriving mode. Although this approach might seem irrational at first glance, the dispersion characteristics of wave modes along a fibre dominated propagation direction in FRP support it since

- differences in group velocities of fundamental  $A_0$  and  $S_0$  modes are large enough to accomplish modal separation within a reasonable distance (see figure 5.33),
- energy is inherently focused along the fibre direction so that information in the higher frequency bands can be preserved for these distances (see figure 7.61) and
- the  $S_0$  mode, that would be considered as evaluation mode, especially for the high frequency events, shows lower attenuation than the  $A_0$  mode (see figure 5.34) and is therefore more likely to preserve this information.

The energy based Hinkley criteria, that is used to adjust signal onset, would thereby allow to identify the first arriving mode in the spectrum.

### 7.7.6 The influence of source depth

For the investigation of the influence of source depth, the evaluation methodology was adjusted based on the results from the previous section. As suggested, evaluation was constrained to events that originated from a distance at which modal separation could be accomplished. This distance could be determined on the basis of the theoretical dispersion curves from figure 5.33. For the 4-ply specimens, analysis could be constrained to the fundamental wave modes  $A_0$  and  $S_0$  for frequencies below 1500 kHz. Assuming their average group velocities to be 1550 and 6900 m/s, a 20  $\mu$ s time difference between both modes could be achieved at a propagation distance of around 40 mm. Based on this minimum distance, two separate areas of evaluation were defined for sensors 1 and 2. These areas were constrained on the other end by the limitation that the inner sensors (1 or 2) had to be triggered before the guard sensors (3 or 4). For the evaluation window, 400 pre-trigger (40  $\mu$ s) and 200 post-trigger samples (20  $\mu$ s) were chosen.

For the 16-ply specimens, modal separation could not be limited to the  $A_0$  and  $S_0$  modes because higher order wave modes could already be excited at frequencies of around 400 kHz (e.g.  $A_1$ ). A separation of wave modes is therefore challenging to achieve. Nevertheless, it is assumed that source characteristics are more likely to be retained by the first arriving mode. The evaluation was therefore realized the same way as for the 4-ply specimens.

#### **$(0^\circ/90^\circ)_s$ and $(90^\circ/0^\circ)_s$ specimens**

Data sets of both specimen types -  $(0^\circ/90^\circ)_s$  and  $(90^\circ/0^\circ)_s$  - are merged again to identify clusters in the feature space in the first step. The analysis was based on 8,389 hits that could be connected to 2,899 events. Figure 7.67 (a) shows acoustic events with respect to their weighted peak frequency (kHz) and partial power 2 between 250 and 500 kHz (1). Features were based on the sensor that was at least 40 mm away from the source. Using GMM, three clusters were identified in the data set. The corresponding number of events per class can be found in 7.67 (b). Whereas some of the clusters are similar to those found in figure 7.59, other clusters are either merged or missing. A big difference can be seen in the number of events with weighted peak frequencies above 600 kHz (class 1 in figure 7.67 and class 3 in figure 7.59). This number increased from 14 to 527 with the new evaluation methodology and therefore shows that, despite the limitation to larger source-to-sensor distances, the new approach is better suited to capture the high frequency characteristics of the source.

Exemplary time signals and corresponding frequency spectra of each class are illus-

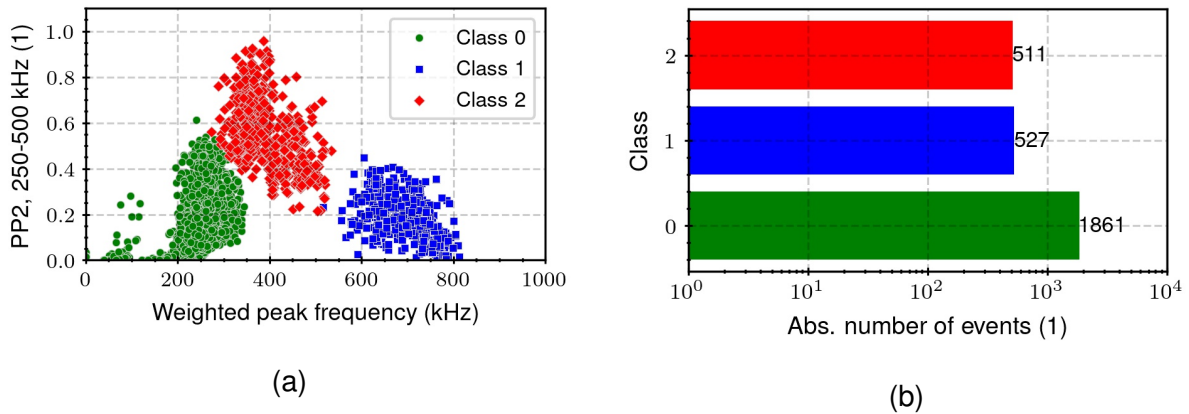


Figure 7.67: Partial power 2 (1) between 250 and 500 kHz and weighted peak frequency (kHz) of AE events from the  $(0^\circ/90^\circ)_s$  and  $(90^\circ/0^\circ)_s$  specimens with corresponding partitioning based on GMM (a) and absolute number of events per class (1) (b). Features were extracted from the sensor that was at least 40 mm away from the source.

trated in figures 7.68 (a-f). Distinct peak frequencies could be recognized in the frequency spectra of each class. For the majority of events, the evaluation window could be constrained to a single mode. In some cases, however, the  $A_0$  and  $S_0$  modes were both present in the evaluation window. These situations arose in particular for low  $S_0$  to  $A_0$  ratios, where the Hinkley picker would define the stronger  $A_0$  mode as signal onset. Consequently, the  $S_0$  mode was present in the pre-trigger samples and therefore contributed to signal characteristics in these situations. However, since the  $S_0$  mode showed comparably lower amplitudes in these events, no shift in weighted peak frequency could be observed (examples can be found in appendix M).

The influence of possible reflections in the evaluation window could not be excluded. However, these reflections should be from the same mode as the primary wave packet and should have lower signal amplitudes so that weighted peak frequency should only slightly be affected by them.

In order to visualize differences between the  $(0^\circ/90^\circ)_s$  and  $(90^\circ/0^\circ)_s$  specimens, a closer look is taken at the number of events per class that occurred in each of these specimen types (see figures 7.69 (a) and (b)). Since the absolute number of events differed between both specimen types ( $(0^\circ/90^\circ)_s$ : 2,058 events,  $(90^\circ/0^\circ)_s$ : 841 events), the relative contribution of each signal class is given as well in brackets based on the individual number of events per specimen type.

Whereas the relative contributions of events from classes 0 and 2 were similar for both specimen types, class 1 events were predominantly found in the  $(0^\circ/90^\circ)_s$  specimens. This difference can be directly observed in figure 7.70, where weighted peak frequency (kHz) and partial power 2 (1) of the acoustic events from  $(0^\circ/90^\circ)_s$  (a) and  $(90^\circ/0^\circ)_s$  (b) specimens are shown separately.

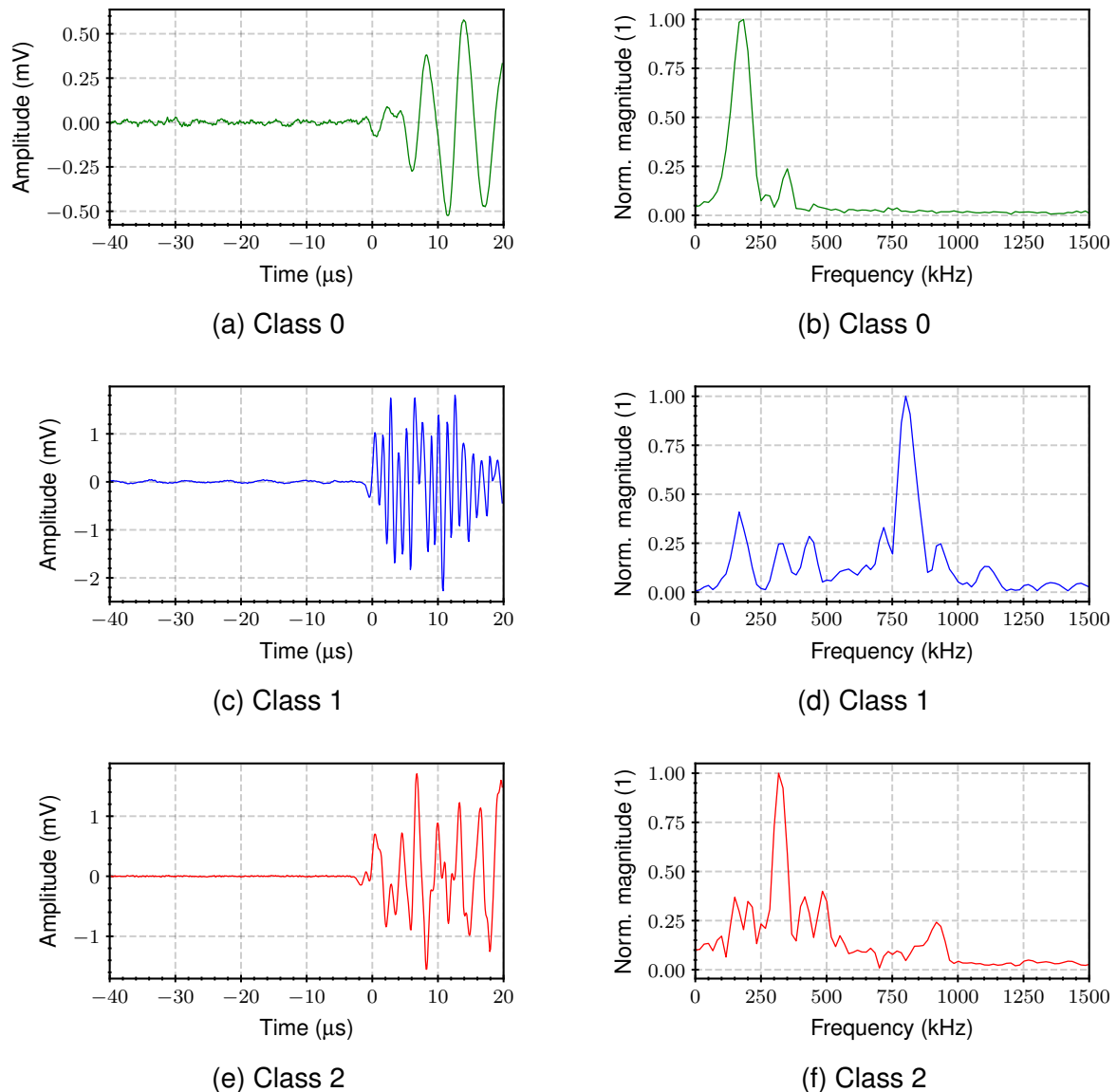


Figure 7.68: Exemplary time signals (a,c,e) and normalized frequency spectra (b,d,f) of class 0, 1 and 2 events from the  $(0^\circ/90^\circ)_s$  and  $(90^\circ/0^\circ)_s$  specimens.

In order to understand why the majority of class 1 events was found in the  $(0^\circ/90^\circ)_s$  specimens, a closer look is taken at the activity of all classes in relation to the external stress and strain level during the test. Exemplary stress versus strain curves are shown in combination with the cumulative number of events per class in the figures 7.71 (a) and (b) for a  $(0^\circ/90^\circ)_s$  and  $(90^\circ/0^\circ)_s$  specimen, respectively.

The overall onset of significant AE was found at around 0.6% strain and 400 MPa stress for the  $(0^\circ/90^\circ)_s$  specimen while it was shifted towards higher stress (600 MPa) and strain levels (0.8%) for the  $(90^\circ/0^\circ)_s$  specimen. Following the general degradation behaviour of cross-ply specimens, as described in section 2.1.2, one would expect matrix cracking in the  $90^\circ$  layers among the first damaging events. This matrix cracking will likely initiate at local stress concentrations that result from inhomogeneities in the



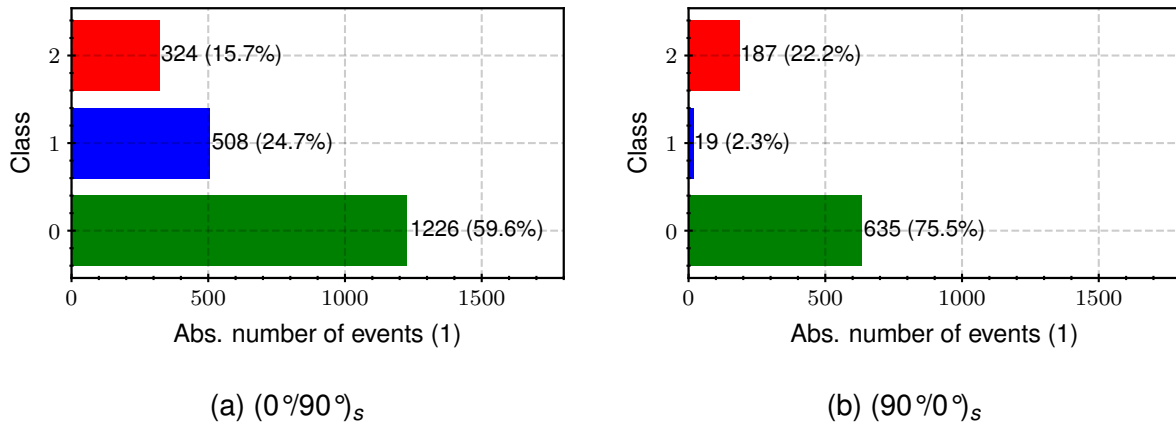


Figure 7.69: Absolute number of acoustic events in each class (1) for the  $(0^\circ/90^\circ)_s$  (a) and  $(90^\circ/0^\circ)_s$  (b) specimens. The corresponding relative amount (%) of events in each class is given in brackets.

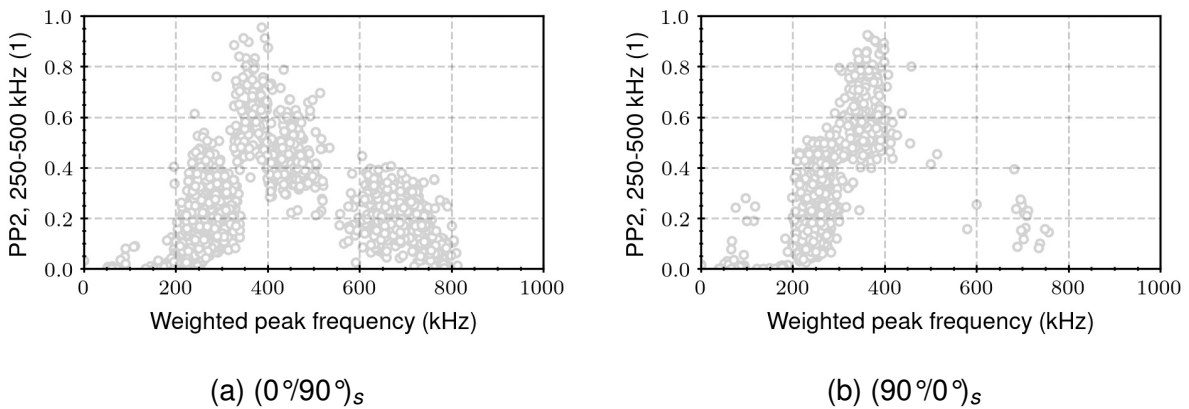


Figure 7.70: Partial power 2 (1) between 250 and 500 kHz and weighted peak frequency (kHz) of AE events from the  $(0^\circ/90^\circ)_s$  (a) and  $(90^\circ/0^\circ)_s$  specimens (b). Features were extracted from the sensor that was at least 40 mm away from the source.

laminated structure. Assuming that these inhomogeneities are equally spread in both types of specimen, the onset of micro cracking should be similar. Likewise, one would expect the number of events to be the same for both laminated types. However, this is not the case. The reason for this could be found in the differences in layer thickness. Due to the double  $90^\circ$  layer in the plane of symmetry, layer thickness of the  $90^\circ$  layer in the  $(0^\circ/90^\circ)_s$  specimen is twice that of the  $(90^\circ/0^\circ)_s$  specimen. As studies have shown, the onset of matrix cracking in cross-ply laminates can be shifted towards lower stress levels when the thickness of the  $90^\circ$  layer is increased [203, 204]. This phenomenon is explained by the supporting effect of the surrounding  $0^\circ$  layers that can shift matrix cracking in the  $90^\circ$  layer towards higher stress levels. However, this effect is constrained to the vicinity of the  $0^\circ$  layer and therefore decreases with increasing distance from the interface. The earlier onset of matrix cracking as well as its larger



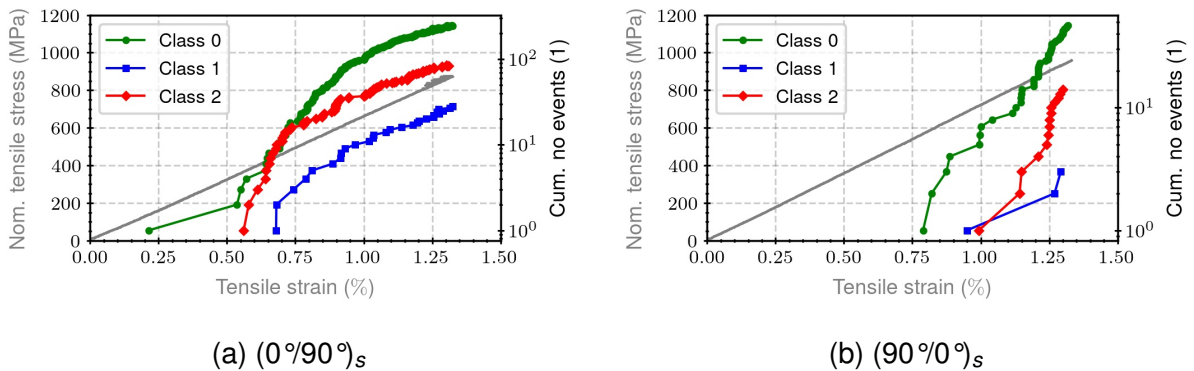


Figure 7.71: Nominal tensile stress (MPa) versus strain (%) and cumulative number of events (1) per class for an exemplary (0°/90°)<sub>s</sub> (a) and (90°/0°)<sub>s</sub> (b) specimen.

quantity in the (0°/90°)<sub>s</sub> specimen could therefore be attributed to this effect.

For a more statistical view on the onset and development of cluster activity, data from all specimens is shown in figures 7.72 (a-c). The cumulative number of events is shown in relation to the tensile stress level (MPa) for every class in a separate figure. Data from the (0°/90°)<sub>s</sub> and (90°/0°)<sub>s</sub> specimens are shown in red and blue, respectively. The theoretical onset of TMC (grey) as well as the stress windows, where TMC could be experimentally detected for each specimen type (red and blue), are shown as well in the form of boxes. The experimental TMC windows were defined based on the lowest and highest stress levels at which TMC could be detected in each specimen type (see figure 7.56).

Similar trends can be discovered regarding the onset and development of each class. For the (0°/90°)<sub>s</sub> specimens, the onset of all three classes can be observed between 200 and 400 MPa. The activity of each class thereby increases till the end of the test for the majority of the specimens. Changes in class activity - identified by a change in slope - can especially be observed for class 1 events within the window of experimentally detected TMC. Regarding the (90°/0°)<sub>s</sub> specimens, the onset of significant AE activity is shifted to stress levels above 600 MPa for the events of classes 0 and 2. The few class 1 events that could be detected, appeared at even higher stresses above 800 MPa. At this stress level, a significant change in AE activity of class 0 and 2 events could be observed as well.

Since fibre filament failure should generate AE with higher peak frequencies than matrix cracking as discussed in section 2.3.3, class 1 events could be correlated with fibre breakage. However, why should fibre filament failure in the (0°/90°)<sub>s</sub> specimens start already at 250 MPa which corresponds to around 25% of the ultimate strength of these specimens? In general, fibre filament failure would be expected at higher stresses around 50 to 70% of the ultimate strength [29]. If, however, fibre filament

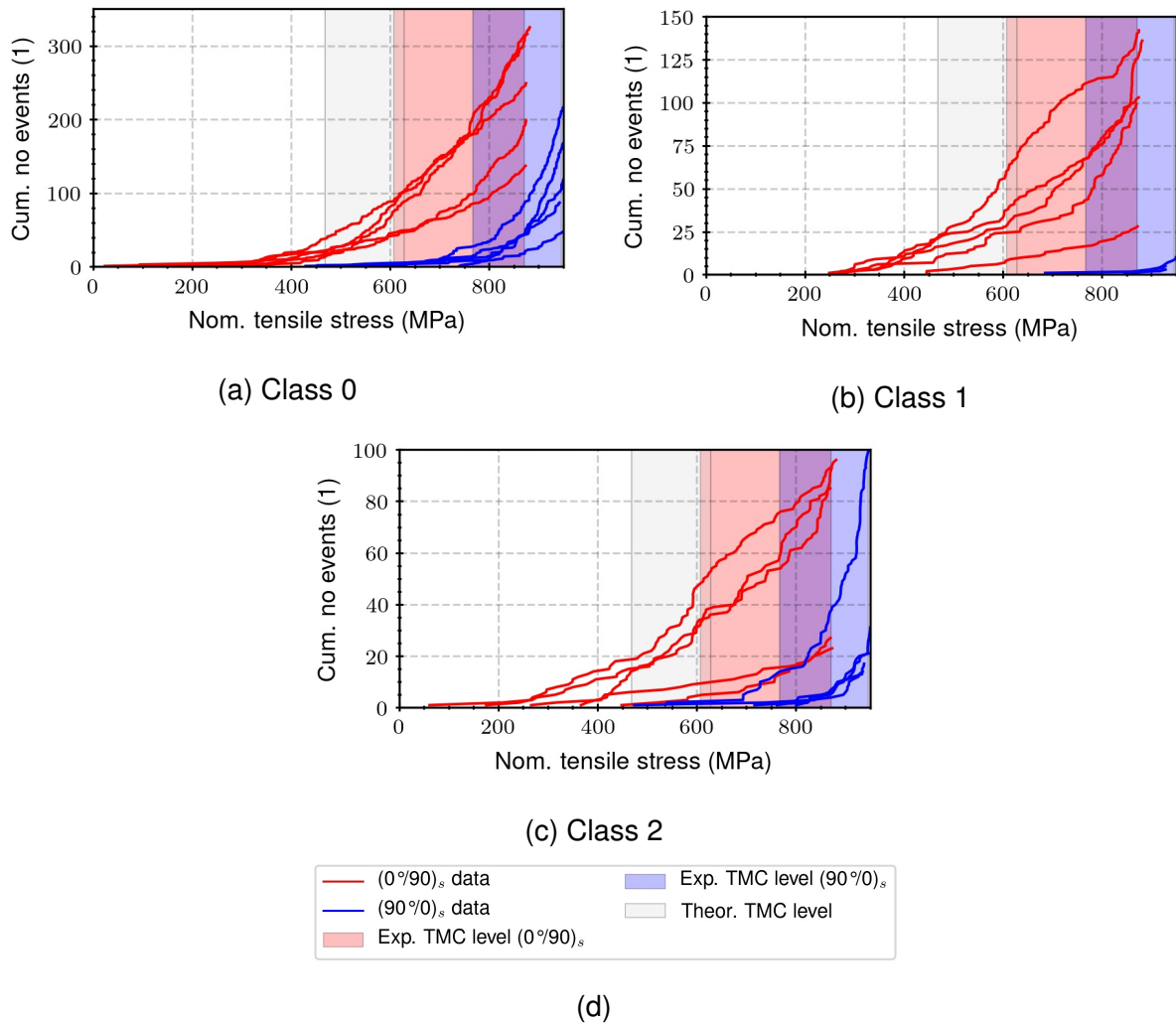


Figure 7.72: Cumulative number of events (1) per class as function of nominal tensile stress (MPa) for class 0 (a), 1 (b) and 2 (c) events from the  $(0^\circ/90^\circ)_s$  and  $(90^\circ/0^\circ)_s$  specimens. The theoretical onset of TMC (grey) as well as the stress windows, where TMC could be experimentally detected for each specimen type (red and blue), are shown as well in the form of boxes.

failure would start earlier, it should be observed in the  $(90^\circ/0^\circ)_s$  specimens as well since fracture strength distribution of the fibres in the  $0^\circ$  layers should be similar. But looking at figure 7.72 (c), the onset of class 1 events was found at stresses above 850 MPa for this layup. Besides this shift in onset, there is also a substantial difference in the number of class 1 events that cannot be explained with fibre filament failure as being the only underlying damaging mode. Consequently, the underlying damaging mode of class 1 events is expected to differ between both types of specimen. For the  $(0^\circ/90^\circ)_s$  specimens, class 1 events could be attributed to TMC in the inner  $90^\circ$  layers due to the early onset and the change in cluster activity at the experimentally determined TMC onset. This would also be in accordance with recent findings from other authors who could show that TMC is capable of generating AE with high peak

frequencies when the  $90^\circ$  layer was situated in the plane of symmetry [24, 25]. The reason for this could indeed lay in the modal spectrum that is excited in this case. As shown in section 6, peak frequency can rise for in-plane sources with increasing source depth up to the plane of symmetry due to the fact that the  $S_0$  mode becomes the most dominant mode in the spectrum. Due to the lower attenuation of this mode - especially in one of the principal fibre directions (see figure 5.34) - high frequency content of the source is retained for longer distances. Besides TMC in the inner  $90^\circ$  layers, fibre fracture in the  $0^\circ$  layers could potentially contribute to class 1 events at higher stresses. A differentiation between both damaging modes could, however, not be accomplished due to their similar frequency content.

For the  $(90^\circ/0^\circ)_s$  specimens on the other hand, class 1 events are unlikely to result from TMC, since similar amounts of TMC were detected for both types of specimen (see figure 7.56). Additionally, several studies could already show that TMC in the outer  $90^\circ$  layers is rather accompanied by AE with low peak frequencies [25, 26, 74]. The underlying damaging mechanism is therefore more likely to be fibre filament failure. TMC is expected to either be correlated to class 0 or class 2 events in this case since it should predominantly excite the  $A_0$  mode that will, in turn, result in lower peak frequencies in the spectrum.

### **$(0^\circ/90^\circ)_{4s}$ and $(90^\circ/0^\circ)_{4s}$ specimens**

Evaluation for the 16-ply specimens was also constrained to events where a minimum distance of 40 mm to one of the evaluation sensors could be guaranteed. Similar results could be observed, however, the differences between both types of specimen were not that obvious as for the 4-ply specimens. Due to the small amount of events with weighted peak frequencies above 500 kHz (around 6) compared to the total amount of events (around 15,000), cluster analysis was not capable of identifying a unique cluster in the data set of the  $(0^\circ/90^\circ)_{4s}$  specimens. Nevertheless, differences could be observed when looking at figure 7.73 (a), where events from the constrained area of evaluation are visualized with respect to their weighted peak frequency (kHz) and partial power between 250 and 500 kHz (1). Again, events with weighted peak frequencies above 500 kHz were limited to the specimens where the  $90^\circ$  layer was situated in the plane of symmetry. The onset of these events corresponded with the detected onset of TMC for the  $(0^\circ/90^\circ)_{4s}$  specimens as can be seen in figure 7.73 (b). The stress levels for TMC were based on the minimum and maximum stress level where TMC could be detected in these specimens. TMC in the inner  $90^\circ$  layers could again be responsible for the events with weighted peak frequencies above 500 kHz based on these results. However, fibre filament failure could be attributed to these events as well due to the high stress level (around 80% of ultimate strength) at which

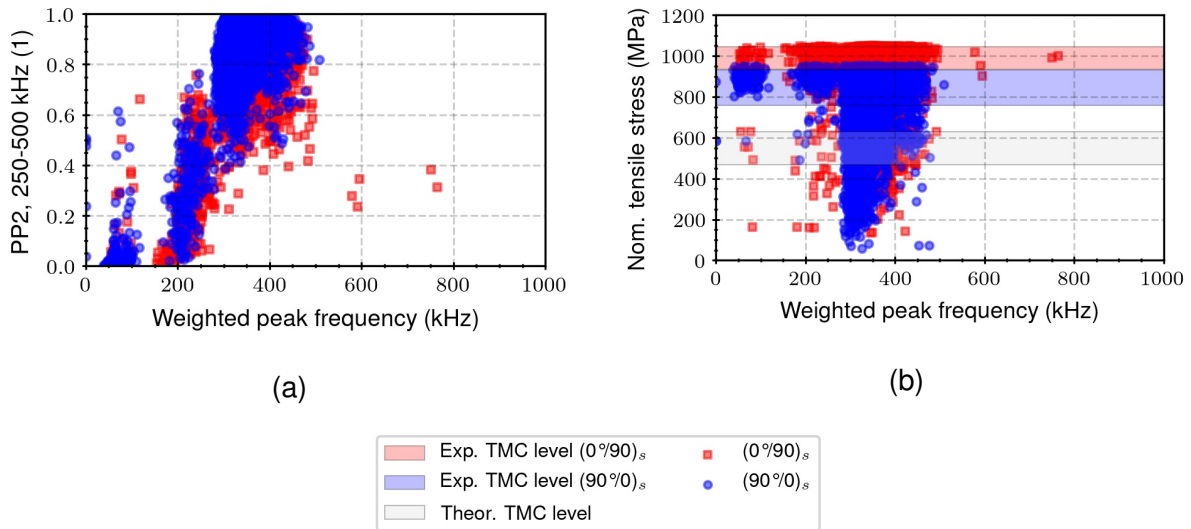


Figure 7.73: Partial power 2 (1) between 250 and 500 kHz and weighted peak frequency (kHz) (a) as well as nominal tensile stress (MPa) versus weighted peak frequency (kHz) (b) of AE events from the  $(0^\circ/90^\circ)_{4s}$  and  $(90^\circ/0^\circ)_{4s}$  specimens. Features were extracted from the sensor that was at least 40 mm away from the source.

these events occurred. The fact that the  $(90^\circ/0^\circ)_{4s}$  specimens were only loaded to 950 MPa could thereby support the fact that none of these events were found here since fibre filament failure might have started at more elevated stresses.

The reason why the influence of source depth is not as obvious as in the 4-ply specimens could again be attributed to the different dispersion characteristics that result from the differences in laminate thickness.

### Stage 3: $(0^\circ/90^\circ)_s$ and $(90^\circ/0^\circ)_s$ specimens

In the first step, acoustic events were analysed based on single sensor data to identify clusters in the data sets. One sensor from each pair was considered for the evaluation. Data sets from the  $(0^\circ/90^\circ)_s$  and  $(90^\circ/0^\circ)_s$  specimens were again merged to identify common and exclusive clusters among specimen types. The evaluation was accomplished following the adapted methodology from stage 2 experiments that was applied to investigate the influence of source depth. The evaluation window was constrained accordingly to 600 samples (400 pre-trigger and 200 post-trigger samples) while only events that were at least 40 mm away from a sensor pair were considered for the evaluation. Analysis was thereby limited to 18,532 hits that could be grouped into 4,633 events. These events are shown with respect to their weighted peak frequency (kHz) and partial power between 250 and 500 kHz (1) in figure 7.74 (a). Features were extracted from a single sensor of the sensor pair that was at least 40 mm away from the

source. The data was grouped into 4 clusters that were fitted with GMM with a full covariance matrix. The number of events per class is shown in figure 7.74 (b).

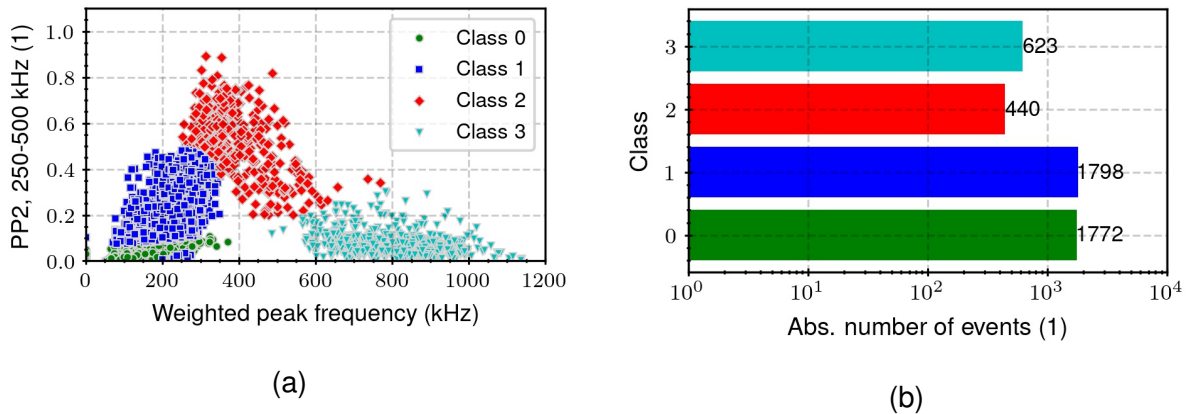


Figure 7.74: Partial power 2 (1) between 250 and 500 kHz and weighted peak frequency (kHz) of AE events from the  $(0^\circ/90^\circ)_s$  and  $(90^\circ/0^\circ)_s$  specimens with corresponding partition based on GMM (a) and absolute number (1) of events per class (b). Features were extracted from the sensor pair that was at least 40 mm away from the source.

Exemplary time signals and corresponding frequency spectra of each class are illustrated in figures 7.75 (a-h). Each class stands out with a characteristic frequency spectrum.

The differences between the  $(0^\circ/90^\circ)_s$  and  $(90^\circ/0^\circ)_s$  specimens become obvious again when looking at the respective number of events per class that occurred in each type of specimen (see figure 7.76).

Since the absolute number of events differed between both specimen types ( $(0^\circ/90^\circ)_s$ : 3,456 events,  $(90^\circ/0^\circ)_s$ : 1177 events), the relative portion of each signal class is given as well in brackets based on the individual number of events per specimen type. Similar to stage 2, there is a class of events that is dominantly found in the  $(0^\circ/90^\circ)_s$  specimens (class 3). This difference can be directly observed in figure 7.77, where weighted peak frequency (kHz) and partial power 2 (1) of the acoustic events from  $(0^\circ/90^\circ)_s$  (a) and  $(90^\circ/0^\circ)_s$  (b) specimens are shown separately. The big majority of events with weighted peak frequencies above 600 kHz can be found in the data from the  $(0^\circ/90^\circ)_s$  specimens. Differences among specimen types can also be seen in the relative percentages of the other classes. Whereas the majority of events is assigned to class 0 in  $(0^\circ/90^\circ)_s$  specimens, it is class 1 for the  $(90^\circ/0^\circ)_s$  specimens. In order to correlate these classes with underlying damaging mechanisms, a closer look is taken at the activity of these classes as a function of global stress and strain level in the specimens. Figure 7.78 shows one example of each specimen type, where the number of events per class (1) is accumulated and plotted on a logarithmic scale against the nominal tensile stress (MPa) and strain (%).

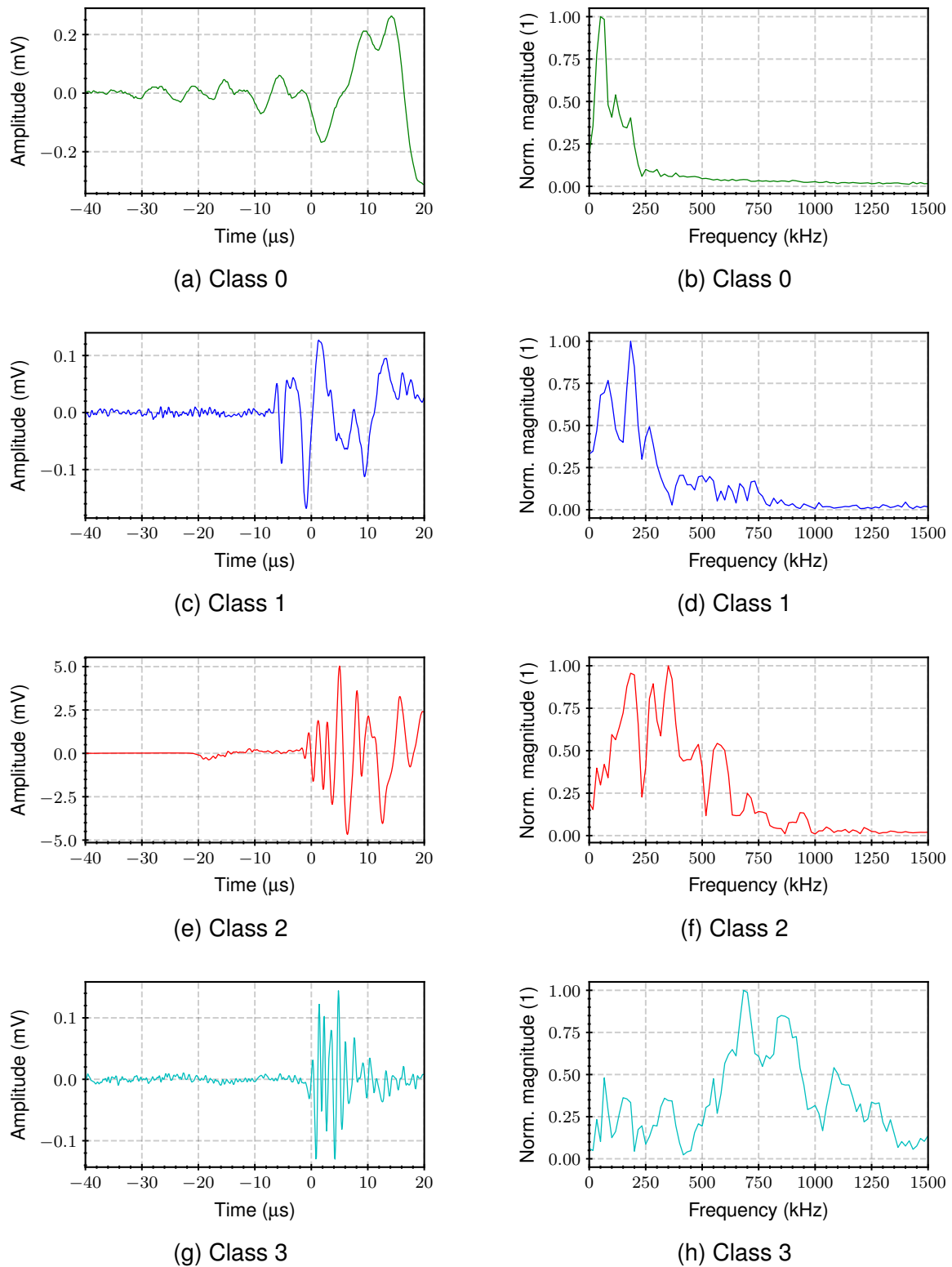


Figure 7.75: Exemplary time signals (a,c,e,g) and normalized frequency spectra (b,d,f,h) of classes 0 to 3 events from the  $(0^\circ/90^\circ)_s$  and  $(90^\circ/0^\circ)_s$  specimens.

The onset of significant AE activity was again shifted from around 200 MPa and 0.4 % strain for the  $(0^\circ/90^\circ)_s$  to around 800 MPa and 1.1% strain for the  $(90^\circ/0^\circ)_s$  (b) speci-

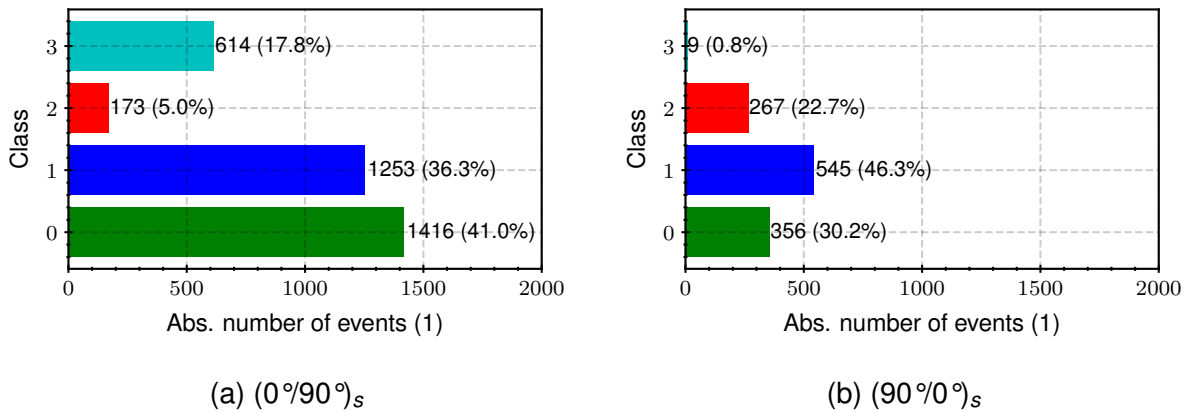


Figure 7.76: Absolute number of acoustic events (1) in each class for the (0°/90°)<sub>s</sub> (a) and (90°/0°)<sub>s</sub> (b) specimens. The corresponding relative amount of events (%) in each class is given in brackets.

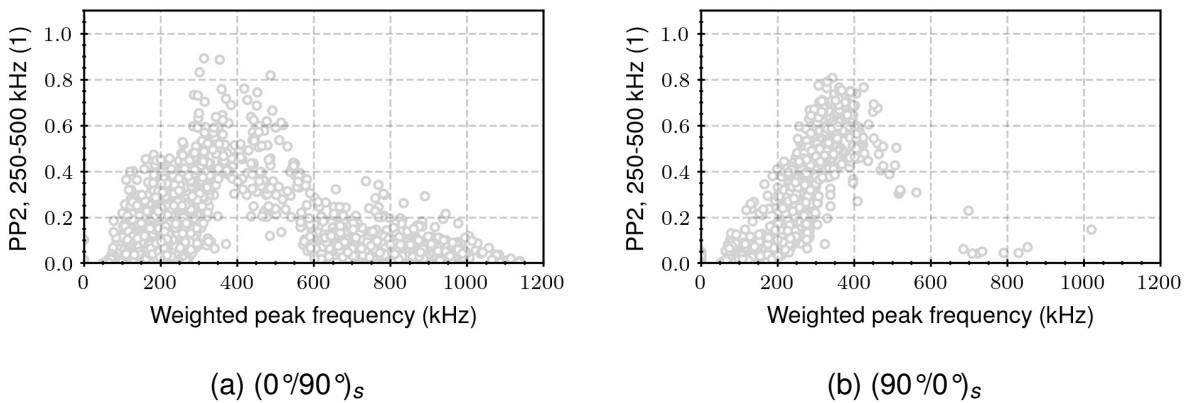


Figure 7.77: Partial power 2 (1) between 250 and 500 kHz and weighted peak frequency (kHz) of AE events from the (0°/90°)<sub>s</sub> (a) and (90°/0°)<sub>s</sub> specimens (b). Features were extracted from the sensor pair that was at least 40 mm away from the source.

men. This effect could again be attributed to the supporting effect of the neighboring 0° layers that could effectively postpone the onset of damaging events in the thinner 90° plies that were found in the (90°/0°)<sub>s</sub> specimen.

For a more statistical view on the onset and development of cluster activity, data from all specimens is shown in figures 7.79 (a-d). The cumulative number of events (1) is shown in relation to the tensile stress level (MPa) for every class in a separate figure. Events from the (0°/90°)<sub>s</sub> and (90°/0°)<sub>s</sub> specimens are shown separately in the form of red and blue lines, respectively. The theoretical onset of TMC as well as the stress levels, where TMC could be experimentally detected in the (0°/90°)<sub>s</sub> and (90°/0°)<sub>s</sub> specimens, are shown as well in the form of grey, red and blue colored boxes. These windows were based on the lowest and highest stress level at which TMC could be detected in each specimen type.



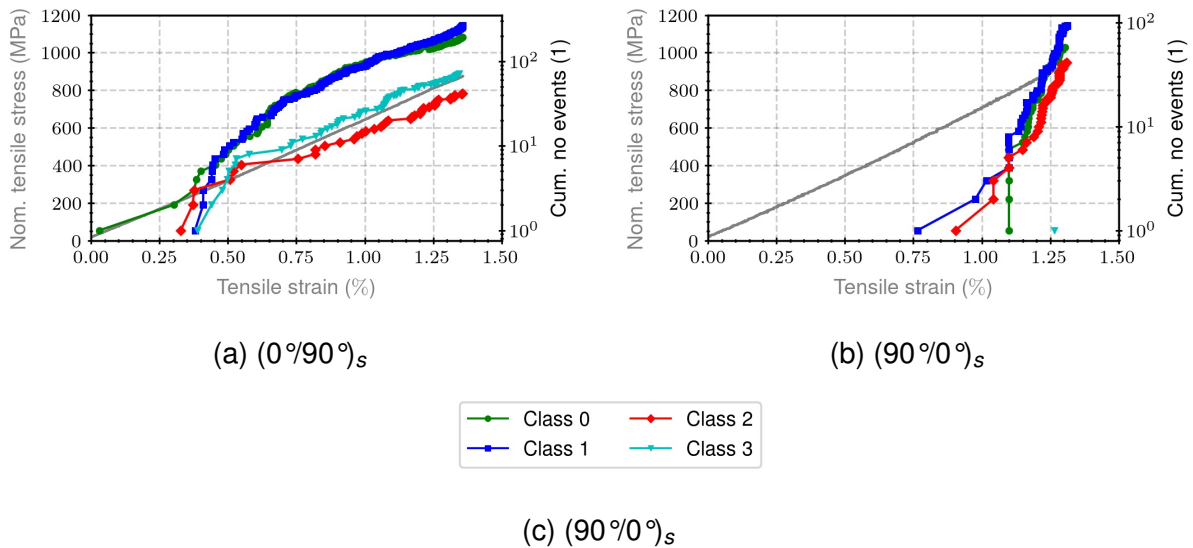


Figure 7.78: Nominal tensile stress (MPa) versus strain (%) and cumulative number of events per class (log scale) for an exemplary  $(0^\circ/90^\circ)_s$  (a) and  $(90^\circ/0^\circ)_s$  (b) specimen from stage 3 experiments.

The onsets of classes 0, 1 and 2 from  $(90^\circ/0^\circ)_s$  specimens were found to fall into the corresponding experimentally determined stress level window for TMC. These classes could therefore be associated with this damaging event in the  $(90^\circ/0^\circ)_s$  specimens. Class 3 events could again be the result of fibre filament failure at the end of the test. For the  $(90^\circ/0^\circ)_s$  specimens, AE onset could already be observed around 200 MPa for all classes. However, significant changes in AE activity around the experimentally determined stress level of TMC could mainly be observed for class 3 events. Similar to stage 2, these events - with weighted peak frequencies above 500 kHz - are likely to result from TMC in the  $90^\circ$  layer since fibre filament failure is again not expected to start around 20% of the ultimate strength. Regarding the classes 0, 1 and 2, the underlying damaging mechanism is likely to be micro cracking in the matrix material. Depending on the source-to-sensor distance, the source depth and the layer ( $0^\circ$  or  $90^\circ$ ) where micro cracking takes place, events could either be grouped to classes 0, 1 or 2.

So far, only a single sensor of a pair was considered for the evaluation. In the next step, the underlying mode (symmetric or antisymmetric) was determined that lead to the characteristics peak frequency of each identified class. With this methodology the distribution of absolute phase differences could be investigated class wise to identify the underlying type of wave mode (symmetric or antisymmetric). The resulting distributions for classes 0, 1, 2 and 3 events are visualized in figures 7.80 (a) to (d).

These distributions should be centred around absolute phase differences of either 0 or  $\pi$ , indicating that either the symmetric or antisymmetric mode determined the eval-



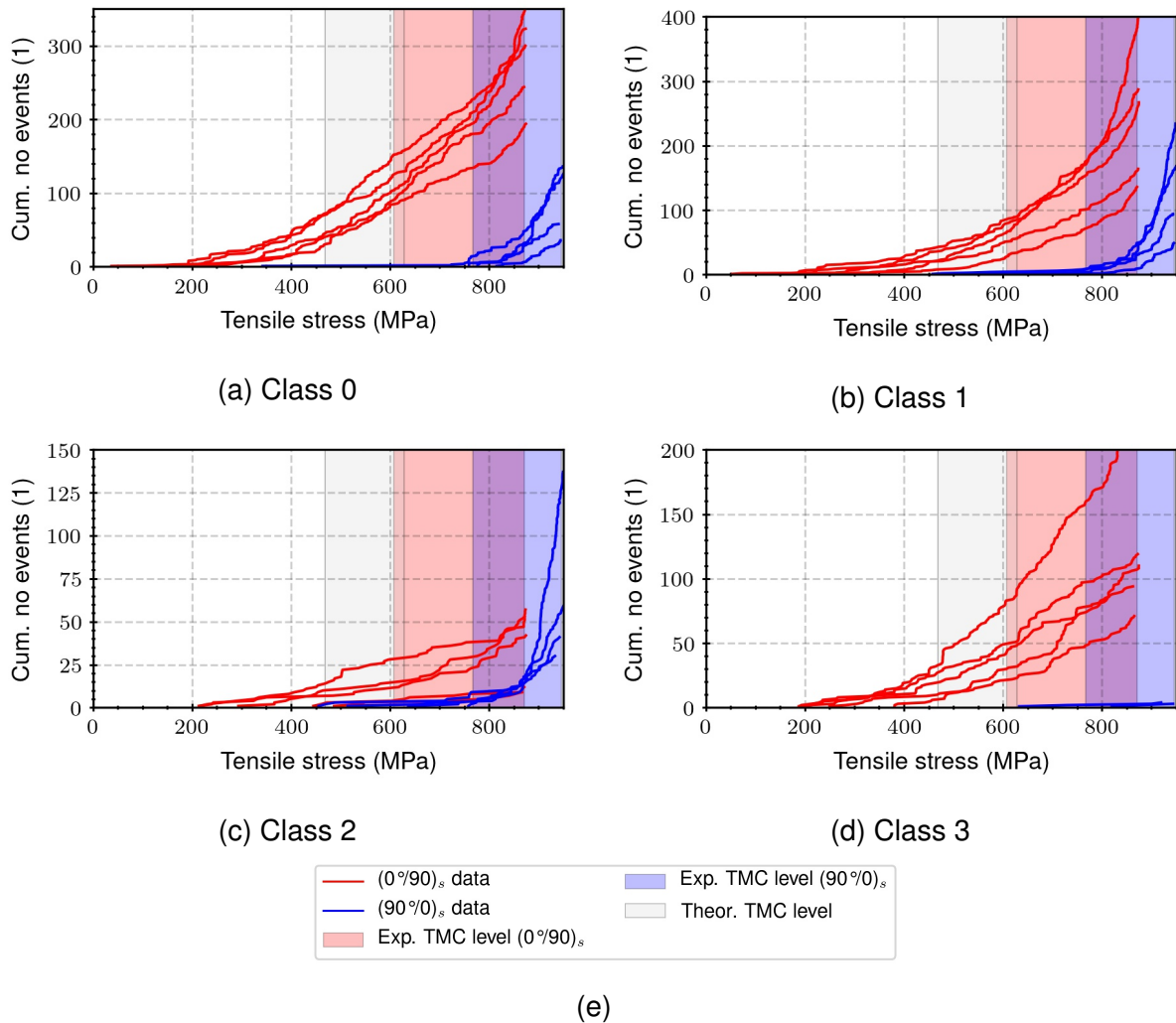


Figure 7.79: Cumulative number of events per class (1) as function of nominal tensile stress (MPa) for classes 0 to 3 (a-d) events from the  $(0^\circ/90^\circ)_s$  and  $(90^\circ/0^\circ)_s$  specimens. The theoretical onset of TMC as well as the stress levels, where TMC could be experimentally detected in each specimen type, are shown in the form of grey, red and blue colored boxes.

uation window and respective feature values. However, the distributions in figure 7.80 show also values in between 0 and  $\pi$ . These could result from potential misalignment between opposing sensors or situations where symmetric and antisymmetric signal portions are still present at the same peak frequency in the evaluation window. Despite these effects, there are significant differences between classes 0, 1 and 2 on one hand and class 3 on the other. For the majority of events from classes 0, 1 and 2, absolute phase differences between the top and bottom sensors were around  $\pi$ , indicating that the antisymmetric wave mode dominated the evaluation window and the respective features. For class 3, however, the majority of phase differences were found around 0, indicating that these features could be traced back mainly to the symmetric wave mode. Figure 7.81 gives examples for typical signals from all classes.

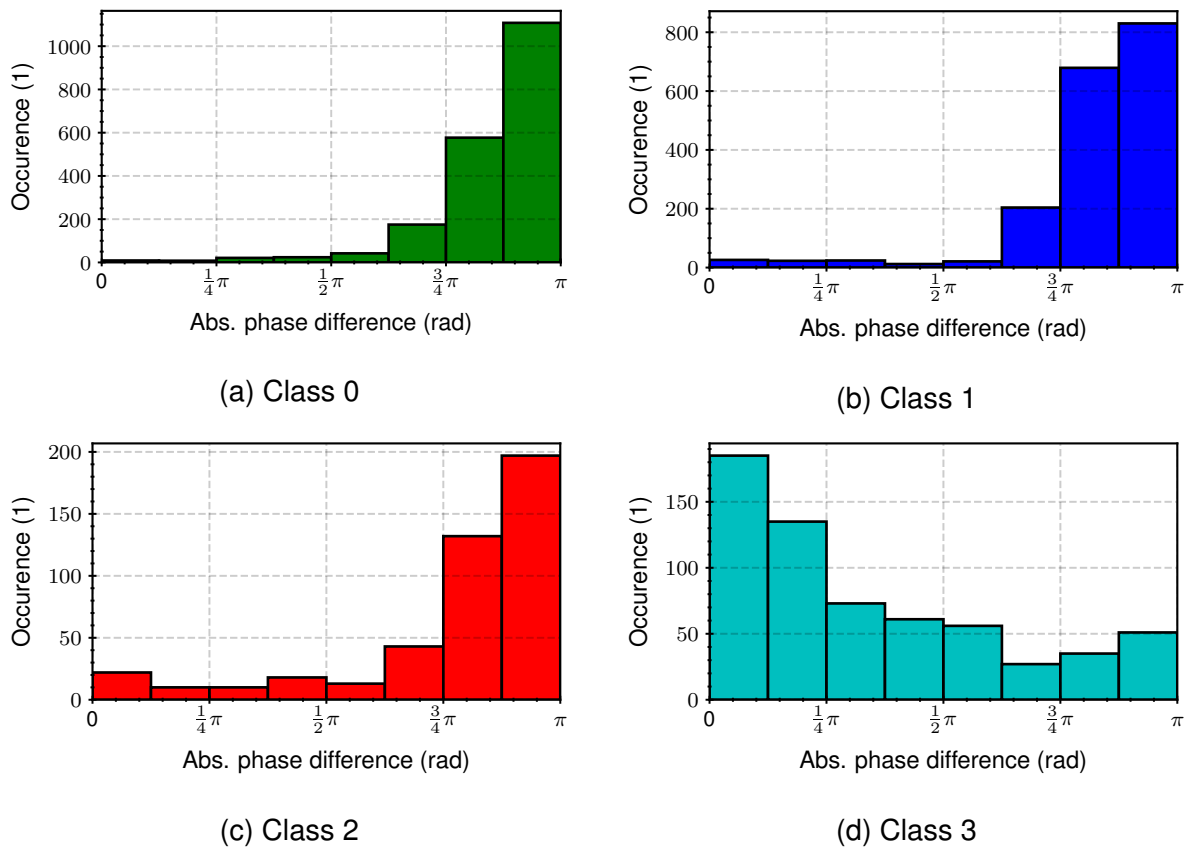


Figure 7.80: Histograms showing the distribution of absolute phase difference (rad) between opposing sensors of a pair for events from classes 0 to 3 (a-d) from  $(0^\circ/90^\circ)_s$  and  $(90^\circ/0^\circ)_s$  specimens. Signals were evaluated at the peak frequency of the corresponding evaluation sensor (1 & 3).

The fact that the symmetric mode is present in class 3 can be an explanation for the high weighted peak frequencies ( $>500$  kHz) that were encountered. Due to the low attenuation of this mode in one of the principal fibre directions, high frequency content of the source can be retained for source-to-sensor distances of 40 mm and more.

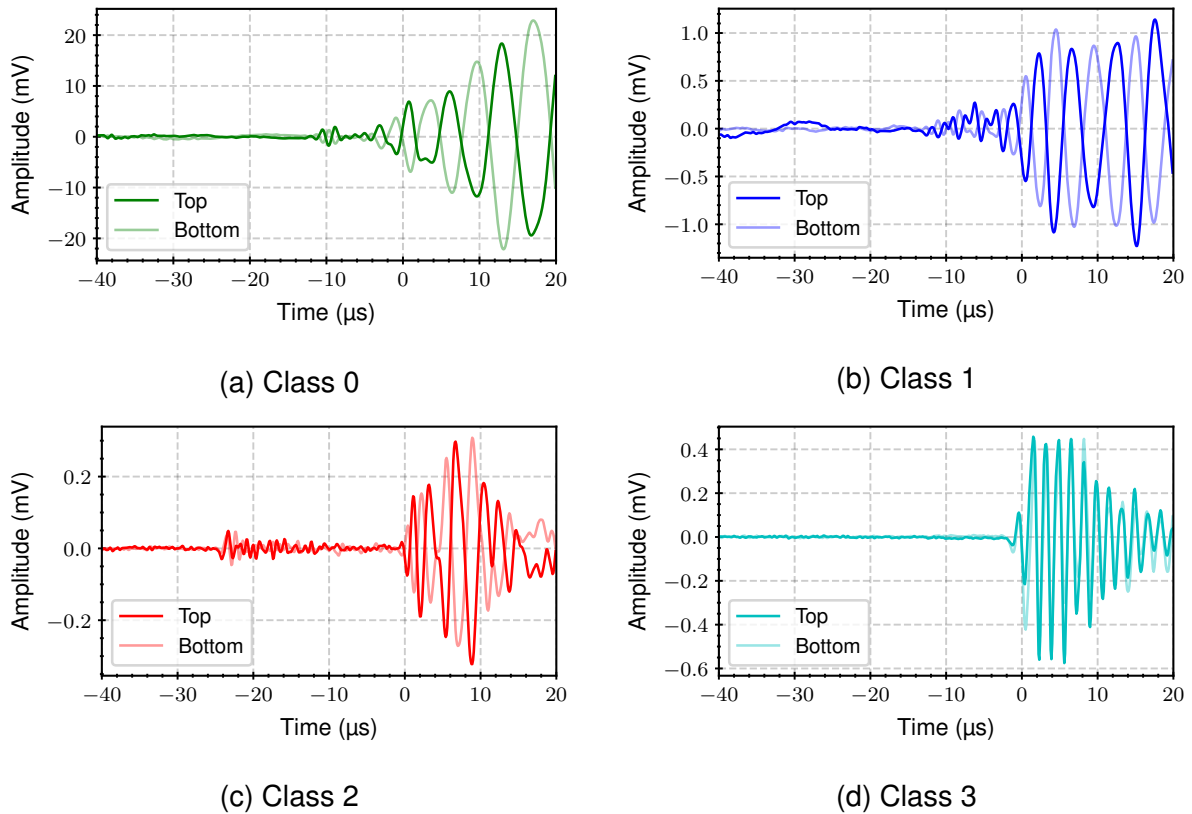


Figure 7.81: Exemplary time signals of opposing sensor signals of class 0 to 3 (a-d) events from the  $(0^\circ/90^\circ)_s$  and  $(90^\circ/0^\circ)_s$  specimens.

### Preliminary conclusion

Source depth can have a strong impact on the modal as well as frequency content of the excited acoustic waves due to the different characteristics of the symmetric and antisymmetric wave modes. The majority of acoustic events with weighted peak frequencies above 500 kHz were found in those specimens where the  $90^\circ$  layer was situated in the plane of symmetry of the laminate. These high weighted peak frequencies could be attributed to the symmetric mode, that is predominantly generated as a result of in-plane acting sources (e.g. transverse matrix cracking) in the plane of symmetry. Due to the low attenuation of this mode especially along one of the principal fibre directions, these high weighted peak frequencies could be retained and detected at propagation distances of 40 mm and more. Transverse matrix cracking in the plane of symmetry could therefore lead to peak frequencies that have been solely attributed to fibre breakage so far. Discrimination between these two damaging modes can therefore only be accomplished reliably if the influences of source depth and source-to-sensor distance are taken into account. Knowledge on the properties of the guided wave modes in the structure is thereby the key to estimate the impact of those parameters.



## 8 Conclusion

Understanding the complex mechanical degradation behaviour of fibre reinforced plastics is crucial in order to exploit their full lightweight potential. Acoustic emission analysis can be a valuable tool in this context. As an integral non-destructive testing method with very high sensitivity, AE analysis allows to characterize damage progression through the detection and analysis of released acoustic emissions from crack initiation and propagation during mechanical loading. This way, AE analysis has been successfully utilized in the scope of material characterization, component testing and quality assurance of high performance products. The discrimination between damaging events such as fibre breakage, matrix cracking or delaminations based on their resulting acoustic emissions has thereby been an ongoing challenge for more than 30 years. Damaging events have been specifically generated to catch their acoustic signatures in order to identify them in various loading scenarios. The peak frequency has been frequently considered to discriminate between fibre breakage and matrix cracking in this context. In accordance with the general theory of acoustic emission and the elastic properties of fibre and matrix material, events with high peak frequencies were attributed to fibre breakage whereas events with lower peak frequencies could be correlated with matrix cracking. Although the absolute borders varied between authors due to differences in material, measurement equipment and evaluation methodology, this common scheme could be found in many studies.

Recent studies questioned this general scheme and thereby set the starting point for this thesis. They could show that matrix cracks that take place in the inner  $90^\circ$  layers of a laminate - in particular in the plane of symmetry - could produce AE with peak frequencies that are similar to those of fibre breakage. A possible explanation was seen in the characteristics of ultrasonic guided wave modes. However, an experimental validation of these wave modes could not be accomplished so far and a comprehensive study on how and to what extent modal content could affect signal features was missing. Besides source depth the influence of source-to-sensor distance was addressed likewise as potential source for wrong interpretations due to the low pass filter characteristic of the material itself.

The goal of this thesis was to systematically investigate the influence of both - source depth and source-to-sensor distance – on the acoustic signatures of damaging events in CFRP laminates. While the focus was put on fibre breaking and transverse matrix cracking as in-plane acting damaging modes, the work was concerned with the question how their acoustic emission signature is modified when source depth and source-to-sensor distance vary. One main goal was to visualize this dependency and create awareness for the underlying mechanisms by incorporating modal acoustic

emission analysis. By evaluating the effect of source depth and source-to-sensor distance on modal content, frequency content and characteristic features, the thesis aimed to create the link between these and highlight the potential of modal acoustic emission for the interpretation of acoustic emission signals.

Balanced ( $0^\circ/90^\circ$ ) cross-ply CFRP laminates with 4 and 16 layers, respectively, have been manufactured for the investigations in this study. As fundamental basis for the interpretation of AE test results, the propagation of ultrasonic guided wave modes was characterized in the first step. Group velocities, attenuation coefficients and displacement fields were determined theoretically and validated experimentally with a new setup and evaluation methodology that allowed the individual extraction and analysis of symmetric and antisymmetric wave modes. The attenuation measurements on the 16-ply laminates could show that the attenuation of the fundamental symmetric mode  $S_0$  at around 600 kHz is comparable to the attenuation of the antisymmetric wave mode  $A_0$  at around 100 kHz for waves propagating in one of the principal fibre directions ( $0^\circ$  or  $90^\circ$ ). This result demonstrated the potential of the  $S_0$  mode of retaining high frequency source information for larger propagation distances.

Besides these differences between wave modes, a mismatch between the experimental data and the theoretical model for the attenuation of guided waves was observed that could be traced back to the anisotropy in FRP.

The impact of source depth and source-to-sensor distance on modal content and signal features was investigated first with pencil lead breaks as artificial in-plane sources. By breaking the pencil in different depths on the edge of the 16-ply plate and detecting the resulting wave at various distances and directions from the source, the resulting modal and frequency content could be systematically analysed as a function of source depth and source-to-sensor distance. The  $A_0$  amplitude was thereby found to decrease linearly with increasing source depth up to the plane of symmetry while the amplitude of the  $S_0$  remained almost constant. This change in modal content affected the frequency spectrum and resulting features such as the peak frequency because both modes could be predominantly found in specific frequency bands. The  $S_0$  mode was found at higher frequencies while the  $A_0$  mode dominated the lower frequency bands. The origin of these bands could be traced back to differences in the wavelengths and displacement fields of both modes.

Similarly, source-to-sensor distance affected the resulting frequency spectrum because modal content varied as a result of the different attenuation coefficients of both modes. With increasing source-to-sensor distance, the  $S_0$  mode became more dominant, shifting the peak frequency towards higher frequencies. The critical distance, at which the peak frequency shifted from the  $A_0$  to the  $S_0$  mode thereby decreased with

increasing source depth up to the plane of symmetry. Consequently, as a result of varying source depth and source-to-sensor distance, AE data split into two separate clusters with distinct peak frequencies that could both be attributed to a single source.

In the main study, artificial sources were replaced by real damaging events. These were systematically generated during quasi-static tensile testing in various depths and distances to the sensors in order to validate the findings from the preliminary study. Whereas the presence of different source-to-sensor distances could be promoted through the asymmetrical sensor configuration, variation of source depth could be realized through the specimen design. Both, 4- and 16-ply laminates were tested in the  $0^\circ$  and  $90^\circ$  direction to alternate the positions of the  $0^\circ$  and  $90^\circ$  layers inside the laminate. Consequently, depth position of transverse matrix cracking as well as fibre breakage could be varied between specimen types.

For reliable source localization, a new evaluation methodology was developed that allowed an in-situ characterization of the group velocity distributions of the dominant wave modes in the structure. With this methodology, the dominant triggering wave mode could be identified while the determination of time of arrival and source localization could be optimized this way.

Source-to-sensor distance showed a strong impact on signal features that could lead to wrong interpretations. The frequency centroid as well as the weighted peak frequency were considered in this context as prominent features for source classification. Whereas a steady decrease in frequency centroid could be observed with increasing source-to-sensor distance, weighted peak frequency was found to either increase or decrease. The increase could thereby be explained through a change in modal content that was accompanied by a change in frequency content. At some point, the  $S_0$  mode could dominate the evaluation window and the resulting frequency spectrum, leading to a shift in peak frequency towards higher frequencies. This result questions the state of the art procedure in which the first hit data of an event is commonly considered for source classification. High frequency characteristics of the source may, however, be suppressed by the presence of the  $A_0$  mode so that the bandwidth of the acoustic event is underestimated.

A comparison between first and second hit data of corresponding events could show that classification significantly differs for the same event depending on which hit is considered for the evaluation. Although these effects could be observed in both - 4- and 16-ply specimens - source-to-sensor distance had a stronger impact in the 4-ply laminates. Especially due to the presence of the  $S_0$  mode at frequencies of around 800 kHz, tremendous shifts in peak frequency could be mainly observed in these

specimens. These differences could be explained through the differences in thickness that directly impact dispersion behaviour of guided wave modes.

Based on the previous results, a new evaluation methodology was proposed to investigate the influence of source depth. This was accomplished with two setups: A standard setup utilizing conventional wideband, resonant sensors and an advanced setup with broadband, non-resonant sensors where the symmetry of the underlying wave mode could be identified through a special sensor configuration. Specimen edge observation was incorporated in both setups in order to identify cracks in the  $90^\circ$  layers. Digital image correlation could be successfully implemented in this context for crack detection based on local strain distribution.

Results for the 4-ply specimens showed significant differences in the AE data from the  $(0^\circ/90^\circ)_s$  and  $(90^\circ/0^\circ)_s$  specimens. Events with weighted peak frequencies above 500 kHz were predominantly found in the  $(0^\circ/90^\circ)_s$  specimens and could be traced back to TMC in the inner  $90^\circ$  plies. These high weighted peak frequencies for TMC could be explained with the characteristics of guided wave modes that were previously discovered. As an ideally in-plane acting source, TMC in the plane of symmetry would predominantly excite the  $S_0$  mode. Due to the low attenuation of this mode - especially in one of the principal fibre directions - high frequency components could be retained and detected by the sensor. With the modal acoustic emission setup, the symmetric mode could indeed be verified as the underlying mode for the majority of these high weighted peak frequency events. This could be realized by evaluating the phase shift between the signals of two opposing sensors. For the 16-ply specimens, events with high weighted peak frequencies were again limited to the specimens where the  $90^\circ$  layer was situated in the plane of symmetry. However, there were significantly less events than in the 4-ply specimens due to different dispersion characteristics.

At the end of the thesis, the scientific questions that were defined in the scope of section 3 are addressed.

*How does released modal content vary as a function of source depth and source-to-sensor distance for in-plane acoustic emission sources in CFRP laminates?*

Wave modes are predominately excited if the resulting displacement field of the crack resembles the displacement field of the wave mode in the depth that the crack occurs. Consequently, modal content of symmetric and antisymmetric wave modes changes with source depth due to their fundamentally different displacement fields. For the 16-ply laminate, a linear decrease in  $A_0$  to  $S_0$  ratio could be observed for in-plane sources with increasing source depth up to the plane of symmetry. The corresponding



slope thereby decreased with increasing frequency.

Due to the different attenuation of symmetric and antisymmetric waves modes, modal content can also substantially vary with increasing source-to-sensor distance. For the 16-ply laminate and propagation in one of the principal fibre directions, it could be shown that the attenuation of the  $A_0$  mode is significantly higher than that of the  $S_0$  mode. With increasing propagation distance, the  $S_0$  mode can therefore become more dominant.

All in all, the  $S_0$  mode is favoured for larger source-to-sensor distances and in-plane sources acting close to the plane of symmetry.

*How can a change in modal content affect signal features for source classification?  
How sensitive are features towards a change in modal content?*

Changes in modal content are likely to result in changes in frequency content due to the differences in attenuation coefficients, displacement fields (detection is generally limited to the out-of-plane component) and wavelengths (aperture effect) of ultrasonic guided wave modes. This could be demonstrated with artificial as well as real AE sources from damaging events. A change in the dominant mode from  $A_0$  to  $S_0$  could thereby lead to a substantial increase in weighted peak frequency. Frequency centroid, on the other hand, was more robust against a change in modal content.

*Can transverse matrix cracks in the plane of symmetry produce acoustic emissions with similar frequency components as fibre breaks?*

As a result of the above mentioned aspects, TMC, acting in the plane of symmetry, could indeed lead to AE with peak frequencies that are similar to those of fibre breaks since the  $S_0$  mode that is predominantly excited this way could retain high frequency components of the source. The fact that events with high weighted peak frequencies ( $> 500$  kHz) were predominantly found in those specimens where the  $90^\circ$  layer was situated in the plane of symmetry, supported this hypothesis.

*What is the critical source-to-sensor distance in cross-ply CFRP laminates where acoustic emissions from transverse matrix cracking and fibre breakage cannot be distinguished anymore? Which parameters affect this critical distance?*

This question could not be answered completely since a differentiation between fibre breaks and TMC in the inner  $90^\circ$  plies could not be achieved. Nevertheless, this distance will certainly be affected by the source depth and the individual attenuation characteristics of guided wave modes in the specimen. In the 4-ply specimens, for

example, peak frequencies of up to 800 kHz could be retained for source-to-sensor distances of 40 mm and more due to the low attenuation of the  $S_0$  mode. However, further research is necessary in order to specify this critical distance.

All in all, this thesis could demonstrate the impact of source depth and source-to-sensor distance on signal features and classification results in the scope of AE source identification in cross-ply CFRP laminates. The role of modal acoustic emission analysis was thereby highlighted as crucial in order to understand the underlying phenomena and to increase reliability of source identification results.

---

## 9 Outlook

This thesis could demonstrate the important role of modal acoustic emission analysis for source identification in CFRP. In the future work, individual properties of guided wave modes should therefore be considered for the interpretation of source classification results. Furthermore, source-to-sensor distance should be incorporated in the analysis to determine the reliability of source classification results. Finite element simulations could support in this context, in order to define critical scenarios where a discrimination between fibre breakage and matrix cracking on the basis of their resulting acoustic emissions could not be accomplished anymore. Besides material, layup, thickness, measurement equipment and propagation direction, source depth should be incorporated as a critical parameter in this context. Based on simulation results, potential features should be identified that would allow a more reliable discrimination between fibre and matrix cracking with respect to variations in source depth and source-to-sensor distance.

In addition to that, a closer look should be taken on the theoretical model that is used to describe the attenuation of guided waves in anisotropic materials. As results have shown, geometrical spreading overestimates the loss in amplitude due to the natural focusing effect of energy towards the principal fibre directions. Adjustments to this model are crucial in order to analyse the influence of source-to-sensor distance in detail.

## References

- [1] M. Sauer. Composites Market Report 2019 - The global CF- and CC- Market 2019.
- [2] FAST special edition: A350 XWB. *Airbus technical magazine*, June 2013.
- [3] How a BMW i is created.
- [4] The markets: Renewable energy (2020).
- [5] R. K. Miller, E. v. K. Hill, P. O. Moore, and American Society for Nondestructive Testing. *Nondestructive Testing Handbook. Vol. 6*. American Society for Nondestructive Testing, ASNT, 2005.
- [6] M. G. R. Sause. *In Situ Monitoring of Fiber-Reinforced Composites: Theory, Basic Concepts, Methods, and Applications*. Number 242 in Springer Series in Materials Science. Springer, 2016.
- [7] M. Saeedifar, M. Fotouhi, M. A. Najafabadi, H. H. Toudeshky, and G. Minak. Prediction of quasi-static delamination onset and growth in laminated composites by acoustic emission. *Composites Part B: Engineering*, 85:113–122, February 2016.
- [8] M. G. R. Sause, M. Ploeckl, S. Horn, and J. Scharringhausen. Bestimmung von GIc und GIIC Kennwerten von thermoplastischen Faserverbundwerkstoffen mittels Schallemissionsanalyse. In *19. Symposium Verbundwerkstoffe Und Werkstoffverbunde*, Karlsruhe, January 2013.
- [9] J. Bohse and J. Chen. Acoustic emission examination of mode I, mode II and mixed-mode I/II interlaminar fracture of unidirectional fiber-reinforced polymers. *Journal of Acoustic Emission*, 19, 2001.
- [10] A. R. Oskouei and M. Ahmadi. Fracture Strength Distribution in E-Glass Fiber Using Acoustic Emission. *Journal of Composite Materials*, 44(6):693–705, March 2010.
- [11] M. G. R. Sause and A. Monden. Comparison of predicted onset of failure mechanisms by nonlinear failure theory and by acoustic emission measurements. In *16th European Conference on Composite Materials*, Seville, 2014.
- [12] M. G. R. Sause, J. Scharringhausen, and S. Horn. Identification of Failure Mechanisms in Thermoplastic Composites by Acoustic Emission Measurements. In *The 19th International Conference on Composite Materials*, Montreal, January 2013.

- 
- [13] L. Li, S. V. Lomov, and X. Yan. Correlation of acoustic emission with optically observed damage in a glass/epoxy woven laminate under tensile loading. *Composite Structures*, 123:45–53, May 2015.
- [14] E. Schulze, A. Pietzsch, L. Schubert, and A. Ulbricht. Schallemissionsprüfung an einem neuartigen Leichtbau-Drehgestellrahmen aus Kohlenstofffaserverbundwerkstoff während statischer und dynamischer Ermüdungstests. In *22. Kolloquium Schallemission*, Karlsruhe, March 2019.
- [15] P. Liu, D. Xu, J. Li, Z. Chen, S. Wang, J. Leng, R. Zhu, L. Jiao, W. Liu, and Z. Li. Damage mode identification of composite wind turbine blade under accelerated fatigue loads using acoustic emission and machine learning. *Structural Health Monitoring*, September 2019.
- [16] J. Tang, S. Soua, C. Mares, and T.-H. Gan. A Pattern Recognition Approach to Acoustic Emission Data Originating from Fatigue of Wind Turbine Blades. *Sensors*, 17(11):2507, November 2017.
- [17] L. Schubert, E. Schulze, R. Neubeck, and B. Weihnacht. Structural Health Monitoring of fibre composite structures by Acoustic Emission Analysis. In *33rd European Conference on Acoustic Emission Testing*, Senlis, September 2018.
- [18] J. Tang, S. Soua, C. Mares, and T.-H. Gan. An experimental study of acoustic emission methodology for in service condition monitoring of wind turbine blades. *Renewable Energy*, 99:170–179, December 2016.
- [19] J. Bohse, G. W. Mair, and P. Novak. Acoustic Emission Testing of High-Pressure Composite Cylinders. *Advanced Materials Research*, 13-14:267–272, February 2006.
- [20] H. Y. Chou, A. P. Mouritz, M. K. Bannister, and A. R. Bunsell. Acoustic emission analysis of composite pressure vessels under constant and cyclic pressure. *Composites Part A: Applied Science and Manufacturing*, 70:111–120, March 2015.
- [21] C. Rowland, L. Butler, and M. Preston. Acoustic Emission Technique to Assist the Formula One Designer in Structural Design. In *26th European Conference on Acoustic Emission Testing*, Berlin, 2004.
- [22] M. Saeedifar and D. Zarouchas. Damage characterization of laminated composites using acoustic emission: A review. *Composites Part B: Engineering*, 195:108039, August 2020.

- [23] F. E. Oz, N. Ersoy, M. Mehdikhani, and S. V. Lomov. Multi-instrument in-situ damage monitoring in quasi-isotropic CFRP laminates under tension. *Composite Structures*, 196:163–180, July 2018.
- [24] F. E. Oz, N. Ersoy, and S. V. Lomov. Do high frequency acoustic emission events always represent fibre failure in CFRP laminates? *Composites Part A: Applied Science and Manufacturing*, 103:230–235, December 2017.
- [25] C. Baker, G. N. Morscher, V. V. Pujar, and J. R. Lemanski. Transverse cracking in carbon fiber reinforced polymer composites: Modal acoustic emission and peak frequency analysis. *Composites Science and Technology*, 116:26–32, September 2015.
- [26] E. Maillet, C. Baker, G. N. Morscher, V. V. Pujar, and J. R. Lemanski. Feasibility and limitations of damage identification in composite materials using acoustic emission. *Composites Part A: Applied Science and Manufacturing*, 75:77–83, August 2015.
- [27] S. K. J. Al-Jumaili. *Damage Assessment in Complex Structures Using Acoustic Emission*. PhD thesis, Cardiff University, May 2016.
- [28] H. M. Deuschle. *3D failure analysis of UD fibre reinforced composites: Puck's theory within FEA*. Inst. für Statik und Dynamik der Luft- und Raumfahrtkonstruktionen, Stuttgart, 2010.
- [29] M. Knops. *Analysis of Failure in Fiber Polymer Laminates: The Theory of Alfred Puck*. Springer, Berlin, corr. 2. print edition, 2008.
- [30] H. Schürmann. *Konstruieren mit Faser-Kunststoff-Verbunden*. Springer-Verlag Berlin Heidelberg, Berlin, Heidelberg, 2007.
- [31] A. Puck. Zur Beanspruchung und Verformung von GFK-Mehrschichtenverbund-Bauelementen. Teil 1. Grundlagen der Spannungs- und Verformungsanalyse. *Kunststoffe*, 57(4):284–293, 1967.
- [32] D. G. Aggelis, N. M. Barkoula, T. E. Matikas, and A. S. Paipetis. Acoustic structural health monitoring of composite materials : Damage identification and evaluation in cross ply laminates using acoustic emission and ultrasonics. *Composites Science and Technology*, 72(10):1127–1133, June 2012.
- [33] Y. Okabe, S. Yashiro, T. Kosaka, and N. Takeda. Detection of transverse cracks in CFRP composites using embedded fiber Bragg grating sensors. *Smart Materials and Structures*, 9(6):832–838, November 2000.

- 
- [34] P. A. Carraro and M. Quaresimin. A stiffness degradation model for cracked multidirectional laminates with cracks in multiple layers. *International Journal of Solids and Structures*, 58:34–51, April 2015.
- [35] J. L. Rose. *Ultrasonic Guided Waves in Solid Media*. Cambridge University Press, New York NY, 2014.
- [36] L. Rayleigh. On Waves Propagated along the Plane Surface of an Elastic Solid. *Proceedings of the London Mathematical Society*, s1-17(1):4–11, 1885.
- [37] H. Lamb. On waves in an elastic plate. *Proceedings of the Royal Society of London. Series A, Containing Papers of a Mathematical and Physical Character*, 93(648):114–128, March 1917.
- [38] Dispersion Calculator Software, March 2020.
- [39] R. D. Mindlin and J. Yang. *An Introduction to the Mathematical Theory of Vibrations of Elastic Plates*. World Scientific, Hackensack, N.J, 2006.
- [40] I. A. Viktorov. *Rayleigh and Lamb Waves Physical Theory and Applications*. Springer, 2013.
- [41] G. Neau. *Lamb Waves in Anisotropic Viscoelastic Plates: Study of the Wave Fronts and Attenuation*. PhD thesis, L'Université Bordeaux, 2003.
- [42] W. T. Thomson. Transmission of Elastic Waves through a Stratified Solid Medium. *Journal of Applied Physics*, 21(2):89–93, February 1950.
- [43] N. A. Haskell. The dispersion of surface waves on multilayered media. *Bulletin of the Seismological Society of America*, 43(1):17–34, January 1953.
- [44] S. I. Rokhlin and L. Wang. Stable recursive algorithm for elastic wave propagation in layered anisotropic media: Stiffness matrix method. *The Journal of the Acoustical Society of America*, 112(3):822–834, September 2002.
- [45] A. M. A. Huber and M. G. R. Sause. Classification of solutions for guided waves in anisotropic composites with large numbers of layers. *The Journal of the Acoustical Society of America*, 144(6):3236–3251, December 2018.
- [46] L. Knopoff. A matrix method for elastic wave problems. *Bulletin of the Seismological Society of America*, 54(1):431–438, 1964.
- [47] M. J. S. Lowe. Matrix techniques for modeling ultrasonic waves in multilayered media. *IEEE Transactions on Ultrasonics, Ferroelectrics, and Frequency Control*, 42(4):525–542, July 1995.

- [48] A. H. Nayfeh. *Wave Propagation in Layered Anisotropic Media: With Applications to Composites*. Elsevier, Amsterdam; New York, 1995.
- [49] M. G. R. Sause, M. A. Hamstad, and S. Horn. Finite element modeling of lamb wave propagation in anisotropic hybrid materials. *Composites Part B: Engineering*, 53:249–257, October 2013.
- [50] A. Velichko and P. D. Wilcox. Modeling the excitation of guided waves in generally anisotropic multilayered media. *The Journal of the Acoustical Society of America*, 121(1):60–69, January 2007.
- [51] H. Mei and V. Giurgiutiu. Guided wave excitation and propagation in damped composite plates. *Structural Health Monitoring*, 18(3):690–714, May 2019.
- [52] Z. A. B. Ahmad, J. M. Vivar-Perez, and U. Gabbert. Semi-analytical finite element method for modeling of lamb wave propagation. *CEAS Aeronautical Journal*, 4(1):21–33, April 2013.
- [53] F. Schubert. Numerical time-domain modeling of linear and nonlinear ultrasonic wave propagation using finite integration techniques—theory and applications. *Ultrasonics*, 42(1):221–229, April 2004.
- [54] C. A. C. Leckey, M. D. Rogge, and F. R. Parker. Guided waves in anisotropic and quasi-isotropic aerospace composites: Three-dimensional simulation and experiment. *Ultrasonics*, 54(1):385–394, January 2014.
- [55] C. A. C. Leckey, K. R. Wheeler, V. N. Hafiychuk, H. Hafiychuk, and D. A. Timuçin. Simulation of guided-wave ultrasound propagation in composite laminates: Benchmark comparisons of numerical codes and experiment. *Ultrasonics*, 84:187–200, 2018.
- [56] O. Putkis, R. P. Dalton, and A. J. Croxford. The anisotropic propagation of ultrasonic guided waves in composite materials and implications for practical applications. *Ultrasonics*, 65:390–399, February 2016.
- [57] W. H. Prosser. Advanced AE techniques in Composite Materials Research. *Journal of Acoustic Emission*, 14(1):1–11, 1996.
- [58] A. A. Pollock. Classical wave theory in practical AE testing. In *Proceedings of the 8th International AE Symposium*, pages 708–721, Tokyo (Japan), 1986.
- [59] M. Calomfirescu. *Lamb Waves for Structural Health Monitoring in Viscoelastic Composite Materials*. Number 3 in Science-Report Aus Dem Faserinstitut Bremen. Logos-Verl, Berlin, 2008.



- 
- [60] K. J. Schubert and A. S. Herrmann. On attenuation and measurement of Lamb waves in viscoelastic composites. *Composite Structures*, 94(1):177–185, December 2011.
- [61] J. Krautkrämer and H. Krautkrämer. *Werkstoffprüfung mit Ultraschall*. Springer Berlin Heidelberg, Berlin, Heidelberg, 1986.
- [62] M. Gresil and V. Giurgiutiu. Prediction of attenuated guided waves propagation in carbon fiber composites using Rayleigh damping model. *Journal of Intelligent Material Systems and Structures*, 26(16):2151–2169, November 2015.
- [63] K. Asamene, L. Hudson, and M. Sundaresan. Influence of attenuation on acoustic emission signals in carbon fiber reinforced polymer panels. *Ultrasonics*, 59:86–93, May 2015.
- [64] K. Ono and A. Gallego. Attenuation of Lamb waves in CFRP plates. *Journal of Acoustic Emission*, 30:109–123, 2012.
- [65] S. F. Wirtz, S. Bach, and D. Söffker. Experimental Results of Acoustic Emission Attenuation Due to Wave Propagation in Composites. *Proceedings of the Annual Conference of the PHM Society*, 11(1), September 2019.
- [66] D. Schmidt. *Modenselektive Übertragung von Lambwellen in Faserverbundstrukturen*. PhD thesis, TU Braunschweig, 2014.
- [67] P. Wilcox, M. Lowe, and P. Cawley. The effect of dispersion on long-range inspection using ultrasonic guided waves. *NDT & E International*, 34(1):1–9, January 2001.
- [68] C. Willberg, S. Koch, G. Mook, J. Pohl, and U. Gabbert. Continuous mode conversion of Lamb waves in CFRP plates. *Smart Materials and Structures*, 21(7):075022, July 2012.
- [69] E. Zimmermann, A. Eremin, and R. Lammering. Analysis of the continuous mode conversion of Lamb waves in fiber composites by a stochastic material model and laser vibrometer experiments. *GAMM-Mitteilungen*, 41(1), 2018.
- [70] Nihon-Hihakai-Kensa-Kyōkai, editor. *Practical Acoustic Emission Testing*. Springer, Tokyo, 2016.
- [71] C. U. Große and M. Ohtsu, editors. *Acoustic Emission Testing: Basics for Research - Applications in Civil Engineering*. Springer, Berlin, 2008.
- [72] S. Gholizadeh, Z. Leman, and B. T. H. T. Baharudin. A review of the application of acoustic emission technique in engineering. *Structural Engineering and Mechanics*, 54(6):1075–1095, 2015.

- [73] V. Carvelli, A. D'Ettoire, and S. V. Lomov. Acoustic emission and damage mode correlation in textile reinforced PPS composites. *Composite Structures*, 163:399–409, March 2017.
- [74] B. Kelkel, V. Popow, and M. Gurka. Inline quantification and localization of transverse matrix cracking in cross-ply CFRP during quasi-static tensile testing by a joint event-based evaluation of acoustic emission and passive IR thermography. *Composites Science and Technology*, 190:108013, April 2020.
- [75] T. Loutas and V. Kostopoulos. Health monitoring of carbon/carbon, woven reinforced composites. Damage assessment by using advanced signal processing techniques. Part I: Acoustic emission monitoring and damage mechanisms evolution. *Composites Science and Technology*, 69(2):265–272, February 2009.
- [76] D. D. Doan, E. Ramasso, V. Placet, S. Zhang, L. Boubakar, and N. Zerhouni. An unsupervised pattern recognition approach for AE data originating from fatigue tests on polymer–composite materials. *Mechanical Systems and Signal Processing*, 64-65:465–478, December 2015.
- [77] D. S. De Vasconcellos, F. Touchard, and L. Chocinski-Arnault. Tension-tension fatigue behaviour of woven hemp fibre reinforced epoxy composite: A multi-instrumented damage analysis. *International Journal of Fatigue*, 59:159–169, 2014.
- [78] M. Kempf, O. Skrabala, and V. Altstädt. Acoustic emission analysis for characterisation of damage mechanisms in fibre reinforced thermosetting polyurethane and epoxy. *Composites Part B: Engineering*, 56:477–483, January 2014.
- [79] A. Marec, J. H. Thomas, and R. El Guerjouma. Damage characterization of polymer-based composite materials: Multivariable analysis and wavelet transform for clustering acoustic emission data. *Mechanical Systems and Signal Processing*, 22(6):1441–1464, August 2008.
- [80] M. Fotouhi and M. A. Najafabadi. Acoustic emission-based study to characterize the initiation of delamination in composite materials. *Journal of Thermoplastic Composite Materials*, 29(4):519–537, April 2016.
- [81] M. G. R. Sause, T. Müller, A. Horoschenkoff, and S. Horn. Quantification of failure mechanisms in mode-I loading of fiber reinforced plastics utilizing acoustic emission analysis. *Composites Science and Technology*, 72(2):167–174, January 2012.

- 
- [82] J. Yousefi, M. Ahmadi, M. N. Shahri, A. R. Oskouei, and F. J. Moghadas. Damage Categorization of Glass/Epoxy Composite Material Under Mode II Delamination Using Acoustic Emission Data: A Clustering Approach to Elucidate Wavelet Transformation Analysis. *Arabian Journal for Science and Engineering*, 39(2):1325–1335, February 2014.
- [83] M. N. Shahri, J. Yousefi, M. Fotouhi, and M. A. Najfabadi. Damage evaluation of composite materials using acoustic emission features and Hilbert transform. *Journal of Composite Materials*, 50(14):1897–1907, June 2016.
- [84] J. M. Waller, C. T. Nichols, D. J. Wentzel, and R. L. Saulsberry. Use of modal acoustic emission to monitor damage progression in carbon fiber/epoxy composites. *AIP Conference Proceedings*, 1335(1):919–926, June 2011.
- [85] D. Aljets. *Acoustic Emission Source Location in Composite Aircraft Structures Using Modal Analysis*. PhD thesis, University of Glamorgan, 2011.
- [86] M. J. Eaton, R. Pullin, and K. M. Holford. Towards improved damage location using acoustic emission. *Proceedings of the Institution of Mechanical Engineers, Part C: Journal of Mechanical Engineering Science*, 226(9):2141–2153, September 2012.
- [87] J. H. Kurz, C. U. Grosse, and H.-W. Reinhardt. Strategies for reliable automatic onset time picking of acoustic emissions and of ultrasound signals in concrete. *Ultrasonics*, 43(7):538–546, June 2005.
- [88] H. Akaike. Markovian representation of stochastic processes and its application to the analysis of autoregressive moving average processes. *Annals of the Institute of Statistical Mathematics*, 26(1):363–387, December 1974.
- [89] N. Maeda. A Method for Reading and Checking Phase Time in Auto-Processing System of Seismic Wave Data. *Zisin (Journal of the Seismological Society of Japan. 2nd ser.)*, 38(3):365–379, 1985.
- [90] P. Sedlak, Y. Hirose, S. A. Khan, M. Enoki, and J. Sikula. New automatic localization technique of acoustic emission signals in thin metal plates. *Ultrasonics*, 49(2):254–262, February 2009.
- [91] D. V. Hinkley. Inference about the Change-Point from Cumulative Sum Tests. *Biometrika*, 58(3):509–523, 1971.
- [92] F. Ciampa and M. Meo. A new algorithm for acoustic emission localization and flexural group velocity determination in anisotropic structures. *Composites Part A: Applied Science and Manufacturing*, 41(12):1777–1786, December 2010.

- [93] M. Hamstad and A. O'Gallagher. A wavelet transform applied to acoustic emission signals: Part 1: Source identification. *Journal of Acoustic Emission*, 20:39–61, 2002.
- [94] Y. Ding, R. L. Reuben, and J. A. Steel. A new method for waveform analysis for estimating AE wave arrival times using wavelet decomposition. *NDT & E International*, 37(4):279–290, June 2004.
- [95] J. Jiao, C. He, B. Wu, R. Fei, and X. Wang. Application of wavelet transform on modal acoustic emission source location in thin plates with one sensor. *International Journal of Pressure Vessels and Piping*, 81(5):427–431, May 2004.
- [96] M. Surgeon and M. Wevers. One sensor linear location of acoustic emission events using plate wave theories. *Materials Science and Engineering: A*, 265(1-2):254–261, June 1999.
- [97] N. Toyama, J.-H. Koo, R. Oishi, M. Enoki, and T. Kishi. Two-dimensional AE source location with two sensors in thin CFRP plates. *Journal of Materials Science Letters*, 20(19):1823–1825, 2001.
- [98] T. Kundu, H. Nakatani, and N. Takeda. Acoustic source localization in anisotropic plates. *Ultrasonics*, 52(6):740–746, August 2012.
- [99] M. J. Eaton, R. Pullin, and K. M. Holford. Acoustic emission source location in composite materials using Delta T Mapping. *Composites Part A: Applied Science and Manufacturing*, 43(6):856–863, June 2012.
- [100] S. K. Al-Jumaili, M. R. Pearson, K. M. Holford, M. J. Eaton, and R. Pullin. Acoustic emission source location in complex structures using full automatic delta T mapping technique. *Mechanical Systems and Signal Processing*, 72-73:513–524, May 2016.
- [101] D. Crivelli, M. Guagliano, M. Eaton, M. Pearson, S. Al-Jumaili, K. Holford, and R. Pullin. Localisation and identification of fatigue matrix cracking and delamination in a carbon fibre panel by acoustic emission. *Composites Part B: Engineering*, 74:1–12, June 2015.
- [102] S. Kalafat and M. G. R. Sause. Acoustic emission source localization by artificial neural networks. *Structural Health Monitoring: An International Journal*, 14(6):633–647, November 2015.
- [103] M. Hamstad. Frequencies and Amplitudes of AE Signals in a Plate as a Function of Source Rise Time. In *29th European Conference on Acoustic Emission Testing*, page 8, Vienna, September 2010.

- 
- [104] M. Ohtsu. Acoustic emission theory for moment tensor analysis. *Research in Nondestructive Evaluation*, 6(3):169–184, September 1995.
- [105] M. Ohtsu and K. Ono. The Generalized Theory and Source Representations of Acoustic Emission. *Journal of Acoustic Emission*, 4(5), 1986.
- [106] M. V. Lysak. Development of the theory of acoustic emission by propagating cracks in terms of fracture mechanics. *Engineering Fracture Mechanics*, 55(3):443–452, October 1996.
- [107] M. G. R. Sause and S. Richler. Finite Element Modelling of Cracks as Acoustic Emission Sources. *Journal of Nondestructive Evaluation*, 34(1):4, March 2015.
- [108] J. Bohse. Acoustic emission characteristics of micro-failure processes in polymer blends and composites. *Composites Science and Technology*, 60(8):1213–1226, June 2000.
- [109] M. Giordano, L. Condelli, and L. Nicolais. Acoustic emission wave propagation in a viscoelastic plate. *Composites Science and Technology*, 59(11):1735–1743, August 1999.
- [110] M. R. Gorman. Plate wave acoustic emission. *The Journal of the Acoustical Society of America*, 90(1):358–364, July 1991.
- [111] M. R. Gorman and S. M. Ziola. Plate waves produced by transverse matrix cracking. *Ultrasonics*, 29(3):245–251, May 1991.
- [112] K. S. Downs and M. Hamstad. Wave propagation effects relative to AE source distinction of wideband AE signals from a composite pressure vessel. *Journal of Acoustic Emission*, 14(1), 1996.
- [113] M. Johnson. Broad-band transient recording and characterization of acoustic emission events in composite laminates. *Composites Science and Technology*, 60(15):2803–2818, November 2000.
- [114] J. Martínez-Jequier, A. Gallego, E. Suárez, F. J. Juanes, and A. Valea. Real-time damage mechanisms assessment in CFRP samples via acoustic emission Lamb wave modal analysis. *Composites Part B: Engineering*, 68:317–326, January 2015.
- [115] J. J. Scholey, P. D. Wilcox, M. R. Wisnom, and M. I. Friswell. Quantitative experimental measurements of matrix cracking and delamination using acoustic emission. *Composites Part A: Applied Science and Manufacturing*, 41(5):612–623, May 2010.

- [116] Y. Mizutani, K. Nagashima, M. Takemoto, and K. Ono. Fracture mechanism characterization of cross-ply carbon-fiber composites using acoustic emission analysis. *NDT & E International*, 33(2):101–110, March 2000.
- [117] R. de Oliveira and A. T. Marques. Health monitoring of FRP using acoustic emission and artificial neural networks. *Computers & Structures*, 86(3-5):367–373, February 2008.
- [118] F. Dahmene, S. Yaacoubi, M. El Mountassir, N. Bendaoud, C. Langlois, and O. Bardoux. On the modal acoustic emission testing of composite structure. *Composite Structures*, 140:446–452, April 2016.
- [119] M. Surgeon and M. Wevers. Modal analysis of acoustic emission signals from CFRP laminates. *NDT & E International*, 32(6):311–322, September 1999.
- [120] M. Eaton, M. May, C. Featherston, K. Holford, S. Hallet, and R. Pullin. Characterisation of Damage in Composite Structures using Acoustic Emission. *Journal of Physics: Conference Series*, 305:012086, July 2011.
- [121] F.-M. Yu, Y. Okabe, Q. Wu, and N. Shigeta. A novel method of identifying damage types in carbon fiber-reinforced plastic cross-ply laminates based on acoustic emission detection using a fiber-optic sensor. *Composites Science and Technology*, 135:116–122, October 2016.
- [122] J. P. McCrory, S. K. Al-Jumaili, D. Crivelli, M. R. Pearson, M. J. Eaton, C. A. Featherston, M. Guagliano, K. M. Holford, and R. Pullin. Damage classification in carbon fibre composites using acoustic emission: A comparison of three techniques. *Composites Part B: Engineering*, 68:424–430, January 2015.
- [123] B. Kelkel, J. Woll, J. Vogtmann, and M. Gurka. Potentiale, Risiken und Herausforderungen der modalen Schallemissionsanalyse bei der Quellenidentifikation in dünnwandigen Faserkunststoffverbunden. In *22. Kolloquium Schallemission*, Karlsruhe, March 2019.
- [124] Markus G. R. Sause. *Identification of Failure Mechanisms in Hybrid Materials Utilizing Pattern Recognition Techniques Applied to Acoustic Emission Signals*. PhD thesis, Universität Augsburg, December 2010.
- [125] J. Unpingco. *Python for Signal Processing*. Springer, New York, 2013.
- [126] M. Meyer. *Signalverarbeitung: analoge und digitale Signale, Systeme und Filter . mit 161 Abbildungen und Tabellen*. Lehrbuch. Springer Vieweg, Wiesbaden, 8., verbesserte auflage edition, 2017.
- [127] I. Daubechies. *Ten Lectures on Wavelets*. SIAM, June 1992.

- 
- [128] H. Suzuki, T. Kinjo, Y. Hayashi, M. Takemoto, and K. Ono. Wavelet Transform of Acoustic Emission Signals. *Journal of Acoustic Emission*, 14, 1995.
- [129] V. Arumugam, C. Suresh Kumar, C. Santulli, F. Sarasini, and A. Joseph Stanley. Identification of Failure Modes in Composites from Clustered Acoustic Emission Data Using Pattern Recognition and Wavelet Transformation. *Arabian Journal for Science and Engineering*, 38(5):1087–1102, May 2013.
- [130] R. Mohammadi, M. A. Najafabadi, M. Saeedifar, J. Yousefi, and G. Minak. Correlation of acoustic emission with finite element predicted damages in open-hole tensile laminated composites. *Composites Part B: Engineering*, 108:427–435, January 2017.
- [131] G. Qi, A. Barhorst, J. Hashemi, and G. Kamala. Discrete wavelet decomposition of acoustic emission signals from carbon-fiber-reinforced composites. *Composites Science and Technology*, 57(4):389–403, January 1997.
- [132] R. Gutkin, C. J. Green, S. Vangrattanachai, S. T. Pinho, P. Robinson, and P. T. Curtis. On acoustic emission for failure investigation in CFRP: Pattern recognition and peak frequency analyses. *Mechanical Systems and Signal Processing*, 25(4):1393–1407, May 2011.
- [133] L. Li, S. V. Lomov, X. Yan, and V. Carvelli. Cluster analysis of acoustic emission signals for 2D and 3D woven glass/epoxy composites. *Composite Structures*, 116:286–299, September 2014.
- [134] M. G. R. Sause, A. Gribov, A. R. Unwin, and S. Horn. Pattern recognition approach to identify natural clusters of acoustic emission signals. *Pattern Recognition Letters*, 33(1):17–23, January 2012.
- [135] N. Morizet, N. Godin, J. Tang, E. Maillet, M. Fregonese, and B. Normand. Classification of acoustic emission signals using wavelets and Random Forests : Application to localized corrosion. *Mechanical Systems and Signal Processing*, 70-71:1026–1037, March 2016.
- [136] G. Peeters. A large set of audio features for sound description (similarity and classification) in the CUIDADO project, 2004.
- [137] F. Eyben, M. Wöllmer, and B. Schuller. Opensmile: The munich versatile and fast open-source audio feature extractor. In *Proceedings of the 18th ACM International Conference on Multimedia*, MM '10, pages 1459–1462, Firenze, Italy, October 2010. Association for Computing Machinery.

- [138] M. Moevus, N. Godin, M. R'Mili, D. Rouby, P. Reynaud, G. Fantozzi, and G. Farizy. Analysis of damage mechanisms and associated acoustic emission in two SiCf/[Si-B-C] composites exhibiting different tensile behaviours. Part II: Unsupervised acoustic emission data clustering. *Composites Science and Technology*, 68(6):1258–1265, May 2008.
- [139] S. K. Al-Jumaili, K. M. Holford, M. J. Eaton, J. P. McCrory, M. R. Pearson, and Rhys Pullin. Classification of acoustic emission data from buckling test of carbon fibre panel using unsupervised clustering techniques. *Structural Health Monitoring: An International Journal*, 14(3):241–251, May 2015.
- [140] Mikael Johnson. Waveform based clustering and classification of AE transients in composite laminates using principal component analysis. *NDT & E International*, 35(6):367–376, September 2002.
- [141] S. Alelyani, J. Tang, and H. Liu. Feature Selection for Clustering: A Review. In C. C. Aggarwal and C. K. Reddy, editors, *Data Clustering*, pages 29–60. Chapman and Hall/CRC, first edition, September 2018.
- [142] J. G. Dy. Feature Selection for Unsupervised Learning. *Journal of Machine Learning Research*, 5:845–889, 2004.
- [143] X. He, D. Cai, and P. Niyogi. Laplacian Score for Feature Selection. In *18th International Conference on Neural Information Processing*, December 2005.
- [144] Z. Zhao and H. Liu. Spectral feature selection for supervised and unsupervised learning. In *Proceedings of the 24th International Conference on Machine Learning - ICML '07*, pages 1151–1157, Corvallis, Oregon, 2007. ACM Press.
- [145] M. Li and J. H. Yang. Feature Selection of Acoustic Emission Signal for the Slow-Speed and Heavy-Load Equipment. *Applied Mechanics and Materials*, 110-116:3199–3203, October 2011.
- [146] J. Cuadra, P. A. Vanniamparambil, K. Hazeli, I. Bartoli, and A. Koutsos. Damage quantification in polymer composites using a hybrid NDT approach. *Composites Science and Technology*, 83:11–21, June 2013.
- [147] V. Munoz, B. Valès, M. Perrin, M.L. Pastor, H. Weleman, A. Cantarel, and M. Karama. Damage detection in CFRP by coupling acoustic emission and infrared thermography. *Composites Part B: Engineering*, 85:68–75, February 2016.
- [148] A. A. Anastassopoulos and T. P. Philippidis. Clustering methodology for the evaluation of acoustic emission from composites. *Journal of Acoustic Emission*, 13(1), 1995.



- 
- [149] B.-L. Yang, X.-M. Zhuang, T.-H. Zhang, and X. Yan. Damage mode identification for the clustering analysis of AE signals in thermoplastic composites. *Journal of Nondestructive Evaluation*, 28(3-4):163–168, 2009.
- [150] V. Kostopoulos, T. H. Loutas, A. Kontsos, G. Sotiriadis, and Y. Z. Pappas. On the identification of the failure mechanisms in oxide/oxide composites using acoustic emission. *NDT & E International*, 36(8):571–580, December 2003.
- [151] D. L. Davies and D. W. Bouldin. A Cluster Separation Measure. *IEEE Transactions on Pattern Analysis and Machine Intelligence*, PAMI-1(2):224–227, April 1979.
- [152] P. J. Rousseeuw. Silhouettes: A graphical aid to the interpretation and validation of cluster analysis. *Journal of Computational and Applied Mathematics*, 20:53–65, November 1987.
- [153] T. Caliński and J. Harabasz. A dendrite method for cluster analysis. *Communications in Statistics*, 3(1):1–27, January 1974.
- [154] J. T. Tou. Dynoc—A dynamic optimal cluster-seeking technique. *International Journal of Computer & Information Sciences*, 8(6):541–547, December 1979.
- [155] J. C. Bezdek. *Pattern Recognition with Fuzzy Objective Function Algorithms*. Springer US, Boston, MA, 1981.
- [156] A. M. Bensaid, L. O. Hall, J. C. Bezdek, L. P. Clarke, M. L. Silbiger, J. A. Arrington, and R. F. Murtagh. Validity-guided (re)clustering with applications to image segmentation. *IEEE Transactions on Fuzzy Systems*, 4(2):112–123, May 1996.
- [157] N. Godin, S. Huguet, and R. Gaertner. Integration of the Kohonen's self-organising map and k-means algorithm for the segmentation of the AE data collected during tensile tests on cross-ply composites. *NDT & E International*, 38(4):299–309, June 2005.
- [158] V. Kostopoulos, T. Loutas, and K. Dassios. Fracture behavior and damage mechanisms identification of SiC/glass ceramic composites using AE monitoring. *Composites Science and Technology*, 67(7):1740–1746, June 2007.
- [159] D. Crivelli, M. Guagliano, and A. Monici. Development of an artificial neural network processing technique for the analysis of damage evolution in pultruded composites with acoustic emission. *Composites Part B: Engineering*, 56:948–959, January 2014.
- [160] S. Theodoridis and K. Koutroumbas. *Pattern Recognition*. Academic Press, Amsterdam ; Boston, second edition, 2003.

- [161] S. K. Al-Jumaili, K. M. Holford, M. J. Eaton, and R. Pullin. Parameter Correction Technique (PCT): A novel method for acoustic emission characterisation in large-scale composites. *Composites Part B: Engineering*, 75:336–344, June 2015.
- [162] S. Huguet, N. Godin, R. Gaertner, L. Salmon, and D. Villard. Use of acoustic emission to identify damage modes in glass fibre reinforced polyester. *Composites Science and Technology*, 62(10-11):1433–1444, August 2002.
- [163] A. R. Oskouei, H. Heidary, M. Ahmadi, and M. Farajpur. Unsupervised acoustic emission data clustering for the analysis of damage mechanisms in glass/polyester composites. *Materials & Design*, 37:416–422, May 2012.
- [164] A. K. Jain. Data clustering: 50 years beyond K-means. *Pattern Recognition Letters*, 31(8):651–666, June 2010.
- [165] M. Z. Rodriguez, C. H. Comin, D. Casanova, O. M. Bruno, D. R. Amancio, L. da F. Costa, and F. A. Rodrigues. Clustering algorithms: A comparative approach. *PLOS ONE*, 14(1), January 2019.
- [166] C. R. Ramirez-Jimenez, N. Papadakis, N. Reynolds, T. H. Gan, P. Purnell, and M. Pharaoh. Identification of failure modes in glass/polypropylene composites by means of the primary frequency content of the acoustic emission event. *Composites Science and Technology*, 64(12):1819–1827, September 2004.
- [167] A. Bussiba, M. Kupiec, S. Ifergane, R. Piat, and T. Böhlke. Damage evolution and fracture events sequence in various composites by acoustic emission technique. *Composites Science and Technology*, 68(5):1144–1155, April 2008.
- [168] M. Naderi, A. Kahirdeh, and M. M. Khonsari. Dissipated thermal energy and damage evolution of Glass/Epoxy using infrared thermography and acoustic emission. *Composites Part B: Engineering*, 43(3):1613–1620, April 2012.
- [169] P. J. de Groot, P. A. M. Wijnen, and R. B. F. Janssen. Real-time frequency determination of acoustic emission for different fracture mechanisms in carbon/epoxy composites. *Composites Science and Technology*, 55(4):405–412, January 1995.
- [170] A. R. Oskouei and M. Ahmadi. Acoustic Emission Characteristics of Mode I Delamination in Glass/Polyester Composites. *Journal of Composite Materials*, 44(7):793–807, April 2010.
- [171] Y. Ech-Choudany, M. Assarar, D. Scida, F. Morain-Nicolier, and B. Bellach. Unsupervised clustering for building a learning database of acoustic emission signals to identify damage mechanisms in unidirectional laminates. *Applied Acoustics*, 123:123–132, August 2017.

- 
- [172] M. G. R. Sause and S. Horn. Simulation of Acoustic Emission in Planar Carbon Fiber Reinforced Plastic Specimens. *Journal of Nondestructive Evaluation*, 29(2):123–142, June 2010.
- [173] S. Kalafat, A.-M. Zelenyak, and M. G. R. Sause. In-Situ Monitoring of Composite Failure by Computing Tomography and Acoustic Emission. In *20th International Conference on Composite Materials*, Copenhagen, July 2015.
- [174] R. D. Crouch, S. B. Clay, and C. Oskay. Experimental and computational investigation of progressive damage accumulation in CFRP composites. *Composites Part B: Engineering*, 48:59–67, May 2013.
- [175] S. Chaki, W. Harizi, G. Bourse, and M. Ourak. Multi-technique approach for non destructive diagnostic of structural composite materials using bulk ultrasonic waves, guided waves, acoustic emission and infrared thermography. *Composites Part A: Applied Science and Manufacturing*, 78:358–361, November 2015.
- [176] P. F. Liu, J. K. Chu, Y. L. Liu, and J. Y. Zheng. A study on the failure mechanisms of carbon fiber/epoxy composite laminates using acoustic emission. *Materials & Design*, 37:228–235, May 2012.
- [177] S. Barré and M. L. Benzeggagh. On the use of acoustic emission to investigate damage mechanisms in glass-fibre-reinforced polypropylene. *Composites Science and Technology*, 52(3):369–376, January 1994.
- [178] F. Pashmforoush, M. Fotouhi, and M. Ahmadi. Acoustic emission-based damage classification of glass/polyester composites using harmony search  $k$ -means algorithm. *Journal of Reinforced Plastics and Composites*, 31(10):671–680, May 2012.
- [179] J. Bohse. Acoustic Emission Examination of Polymer-Matrix Composites. *Journal of Acoustic Emission*, 22, 2004.
- [180] T. Le Gall, T. Monnier, C. Fusco, N. Godin, and S.-E. Hebaz. Towards Quantitative Acoustic Emission by Finite Element Modelling: Contribution of Modal Analysis and Identification of Pertinent Descriptors. *Applied Sciences*, 8(12):2557, December 2018.
- [181] U. Holder, C. Schreiber, E. Schulze, and L. Schubert. Zuordnung von Schallemissionsparametern zu spezifischen Schadensarten in CFK-Werkstoffen. In *21. Kolloquium Schallemission*, Fulda, March 2017.
- [182] N. Godin, P. Reynaud, and G. Fantozzi. Challenges and Limitations in the Identification of Acoustic Emission Signature of Damage Mechanisms in Composites Materials. *Applied Sciences*, 8(8):1267, July 2018.

- [183] K. Ono. Through-Transmission Characteristics of AE Sensor Couplants. *Journal of Acoustic Emission*, 34, 2017.
- [184] P. Theobald, B. Zeqiri, and J. Avison. Couplants and Their Influence on AE Sensor Sensitivity. *Journal of Acoustic Emission*, 26, 2008.
- [185] T. Monnier, S. Dia, N. Godin, and F. Zhang. Primary Calibration of Acoustic Emission Sensors by the Method of Reciprocity, Theoretical and Experimental Considerations. *Journal of Acoustic Emission*, 30, 2012.
- [186] M. A. Hamstad, A. O’Gallagher, and J. Gary. A Wavelet Transform Applied to Acoustic Emission Signals: Part 2: Source Location. *Journal of Acoustic Emission*, 20, 2002.
- [187] M. Eaton. *Acoustic Emission (AE) Monitoring of Buckling and Failure in Carbon Fibre Composite Structures*. PhD thesis, Cardiff University, September 2007.
- [188] D. G. Aggelis and T. E. Matikas. Effect of plate wave dispersion on the acoustic emission parameters in metals. *Computers & Structures*, 98-99:17–22, May 2012.
- [189] Solvay GmbH.
- [190] Data sheet Teijin Carbon – Tenax® Filament Yarn.
- [191] Data sheet CYCOM 977-2.
- [192] S. Heimbs, S. Heller, P. Middendorf, F. Hähnel, and J. Weiße. Low velocity impact on CFRP plates with compressive preload: Test and modelling. *International Journal of Impact Engineering*, 36(10-11):1182–1193, October 2009.
- [193] A. Jumahat, C. Soutis, F. R. Jones, and A. Hodzic. Fracture mechanisms and failure analysis of carbon fibre/toughened epoxy composites subjected to compressive loading. *Composite Structures*, 92(2):295–305, January 2010.
- [194] Solvay CYCOM® 977-2 Neat Epoxy Resin.
- [195] W. Hintze and D. Hartmann. Modeling of Delamination During Milling of Unidirectional CFRP. *Procedia CIRP*, 8:444–449, 2013.
- [196] C. U. Grosse and H. W. Reinhardt. Entwicklung eines Algorithmus zur automatischen Lokalisierung von Schallemissionsquellen. *Die Materialprüfung*, 41:342–347, 1999.
- [197] V. Giurgiutiu and G. Santoni-Bottai. Structural Health Monitoring of Composite Structures with Piezoelectric-Wafer Active Sensors. *AIAA Journal*, 49(3):565–581, March 2011.

- 
- [198] Data sheet VS900-M (Vallen Systeme).
- [199] Data sheet KRNBB-PCP (KRN Services).
- [200] A. V. A. Raju. *Effect of Environmental Conditions on Deformation of Thin Composite Laminates Made by 4D Printing*. PhD thesis, Concordia University, Montreal, July 2018.
- [201] B. Wetzel, P. Rosso, F. Hauptert, and K. Friedrich. Epoxy nanocomposites – fracture and toughening mechanisms. *Engineering Fracture Mechanics*, 73(16):2375–2398, November 2006.
- [202] A. C. Garg and Y. Mai. Failure mechanisms in toughened epoxy resins—A review. *Composites Science and Technology*, 31(3):179–223, January 1988.
- [203] L.-Y. Xu. Influence of Stacking Sequence on the Transverse Matrix Cracking in Continuous Fiber Crossply Laminates:. *Journal of Composite Materials*, 29(10), 1995.
- [204] P. W. M. Peters. Querrißbildung in 0/90/0 CFK-Laminaten. *Materialwissenschaft und Werkstofftechnik*, 18(9):313–322, 1987.
- [205] R. Förster and W. Knappe. Experimentelle und theoretische Untersuchungen zur Rißbildungsgrenze an zweischichtigen Wickelrohren aus Glasfaser/Kunststoff unter Innendruck. *Kunststoffe*, 8(61):583–588, 1971.
- [206] R. L. Foye. The Transverse Poisson's Ratio of Composites. *Journal of Composite Materials*, 6(2):293–295, April 1972.

# List of figures

- 2.1 Schematic evolution of damage in a cross-ply laminate under quasi-static tensile loading in the 0° direction. . . . . 5
- 2.2 Schematic displacement fields of fundamental Lamb wave modes - generated with [38]. . . . . 6
- 2.3 Dispersion diagram showing the group velocities (m/s) (a) and wavelengths (mm) (b) of guided wave modes as a function of frequency (kHz) for a 2 mm UD CFRP laminate and propagation in the fibre direction. Calculations were realized with [38]. . . . . 10
- 2.4 Group velocity (m/s) of fundamental Lamb wave modes  $A_0$  and  $S_0$  as a function of propagation direction (°) for a 2 mm UD CFRP laminate at 200 kHz. Calculations were realized with [38]. . . . . 10
- 2.5 In-plane (red), out-of-plane (blue) and shear horizontal displacement (green) components of the fundamental Lamb wave modes  $A_0$  (a,b,c) and  $S_0$  (d,e,f) as a function of frequency (200, 400 and 600 kHz) for a 2 mm UD CFRP laminate and propagation in the fibre direction. Calculations were realized with [38]. . . . . 11
- 2.6 Experimentally determined attenuation coefficients (Np/m and dB/m) of the fundamental Lamb wave modes  $A_0$  (blue) and  $S_0$  (red) in unidirectional (a,b) and cross-ply (c,d) CFRP laminates as a function of frequency (kHz) and propagation direction (a,c: 0°; b,d: 90°). . . . . 14
- 2.7 Typical setup for acoustic emission analysis. . . . . 16
- 2.8 Typical procedure for the source identification of damaging events in fibre reinforced plastics. . . . . 23
- 2.9 Typical example for an acquired waveform from a damaging event in a cross-ply CFRP laminate. The evaluation window is shown in blue. . . . 24
- 2.10 Normalized FFT spectrum of the time signal in figure 2.9. . . . . 25
- 2.11 Time signal (a) from figure 2.9 and its CWT (b) showing the normalized wavelet magnitude (1) as a function of time (µs) and frequency (kHz). The complex Morlet Wavelet was used as mother wavelet. . . . . 26
- 2.12 Normalized FFT spectrum from 2.10 with characteristic features. . . . . 27
- 2.13 Identification of clusters in an AE data set from quasi-static tensile tests of a cross-ply CFRP laminate. AE events are represented based on weighted peak frequency (kHz) and partial power 2 between 200 and 300 kHz (1). . . . . 29
- 2.14 Classification windows for damaging events in FRP that were derived by different authors [80, 114, 129, 130, 132, 133, 166, 167, 169, 178] based on the value of peak frequency (kHz) of the resulting AE. . . . . 32
- 3.15 Work schedule . . . . . 40

4.16 Layups and loading directions were selected to create transverse matrix cracking (TMC) and fibre fracture (FF) in different depths and lateral positions. . . . .	45
4.17 Autoclave cycle for the manufacturing of the Cycom 977-2 HTS40 laminates. Autoclave pressure (bar) and temperature ( $^{\circ}\text{C}$ ) are shown as a function of processing time (in min). . . . .	46
5.18 Group velocities (m/s) of the fundamental Lamb wave modes $A_0$ (a) and $S_0$ (b) for the $(0^{\circ}/90^{\circ})_{4s}$ laminate as a function of frequency (kHz), fibre volume content $V_f$ (%) and layer thickness $d_i$ ( $\mu\text{m}$ ) for propagation in the $0^{\circ}$ direction. . . . .	53
5.19 Group velocities (m/s) of the Lamb wave and shear horizontal wave modes as a function of frequency (kHz) for the $(0^{\circ}/90^{\circ})_{4s}$ (a) and $(0^{\circ}/90^{\circ})_s$ (b) laminates and propagation in the $0^{\circ}$ direction. . . . .	54
5.20 Group velocities (m/s) of the Lamb wave and shear horizontal wave modes as a function of propagation direction ( $^{\circ}$ ) for the $(0^{\circ}/90^{\circ})_{4s}$ (a) and $(0^{\circ}/90^{\circ})_s$ (b) laminates at 250 kHz. . . . .	55
5.21 Wavelengths (mm) of the Lamb wave and shear horizontal wave modes for the $(0^{\circ}/90^{\circ})_{4s}$ (a) and $(0^{\circ}/90^{\circ})_s$ (b) laminates for propagation in the $0^{\circ}$ direction. . . . .	56
5.22 In-plane (red), out-of-plane (blue) and shear horizontal displacement (green) components of the fundamental Lamb wave modes $A_0$ (a,b,c) and $S_0$ (d,e,f) as a function of frequency (200, 400 and 600 kHz) for the $(0^{\circ}/90^{\circ})_{4s}$ laminate and propagation in the $0^{\circ}$ direction. . . . .	57
5.23 In-plane (red), out-of-plane (blue) and shear horizontal displacement (green) components of the guided wave modes $A_0$ (a,b,c), $S_0$ (d,e,f) and $SH_0$ (g,h,i) as a function of frequency (200, 400 and 600 kHz) for the $(0^{\circ}/90^{\circ})_{4s}$ laminate and propagation in the $45^{\circ}$ direction. . . . .	58
5.24 Experimental setup for the characterization of Lamb wave propagation shown in side view. More views can be found in appendix E. . . . .	59
5.25 Experimental setup for the characterization of Lamb wave propagation in the laboratory (a) with a closeup of a sensor pair (b). . . . .	60
5.26 Evaluation methodology for the characterization of wave propagation. . . . .	62
5.27 Extraction of symmetric and antisymmetric time signals through the addition and subtraction of time signals from the top and bottom sensors of a sensor pair. . . . .	63
5.28 Picking the time of arrival of symmetric and antisymmetric time signals through the Hinkley picker [196]. The time of arrival is defined as the minimum in the characteristic function from equation 2.10. . . . .	64

5.29 Linear regression analysis for the determination of group velocities (a) and attenuation coefficients (b) of the symmetric (red) and antisymmetric modes (b) at an excitation frequency of 225 kHz in the $(0^\circ/90^\circ)_{4s}$ laminate.	65
5.30 Minimum number of wavelengths (1) of the $A_0$ and $S_0$ modes as a function of frequency (kHz) for the $(0^\circ/90^\circ)_{4s}$ and $(0^\circ/90^\circ)_s$ setup from table 5.9.	66
5.31 Energy portions of the symmetric and antisymmetric signals (1) as a function of excitation frequency (kHz). The values were experimentally determined from acquired signals in the $0^\circ$ fibre direction in the $(0^\circ/90^\circ)_{4s}$ (a) and $(0^\circ/90^\circ)_s$ (b) laminate.	67
5.32 Relative amplitude (1) as a function of frequency (kHz) and spatial offset (mm) for the superposition of wave packets from the $A_0$ and $S_0$ mode propagating in the $0^\circ$ direction in the $(0^\circ/90^\circ)_{4s}$ (a,b) and $(0^\circ/90^\circ)_s$ (c,d) laminate.	69
5.33 Experimental (dots) and theoretical results (lines) for the group velocities (m/s) of wave modes as a function of frequency (kHz) for the $(0^\circ/90^\circ)_{4s}$ and $(0^\circ/90^\circ)_s$ laminate in the $0^\circ$ (a,c) and $90^\circ$ (b,d) direction.	70
5.34 Attenuation coefficients $k''$ (dB/m and Np/m) as a function of frequency (kHz) for the $(0^\circ/90^\circ)_{4s}$ laminate in the $0^\circ$ (a) and $90^\circ$ (b) direction. Experimental results (dots) from symmetric (red) and antisymmetric data (blue) are shown along with results for the $S_0$ (red) and $A_0$ modes (blue) from literature as previously presented in figure 2.6.	72
6.35 Fixture for the systematic introduction of in-plane Hsu-Nielsen sources in different depths in the CFRP laminate.	75
6.36 Schematic sketch on the experimental setup for the preliminary study (a) and closeup from the setup in the laboratory (b). Dimensions are given in millimeters.	76
6.37 Normalized wavelet magnitude (1) as a function of time ( $\mu$ s) and frequency (kHz) for relative source depths of 12.5, 25.0, 37.5 and 50.0% for detection in the $45^\circ$ direction at 100 mm distance. Theoretical dispersion curves of the $S_0$ and $A_0$ mode are shown with mean values (solid line) and lower and upper borders (dashed line).	78
6.38 Maximum magnitude (1) of the $A_0$ (a,c) and $S_0$ (b,d) mode as a function of relative source depth (1) and frequency (kHz) for detection in the $0^\circ$ (c,d) and $45^\circ$ (a,b) direction at 150 mm distance from the source.	79
6.39 $A_0$ to $S_0$ ratio (1) as a function of relative source depth (1) and frequency (kHz) for detection in the $45^\circ$ (a) and $0^\circ$ (b) direction at 150 mm distance from the source.	80



6.40 Normalized FFT magnitude (1) for relative source depths of 12.5, 25.0, 37.5 and 50.0%. Signals were acquired in the 45° direction at 100 mm distance from the source. . . . .	81
6.41 Matrix plot of normalized FFT magnitude (1) as function of source-to-sensor distance (50, 100 and 150 mm) and relative source depth (12.5, 25.0, 37.5 and 50.0%). Signals were acquired in the 45° direction. . . .	82
6.42 Normalized peak frequency (1), weighted peak frequency (1) and partial power 2 between 100-200 kHz (1) as a function of relative source depth (1) and source-to-sensor distance (mm) for the 0° (b,d,f) and 45° (a,c,e) direction. . . . .	83
6.43 Weighted peak frequency (kHz) and partial power 2 between 100 and 200 kHz (1) of signals acquired at various source depths and source-to-sensor distances in the 0° and 45° direction. Evaluation window from 0 to 150 μs. . . . .	84
6.44 Weighted peak frequency (kHz) and partial power 2 between 100 and 200 kHz (1) of signals acquired at various source depths and source-to-sensor distances in the 0° and 45° direction. Evaluation window from 0 to 75 μs. . . . .	85
7.45 Specimen geometry for the quasi-static tensile tests. Dimensions are given in millimeters. . . . .	88
7.46 Experimental setup for stage 2 experiments. . . . .	91
7.47 Front (a) and rear view (b) of the fixture for stage 3 experiments. . . . .	92
7.48 Experimental setup for stage 3 experiments. . . . .	93
7.49 Top and bottom sensor signals and resulting symmetric and antisymmetric signal portions. . . . .	97
7.50 Time signals of top and bottom sensors of a pair for an event with symmetric (a) and antisymmetric (b) signal portions. The corresponding absolute phase differences were determined to $0.07\pi$ and $0.99\pi$ at the respective peak frequencies of around 600 and 200 kHz. . . . .	98
7.51 Cross-section of a $(0^\circ/90^\circ)_{4s}$ coupon specimen where DIC was utilized to track local displacement in the 90° oriented layers. The axial strain (%) in the x-direction is shown color coded. . . . .	99
7.52 Cross-section of a $(0^\circ/90^\circ)_s$ coupon specimen where DIC was utilized to identify transverse matrix cracks in the 90° oriented layers. The axial strain (%) in the x-direction is shown color coded. . . . .	100
7.53 Tensile strain (%) in x-direction as a function of relative x position (mm) from the centre of the specimen. . . . .	100

7.54 Nominal tensile stress (MPa) versus machine head displacement (mm) for the $(0^\circ/90^\circ)_s$ and $(90^\circ/0^\circ)_s$ (a) as well as $(0^\circ/90^\circ)_{4s}$ and $(90^\circ/0^\circ)_{4s}$ specimens (b). . . . .	101
7.55 Nominal tensile stress (MPa) versus tensile strain (%) for the determination of Young's modulus $E_x$ for the $(0^\circ/90^\circ)_s$ and $(90^\circ/0^\circ)_s$ (a) as well as $(0^\circ/90^\circ)_{4s}$ and $(90^\circ/0^\circ)_{4s}$ specimens (b). Strain data is based on DIC of the specimen edge. . . . .	102
7.56 Histograms showing the number of detected transverse matrix cracks in the $90^\circ$ layers (1) with respect to the nominal tensile stress (MPa) and tensile strain (%) for the $(0^\circ/90^\circ)_s$ and $(90^\circ/0^\circ)_s$ (a,b) and $(0^\circ/90^\circ)_{4s}$ and $(90^\circ/0^\circ)_{4s}$ specimens (c,d). . . . .	105
7.57 Histograms showing the differential (a,c) and cumulative (b,d) distributions of group velocities (m/s) resulting from AE events registered in the 4- (a,b) and 16-ply (c,d) specimens. The arrival times were estimated based on band-pass filtered signals following the approach from section 7.6.1. . . . .	107
7.58 Histograms showing the differential distributions of group velocities (m/s) resulting from AE events registered in the 4- (a) and 16-ply (b) specimens with fitted Gaussian distributions. . . . .	108
7.59 Partial power 2 (1) between 250 and 500 kHz and weighted peak frequency (kHz) of AE events from the $(0^\circ/90^\circ)_s$ and $(90^\circ/0^\circ)_s$ specimens with corresponding partitioning based on GMM (a) and absolute number of events per class (1) (b). Features were extracted from the first triggering evaluation sensor. . . . .	110
7.60 Weighted peak frequency (kHz) (a,c,e) and frequency centroid (kHz) (b,d,f) as a function of source-to-sensor distance (mm) for AE events from classes 1 (a,b), 2 (c,d) and 3 (e,f). Classification was based on the signals of the first triggering evaluation sensor. . . . .	111
7.61 Time signals (a,b), normalized frequency spectra (c,d) and continuous wavelet transforms (e,f) of first (a,c,e) and second hit data (b,d,f) of the same event. . . . .	112
7.62 Partial power 2 (1) between 250 and 500 kHz and weighted peak frequency (kHz) of AE events from the $(0^\circ/90^\circ)_s$ and $(90^\circ/0^\circ)_s$ specimens based on the second triggered evaluation sensor with corresponding class labels from the first (a) and heatmap showing the correlation of classes derived from first and second hit data. . . . .	113

7.63 Partial power 2 (1) between 250 and 500 kHz and weighted peak frequency (kHz) of AE events from the (0°/90°) <sub>4s</sub> and (90°/0°) <sub>4s</sub> specimens with corresponding partitioning based on GMM (a) and absolute number of events per class (1) (b). Features were extracted from the first triggering evaluation sensor. . . . .	114
7.64 Weighted peak frequency (kHz) and frequency centroid (kHz) as a function of source-to-sensor distance (mm) for AE events from classes 0 and 2 (a-d). Classification was based on the signals of the first triggering evaluation sensor. . . . .	115
7.65 Partial power 2 (1) between 250 and 500 kHz and weighted peak frequency (kHz) of AE events from the (0°/90°) <sub>4s</sub> and (90°/0°) <sub>4s</sub> specimens based on the second triggered evaluation sensor with corresponding class labels from the first (a) and heatmap showing the correlation of classes derived from first and second hit data. . . . .	116
7.66 In-plane (red), out-of-plane (blue) and shear horizontal displacement (green) components of the fundamental Lamb wave mode S <sub>0</sub> at 800 kHz for the (0°/90°) <sub>s</sub> (a) and (0°/90°) <sub>4s</sub> (b) laminate and propagation in the 0° direction. . . . .	117
7.67 Partial power 2 (1) between 250 and 500 kHz and weighted peak frequency (kHz) of AE events from the (0°/90°) <sub>s</sub> and (90°/0°) <sub>s</sub> specimens with corresponding partitioning based on GMM (a) and absolute number of events per class (1) (b). Features were extracted from the sensor that was at least 40 mm away from the source. . . . .	120
7.68 Exemplary time signals (a,c,e) and normalized frequency spectra (b,d,f) of class 0, 1 and 2 events from the (0°/90°) <sub>s</sub> and (90°/0°) <sub>s</sub> specimens. . . . .	121
7.69 Absolute number of acoustic events in each class (1) for the (0°/90°) <sub>s</sub> (a) and (90°/0°) <sub>s</sub> (b) specimens. The corresponding relative amount (%) of events in each class is given in brackets. . . . .	122
7.70 Partial power 2 (1) between 250 and 500 kHz and weighted peak frequency (kHz) of AE events from the (0°/90°) <sub>s</sub> (a) and (90°/0°) <sub>s</sub> specimens (b). Features were extracted from the sensor that was at least 40 mm away from the source. . . . .	122
7.71 Nominal tensile stress (MPa) versus strain (%) and cumulative number of events (1) per class for an exemplary (0°/90°) <sub>s</sub> (a) and (90°/0°) <sub>s</sub> (b) specimen. . . . .	123

7.72 Cumulative number of events (1) per class as function of nominal tensile stress (MPa) for class 0 (a), 1 (b) and 2 (c) events from the $(0^\circ/90^\circ)_s$ and $(90^\circ/0^\circ)_s$ specimens. The theoretical onset of TMC (grey) as well as the stress windows, where TMC could be experimentally detected for each specimen type (red and blue), are shown as well in the form of boxes. . . . .	124
7.73 Partial power 2 (1) between 250 and 500 kHz and weighted peak frequency (kHz) (a) as well as nominal tensile stress (MPa) versus weighted peak frequency (kHz) (b) of AE events from the $(0^\circ/90^\circ)_{4s}$ and $(90^\circ/0^\circ)_{4s}$ specimens. Features were extracted from the sensor that was at least 40 mm away from the source. . . . .	126
7.74 Partial power 2 (1) between 250 and 500 kHz and weighted peak frequency (kHz) of AE events from the $(0^\circ/90^\circ)_s$ and $(90^\circ/0^\circ)_s$ specimens with corresponding partition based on GMM (a) and absolute number (1) of events per class (b). Features were extracted from the sensor pair that was at least 40 mm away from the source. . . . .	127
7.75 Exemplary time signals (a,c,e,g) and normalized frequency spectra (b,d,f,h) of classes 0 to 3 events from the $(0^\circ/90^\circ)_s$ and $(90^\circ/0^\circ)_s$ specimens. . . . .	128
7.76 Absolute number of acoustic events (1) in each class for the $(0^\circ/90^\circ)_s$ (a) and $(90^\circ/0^\circ)_s$ (b) specimens. The corresponding relative amount of events (%) in each class is given in brackets. . . . .	129
7.77 Partial power 2 (1) between 250 and 500 kHz and weighted peak frequency (kHz) of AE events from the $(0^\circ/90^\circ)_s$ (a) and $(90^\circ/0^\circ)_s$ specimens (b). Features were extracted from the sensor pair that was at least 40 mm away from the source. . . . .	129
7.78 Nominal tensile stress (MPa) versus strain (%) and cumulative number of events per class (log scale) for an exemplary $(0^\circ/90^\circ)_s$ (a) and $(90^\circ/0^\circ)_s$ (b) specimen from stage 3 experiments. . . . .	130
7.79 Cumulative number of events per class (1) as function of nominal tensile stress (MPa) for classes 0 to 3 (a-d) events from the $(0^\circ/90^\circ)_s$ and $(90^\circ/0^\circ)_s$ specimens. The theoretical onset of TMC as well as the stress levels, where TMC could be experimentally detected in each specimen type, are shown in the form of grey, red and blue colored boxes. . . . .	131
7.80 Histograms showing the distribution of absolute phase difference (rad) between opposing sensors of a pair for events from classes 0 to 3 (a-d) from $(0^\circ/90^\circ)_s$ and $(90^\circ/0^\circ)_s$ specimens. Signals were evaluated at the peak frequency of the corresponding evaluation sensor (1 & 3). . . . .	132
7.81 Exemplary time signals of opposing sensor signals of class 0 to 3 (a-d) events from the $(0^\circ/90^\circ)_s$ and $(90^\circ/0^\circ)_s$ specimens. . . . .	133

B.1 Exemplary cross-sections of $(0^\circ/90^\circ)_s$ laminates. The cuts were realized along the $0^\circ$ (a) and $90^\circ$ direction (b). . . . .	172
B.2 Exemplary cross-section of $(0^\circ/90^\circ)_{4s}$ laminate. The cut was realized along the $0^\circ$ direction. . . . .	173
B.3 Exemplary cross-section of $(0^\circ/90^\circ)_{4s}$ laminate. The cut was realized along the $90^\circ$ direction. . . . .	174
D.4 Group velocities (m/s) (a,b,c) of Lamb wave modes in $(0^\circ/90^\circ)_s$ laminates for propagation in the $0^\circ$ , $45^\circ$ and $90^\circ$ direction. . . . .	177
D.5 Wavelengths (mm) (a,b,c) of Lamb wave modes in $(0^\circ/90^\circ)_s$ laminates for propagation in the $0^\circ$ , $45^\circ$ and $90^\circ$ direction. . . . .	178
D.6 Group velocities (m/s) (a,b,c) of Lamb wave modes in $(0^\circ/90^\circ)_{4s}$ laminates for propagation in the $0^\circ$ , $45^\circ$ and $90^\circ$ direction. . . . .	179
D.7 Wavelengths (mm) (a,b,c) of Lamb wave modes in $(0^\circ/90^\circ)_{4s}$ laminates for propagation in the $0^\circ$ , $45^\circ$ and $90^\circ$ direction. . . . .	180
E.8 Side view . . . . .	181
E.9 Top view . . . . .	182
E.10 Isometric view . . . . .	183
F.11 Minimum number of wavelengths (1) of the $A_0$ and $S_0$ mode as a function of frequency (kHz) for the $(0^\circ/90^\circ)_{4s}$ and $(0^\circ/90^\circ)_s$ setups from table 5.9. . . . .	184
F.12 Energy portions of symmetric and antisymmetric signals (1) as a function of excitation frequency (kHz). The values were experimentally determined from acquired signals in the $0^\circ$ and $90^\circ$ direction in the $(0^\circ/90^\circ)_{4s}$ (a,b) and $(0^\circ/90^\circ)_s$ (c,d) laminate. . . . .	185
F.13 Relative amplitude (1) as a function of frequency (kHz) and spatial offset (mm) for the superposition of wave packets from the $A_0$ and $S_0$ mode propagating in the $0^\circ$ direction in the $(0^\circ/90^\circ)_{4s}$ (a,b) and $(0^\circ/90^\circ)_s$ (c,d) laminate. . . . .	186
F.14 Relative amplitude (1) as a function of frequency (kHz) and spatial offset (mm) for the superposition of wave packets from the $A_0$ and $S_0$ mode propagating in the $90^\circ$ direction in the $(0^\circ/90^\circ)_{4s}$ (a,b) and $(0^\circ/90^\circ)_s$ (c,d) laminate. . . . .	187
G.15 Filtered (full color) and non-filtered (pale color) experimental results (dots) as well as theoretical results (lines) for the group velocities of wave modes as a function of frequency for the $(0^\circ/90^\circ)_{4s}$ and $(0^\circ/90^\circ)_s$ laminate in the $0^\circ$ (a,c) and $90^\circ$ (b,d) direction. . . . .	188
H.16 Matrix plot of normalized time signals as function of source-to-sensor distance (50, 100 and 150 mm) and relative source depth (12.5, 25.0, 37.5 and 50.0%). Signals were acquired in the $45^\circ$ direction. . . . .	189

H.17	Matrix plot of normalized time signals as function of source-to-sensor distance (50, 100 and 150 mm) and relative source depth (12.5, 25.0, 37.5 and 50.0%). Signals were acquired in the 0° direction. . . . .	190
I.18	Matrix plot of normalized CWTs as function of source-to-sensor distance (50, 100 and 150 mm) and relative source depth (12.5, 25.0, 37.5 and 50.0%). Signals were acquired in the 45° direction. . . . .	191
I.19	Matrix plot of normalized CWTs as function of source-to-sensor distance (50, 100 and 150 mm) and relative source depth (12.5, 25.0, 37.5 and 50.0%). Signals were acquired in the 0° direction. . . . .	192
J.20	Matrix plot of normalized FFT spectra as function of source-to-sensor distance (50, 100 and 150 mm) and relative source depth (12.5, 25.0, 37.5 and 50.0%). Signals were acquired in the 45° direction. . . . .	193
J.21	Matrix plot of normalized FFT spectra as function of source-to-sensor distance (50, 100 and 150 mm) and relative source depth (12.5, 25.0, 37.5 and 50.0%). Signals were acquired in the 0° direction. . . . .	194
K.22	Nominal tensile stress (MPa) versus machine head displacement (mm) for the (0°/90°) <sub>s</sub> (a) and (90°/0°) <sub>s</sub> (b) specimens. . . . .	195
K.23	(0°/90°) <sub>s</sub> (a) and (90°/0°) <sub>s</sub> (b) specimens after mechanical testing. . . .	195
K.24	Nominal tensile stress (MPa) versus machine head displacement (mm) for the (0°/90°) <sub>4s</sub> (a) and (90°/0°) <sub>4s</sub> (b) specimens. . . . .	196
K.25	(0°/90°) <sub>4s</sub> (a) and (90°/0°) <sub>4s</sub> (b) specimens after mechanical testing. . .	196
L.26	Weighted peak frequency (kHz) as a function of source-to-sensor distance (mm) for AE events from classes 0 to 4 (a-e). Classification was based on the signals of the first triggering evaluation sensor. . . . .	197
L.27	Frequency centroid (kHz) as a function of source-to-sensor distance (mm) for AE events from classes 0 to 4 (a-e). Classification was based on the signals of the first triggering evaluation sensor. . . . .	198
L.28	Weighted peak frequency (kHz) as a function of source-to-sensor distance (mm) for AE events from classes 0 to 3 (a-d). Classification was based on the signals of the first triggering evaluation sensor. . . . .	199
L.29	Frequency centroid (kHz) as a function of source-to-sensor distance (mm) for AE events from classes 0 to 3 (a-d). Classification was based on the signals of the first triggering evaluation sensor. . . . .	200
M.30	Exemplary time signals (a,c) and normalized frequency spectra (b,d) of class 0 events from (0°/90°) <sub>s</sub> and (90°/0°) <sub>s</sub> specimens where more than one mode was present in the evaluation window. . . . .	201

# List of tables

- 4.1 Properties of the 12k HTS40 carbon fibre (a) and Cycom 977-2 toughened epoxy resin (b) [190, 191, 193, 194] . . . . . 43
- 4.2 Statistical overview on the properties of the supplied Cycom 977-2-35-12kHTS-134-1500 prepreg material . . . . . 44
- 4.3 Properties of the manufactured  $(0^\circ/90^\circ)_s$  laminates . . . . . 48
- 4.4 Properties of the manufactured  $(0^\circ/90^\circ)_{4s}$  laminates . . . . . 48
- 5.5 Properties of the manufactured cross-ply laminates based on the combination of  $(0^\circ/90^\circ)_s$  and  $(0^\circ/90^\circ)_{4s}$  properties from tables 4.3 and 4.4 . . 51
- 5.6 Elastic properties of Cycom 977-2 HTS40 from [195]. The fibre volume content was estimated based on a rule of mixture [30] on the basis of Young's modulus  $E_{||}$ . . . . . 52
- 5.7 Calculated elastic properties of Cycom 977-2 HTS40 with 53.7, 55.8 and 57.9% fibre volume content . . . . . 52
- 5.8 Vallen AMSY 5 acquisition parameters for the characterization of wave propagation . . . . . 60
- 5.9 Sensor and actuator positions for the characterization of wave propagation according to the coordinate system in figure 5.24 . . . . . 61
- 5.10 Summary on resulting frequency windows for the  $(0^\circ/90^\circ)_s$  and  $(0^\circ/90^\circ)_{4s}$  laminates for propagation in the  $0^\circ$  and  $90^\circ$  direction . . . . . 69
- 6.11 Vallen AMSY 5 acquisition parameters for the preliminary study . . . . . 76
- 7.12 Test matrix for the quasi-static tensile tests in the scope of the main study 87
- 7.13 Statistical overview on environmental conditions during quasi-static tensile tests . . . . . 89
- 7.14 Vallen AMSY 5 acquisition parameters for stage 2 experiments . . . . . 91
- 7.15 Vallen AMSY 5 acquisition parameters for stage 3 experiments . . . . . 93
- 7.16 Statistical overview on the tensile strengths  $\sigma_m$  (MPa) derived from quasi-static tensile tests in the  $0^\circ$  direction . . . . . 101
- 7.17 Tensile stress limits (MPa) for stage 2 and 3 experiments . . . . . 102
- 7.18 Statistical overview on Young's moduli  $E_x$  (GPa) derived from quasi-static tensile tests in the  $0^\circ$  direction . . . . . 103
- A1 Properties of the manufactured  $(0^\circ/90^\circ)_s$  laminates from batch 1 . . . . . 170
- A2 Properties of the manufactured  $(0^\circ/90^\circ)_s$  laminates from batch 2 . . . . . 170
- A3 Properties of the manufactured  $(0^\circ/90^\circ)_{4s}$  laminates from batch 1 . . . . . 171
- A4 Properties of the manufactured  $(0^\circ/90^\circ)_{4s}$  laminates from batch 2 . . . . . 171

## A Laminate properties

Overview on properties of the manufactured cross-ply laminates. The corresponding measurement procedures are described in section 4.4.

### A.1 $(0^\circ/90^\circ)_s$ laminates

Table A1: Properties of the manufactured  $(0^\circ/90^\circ)_s$  laminates from batch 1

Property	$N$	$\mu$	$\sigma$	Min	Max
Laminate thickness $d$ (mm)	12	0.53	0.01	0.51	0.55
Laminate density $\rho$ (g/cm <sup>3</sup> )	5	1.58	0.005	1.575	1.587
$T_g$ , Onset $E'$ (°C), 1 <sup>st</sup> cycle	5	174.0	2.2	171.6	177.5
$T_g$ , Onset $E'$ (°C), 2 <sup>nd</sup> cycle	5	189.7	0.9	188.8	191.0
$T_g$ , Peak $\tan(\delta)$ (°C), 1 <sup>st</sup> cycle	5	197.7	0.8	196.9	198.8
$T_g$ , Peak $\tan(\delta)$ (°C), 2 <sup>nd</sup> cycle	5	210.5	0.6	209.7	211.3
Layer thickness $d_i$ (μm)	54	121.8	8.8	96.2	138.0
Fibre volume content $V_f$ (Vol.-%)	18	56.7	1.7	52.7	59.4

Table A2: Properties of the manufactured  $(0^\circ/90^\circ)_s$  laminates from batch 2

Property	$N$	$\mu$	$\sigma$	Min	Max
Laminate thickness $d$ (mm)	12	0.51	0.01	0.50	0.54
Laminate density $\rho$ (g/cm <sup>3</sup> )	5	1.578	0.007	1.572	1.589
$T_g$ , Onset $E'$ (°C), 1 <sup>st</sup> cycle	5	187.3	0.9	186.1	188.6
$T_g$ , Onset $E'$ (°C), 2 <sup>nd</sup> cycle	5	199.2	0.4	198.6	199.7
$T_g$ , Peak $\tan(\delta)$ (°C), 1 <sup>st</sup> cycle	5	208.7	0.4	208.3	209.2
$T_g$ , Peak $\tan(\delta)$ (°C), 2 <sup>nd</sup> cycle	5	219.2	0.3	218.8	219.5
Layer thickness $d_i$ (μm)	54	132.7	5.4	121.3	153.2
Fibre volume content $V_f$ (Vol.-%)	18	54.2	1.7	51.8	57.9



## A.2 (0°/90°)<sub>4s</sub> laminates

Table A3: Properties of the manufactured (0°/90°)<sub>4s</sub> laminates from batch 1

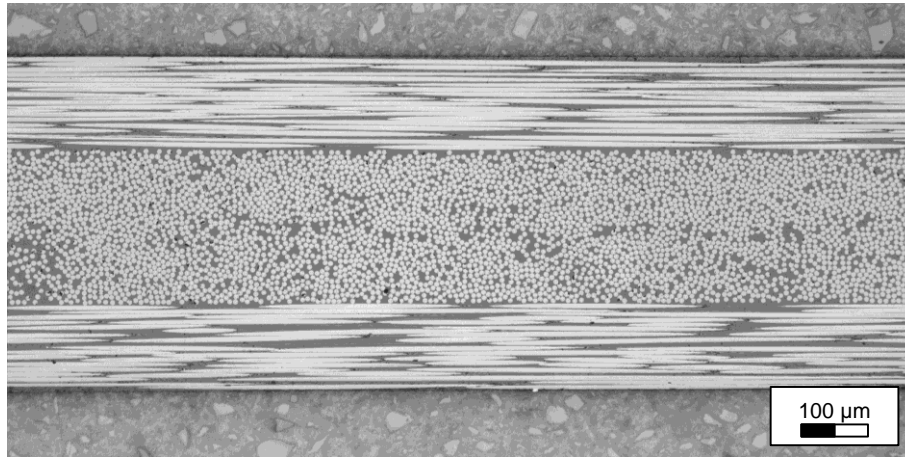
Property	<i>N</i>	$\mu$	$\sigma$	<i>Min</i>	<i>Max</i>
Laminate thickness <i>d</i> (mm)	12	2.06	0.05	2.00	2.14
Laminate density $\rho$ (g/cm <sup>3</sup> )	5	1.582	0.003	1.576	1.585
<i>T<sub>g</sub></i> , Onset <i>E'</i> (°C), 1 <sup>st</sup> cycle	5	171.2	0.8	170.0	172.5
<i>T<sub>g</sub></i> , Onset <i>E'</i> (°C), 2 <sup>nd</sup> cycle	5	179.4	1.0	178.0	180.9
<i>T<sub>g</sub></i> , Peak tan( $\delta$ ) (°C), 1 <sup>st</sup> cycle	5	196.8	0.3	196.4	197.2
<i>T<sub>g</sub></i> , Peak tan( $\delta$ ) (°C), 2 <sup>nd</sup> cycle	5	205.4	0.5	204.8	206.2
Layer thickness <i>d<sub>i</sub></i> (μm)	270	128.2	7.5	106.9	157.4
Fibre volume content <i>V<sub>f</sub></i> (Vol.-%)	18	56.8	2.0	52.8	59.1

Table A4: Properties of the manufactured (0°/90°)<sub>4s</sub> laminates from batch 2

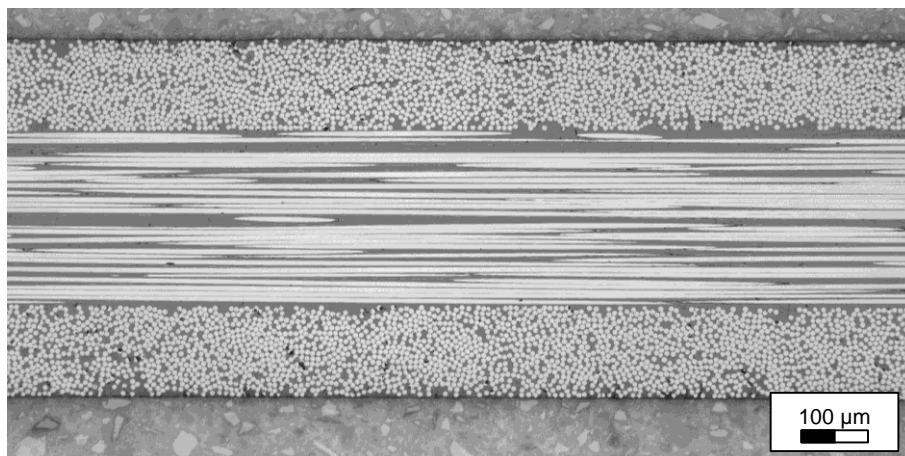
Property	<i>N</i>	$\mu$	$\sigma$	<i>Min</i>	<i>Max</i>
Laminate thickness <i>d</i> (mm)	12	2.04	0.02	2.00	2.06
Laminate density $\rho$ (g/cm <sup>3</sup> )	5	1.571	0.003	1.567	1.576
<i>T<sub>g</sub></i> , Onset <i>E'</i> (°C), 1 <sup>st</sup> cycle	5	183.1	0.6	182.2	183.8
<i>T<sub>g</sub></i> , Onset <i>E'</i> (°C), 2 <sup>nd</sup> cycle	5	190.2	0.9	189.1	191.5
<i>T<sub>g</sub></i> , Peak tan( $\delta$ ) (°C), 1 <sup>st</sup> cycle	5	207.5	0.8	206.9	208.8
<i>T<sub>g</sub></i> , Peak tan( $\delta$ ) (°C), 2 <sup>nd</sup> cycle	5	214.7	0.7	214.2	215.9
Layer thickness <i>d<sub>i</sub></i> (μm)	270	132.9	8.2	115.0	156.5
Fibre volume content <i>V<sub>f</sub></i> (Vol.-%)	18	55.3	1.8	52	58.6

## B Microscopic images

### B.1 $(0^\circ/90^\circ)_s$ laminates



(a)



(b)

Figure B.1: Exemplary cross-sections of  $(0^\circ/90^\circ)_s$  laminates. The cuts were realized along the  $0^\circ$  (a) and  $90^\circ$  direction (b).

## B.2 $(0^\circ/90^\circ)_{4S}$ laminates



Figure B.2: Exemplary cross-section of  $(0^\circ/90^\circ)_{4S}$  laminate. The cut was realized along the  $0^\circ$  direction.

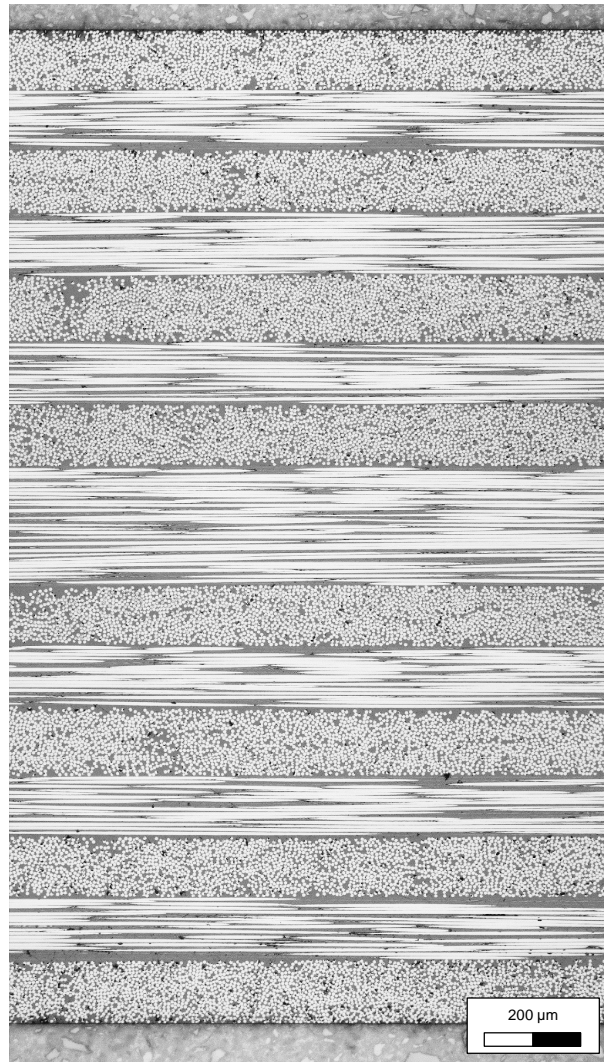


Figure B.3: Exemplary cross-section of  $(0^\circ/90^\circ)_{4s}$  laminate. The cut was realized along the  $90^\circ$  direction.

## C Recalculation of elastic properties

This section deals with the recalculation of elastic properties through analytical models from the literature [30]. The presented approach was utilized to recalculate the elastic constants of a single layer of Cycom 977-2 HTS40 based on reference properties that were given in the literature [190, 191, 195]. Recalculation had to be done due to the differences in fibre volume content between the reference ( $V_f$ ) and manufactured ( $V'_f$ ) laminates. In order to fully describe the elastic properties of a single layer, the elastic moduli  $E'_{||}$ ,  $E'_{\perp}$ ,  $G'_{\perp||}$  and Poisson's ratios  $\nu'_{\perp||}$  and  $\nu'_{\perp\perp}$  are derived from the original properties in the following. Derived properties are denoted with an apostrophe (') to distinguish them from the original properties in the following.

Due to a linear relationship of Young's modulus  $E_{||}$  with fibre volume content  $V_f$ , the Young's modulus  $E'_{||}$  at fibre volume content  $V'_f$  can be directly derived from the original value  $E_{||}$  according to equation C.28 [30].

$$E'_{||} = E_{||} \cdot \frac{V'_f}{V_f} \quad (\text{C.28})$$

For the Young's modulus  $E'_{\perp}$  perpendicular to the fibre direction, Puck derived the following relationship [31]:

$$E'_{\perp} = \frac{E_m}{1 - \nu_m^2} \cdot \left( \frac{1 + 0.85 \cdot V_f'^2}{(1 - V_f')^{1.25} + \frac{E_m}{(1 - \nu_m^2) \cdot E_{f\perp}} \cdot V_f'} \right) \quad (\text{C.29})$$

The Young's modulus  $E_{f\perp}$  of the single fibre can thereby be determined from the original properties by rearranging equation C.29 and inserting the original properties. This leads to the relationship

$$E_{f\perp} = \frac{1}{\frac{1}{E_{\perp}} \cdot \frac{1}{V_f} \cdot (1 + 0.85 \cdot V_f^2) - \frac{(1 - \nu_m^2)}{E_m} \cdot \frac{(1 - V_f)^{1.25}}{V_f}} \quad (\text{C.30})$$

To obtain the shear modulus  $G_{\perp||}$ , the semi-empirical relationship derived by Förster [205] can be utilized. The shear modulus  $G_{\perp||}$  follows as a function of fibre volume fraction  $V_f$  and shear moduli of the matrix ( $G_m$ ) and the fibre ( $G_{f\perp||}$ ) according to

$$G'_{\perp||} = G_m \cdot \frac{1 + 0.4 \cdot V_f'^{0.5}}{(1 - V_f')^{1.45} + \frac{G_m}{G_{f\perp||}} \cdot V_f'} \quad (\text{C.31})$$

The shear modulus  $G_{f\perp||}$  in equation C.31 can, in turn, be determined from the original values by again rearranging the equation and inserting the original values (see equation C.32).

$$G_{f\perp||} = \frac{1}{\frac{1}{G_{\perp||}} \cdot \frac{1}{V_f} \cdot (1 + 0.4 \cdot V_f^{0.5}) - \frac{(1 - V_f)^{1.45}}{G_m \cdot V_f}} \quad (\text{C.32})$$

Based on a rule of mixture, the Poisson's ratio  $\nu'_{\perp\parallel}$  can be directly estimated. It follows as a function of fibre volume content  $V'_f$  and Poisson's ratios of fibre  $\nu_{f\perp\parallel}$  and matrix  $\nu_m$  according to equation C.33.

$$\nu'_{\perp\parallel} = V'_f \cdot \nu_{f\perp\parallel} + (1 - V'_f) \cdot \nu_m. \quad (\text{C.33})$$

The unknown Poisson's ratio  $\nu_{f\perp\parallel}$  can be derived from the original properties according to

$$\nu_{f\perp\parallel} = \nu_{\perp\parallel} - \frac{(1 - V_f) \cdot \nu_m}{V_f}. \quad (\text{C.34})$$

By combining Poisson's ratios  $\nu'_{\perp\parallel}$  and  $\nu_f$ , Young's moduli  $E'_{\parallel}$  and  $E_m$ , as well as fibre volume content  $V'_f$ , the Poisson's ratio  $\nu'_{\perp\perp}$  can be estimated according to the refined rule of mixture from Foye [206] as follows:

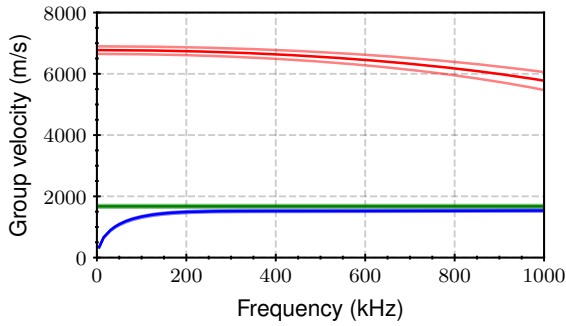
$$\nu'_{\perp\perp} = V'_f \cdot \nu_f + (1 - V'_f) \cdot \nu_m \cdot \left( \frac{1 + \nu_m - \nu'_{\perp\parallel} \cdot \frac{E_m}{E'_{\parallel}}}{1 - \nu_m^2 + \nu_m \cdot \nu'_{\perp\parallel} \cdot \frac{E_m}{E'_{\parallel}}} \right) \quad (\text{C.35})$$

The Poisson's ratio  $\nu_f$  of the fibre can thereby be derived again from the original laminate properties following equation C.36.

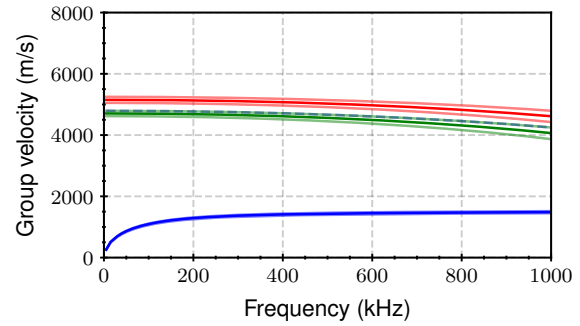
$$\nu_f = \frac{\left( \nu_{\perp\perp} - \left( (1 - V_f) \cdot \nu_m \cdot \left( \frac{1 + \nu_m - \nu_{\perp\parallel} \cdot \frac{E_m}{E_{\parallel}}}{1 + \nu_m^2 + \nu_m \cdot \nu_{\perp\parallel} \cdot \frac{E_m}{E_{\parallel}}} \right) \right) \right)}{V_f} \quad (\text{C.36})$$

## D Theoretical dispersion diagrams

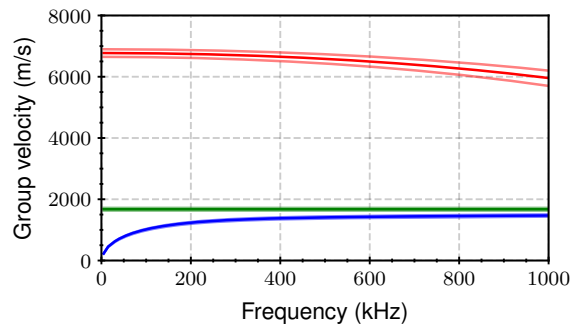
### D.1 $(0^\circ/90^\circ)_s$ laminates



(a) Group velocity,  $0^\circ$  direction



(b) Group velocity,  $45^\circ$  direction



(c) Group velocity,  $90^\circ$  direction

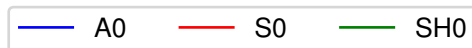


Figure D.4: Group velocities (m/s) (a,b,c) of Lamb wave modes in  $(0^\circ/90^\circ)_s$  laminates for propagation in the  $0^\circ$ ,  $45^\circ$  and  $90^\circ$  direction.

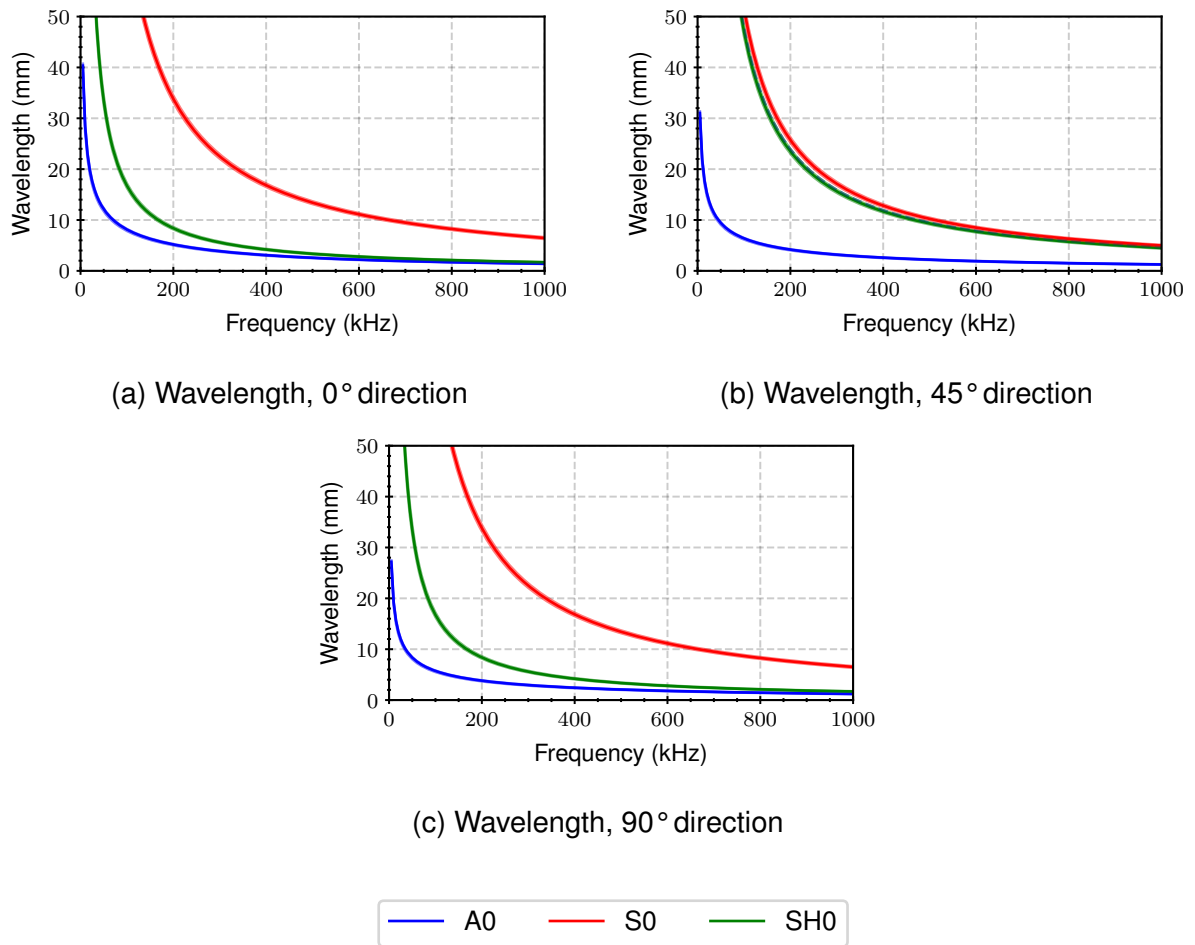
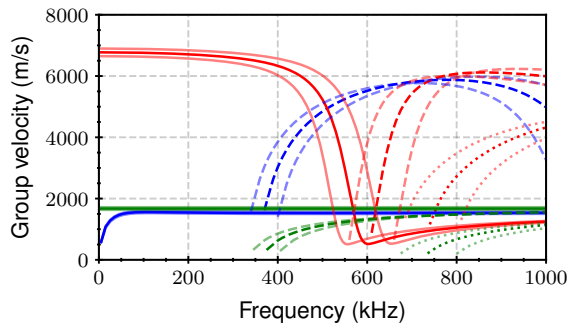


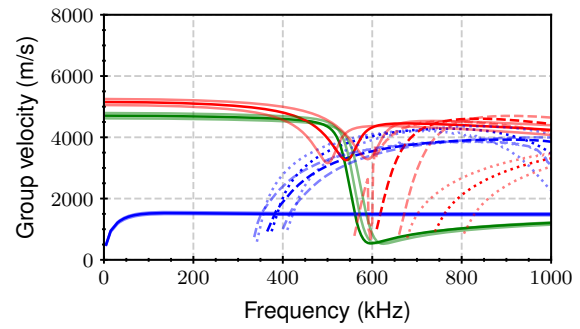
Figure D.5: Wavelengths (mm) (a,b,c) of Lamb wave modes in  $(0^\circ/90^\circ)_s$  laminates for propagation in the  $0^\circ$ ,  $45^\circ$  and  $90^\circ$  direction.



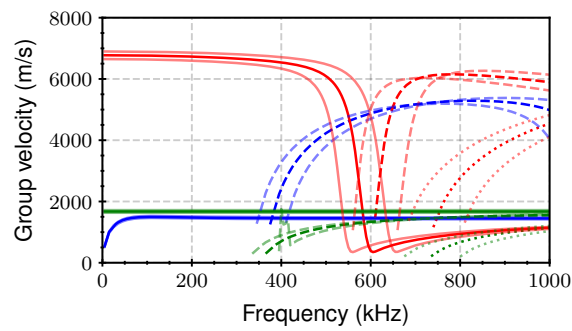
## D.2 $(0^\circ/90^\circ)_{4s}$ laminates



(a) Group velocity,  $0^\circ$  direction



(b) Group velocity,  $45^\circ$  direction



(c) Group velocity,  $90^\circ$  direction

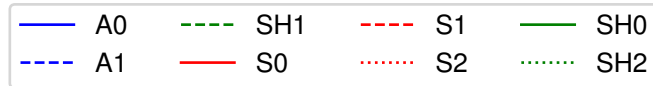


Figure D.6: Group velocities (m/s) (a,b,c) of Lamb wave modes in  $(0^\circ/90^\circ)_{4s}$  laminates for propagation in the  $0^\circ$ ,  $45^\circ$  and  $90^\circ$  direction.

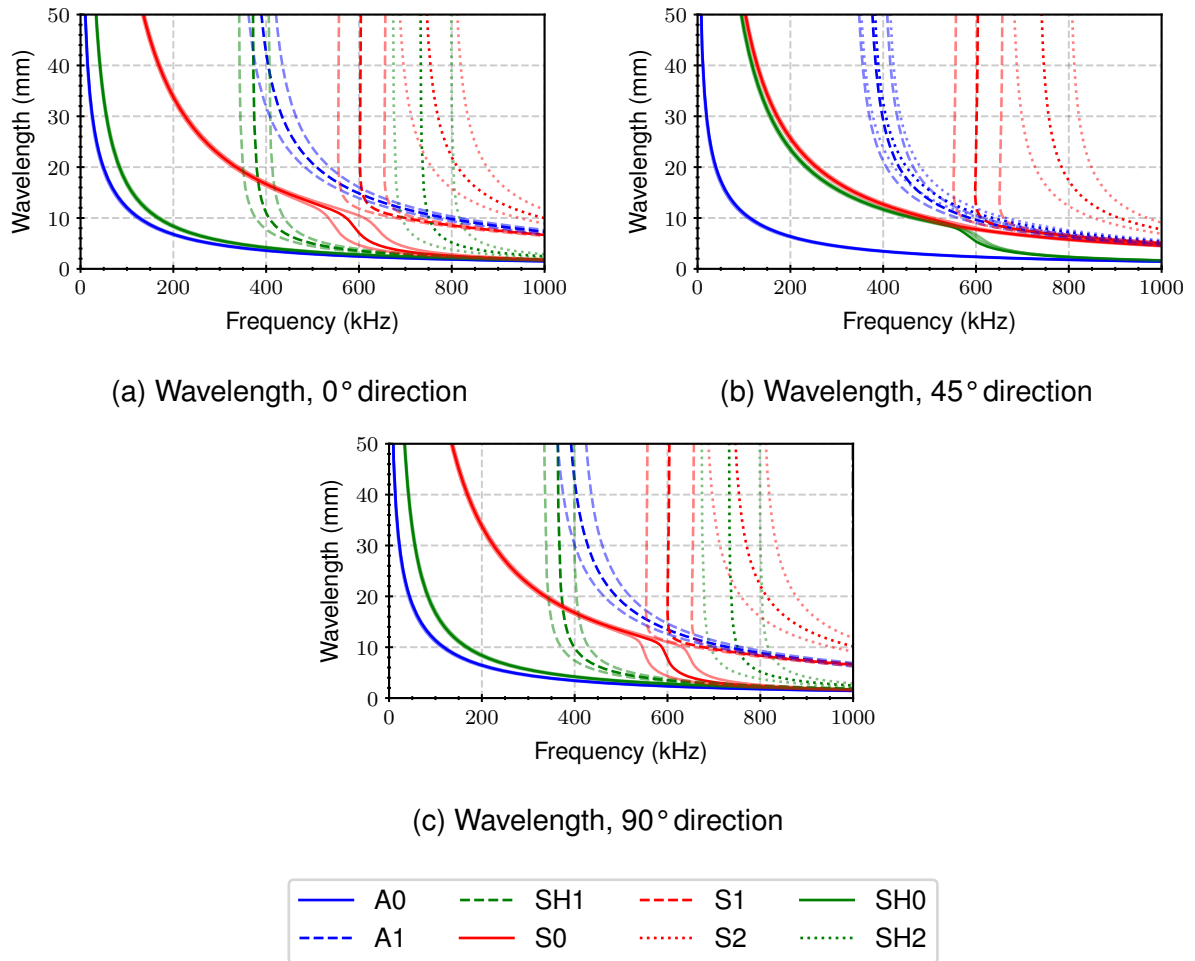


Figure D.7: Wavelengths (mm) (a,b,c) of Lamb wave modes in  $(0^\circ/90^\circ)_{4s}$  laminates for propagation in the  $0^\circ$ ,  $45^\circ$  and  $90^\circ$  direction.

## E Fixture for the characterization of wave propagation

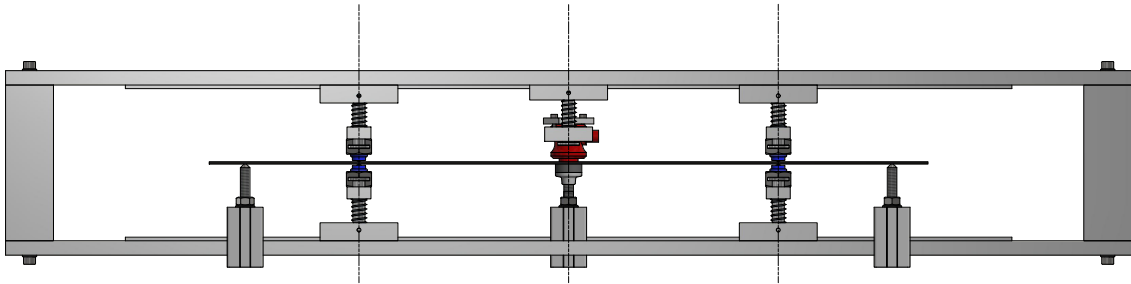


Figure E.8: Side view

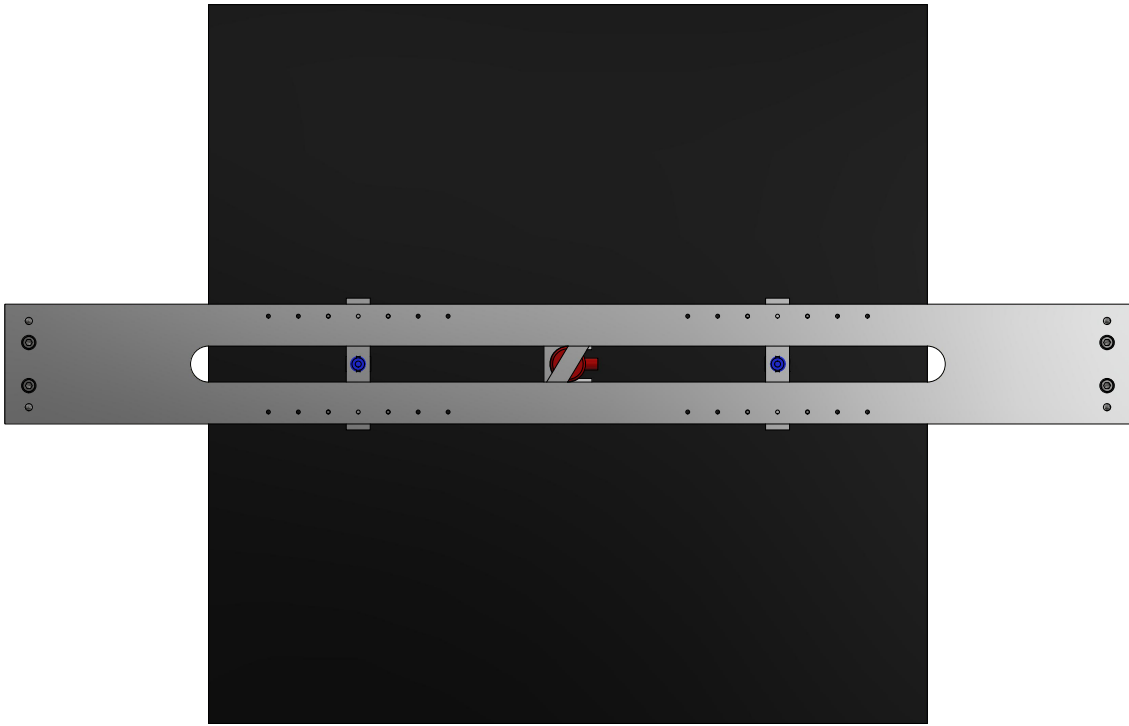


Figure E.9: Top view

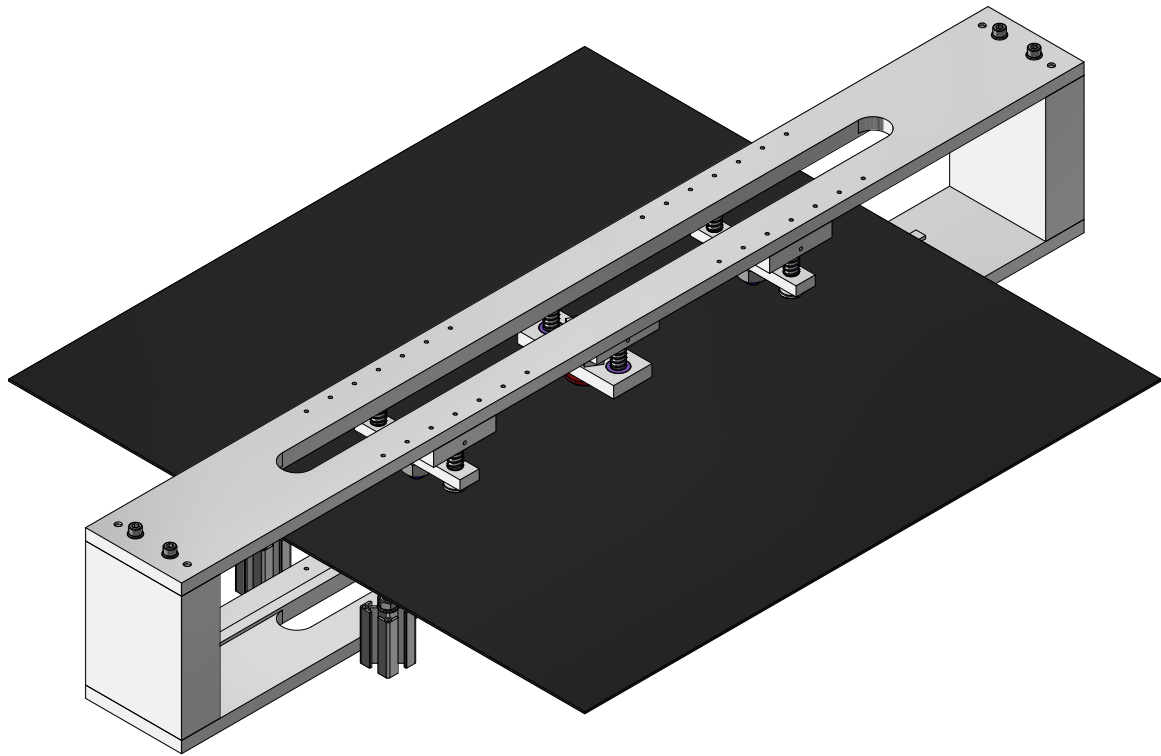


Figure E.10: Isometric view

## F Limitations to wave characterization

### F.1 Near field effects

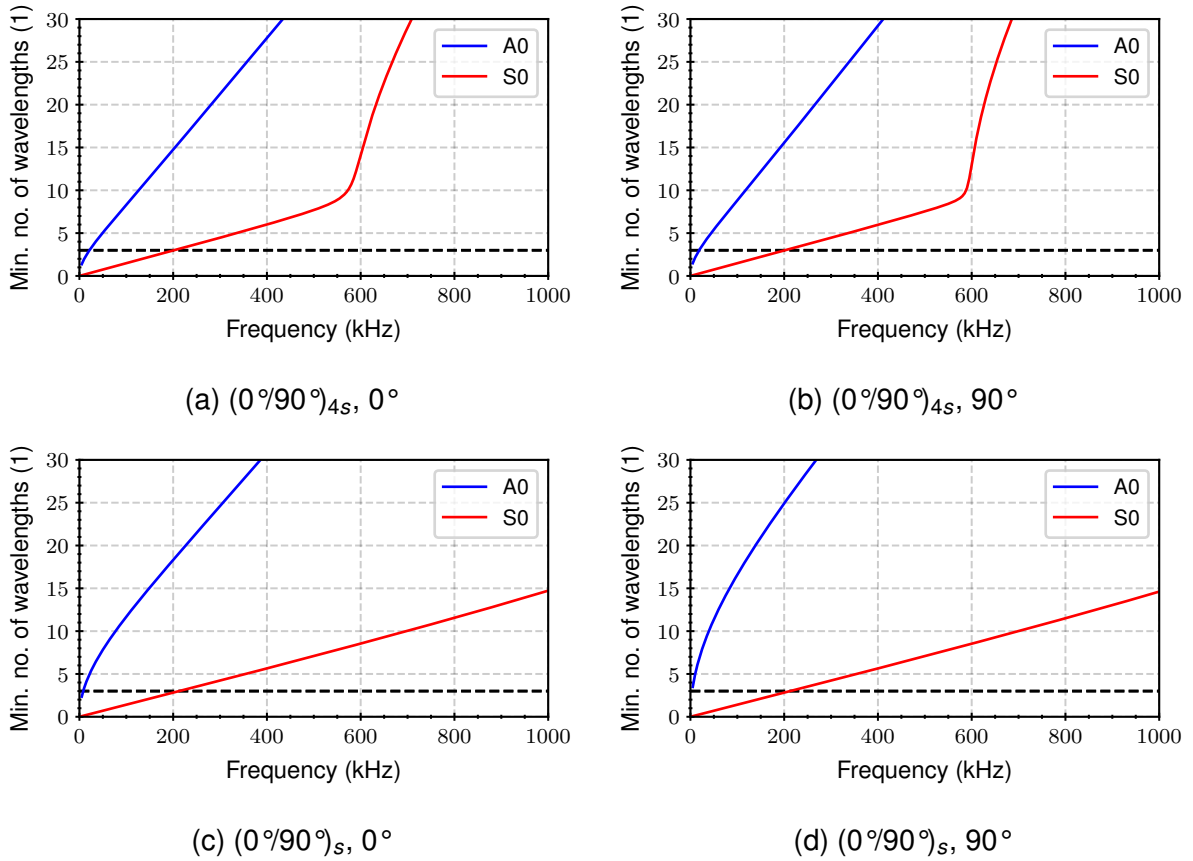


Figure F.11: Minimum number of wavelengths ( $l$ ) of the  $A_0$  and  $S_0$  mode as a function of frequency (kHz) for the  $(0^\circ/90^\circ)_{4s}$  and  $(0^\circ/90^\circ)_s$  setups from table 5.9.

## F.2 Excitability & detectability

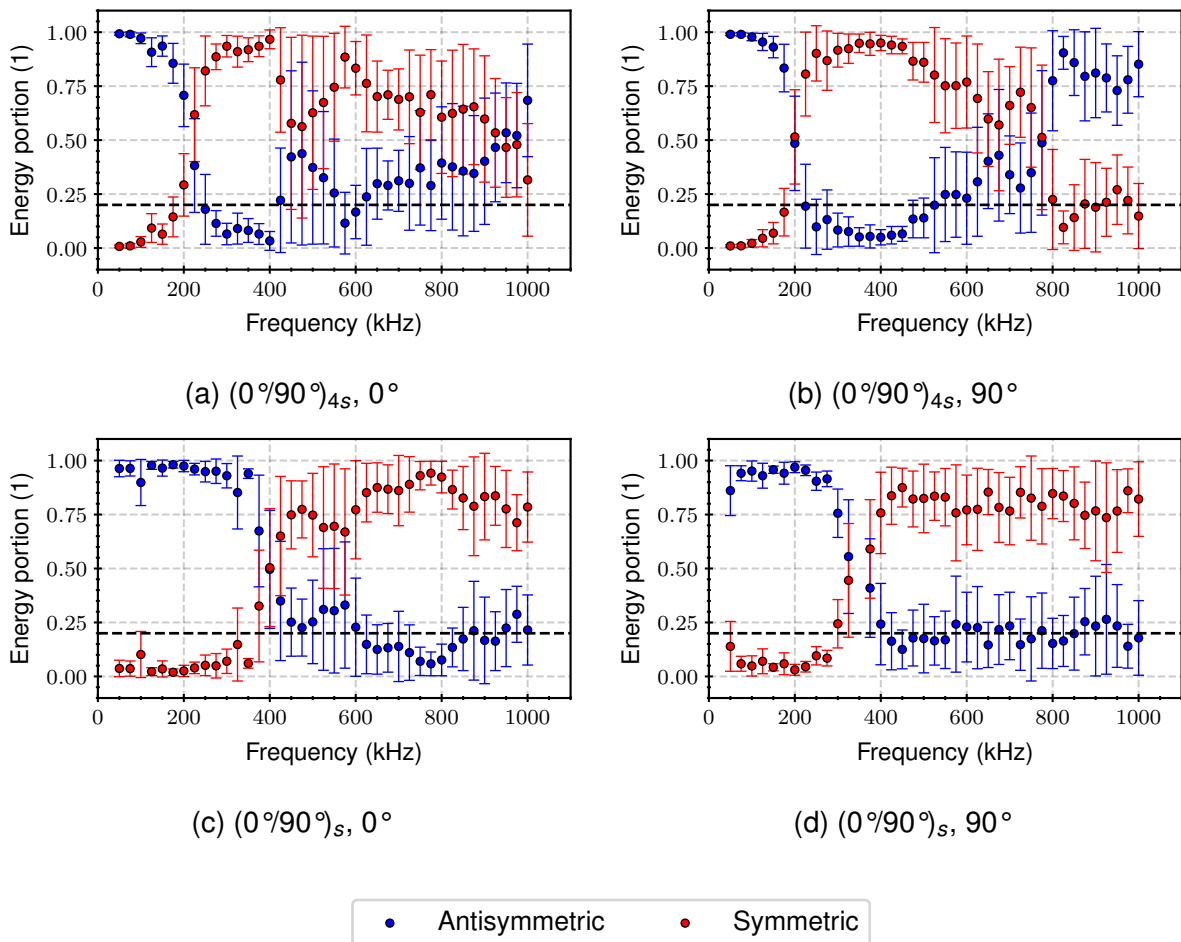


Figure F.12: Energy portions of symmetric and antisymmetric signals (1) as a function of excitation frequency (kHz). The values were experimentally determined from acquired signals in the  $0^\circ$  and  $90^\circ$  direction in the  $(0^\circ/90^\circ)_{4s}$  (a,b) and  $(0^\circ/90^\circ)_s$  (c,d) laminate.

### F.3 Modal separation

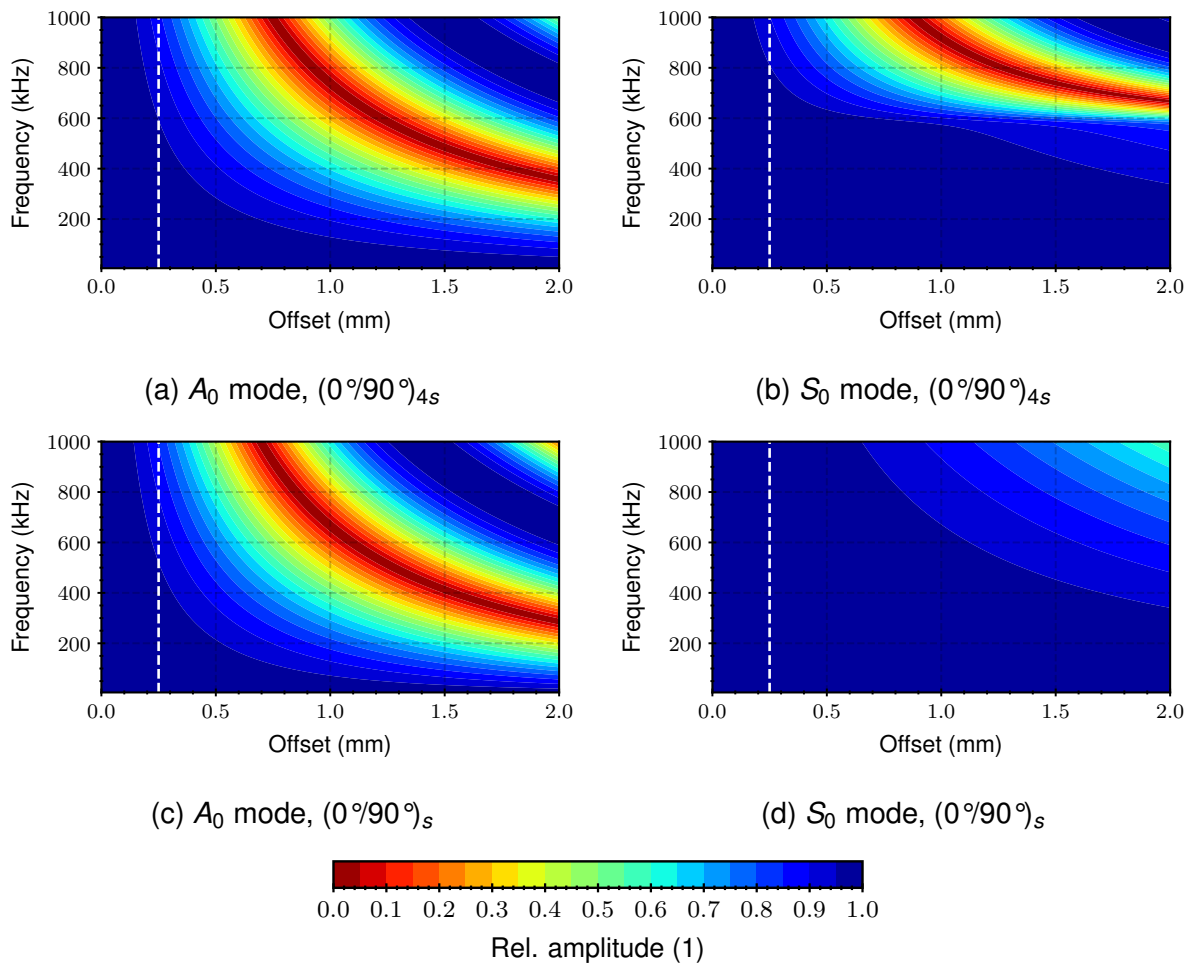


Figure F.13: Relative amplitude (1) as a function of frequency (kHz) and spatial offset (mm) for the superposition of wave packets from the  $A_0$  and  $S_0$  mode propagating in the  $0^\circ$  direction in the  $(0^\circ/90^\circ)_{4s}$  (a,b) and  $(0^\circ/90^\circ)_s$  (c,d) laminate.



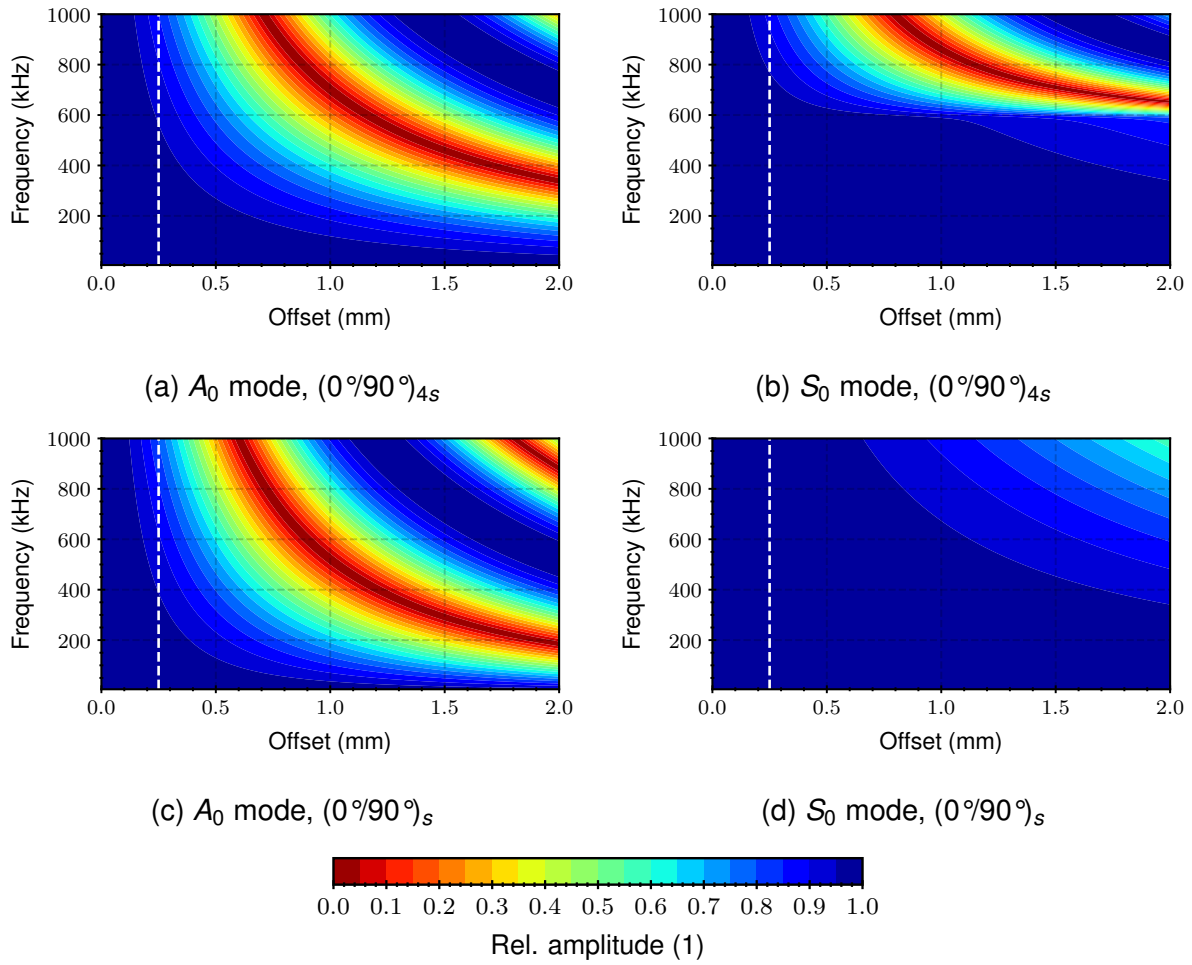


Figure F.14: Relative amplitude (1) as a function of frequency (kHz) and spatial offset (mm) for the superposition of wave packets from the  $A_0$  and  $S_0$  mode propagating in the  $90^\circ$  direction in the  $(0^\circ/90^\circ)_{4s}$  (a,b) and  $(0^\circ/90^\circ)_s$  (c,d) laminate.

## G Experimental dispersion diagrams

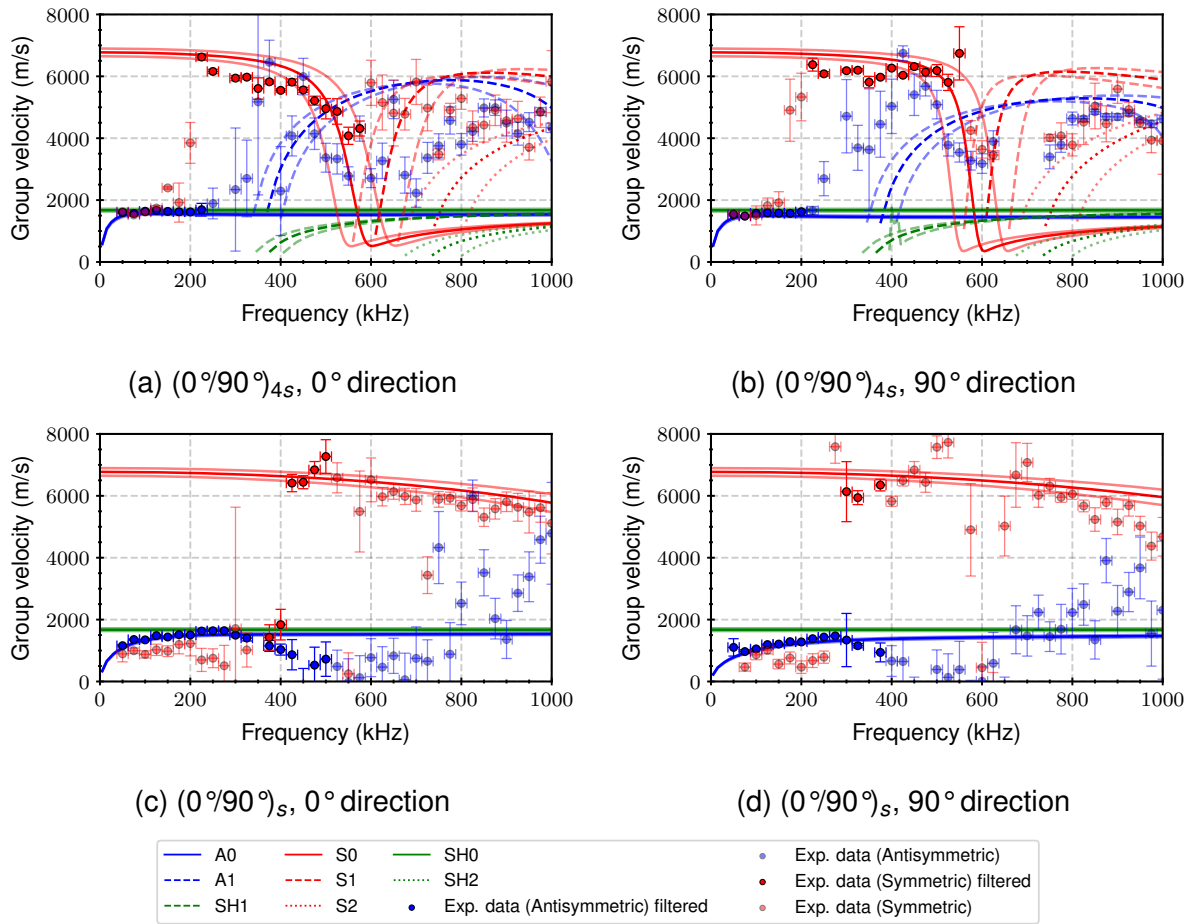


Figure G.15: Filtered (full color) and non-filtered (pale color) experimental results (dots) as well as theoretical results (lines) for the group velocities of wave modes as a function of frequency for the  $(0^\circ/90^\circ)_{4s}$  and  $(0^\circ/90^\circ)_s$  laminate in the  $0^\circ$  (a,c) and  $90^\circ$  (b,d) direction.

## H Preliminary study: Time signals

### H.1 45° direction

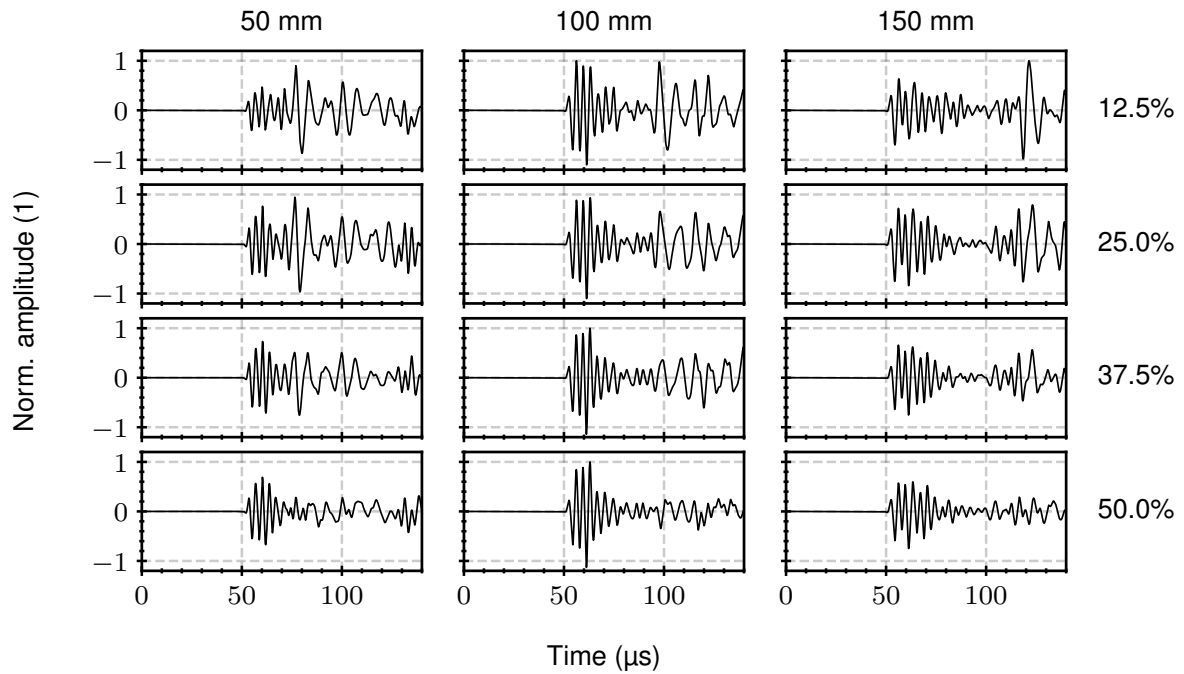


Figure H.16: Matrix plot of normalized time signals as function of source-to-sensor distance (50, 100 and 150 mm) and relative source depth (12.5, 25.0, 37.5 and 50.0%). Signals were acquired in the 45° direction.

## H.2 0° direction

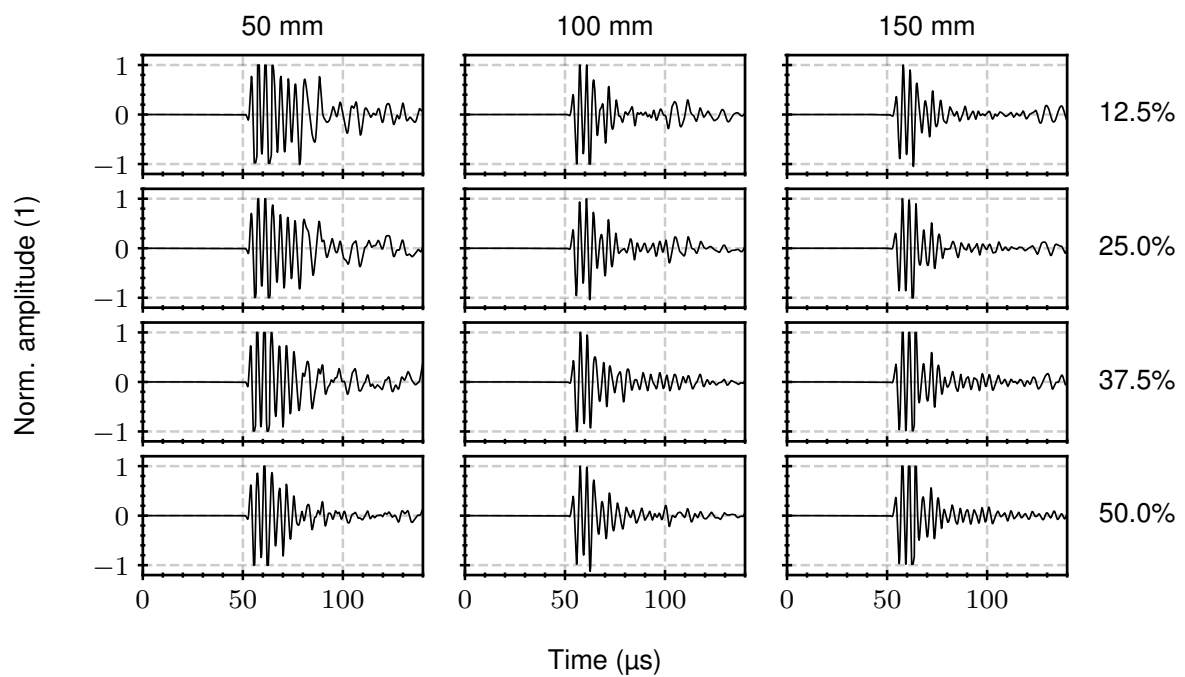


Figure H.17: Matrix plot of normalized time signals as function of source-to-sensor distance (50, 100 and 150 mm) and relative source depth (12.5, 25.0, 37.5 and 50.0%). Signals were acquired in the 0° direction.

# I Preliminary study: Continuous wavelet transforms

## I.1 45° direction

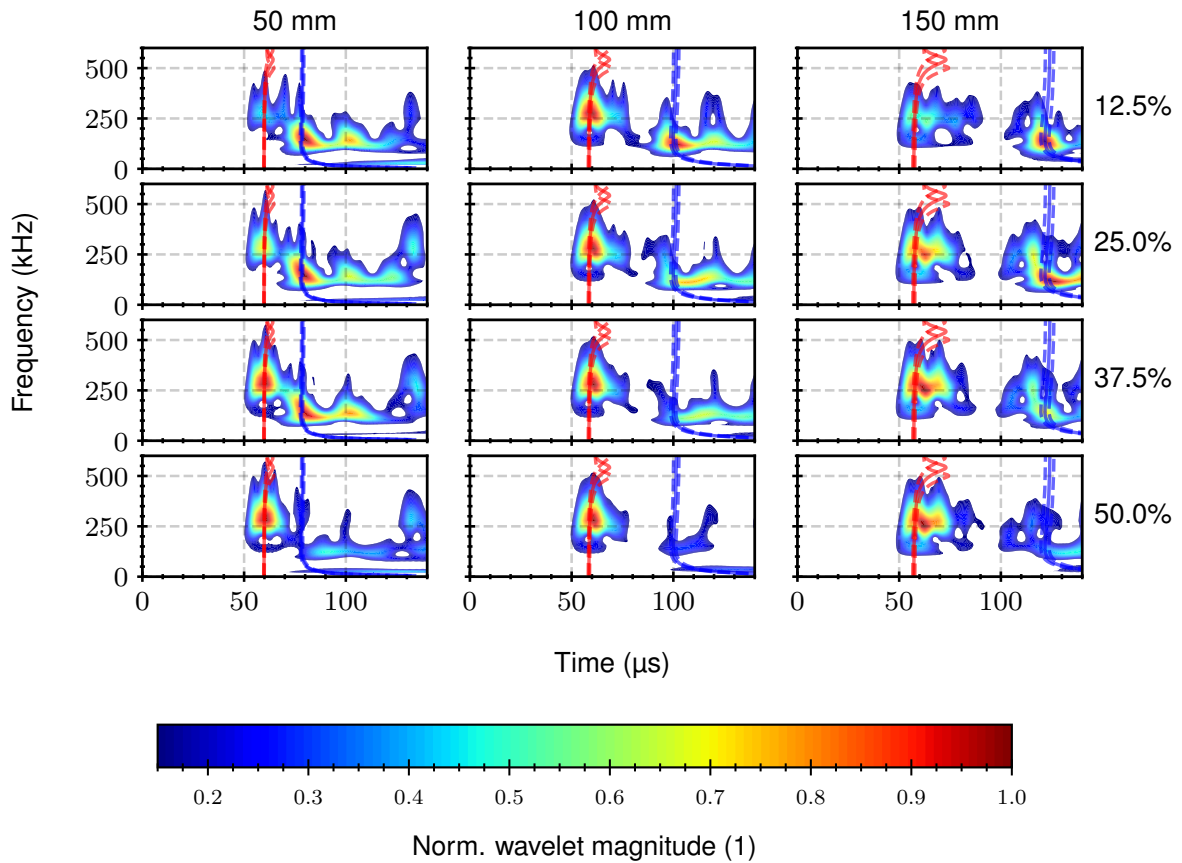


Figure I.18: Matrix plot of normalized CWTs as function of source-to-sensor distance (50, 100 and 150 mm) and relative source depth (12.5, 25.0, 37.5 and 50.0%). Signals were acquired in the 45° direction.

## I.2 0° direction

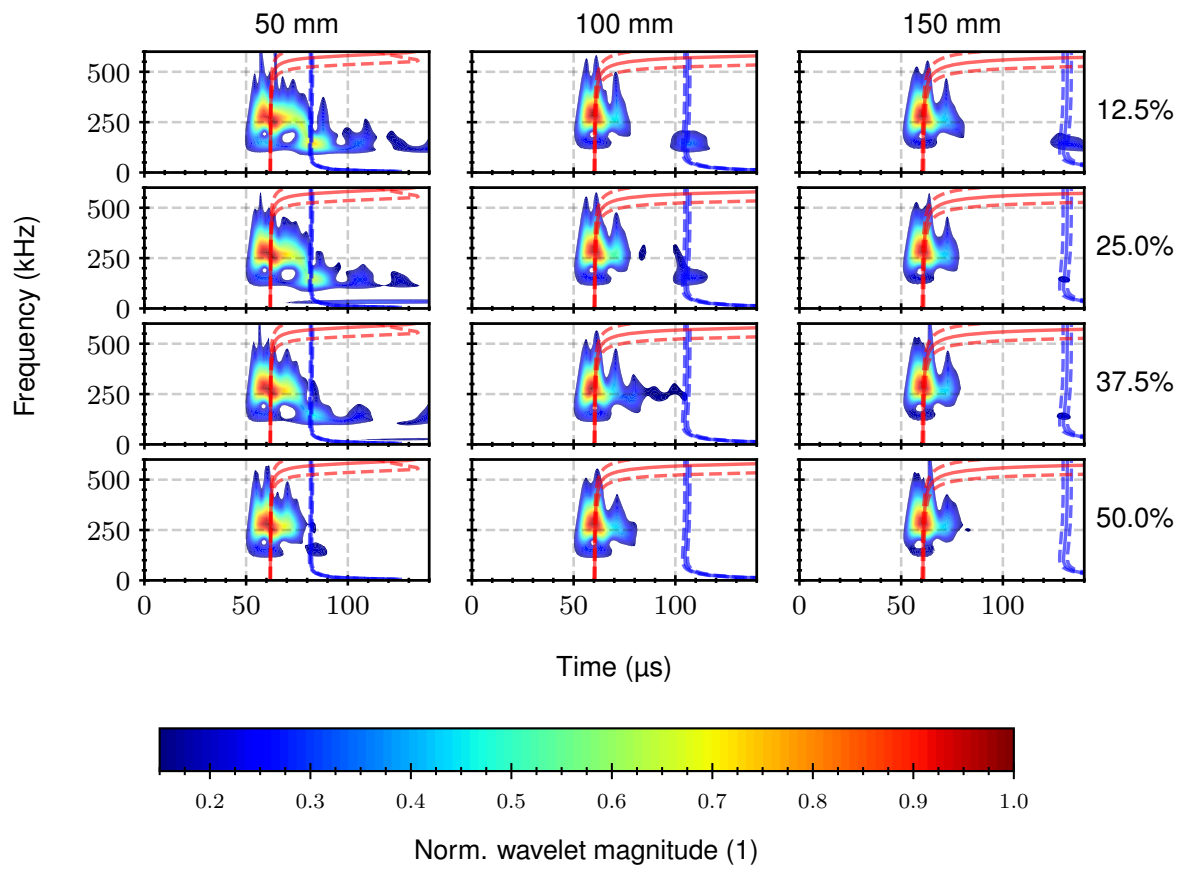


Figure I.19: Matrix plot of normalized CWTs as function of source-to-sensor distance (50, 100 and 150 mm) and relative source depth (12.5, 25.0, 37.5 and 50.0%). Signals were acquired in the 0° direction.

## J Preliminary study: Frequency spectra

### J.1 45° direction

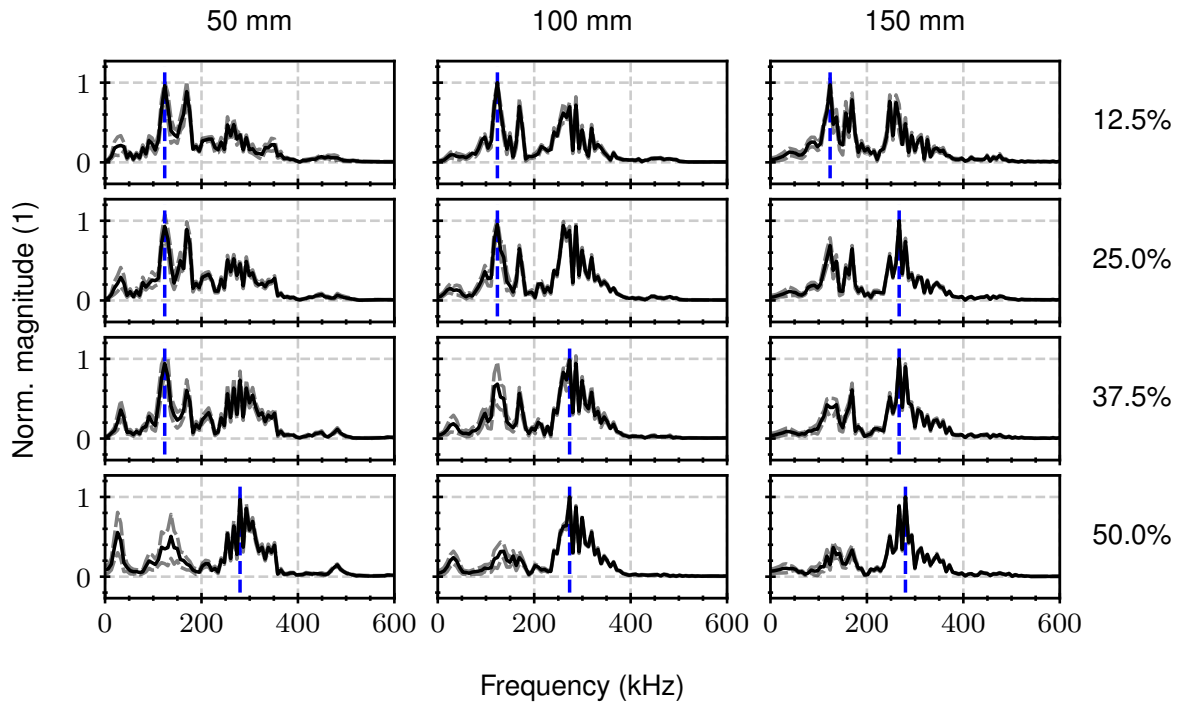


Figure J.20: Matrix plot of normalized FFT spectra as function of source-to-sensor distance (50, 100 and 150 mm) and relative source depth (12.5, 25.0, 37.5 and 50.0%). Signals were acquired in the 45° direction.

## J.2 0° direction

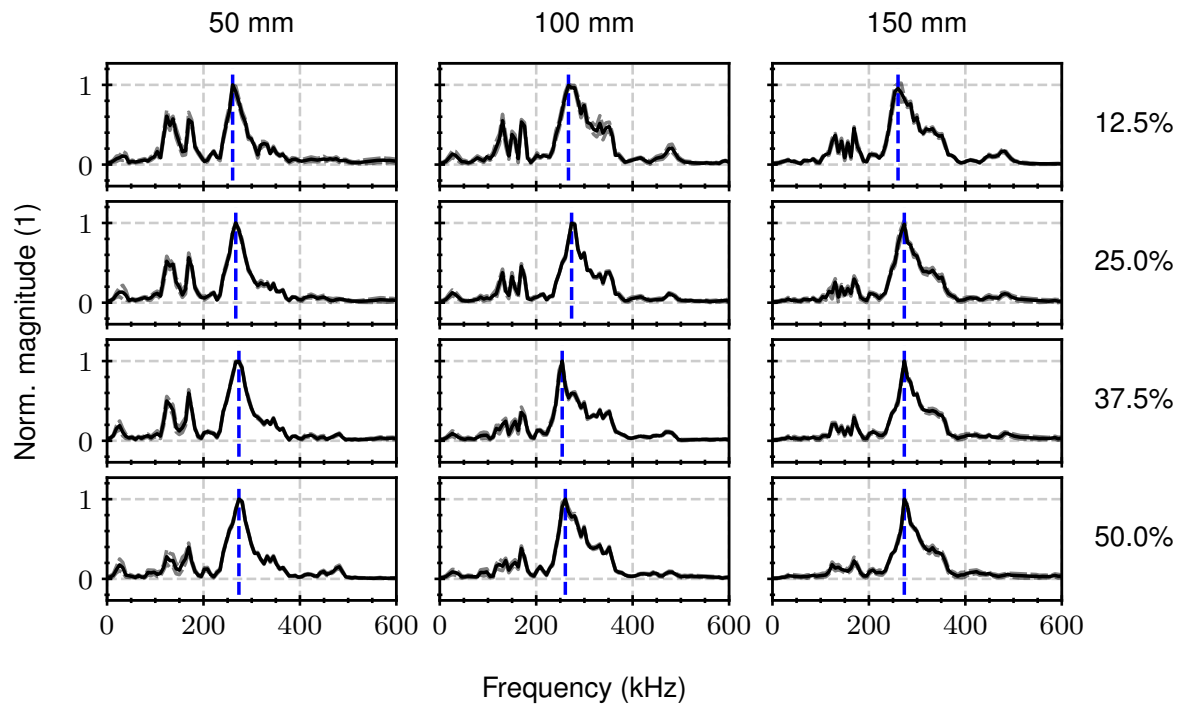


Figure J.21: Matrix plot of normalized FFT spectra as function of source-to-sensor distance (50, 100 and 150 mm) and relative source depth (12.5, 25.0, 37.5 and 50.0%). Signals were acquired in the 0° direction.



## K Main study: Tensile strength

### K.1 $(0^\circ/90^\circ)_s$ and $(90^\circ/0^\circ)_s$ specimens

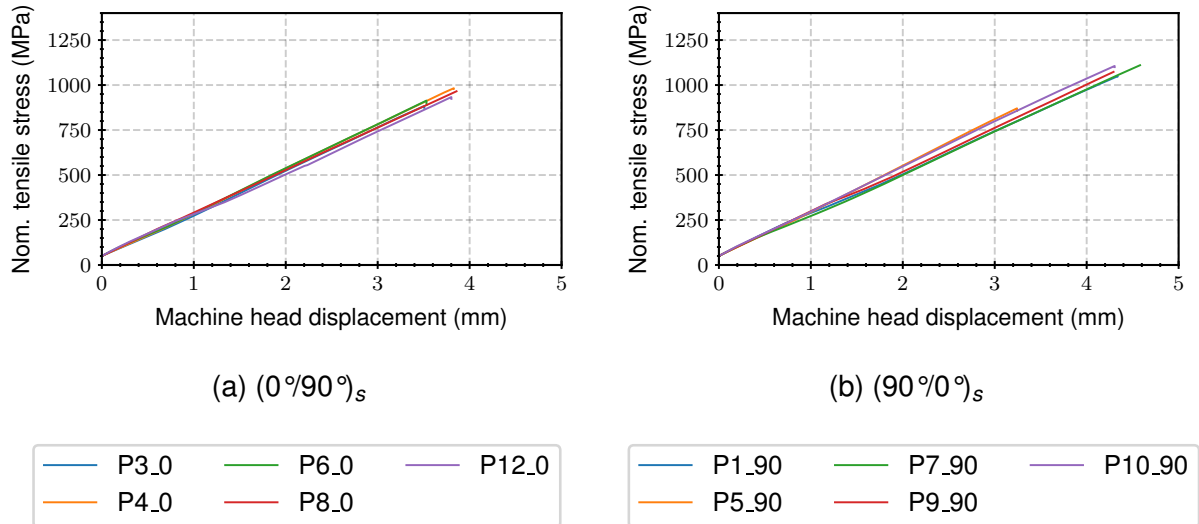


Figure K.22: Nominal tensile stress (MPa) versus machine head displacement (mm) for the  $(0^\circ/90^\circ)_s$  (a) and  $(90^\circ/0^\circ)_s$  (b) specimens.

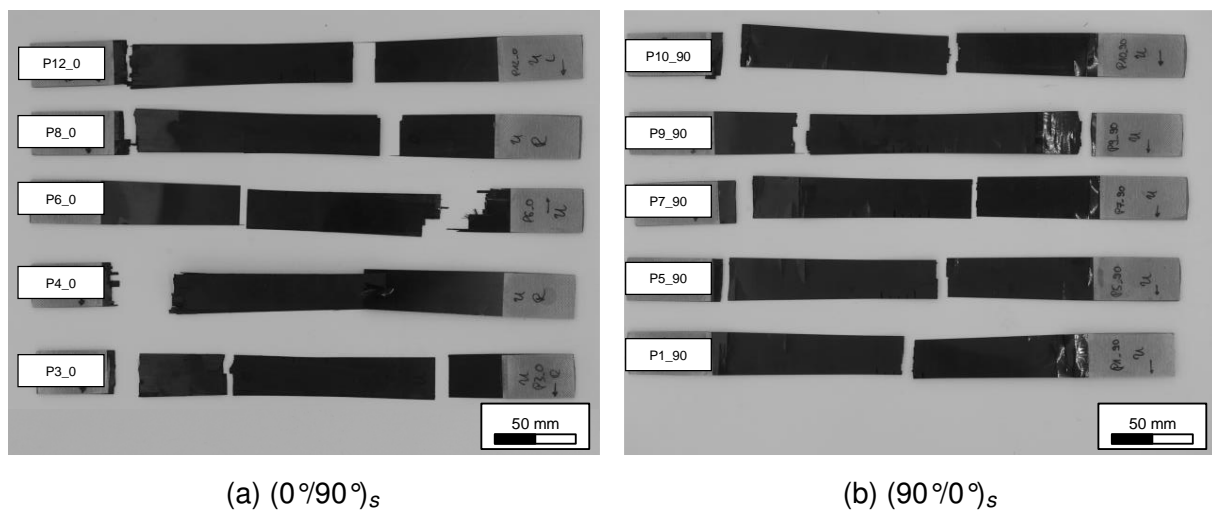


Figure K.23:  $(0^\circ/90^\circ)_s$  (a) and  $(90^\circ/0^\circ)_s$  (b) specimens after mechanical testing.

## K.2 $(0^\circ/90^\circ)_{4s}$ and $(90^\circ/0^\circ)_{4s}$ specimens

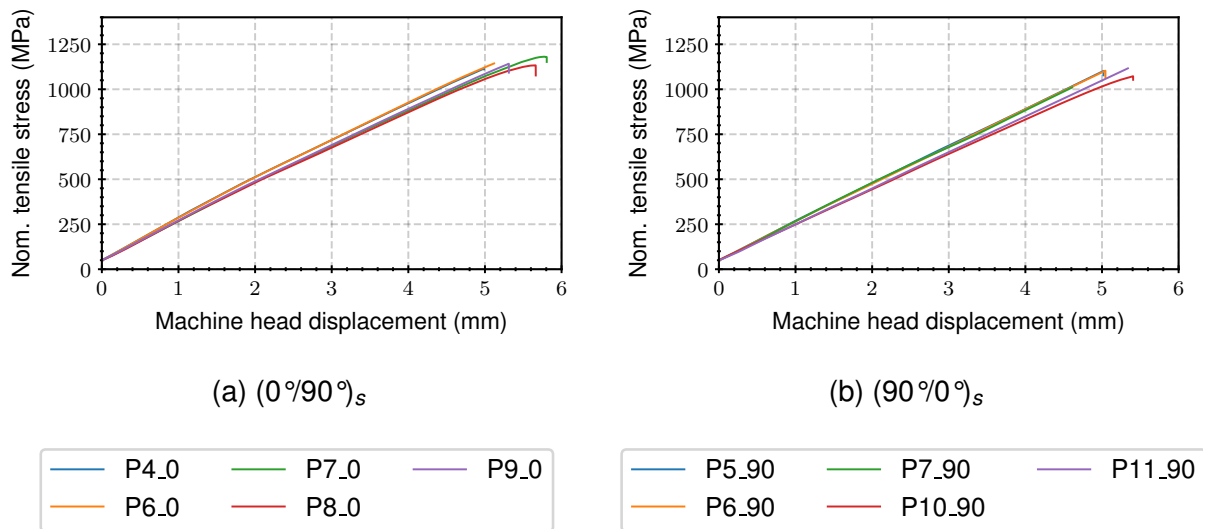


Figure K.24: Nominal tensile stress (MPa) versus machine head displacement (mm) for the  $(0^\circ/90^\circ)_{4s}$  (a) and  $(90^\circ/0^\circ)_{4s}$  (b) specimens.

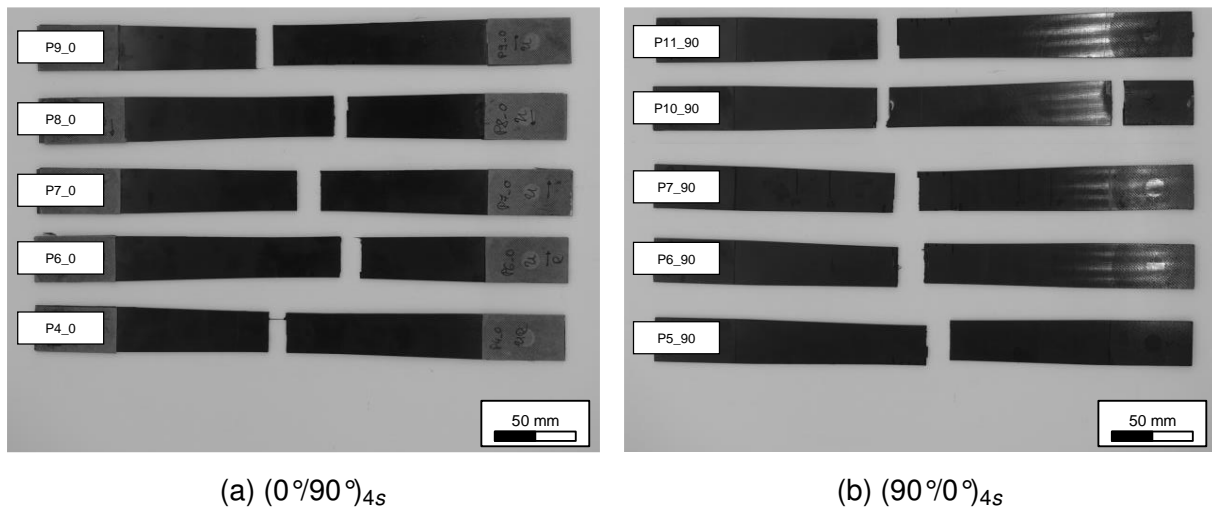


Figure K.25:  $(0^\circ/90^\circ)_{4s}$  (a) and  $(90^\circ/0^\circ)_{4s}$  (b) specimens after mechanical testing.

## L Influence of source-to-sensor distance: Feature development

### L.1 $(0^\circ/90^\circ)_s$ and $(90^\circ/0^\circ)_s$ specimens

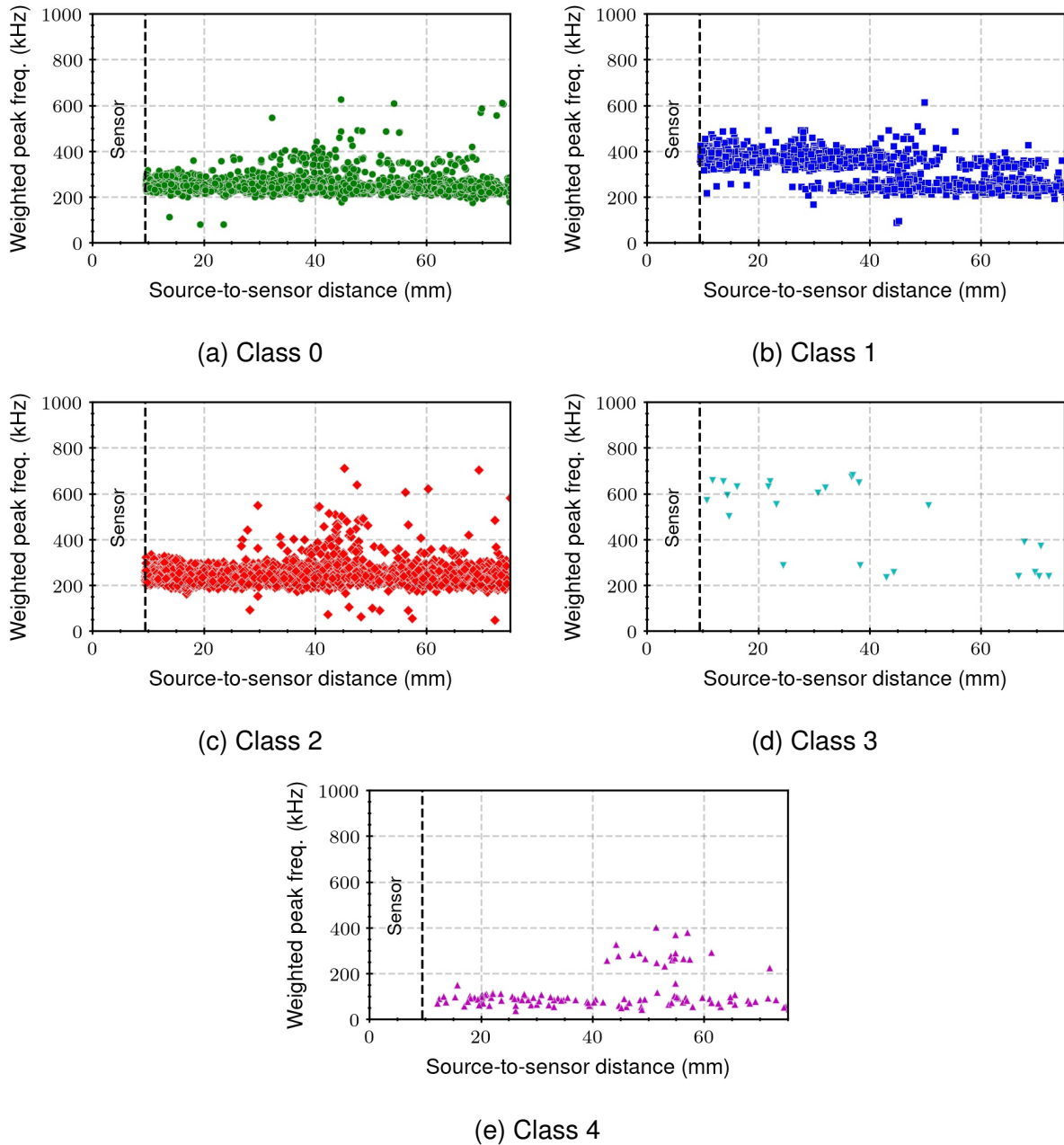


Figure L.26: Weighted peak frequency (kHz) as a function of source-to-sensor distance (mm) for AE events from classes 0 to 4 (a-e). Classification was based on the signals of the first triggering evaluation sensor.

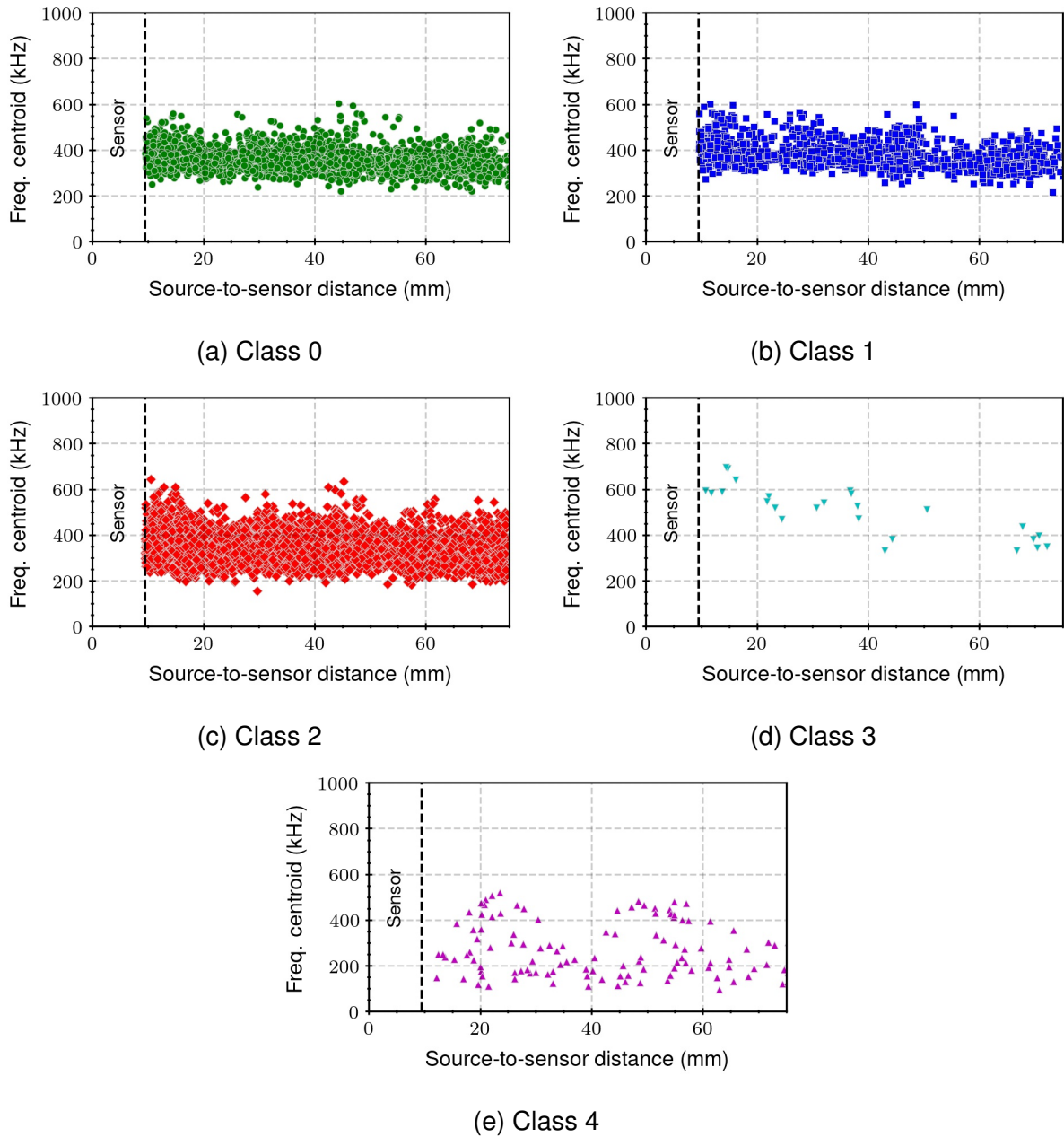
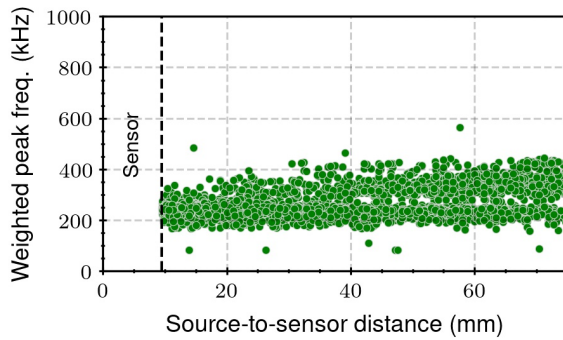
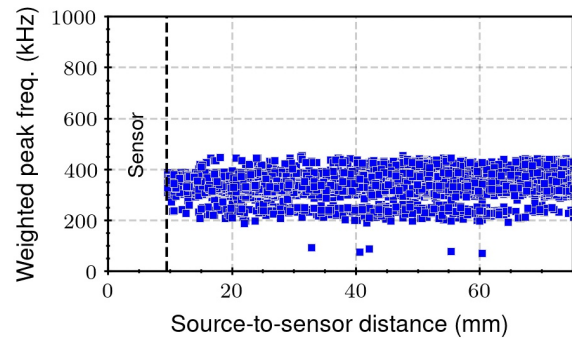


Figure L.27: Frequency centroid (kHz) as a function of source-to-sensor distance (mm) for AE events from classes 0 to 4 (a-e). Classification was based on the signals of the first triggering evaluation sensor.

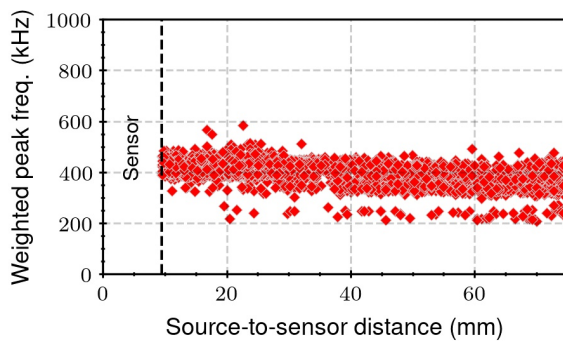
## L.2 $(0^\circ/90^\circ)_{4S}$ and $(90^\circ/0^\circ)_{4S}$ specimens



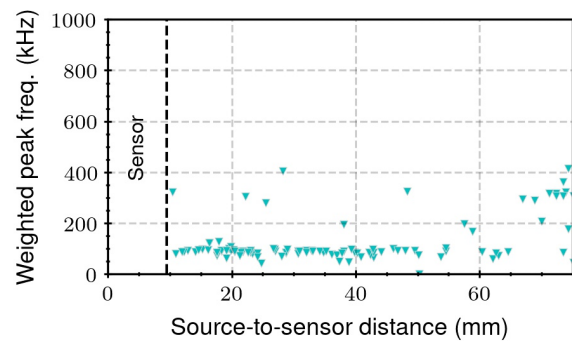
(a) Class 0



(b) Class 1



(c) Class 2



(d) Class 3

Figure L.28: Weighted peak frequency (kHz) as a function of source-to-sensor distance (mm) for AE events from classes 0 to 3 (a-d). Classification was based on the signals of the first triggering evaluation sensor.

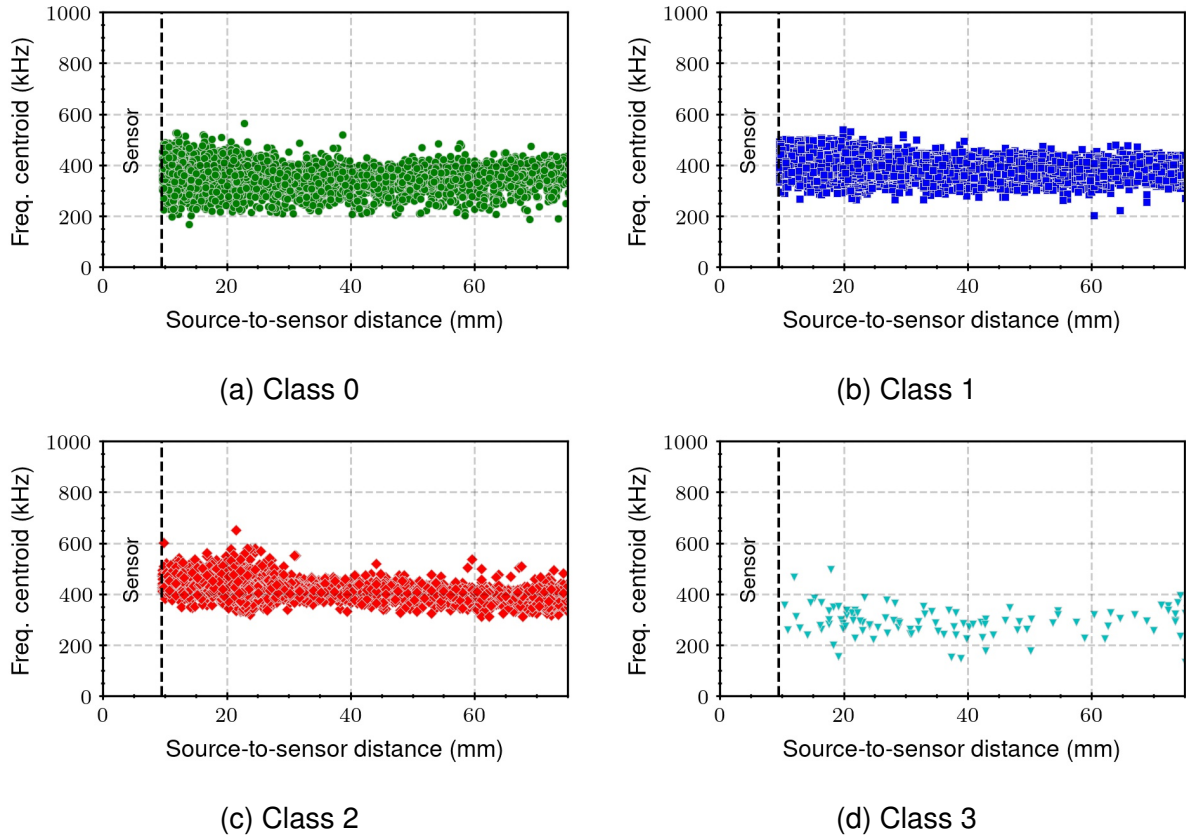


Figure L.29: Frequency centroid (kHz) as a function of source-to-sensor distance (mm) for AE events from classes 0 to 3 (a-d). Classification was based on the signals of the first triggering evaluation sensor.

## M Influence of source depth: Exemplary signals

Exemplary time signals and frequency spectra of class 0 events from figure 7.67 are visualized where more than one mode is present in the evaluation window.

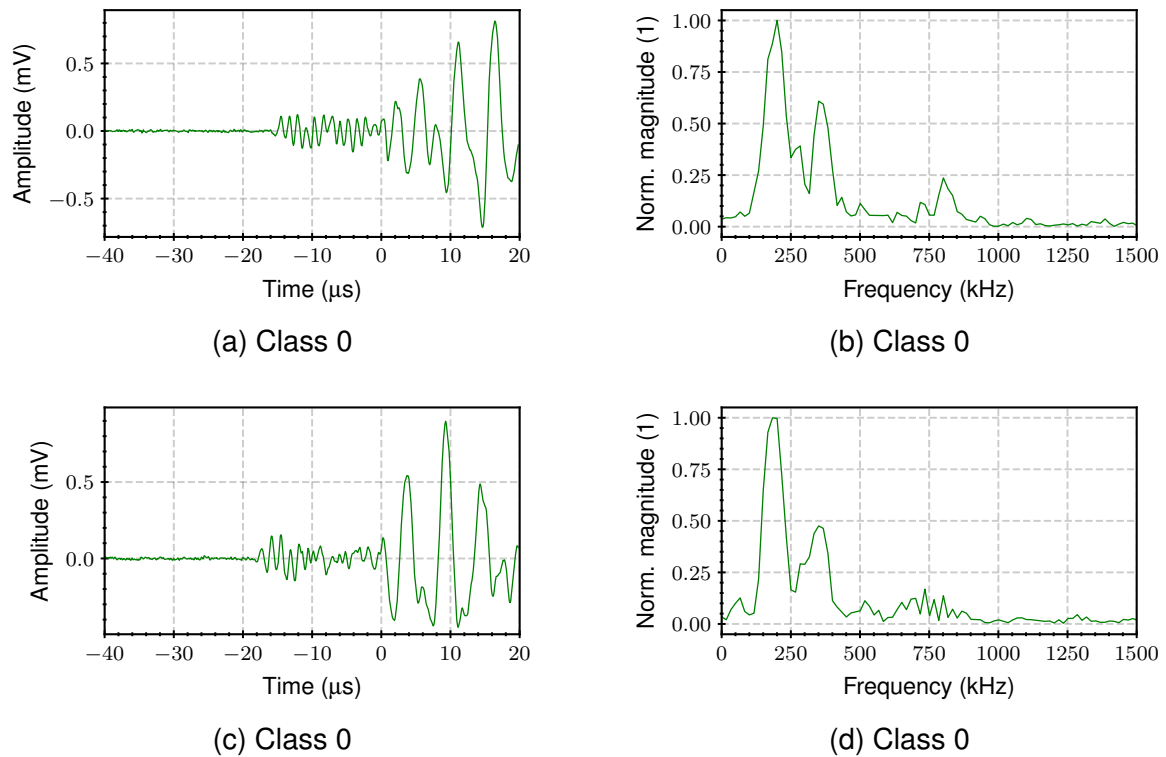


Figure M.30: Exemplary time signals (a,c) and normalized frequency spectra (b,d) of class 0 events from  $(0^\circ/90^\circ)_s$  and  $(90^\circ/0^\circ)_s$  specimens where more than one mode was present in the evaluation window.

## Conferences & Publications

1. Kelkel, B., Sebastian, R., Hübler, M., Gurka, M.: *New Approaches for the Manufacturing and Characterization of Smart Structures made of Fiber-Reinforced Plastics*, 7<sup>th</sup> ECCOMAS Thematic Conference on Smart Structures and Materials (SMART-2015), Ponta Delgada, Azores, 3-6 June 2015
2. Kelkel, B.: *Local Characterization of Lamb Wave Propagation in Carbon Fiber-Reinforced Plastics*, 6<sup>th</sup> International Symposium on Piezocomposite Applications (ISPA-2015), Dresden, Germany, 17-18 September 2015
3. Kelkel, B., Sebastian, R., Gurka, M., Traub, T., L'huillier, J., Poltawski, J., Günster, S.: *A New Concept for the Non-Destructive Testing of Fiber-Reinforced Plastics via Laser Generated Ultrasonic Guided Waves*, 19<sup>th</sup> World Conference on Non-Destructive Testing (WCNDT-2016), Munich, Germany, 13-17 June 2016
4. Kelkel, B., Popow, V., Gurka, M.: *Combining acoustic emission with passive thermography to characterize damage progression in cross-ply CFRP laminates during quasi-static tensile loading*, 12<sup>th</sup> European Conference on Non-Destructive Testing (ECNDT-2018), Gothenburg, Sweden, 11-15 June 2018
5. Popow, V., Kelkel, B., Gurka, M.: *Passive impulse thermography during quasi-static tensile tests of fiber reinforced composites*, 12<sup>th</sup> European Conference on Non-Destructive Testing (ECNDT-2018), Gothenburg, Sweden, 11-15 June 2018
6. Kelkel, B., Vogtmann, J., Gurka, M.: *The influence of source depth and source-to-sensor distance on the AE signal characteristics of damaging events in thin-walled CFRP laminates*, 33<sup>rd</sup> European Conference on Acoustic Emission Testing (EWGAE-2018), Senlis, France, 12-14 September 2018
7. Kelkel, B., Woll, J., Vogtmann, J., Gurka, M.: *Potentiale, Risiken und Herausforderungen der modalen Schallemissionsanalyse bei der Quellenidentifikation in dünnwandigen Faserkunststoffverbunden*, 22. DGZfP Kolloquium Schallemission und 3. Anwenderseminar Zustandsüberwachung mit geführten Wellen, Karlsruhe, Germany, 27-28 March 2019
8. Kelkel, B., Argus, P., Gurka, M.: *Demonstrator zur in-situ Lokalisierung von Schädigungsereignissen in dünnwandigen CFK Strukturen*, 3. Symposium für Smarte Strukturen und Systeme (4SMARTS-2019), Darmstadt, Germany, 22-23 May 2019
9. Kelkel, B., Gurka, M.: *Anwendung der modalen Schallemissionsanalyse zur Charakterisierung des Degradationsverhaltens dünnwandiger CFK Laminat*



---

*unter quasi-statischer Zugbelastung*, DGZfP Jahrestagung 2019 (DGZfP-2019), Friedrichshafen, Germany, 27-29 May 2019

10. Kelkel, B., Argus, P., Gurka, M.: Scalable monitoring system for the localization of damaging events in thin-walled CFRP structures based on acoustic emission analysis and neural networks. *Key Engineering Materials*, 809:401-406, June 2019
11. Kelkel, B., Argus, P., Gurka, M.: *Scalable monitoring system for the localization of damaging events in thin-walled CFRP structures based on acoustic emission analysis and neural networks*, 22. Symposium Verbundwerkstoffe und Werkstoffverbunde (DGM-2019), Kaiserslautern, Germany, 26-28 June 2019
12. Klingler, A., Kelkel, B., Gurka, M., Wetzel, B.: *Charakterisierung der Faser-Matrix Haftung mittels Einzelfaser-Broutman-Test und Schallemissionsanalyse*, 22. Symposium Verbundwerkstoffe und Werkstoffverbunde (DGM-2019), Kaiserslautern, Germany, 26-28 June 2019
13. Kelkel, B., Popow, V., Gurka, M.: Inline quantification and localization of transverse matrix cracking in cross-ply CFRP during quasi-static tensile testing by a joint event-based evaluation of acoustic emission and passive IR thermography. *Composites Science and Technology*, 190:108013, April 2020

## Student thesis

1. Popow, Vitalij: *Analyse der Amplitudenabschwächung von Lamb-Wellen in CFK Verbundstrukturen*, Masterarbeit, IVW Bericht 15-035, 06/2015
2. Brill, Kim: *Integration eines Moduls zur Berechnung und Analyse von Dispersionskurven von Lamb-Wellen in Faserkunststoffverbundstrukturen innerhalb der Programmierumgebung LabVIEW*, Bachelorarbeit, IVW Bericht 16-021, 03/2016
3. Dolezel, Christian: *Identifizierung und Realisierung von Konzepten zur modenselektiven Anregung von Lamb-Wellen zur zerstörungsfreien Prüfung von Faserkunststoffverbunden*, Diplomarbeit, IVW Bericht 16-025, 04/2016
4. Günster, Sven: *Entwicklung eines Prüfstandes zur Messung und Analyse der Lamb-Wellenausbreitung in plattenförmigen Probekörpern mittels Laservibrometrie*, Diplomarbeit, IVW Bericht 16-035, 05/2016
5. Winter, Thorsten: *Vergleich zwischen der thermischen Anregung durch Heizfolien und einem Halogenstrahler bei der zerstörungsfreien Prüfung von CFKBauteilen mittels Shearografie*, Studienarbeit, IVW Bericht 16-020, 06/2016
6. Poltawski, Jurij: *Modenselektive Anregung von Lamb-Wellen mittels Puls-LASER*, Masterarbeit, IVW Bericht 16-044, 06/2016
7. Schweigert, Hans: *Analyse der Amplitudenabschwächung von Lamb-Wellen in Aluminium*, Masterarbeit, IVW Bericht 16-069, 08/2016
8. Stemler, Marius: *Untersuchung des Einflusses der Laufstrecke auf ausgewählte Schallemissionsparameter in Platten isotroper und anisotroper Werkstoffe*, Masterarbeit, IVW Bericht 17-038, 07/2017
9. Vogtmann, Julia: *Untersuchung zum Einfluss der Quelltiefe auf ausgewählte Charakteristika des resultierenden akustischen Signals in Aluminium und unidirektionalen CFK Platten*, Studienarbeit, IVW Bericht 18-018, 03/2018
10. Boos, Wladimir: *Anwendung der aktiven und passiven Thermographie zur Visualisierung von Schadensereignissen während der quasi-statischen Zugprüfung von kontinuierlich faserverstärkten Kunststoffen*, Masterarbeit, IVW Bericht 18-014, 03/2018
11. Zerwes, Marius: *Anwendung künstlicher neuronaler Netzwerke zur Lokalisierung von Schadensereignissen in dünnwandigen Faserkunststoffverbunden im Rahmen der Schallemissionsanalyse*, Diplomarbeit, IVW Bericht 18-032, 05/2018

12. Woll, Johannes: *Simulation geführter Wellen in isotropen und anisotropen Werkstoffen bei unterschiedlichen Anregungstiefen*, Diplomarbeit, IVW Bericht 19-011, 02/2019
13. Argus, Philipp: *Entwicklung eines Demonstrators zur Lokalisierung von künstlichen Schallquellen in dünnwandigen Faserverbundstrukturen auf Basis der Schallemissionsanalyse und künstlicher neuronaler Netzwerke*, Studienarbeit, IVW Bericht 19-023, 04/2019

## Curriculum Vitae

### Personal information

---

Name Benjamin Kelkel

### Work experience

---

05/2020 – present August-Wilhelm Scheer Institute, Saarbrücken (Germany)  
Digitization Professional

07/2014 – 12/2019 Institute for Composite Materials GmbH, Kaiserslautern (Germany)  
Research Associate

08/2012 – 06/2014 Ferchau Engineering GmbH, Heilbronn (Germany)  
Development Engineer (Automotive)

02/2012 – 07/2012 Robert Bosch GmbH, Gerlingen Schillerhöhe (Germany)  
Diploma thesis

09/2011 – 01/2012 Robert Bosch GmbH, Gerlingen Schillerhöhe (Germany)  
Internship

### Education

---

10/2005 – 09/2012 University of Saarland, Saarbrücken (Germany)  
Diploma, Materials Science

09/2009 – 09/2010 Oregon State University, Corvallis (United States)  
Bachelor of Science, Mechanical Engineering

03/2009 – 06/2009 Luleå University of Technology, Luleå (Sweden)  
Semester abroad

08/1996 – 06/2005 High school, Warndtgymnasium, Geislautern (Germany)

08/1992 – 07/1996 Elementary school, Werbeln (Germany)



